CH formation in premixed flames of C_1–C_4 alkanes: assessment of current chemical modelling capability against experiments

Philippe Versailles

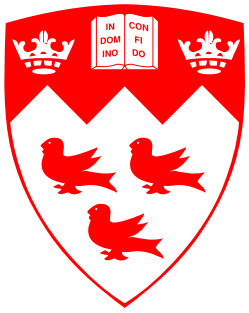

Department of Mechanical Engineering

McGill University

Montréal, QC, Canada

April 2017

A thesis submitted to McGill University in partial fulfillment of the requirements of the degree of Doctor of Philosophy

Abstract

Nitric oxide, NO, is a primary pollutant produced by the oxidation of nitrogen mainly in combustion-based applications. In the atmosphere, NO is rapidly oxidized to $\mathrm{NO_2}$, which is involved in the formation of ground-level ozone, acid precipitations, fine particulate matter, and nutrient pollution, affecting human health and the environment. Four NO formation pathways are recognized in gaseous flames: thermal (Zel'dovich), prompt (Fenimore), $\mathrm{N_2O}$, and NNH. The prompt route, initiated by the reaction $\mathrm{CH+N_2 \leftrightarrow NCN+H}$, is responsible for the rapid production of NO within the front of hydrocarbon flames. A strong correlation exists between the maximum concentration of the methylidyne radical, $[\mathrm{CH}]_{\mathrm{peak}}$, and the formation of NO in the flame front region.

This work presents absolute measurements of $[\mathrm{CH}]_{\mathrm{peak}}$ taken in atmospheric-pressure, premixed, stagnation flames of methane, ethane, propane, and *n*-butane. One-dimensional (1D) CH fluorescence profiles are extracted from 2D Planar Laser-Induced Fluorescence (PLIF) measurements made quantitative through normalization by the Rayleigh scattering signal of nitrogen. For all fuels, the CH-LIF signal is maximized at an equivalence ratio of 1.2, and decreases monotonically for leaner and richer mixtures. The consistency of this behaviour for all fuels suggests that CH formation is determined by fuel-independent elementary reactions.

Axial velocity profiles are measured by Particle Tracking Velocimetry (PTV) and, along with mixture composition and temperature measurements, provide the required boundary conditions for quasi-one-dimensional flame simulations. A purposely developed, time-resolved, four-level LIF model considering rotational energy transfer in the ground and electronically excited states is used to convert the modelled CH concentration profiles into units compatible with the quantitative CH-LIF measurements.

Large variations in the CH concentrations predicted by four thermochemical mechanisms are observed for all fuels and equivalence ratios considered. A detailed study of the mechanisms, through reaction pathway and sensitivity analyses, shows that the principal reactions impacting CH formation are: a) involved in the CH formation route ($\mathrm{CH_3 \rightarrow CH_2^* \rightarrow CH_2 \rightarrow CH}$), b) bypass and remove carbon atoms from the CH formation route, or c) affect the pool of reaction partners in the aforementioned reactions. The order of magnitude variability in the model predictions is caused by significant disagreements among the mechanisms in terms of rate coefficients and reactions included in these pathways.

As observed previously, the thermochemical mechanisms overestimate the decline of $[\mathrm{CH}]_{\mathrm{peak}}$ as the stoichiometry is shifted to lean mixtures. To identify the source of this behaviour, an optimization procedure is applied to the San Diego mechanism. The pre-exponential factor of nine

elementary reactions interacting with the CH formation route is adjusted to yield two separate thermochemical mechanisms that agree, within uncertainty, with the experimental data. These models will enable accurate predictions of prompt-NO formation over a wide range of equivalence ratios.

Résumé

Le monoxyde d'azote (NO) est un polluant primaire formé par l'oxydation de l'azote lors de la combustion de carburants avec l'air. Dans l'atmosphère, le monoxyde d'azote est rapidement oxydé en dioxyde d'azote ($\mathrm{NO_2}$) qui est impliqué dans la formation d'ozone troposphérique, de précipitations acides, de particules fines et de pollution azotée des eaux de surface. Ces différents types de pollution ont des impacts majeurs sur la santé humaine et l'environnement. Quatre principaux mécanismes chimiques participent à la formation de NO dans les flammes de carburants gazeux. La réaction $\mathrm{CH} + \mathrm{N_2} \leftrightarrow \mathrm{NCN} + \mathrm{H}$ enclenche le mécanisme de Fenimore (*prompt*) qui entraîne la formation rapide de NO au travers du front des flammes d'hydrocarbures. Une forte corrélation existe entre la concentration maximale du radical libre CH (méthylidyne, $[\mathrm{CH}]_{\mathrm{peak}}$) dans le front de flamme et la quantité de monoxyde d'azote formée par le mécanisme de Fenimore.

Cette thèse présente des mesures quantitatives de $[\mathrm{CH}]_{\mathrm{peak}}$ prises dans des flammes prémélangées de méthane, d'éthane, de propane, et de *n*-butane à pression atmosphérique. Des profils unidimensionnels d'intensité de fluorescence du CH sont extraits de mesures bidimensionnelles obtenues par Fluorescence Induite par Laser (2D-FIL). La calibration du système optique, nécessaire afin de rendre les mesures quantitatives, est réalisée à partir du signal de diffusion de Rayleigh d'un écoulement d'azote pur. Pour tous les alcanes, le signal de fluorescence du CH atteint son maximum à une richesse de 1.2, et décroit pour des mélanges plus riches ou pauvres en carburant. Une variation similaire du signal de fluorescence avec la richesse du mélange est observée pour tous les alcanes suggérant que la formation de méthylidyne est déterminée par un ensemble limité et commun de réactions élémentaires qui ne dépendent pas du type de carburant.

Des profils unidimensionnels de vitesse d'écoulement sont obtenus par vélocimétrie par suivi de particules qui, conjointement avec les mesures de températures et de débits d'air et de carburant, fournissent toutes les conditions limites nécessaires aux simulations de flammes à une dimension. Dans le cadre de cette recherche, un modèle numérique de FIL transitoire à quatre niveaux, qui inclut le transfert d'énergie rotationnelle dans les états fondamental et excité électroniquement, a été développé et permet de convertir les profils de concentrations de méthylidyne prédits par les simulations de flammes en unités compatibles avec les résultats expérimentaux.

D'importantes variations entre les prédictions de quatre modèles de cinétique chimique sont observées pour tous les carburants et toutes les richesses étudiés. Une étude détaillée des modèles faite à l'aide d'analyses de sensibilité et des routes chimiques démontre que les principales réactions causant cette importante disparité entre les modèles sont impliquées dans le mécanisme de formation du CH ($\mathrm{CH_3} \rightarrow \mathrm{CH_2^*} \rightarrow \mathrm{CH_2} \rightarrow \mathrm{CH}$), injectent ou retirent des atomes de carbone du mécanisme de formation du CH, ou interfèrent avec les espèces chimiques qui sont impliquées

dans les réactions mentionnées précédemment. Les variations dans les prédictions de $[\mathrm{CH}]_{\mathrm{peak}}$, qui s'échelonnent sur plus d'un ordre de grandeur, sont causées par des différences importantes en termes de vitesses de réaction et des réactions incluses dans ces mécanismes. Tel qu'observé précédemment, les modèles de cinétique chimique prédisent une décroissance trop rapide de la concentration de méthylidyne au fur et à mesure que la richesse du mélange est réduite en deçà de 1.2. Pour identifier la cause de ce comportement, une procédure d'optimisation est appliquée au modèle de l'Université de San Diego. Le facteur pré-exponentiel de neuf réactions chimiques élémentaires, qui interagissent avec le mécanisme de formation du CH, est ajusté à l'intérieur de plages d'optimisation minutieusement sélectionnées. Au final, deux modèles de cinétique chimique qui prédisent de façon juste, c'est-à-dire à l'intérieur de l'incertitude expérimentale, la concentration maximale de méthylidyne sont obtenus. Ces derniers permettront de décrire avec justesse la formation de monoxyde d'azote par le mécanisme de Fenimore, et ce, pour une large plage de richesses et de carburants.

Acknowledgements

This thesis benefited from the support of many individuals and organizations, whose contribution must be recognized.

I am very grateful to my supervisor, Prof. Jeffrey M. Bergthorson, for his mentorship and sound advice. I admire his intelligence and dedication at work. I greatly appreciated the freedom I was given to pursue my own ideas, as well as the trust he had in me over the years. I also want to thank past and current colleagues of the Alternative Fuels Laboratory (AFL) for their help and friendship. For this work, I particularly acknowledge the assistance of Graeme M.G. Watson and Antonio C.A. Lipardi in performing the experiments and simulations, and reviewing the journal paper manuscripts. Special thanks to former and present McGill employees, namely John Boisvert and Gary Savard for their invaluable technical support, and to the staff of the departmental office for receiving our many packages and helping with administrative issues.

This project was jointly funded by the Natural Sciences and Engineering Research Council of Canada through research grants awarded to the AFL and an Alexander Graham Bell Canada Graduate Scholarship, the Faculty of Engineering of McGill University via a McGill Engineering Doctoral Award supported by the Brace Water Resources Fund Fellowship and the Total ISEAD Fellowship, BioFuelNet Canada, and Siemens Canada Limited, whose support is gratefully acknowledged.

Je tiens finalement à remercier ma famille, mes parents, Chantal et André, et mes amis pour leurs encouragements et leur compréhension tout au long de mon parcours doctoral. Particulièrement, merci à toi, Véronique, d'avoir su m'écouter dans ces fréquents moments de découragement, et d'avoir pris soin de notre famille alors que je donnais toutes mes énergies à compléter ce doctorat. Pardon pour toutes ces fois où, le corps à la maison, mais la tête au travail, je ne t'écoutais que partiellement. Merci aussi à mes filles, Mélianne et Coralie, d'avoir mis du soleil dans mes journées et ma vie. Vous êtes, et resterez, ma plus grande fierté.

Contribution of author

Since its inception, a significant component of the research program of the Alternative Fuels Laboratory is the experimental determination of the reactivity and nitric oxide (NO) production of premixed, stagnation, laminar flames. Three laser-based diagnostic techniques are commonly used in the laboratory: 1) one-dimensional (1D), NO Laser-Induced Fluorescence (LIF); 2) two-dimensional (2D), CH-LIF; and 3) Particle Tracking Velocimetry (PTV). The NO-LIF technique initiated by G. Chung [Ca.1] was subsequently refined and extended to perform temperature profile measurements by J.D. Munzar and G.M.G. Watson [Ca.2, Ca.3]. G.M.G. Watson and I, we implemented the CH-LIF method in the laboratory (see section 2.3), and I developed the LIF model required to translate the output of flame simulations in units compatible with the experimental data, as well as verified the underlying assumptions and assessed the uncertainty in the LIF signal predicted by the model (see chapter 3). Originally (see for example [Ca.2, Ca.3]), flame speeds were extracted from 2D velocity fields measured using Particle Image Velocimetry (PIV), but the method was eventually replaced by the PTV technique (see section 2.2). With the exception of the laser, the experimental configuration of both methods is identical. With regards to the processing of the data, only a rudimentary program to extract the location of the particles on the PTV images was inherited from the work of L. Benezech, J.M. Bergthorson and P. Dimotakis at the California Institute of Technology. No program was provided to convert the position of the particles into velocity fields. To ease and accelerate the processing of the PTV images, I developed a series of user-interfaced programs, which reduced by more than one order of magnitude the time required to translate the information contained in the raw images into velocity profiles (1D) or fields (2D). In addition, I performed a complete uncertainty analysis of the method, and implemented an enhanced mathematical scheme in comparison to [Ca.4, Ca.5] to improve the accuracy of the measurements. The PTV method I developed, which is discussed in section 2.2, was used to measure flow velocity fields in a series of publications [Ca.6–Ca.11].

The current thesis takes place in a larger project interested in the formation of NO in premixed flames of C_1-C_4 alkane and alcohol fuels. Partnering with G.M.G. Watson, we used the laser diagnostic techniques discussed above to obtain NO, CH, temperature, and axial velocity profiles, which allowed us to benchmark existing thermochemical mechanisms, and to provide a better understanding of NO production in premixed flames. These results, reviewed in the introduction, were presented in recent publications I co-authored with G.M.G. Watson and J.M. Bergthorson [Ca.8, Ca.9]. For the collection of the experimental data presented herein, G.M.G. Watson and I, we were assisted by A.C.A. Lipardi, and I post-processed the CH-LIF images to yield the experimental data presented in Chapter 4. I performed the flame simulations with the help of A.C.A.

Lipardi, and I obtained the predicted LIF signals using the CH-LIF model I assembled. I analyzed the experimental data and benchmarked the thermochemical models by myself and, for that purpose, I implemented the reaction pathway analysis described in section 2.1.2.3 and Appendix A. This work was reported in a paper published in Combustion and Flame [Ca.7]. I also executed the adjustment of the San Diego mechanism [Ca.12] to the experimental data (see Chapter 5) using a method similar to [Ca.9, Ca.13], but much improved in terms of computation time and flexibility to initial and limit values of the optimized parameters, as well as prepared the manuscript accepted for presentation at the ASME Turbo Expo 2017 [Ca.14].

The main contributions to knowledge of this thesis, detailed in the conclusion chapter, include 1) the development of the time-resolved LIF model and the assessment of the adequacy of the commonly made assumptions in modelling CH-LIF in the A-X electronic system; 2) a first set of quantitative, experimental CH concentration data at atmospheric pressure for a variety of alkane fuels and equivalence ratios; 3) a discussion on the sources of the order-of-magnitude variability in CH predictions among currently available thermochemical mechanisms; 4) the identification, via the optimization method, of the reactions requiring further attention from the combustion community for future thermochemical models to accurately capture the sensitivity of the CH concentration to changes in the stoichiometry of the reactant mixture; and 5) optimized mechanisms properly describing CH production and enabling accurate predictions of prompt-NO formation.

In the conclusion remarks, the significant contribution of the AFL in understanding NO formation in atmospheric-pressure flames is reviewed, and the need for experimental data at supra-atmospheric pressures discussed. I am the designer of the high-pressure (HP) combustion facility presented in section 6.3.1, which includes a scaled-down, jet-wall burner optimized for HP operation and a vessel. I improved and validated the method used in the past by members of the AFL to design the interior contour of the inner nozzle of the burner [Ca.15], used Computational Fluid Dynamics (CFD) and computer-aided design tools to create the other components, and assembled the burner. Continuing on the preliminary work of an honour thesis student I supervised, G. Costa Del Pozo, I laid out the final concept of the vessel, performed the stress analyses to determine the dimensions of all components, prepared the technical drawings, found and ordered the raw stainless steel pieces of very peculiar grades and, with the help of A.C.A. Lipardi, I assembled and hydro-statically tested the enclosure for safe operation. I installed the jet-wall burner in the vessel, coupled the flow delivery and control systems, and integrated the laser diagnostics to the apparatus. Numerous, important equipment failures in the laboratory significantly delayed the HP research program. However, as witnessed from the preliminary results presented in section 6.3.1, this rig will yield important flame reactivity and NO concentration measurements at gas turbine relevant pressures in the years to come.

Other contributions

As a senior student in the AFL, I assisted A.C.A. Lipardi in his experimental assessment of the effects of exhaust gas addition to the reactant mixture of lean, premixed flames on the formation of nitric oxide. In this context, I implemented a new set of collection optics to improve the signal-to-noise ratio of the NO-LIF measurements, supervised the experiments, mentored the post-processing and analysis of the data, and reviewed the manuscript [Ca.10].

Over the last years, I was also involved in a collaborative project between the AFL and the Plasma Processing Laboratory of Prof. Sylvain Coulombe studying Plasma-Assisted Combustion (PAC) and Plasma-Assisted Fuel Reforming (PAFR). Preliminary PAC results, suggesting an increase in the reactivity of premixed laminar flames under the direct influence of non-thermal plasma discharges, were reported in [Ca.16]. A feasibility study was also presented at the ASME Turbo Expo 2016 demonstrating the potential of PAFR to increase and control the reactivity of flames at gas turbine relevant conditions through reformation of methane and/or biogas to syngas [Ca.17].

Authored and co-authored publications

[Ca.6] J.D. Munzar, A. Zia, P. Versailles, R. Jiménez, B. Akih-Kumgeh, and J.M. Bergthorson. "Comparison of laminar flame speeds, extinction strain rates and vapour pressures of Jet A-1/HRJ biojet fuel blends". In: *Proc. ASME Turbo Expo 2014*. Paper GT2014-25951. Düsseldorf, Germany, 2014.

[Ca.7] P. Versailles, G.M.G. Watson, A.C.A. Lipardi, and J.M. Bergthorson. "Quantitative CH measurements in atmospheric-pressure, premixed flames of $\mathrm{C_1}$-$\mathrm{C_4}$ alkanes". In: *Combust. Flame* 165 (2016), pp. 109–124.

[Ca.8] G.M.G. Watson, P. Versailles, and J.M. Bergthorson. "NO formation in rich premixed flames of $\mathrm{C_1}$-$\mathrm{C_4}$ alkanes and alcohols". In: *Proc. Combust. Inst.* 36.31 (2017), pp. 627–635.

[Ca.9] G.M.G. Watson, P. Versailles, and J.M. Bergthorson. "NO Formation in premixed flames of $\mathrm{C_1}$-$\mathrm{C_3}$ alkanes and alcohols". In: *Combust. Flame* 169 (2016), pp. 242–260.

[Ca.10] A.C.A Lipardi, P. Versailles, G.M.G. Watson, G. Bourque, and J.M. Bergthorson. "Experimental and numerical study on NO_x formation in $\mathrm{CH_4}$-air mixtures diluted with exhaust gas components". In: *Combust. Flame* 179 (2017), pp. 325–337.

[Ca.14] P. Versailles, G.M.G Watson, A. Durocher, G. Bourque, and J.M. Bergthorson. “Thermochemical mechanism optimization for accurate predictions of CH concentrations in premixed flames of C_1-C_3 alkane fuels”. In: *Proc. ASME Turbo Expo 2017*. Paper GT2017-64995. Charlotte, USA, 2017.

[Ca.15] P. Versailles and J.M. Bergthorson. “Optimized laminar axisymmetrical nozzle design using a numerically-validated Thwaites method”. In: *J. Fluids Eng.* 134.10 (2012).

[Ca.16] M.D.G. Evans, P. Versailles, F.P. Sainct, J.M. Bergthorson, and S. Coulombe. “Increased flame reactivity of a lean premixed flame through the use of a custom-built high-voltage pulsed plasma source”. In: *IEEE Trans. Plasma Sci.* 42.10 (2014), pp. 2844–2845.

[Ca.17] P.D.G. Maqueo, P. Versailles, G. Bourque, and J.M. Bergthorson. “A numerical study on the reactivity of biogas/reformed gas/air and methane/reformed gas/air mixtures at gas turbine relevant conditions”. In: *Proc. ASME Turbo Expo 2016*. Paper GT2016-56655. Seoul, Korea, 2016, pp. 1–9.

Other, non-authored publications

[Ca.1] G.A. Chung, B. Akih-Kumgeh, G.M.G. Watson, and J.M. Bergthorson. “NO_x formation and flame velocity profiles of iso- and n- isomers of butane and butanol”. In: *Proc. Combust. Inst.* 34.1 (2012), pp. 831–838.

[Ca.2] G.M.G. Watson, J.D. Munzar, and J.M. Bergthorson. “Diagnostics and modeling of stagnation flames for the validation of thermochemical combustion models for NO_x predictions”. In: *Energy Fuels* 27 (2013), pp. 7031–7043.

[Ca.3] G.M.G. Watson, J.D. Munzar, and J.M. Bergthorson. “NO formation in model syngas and biogas blends”. In: *Fuel* 124 (2014), pp. 113–124.

[Ca.4] L. Benezech. “Premixed hydrocarbon stagnation flames: Experiments and simulations to validate combustion chemical-kinetic models”. Engineer’s Thesis. California Institute of Technology, 2008.

[Ca.5] L. Benezech, J.M. Bergthorson, and P. Dimotakis. “Premixed laminar C_3H_8- and C_3H_6-air stagnation flames: Experiments and simulations with detailed kinetic models”. In: *Proc. Combust. Inst.* 32.1 (2009), pp. 1301–1309.

[Ca.11] S.D. Salusbury and J.M. Bergthorson. “Maximum stretched flame speeds of laminar premixed counter-flow flames at variable Lewis number”. In: *Combust. Flame* 162.9 (2015), pp. 3324–3332.

[Ca.12] University of California at San Diego. *“Chemical-Kinetic Mechanisms for Combustion Applications”, San Diego Mechanism web page, Mechanical and Aerospace Engineering (Combustion Research)*. http://combustion.ucsd.edu. 2005.

[Ca.13] M. Frenklach, H. Wang, and M.J. Rabinowitz. “Optimization and analysis of large chemical kinetic mechanisms using the solution mapping method - combustion of methane”. In: *Prog. Energy Combust. Sci.* 18 (1992), pp. 47–73.

Contents

List of Figures

List of Tables

Nomenclature

$2\gamma_{\mathrm{CH}-i}$	Collisional broadening parameter	$\mathrm{cm}^{-1}/\mathrm{atm}$
A	Pre-exponential factor	[cm^3, mol, s]
A_{2i1j}	Einstein rate constant of spontaneous emission from the $2i$ to the $1j$ states	s^{-1}
A_{B}	Cross-sectional area of the laser sheet	m^2
b_{12}	Rate constant of photon absorption	s^{-1}
b_{21}	Rate constant of stimulated emission	s^{-1}
B_{12}	Einstein absorption coefficient	$\mathrm{m}^2/\left(\mathrm{J}\cdot\mathrm{s}\right)$
B_{21}	Einstein stimulated emission coefficient	$\mathrm{m}^2/\left(\mathrm{J}\cdot\mathrm{s}\right)$
c	Speed of light	cm/s
C	Spatial calibration coefficient	$\mathrm{m}/\mathrm{pixel}$
C_{opt}	Optical collection constant	$\mathrm{count}/\mathrm{photon}$
d_{p}	Diameter of the particulate matter	$\mu\mathrm{m}$
E_{a}	Activation energy	$\mathrm{cal}/\mathrm{mol}$
E_{B}	Average laser energy per pulse	J
$E_{\mathrm{d}u_{\mathrm{p}}/\mathrm{d}z}$	Error on ${\mathrm{d}u_{\mathrm{p}}}/{\mathrm{d}z}$ induced by the finite difference scheme	s^{-1}
$E_{u_{\mathrm{p},i}}$	Error on $u_{\mathrm{p}}\left(z_i, r_i\right)$ induced by the finite difference scheme	m/s
$E_{v_{\mathrm{p},i}}$	Error on $v_{\mathrm{p}}\left(z_i, r_i\right)$ induced by the finite difference scheme	m/s
f	Laser repetition rate	Hz
f_{LIF}	Number of photons emitted via fluorescence per unit volume and solid angle	$\mathrm{photon}/\left(\mathrm{sr}\cdot\mathrm{m}^3\right)$
f_{R}	Number of Rayleigh scattered photons per unit volume and solid angle	$\mathrm{photon}/\left(\mathrm{sr}\cdot\mathrm{m}^3\right)$
$g(\nu)$	Spectral shape of the absorption line normalized to unity	s
$\bar{h}_j^{\circ}$	Heat of formation at constant pressure	J/mol
$h\nu$	Energy of a photon	J
I	Irradiance	W/m^2
I_{pixel}	Pixel intensity	count
I_{sat}	Saturation irradiance	W/m^2
I_ν	Spectral irradiance	$\mathrm{W}/(\mathrm{cm}^2\mathrm{cm}^{-1})$

k	Specific rate	[cm^3, mol, s]
k_B	Boltzmann constant	$\mathrm{J/K}$
l_R	Reaction zone thickness	m
$\dot{m}_j$	Mass flow rate of species j	$\mathrm{kg/s}$
$[\mathrm{M}_j]$	Concentration of species M_j	$\mathrm{mol/m}^3$
$\dot{n}_j$	Molar flow rate of species j	$\mathrm{kmol/s}$
N	Number density	m^{-3}
$N_{0,\mathrm{CH}}$	Number density of CH molecules in the ground electronic energy level prior to the laser pulse	m^{-3}
N_{0,CH^*}	Number density of CH molecules in the electronically excited energy level prior to the laser pulse	m^{-3}
N_A	Avogadro constant	mol^{-1}
N_k	Total number density of CH molecules in the electronic level k	m^{-3}
N_{ki}	Number density of CH molecules in the electronic level k and energy state i	m^{-3}
N_p	Number of photons emitted per unit volume	$\mathrm{photon/m}^3$
P	Pressure	Pa
P_j	Partial pressure of species j	atm
$q_{c,j}$	Rate of consumption of species j	$1/\left(\mathrm{m}^3 \cdot \mathrm{s}\right)$
$q_{f,j}$	Rate of production of species j	$1/\left(\mathrm{m}^3 \cdot \mathrm{s}\right)$
q_j	Overall (net) rate of production of species j	$1/\left(\mathrm{m}^3 \cdot \mathrm{s}\right)$
q_l	Rate of progress variable of reaction l	$\mathrm{kmol}/\left(\mathrm{m}^3 \cdot \mathrm{s}\right)$
$q_{\mathrm{LIF},j}$	Overall (net) rate of production of species j included in the LIF model	$1/\left(\mathrm{m}^3 \cdot \mathrm{s}\right)$
Q_{2i1}	Rate constant of collisional quenching from state $2i$ to the ground electronic energy level	s^{-1}
Q_j	Quenching rate coefficient of species j	cm^3/s
r	Radial coordinate	m
r_CV	Radius of the control volume of the reaction pathway analysis	m
r_i	Radial position of a given particle in the burner reference frame at time t_i	m
$r_{\mathrm{p},i}$	Radial position of a given particle in the image reference frame at time t_i	pixel
$r_{\mathrm{pixel},j}$	Radial position of individual pixels	pixel
$R(e, s_1, s_2)$	Rate of transfer of element e from species s_1 to s_2	$\mathrm{kmol/s}$

R_{kakb}	Forward rate constant of rotational energy transfer in the electronic level k	s^{-1}
R_{kbka}	Backward rate constant of rotational energy transfer in the electronic level k	s^{-1}
R_{u}	Universal gas constant	$\mathrm{J}/\left(\mathrm{mol}\cdot\mathrm{K}\right)$
S_{He}	Scattering signal measured in a cold helium flow	count
S_{L}	Laminar flame speed	$\mathrm{m/s}$
S_{LIF}	CH laser-induced fluorescence signal	count
$S_{\mathrm{N_2}}$	Scattering signal measured in a cold nitrogen flow	count
S_{NO}	NO laser-induced fluorescence signal	count
S_{R}	Rayleigh scattering signal of nitrogen ($S_{\mathrm{R}} = S_{\mathrm{N_2}} - S_{\mathrm{He}}$)	count
S_{u}	Strained reference flame speed	$\mathrm{m/s}$
t	Time	s
T	Temperature	K
T_e	Electronic energy measured at the minimum of the Morse potential	cm^{-1}
T_{R}	Temperature of the flow during the Rayleigh scattering measurements	K
u	Axial flow velocity	$\mathrm{m/s}$
u_{FD}	u_{p} estimated with a finite difference scheme	$\mathrm{m/s}$
u_{p}	Axial velocity of the tracer particles	$\mathrm{m/s}$
v	Radial flow velocity	$\mathrm{m/s}$
v_{p}	Radial velocity of the tracer particles	$\mathrm{m/s}$
V	Volume	m^3
V_j	Diffusion velocity of species j	$\mathrm{m/s}$
W_j	Molar mass of species j	$\mathrm{kg/kmol}$
$Y_{\mathrm{E}}(\lambda)$	Spontaneous emission spectrum normalized to unity	nm^{-1}
z	Axial coordinate	m
z_i	Axial position of a given particle in the burner reference frame at time t_i	m
$z_{\mathrm{p},i}$	Axial position of a given particle in the image reference frame at time t_i	pixel
$z_{\mathrm{pixel},j}$	Axial position of individual pixels	pixel
α	Thermal diffusivity	m^2/s
δ_{CH}	Width of the CH layer taken at half-maximum	mm

δ_{PSF}	Width of the point-spread function	mm
ΔC	Uncertainty on the spatial calibration coefficient	$\mathrm{m/pixel}$
$\Delta {}^{\mathrm{d}u}/_{\mathrm{d}z}$	Overall uncertainty on ${}^{\mathrm{d}u}/_{\mathrm{d}z}$	s^{-1}
Δf	Uncertainty on the laser repetition rate	Hz
Δu	Overall uncertainty on the axial velocity	$\mathrm{m/s}$
$\Delta \nu_c$	Width of the Lorentzian distribution (collisional line-broadening)	cm^{-1}
$\Delta \nu_{\mathrm{L}}$	Laser line width	cm^{-1}
ϵ	Unknown instant within the interval $t_i - {}^{1}/_{f} \leq \epsilon \leq t_i + {}^{1}/_{f}$	s
λ	Wavelength	nm
ν	Frequency of light	Hz
ρ	Density	$\mathrm{kg/m}^3$
σ_j	Quenching cross-section of species j	$\mathrm{Å}^2$
τ_{cam}	Camera exposure time	s
τ_{CH}	Residence time in the CH layer	s
τ_{Laser}	Laser pulse duration	s
τ_{R}	Duration of the Rayleigh scattering signal	s
$\omega_{\mathrm{b},i}$	Backward rate of reaction i	$\mathrm{mol}/\left(\mathrm{m}^3 \cdot \mathrm{s}\right)$
Ω	Solid angle	sr
$\left(\frac{\partial \sigma}{\partial \Omega}\right)$	Rayleigh scattering cross-section	m^2/sr

Dimensionless variables

$2S+1$	Multiplicity (spin-splitting factor)
$f_{\mathrm{B},N_{1a}}$	Fraction of the $\mathrm{X}^2\Pi$ CH molecules in the laser-coupled ($1a$) state at thermal equilibrium
$f_{\mathrm{B},N_{2a}}$	Fraction of the $\mathrm{A}^2\Delta$ CH molecules in the laser-coupled ($2a$) state at thermal equilibrium
$f_{i,\mathrm{high}}$	Upper bound of optimization of the multiplier applied to the pre-exponential factor A_i
$f_{i,\mathrm{inv}}$ and $f_{i,\mathrm{orig}}$	Optimized multipliers applied to the pre-exponential factor A_i
$f_{i,\mathrm{low}}$	Lower bound of optimization of the multiplier applied to the pre-exponential factor A_i
F	Optimization objective function
J	Quantum number for the total angular momentum

$L(\nu)$	Laser spectral distribution normalized such that its integral over the frequency ν is equal to $c \cdot \Delta\nu_{\mathrm{L}}$
M	Arbitrary species
n	Temperature exponent for the computation of $k(T)$
n_{DOF}	Number of degrees of freedom
$n_i(e, s_1, s_2)$	Number of atoms of element e transferred from species s_1 to s_2 through reaction i
N	Quantum number for the total angular momentum apart from electron spin
p	Parity (e or f)
q_{cons}	Rate of consumption normalized to unity
q_{net}	Overall (net) reaction rate normalized to unity
R	Arbitrary radical
R_{in}	Number of reactions producing CH
R_{out}	Number of reactions consuming CH
S	Electron spin quantum number
S/N	Signal-to-noise ratio
v	Vibrational quantum number
X_j	Mole fraction of species j
Y_j	Mass fraction of species j
Z_{el}	Molecular partition function
Γ	Overlap fraction
$\Delta k_i/k_i$	Relative error in the specific rate of reaction i
ν' and ν''	Stoichiometric coefficients
$\nu_{e,i}$	Number of e-atoms per molecule of species s_i
$\sigma_{(S_{\mathrm{LIF}}/S_{\mathrm{R}})_{\mathrm{exp}}}$	Relative random uncertainty in the experimental LIF data
$\sigma_{(S_{\mathrm{LIF}}/S_{\mathrm{R}})_{\mathrm{num}},\mathrm{BC}+\delta_{\mathrm{PSF}}}$	Relative error induced in the LIF response by the uncertainties in the PSF-width and in the experimentally measured boundary conditions
$\sigma_{(S_{\mathrm{LIF}}/S_{\mathrm{R}})_{\mathrm{num}},\mathrm{LIF\ model}}$	Relative error in the LIF model
$\sigma_{\frac{(S_{\mathrm{LIF}}/S_{\mathrm{R}})_{\mathrm{num}}}{(S_{\mathrm{LIF}}/S_{\mathrm{R}})_{\mathrm{exp}}}=1}$	Overall error in $(S_{\mathrm{LIF}}/S_{\mathrm{R}})_{\mathrm{num}} \,/\, (S_{\mathrm{LIF}}/S_{\mathrm{R}})_{\mathrm{exp}} = 1$
σ_{x_j}	Relative uncertainty in the parameter x_j
τ_{B}	Transmissivity of the beam shaping optics downstream of the laser energy measurement point
$\tau_{\mathrm{Filter}}(\lambda)$	Wavelength-resolved filter transmissivity

$\tau_{\lambda,\mathrm{LIF}}$	Average transmissivity of the bandpass filter over the CH emission spectrum
$\tau_{\lambda,\mathrm{R}}$	Transmissivity of the bandpass filter at the wavelength of the Rayleigh scattering signal
ϕ	Equivalence ratio
ϕ_Λ	Λ-doubling factor
$\omega_{\mathrm{el,eff}}$	Effective electronic degeneracy

Subscripts

axis	On the centreline axis of the jet-wall burner
exp	Experimental value
inlet	At the inlet of the computational domain of the quasi-1D flame simulations
num	Numerical value
off	Following laser irradiation
on	During laser irradiation
opt	Optimized value
peak	Maximum value
plate	At the location of the stagnation surface of the jet-wall burner
rand	Random uncertainty
sys	Systematic uncertainty

Superscripts

$'$	Electronically excited ($\mathrm{A}^2\Delta$) state
$''$	Ground electronic ($\mathrm{X}^2\Pi$) state

Acronyms

1D	One-dimensional
2D	Two-dimensional
BC	Boundary condition
CFD	Computational fluid dynamics
CV	Control volume
GRI	GRI-Mech 3.0 mechanism [65]
HP	High pressure
KON	Konnov mechanism, revision 0.6 [67]

LIF	Laser-induced fluorescence
L.S.	Logarithmic sensitivity
NUIG	AramcoMech 1.3 mechanism [134]
NUIG2	AramcoMech 2.0 mechanism [135]
ODE	Ordinary differential equation
PAN	Peroxyacetyl nitrate
PIV	Particle image velocimetry
PLIF	Planar laser-induced fluorescence
PSF	Point-spread function
PTV	Particle tracking velocimetry
RET	Rotational energy transfer
RPA	Reaction pathway analysis
SD	San Diego mechanism, version 2005 [128]
SS	Steady-state conditions
USC	USC Mech II mechanism [133]
VOC	Volatile organic compound

Chapter 1

Introduction

1.1 Energy demand, production, and climate change

The development of modern societies is supported by the consumption of energy; the world yearly energy use is expected to reach 860 exajoules by 2040, a rise of 48% in comparison to 2012 mostly induced by the economic growth in emerging countries [1]. Fossil fuels are forecasted to remain the primary source of energy, fulfilling 78% of the demand in 2040, and raising the annual energy-related emissions of $\mathrm{CO_2}$ in the atmosphere to 43 billion metric tons. This will result in the cumulative emission of ~1100 gigatons of carbon dioxide ($\mathrm{GtCO_2}$) over the period 2012-2040, essentially wasting the remaining budget of ~1000 $\mathrm{GtCO_2}$ to prevent a global warming of more than 2°C above the pre-industrial level[1] [2]. The transition to low-carbon energy sources must be significantly more rapid than the predicted 2.6% yearly averaged growth in renewable energy production over the period 2012-2040 [1].

Energy is available from a variety of renewable sources including solar, wind, water, and geothermal. Numerous technologies exist, such as concentrated solar power plants, photovoltaic panels, wind turbines, hydropower plants, wave devices, tidal turbines, geothermal plants, etc., that can produce carbon-free energy in sufficient quantities to fulfil the global demand using only a fraction (1%) of the available land [3, 4]. However, many of these renewable sources are intermittent, which implies that the energy must be harvested when available, efficiently stored, and redistributed as needed [5–7]. At the moment, storage of renewable energy in convenient energy carriers for global market exchange, at sufficiently high energy and power densities, remains a challenge [6, 8]. Among the solutions is the conversion of renewable energy into chemical energy that can be restored through combustion of the energy carriers. Examples are 1) the growth of

[1] In its most recent report, the Intergovernmental Panel on Climate Change (IPCC) mentions a limit on the anthropogenic carbon dioxide emissions, based on various modelling results, of 2900 $\mathrm{GtCO_2}$ cumulated since 1870 to restrict the global warming to 2°C in comparison to the period 1861-1880, with a probability $> 66\%$. In 2011, approximately 1900 $\mathrm{GtCO_2}$ had already been emitted, yielding a remaining budget of ~1000 $\mathrm{GtCO_2}$ [2].

biomass, such as crops and algae, through photosynthesis, which can be used to synthesize biofuels (biogas, syngas, alcohols and other oxygenated biofuels, and synthetic hydrocarbons) [9, 10]; 2) the use of renewable energy to recycle metal oxides into metal powders to be used as fuels [5, 8]; and 3) the production of so-called "solar fuels" using the sunlight, or the electricity produced from it, to a) split water and carbon dioxide in $\mathrm{H_2}$ and CO that can be used as is and to synthesize hydrocarbons, or to b) thermally decompose fossil fuels into solid-phase graphite and hydrogen fuel [7, 11, 12]. Although the optimal storage technology, or portfolio of technologies, has yet to emerge, combustion-based energy carriers have the potential to provide comparable convenience, and power and energy densities to conventional fossil fuels, while significantly reducing carbon dioxide emissions.

It appears very likely that combustion will remain a primary conversion process whether energy production relies on renewable sources or fossil fuels. However, any technology based on the combustion of fuels with air will result in the oxidation of nitrogen into nitrogen oxides, NO_x, which are known to have many deleterious, direct and indirect, effects on human health and the environment. This warrants further research on the formation of NO_x and their precursors.

1.2 Atmospheric chemistry of nitrogen oxides and their effects on human health and the environment

NO_x emissions, oxidation, and effects

In 2011, more than 92% of NO_x emissions in the United States of America originated from anthropogenic sources, mostly from the burning of fossil fuels in the transportation sector (57.5%) and for electricity generation (13.5%) [13]. The principal nitrogen oxide emitted by combustion-based applications is nitric oxide, NO [14, 15]. Once released in the atmosphere, NO is rapidly oxidized in the presence of volatile organic compounds (VOC) to nitrogen dioxide, $\mathrm{NO_2}$, via the reaction:

$$\mathrm{RO_2} + \mathrm{NO} \rightarrow \mathrm{RO} + \mathrm{NO_2}, \tag{1.1}$$

where the radical R is primarily H and $\mathrm{CH_3}$ [16, 17]. Exposed to solar radiation, nitrogen dioxide is photo-dissociated:

$$\mathrm{NO_2} + h\nu \rightarrow \mathrm{NO} + \mathrm{O}, \tag{1.2}$$

producing nitric oxide and atomic oxygen. NO is recycled in reaction 1.1, thus rapidly establishing a continuous cycle, which results in the net production of atomic oxygen without consumption of

NO_x ($NO + NO_2$) molecules [15, 16].

Nitrogen oxides are toxic substances at sufficiently high concentrations, which are well-beyond the levels observed in ambient air [15]. In fact, administered in small quantities, NO is widely used in medicine as a vasodilator [18]. NO_2 is more harmful than NO [19], and is known to incur bronchitis in asthmatic children, as well as to reduce the human pulmonary function, at concentrations currently observed in occidental cities [20]. In addition, NO_2 is a "reddish-orange-brown" gas involved in the formation of photochemical smog [21, 22]. However, the main motive for regulating the emissions of nitrogen oxides is their involvement in the formation of more deleterious, secondary pollutants as discussed below [15].

Ozone formation and effects

The oxygen atoms produced via the NO_x cycle of reactions 1.1 and 1.2 react with O_2 to form ozone:

$$O + O_2 + M \rightarrow O_3 + M. \tag{1.3}$$

Exposition to ozone, a strong oxidizing gas, has numerous detrimental, acute and chronic, impacts on human health. It causes bronchoconstriction rendering breathing difficult, irritates the inner surface of the air passages, favours the development and repetition of asthma episodes, reduces the ability of the respiratory system to defend against infections, and causes and worsens chronic obstructive pulmonary diseases [19, 20, 23, 24]. A correlation between the O_3 concentration in ambient air with the rates of deaths and heart diseases has been observed in European countries [20] and, in many U.S. counties, the ozone concentration reaches levels sufficient to cause respiratory problems [24, 25]. Furthermore, ozone affects the photosynthesis process of sensitive plants and trees. This slows down their growth, injures vegetation and, as a consequence, impacts the production, both the quality and yield, in the agricultural sector [19, 24, 26]. It is also the third most important greenhouse gas after CO_2 and CH_4 [24].

Acid precipitations: NO_x sinks

The principal mechanism of tropospheric NO_x removal is through oxidation to nitric acid, HNO_3, and subsequent deposition as acid precipitations [16]. In the daytime, HNO_3 is formed via the reaction:

$$NO_2 + OH + M \rightarrow HNO_3 + M. \tag{1.4}$$

At night, a different mechanism of HNO_3 formation takes place because of the significantly lower concentration of the OH radical [16, 27, 28]:

$$NO_2 + O_3 \rightarrow NO_3 + O_2, \tag{1.5}$$

$$\mathrm{NO_3 + NO_2 + M \rightarrow N_2O_5 + M}, \tag{1.6}$$

and,

$$\mathrm{N_2O_5 + H_2O \rightarrow 2\,HNO_3}. \tag{1.7}$$

Other reactions of the nitrate radical ($\mathrm{NO_3}$) with volatile organic compounds, namely aldehydes, participate, but to a lesser extent, to the formation of nitric acid [28]:

$$\mathrm{NO_3 + RH \rightarrow HNO_3 + R}. \tag{1.8}$$

Due to its high solubility with water, nitric acid contributes to the formation of acid precipitations and fog [16]. Acid deposition negatively impacts the environment, namely 1) the marine fauna through acidification of the water, and by leaching out of the soil toxic aluminum that is transported via surface water runoff into lakes and streams [29, 30], and 2) the terrestrial flora by removing from the ground the nutrients and minerals the plants and trees need to grow. In addition, acid fog extracts nutrients from their leaves and needles, which impacts their ability to perform photosynthesis [30–32]. Also, wet ($\mathrm{HNO_3}$ dissolved in water and falling as precipitations) and dry (direct settling) depositions of nitric acid soil and damage buildings and historic monuments [30, 33, 34]. Furthermore, wet and dry depositions of nitrogen-containing species originating from the oxidation of NO, such as $\mathrm{HNO_3}$, $\mathrm{NO_3}$ and $\mathrm{NO_2}$, are significant contributors to nutrient pollution of coastal waters, which causes algae blooms that hurt and kill marine animals, and are harmful to humans getting in contact with the toxic algae [35, 36].

Particulate matter

NO_x are also important precursors to the formation of fine aerosols in the troposphere. The nitric acid, formed by reactions 1.4 to 1.8, reacts with ammonia, $\mathrm{NH_3}$, which is emitted in the atmosphere principally by the agricultural sector from manure, urine and fertilizers [37], to form ammonium nitrate salt particles, $\mathrm{NH_4NO_3}$ [27, 38, 39]. The overall composition of $\mathrm{PM}_{2.5}$, *i.e.*, airborne particles with diameter $d_\mathrm{p} \leq 2.5\ \mu\mathrm{m}$, varies geographically and throughout the year [40]. However, during episodes of intense pollution where favourable conditions of high ammonia and nitric acid concentrations, low ambient temperature, and high humidity are encountered [39], most of the $\mathrm{PM}_{2.5}$ mass distribution is made of ammonium nitrate, produced in sufficiently high concentrations to reach the "Very Unhealthy Level of Concern" of the Air Quality Index of the United States Environmental Protection Agency [27, 38, 41]. Also, waves on the surface of oceans and inland seas entrain sea salt (sodium chloride, NaCl) particles in the atmosphere [16]. In marine

areas with low ammonia emissions, the principal nitrate particulate is $\mathrm{NaNO_3}$ (sodium nitrate) formed through the surface reaction [28]:

$$\mathrm{HNO_3 + NaCl \leftrightarrow NaNO_3 + HCl.} \tag{1.9}$$

In addition to the particulate matter originating from nitric acid, aerosols can be generated by the reaction of $\mathrm{NO_3}$, formed primarily at night through reaction 1.5 [28, 42], with volatile organic compounds [43]. Most of the anthropogenic VOCs are alkanes and aromatics, which do not react readily with the nitrate radical. In contrast, $\mathrm{NO_3}$ is much more reactive with non-aromatic, non-saturated hydrocarbons emitted in significant quantities by plants and trees [28, 39, 43]. The exact chemical mechanism is complex and not fully understood, but the reaction of anthropogenic $\mathrm{NO_3}$ with biogenic VOCs to form organic nitrate aerosols of the form $\mathrm{RONO_2}$ produces significant concentrations of $\mathrm{PM_{2.5}}$, particularly in rural areas [28, 43].

Aerosols, particularly inhalable $\mathrm{PM_{10}}$ ($d_\mathrm{p} \leq 10\,\mu\mathrm{m}$), are serious threats to human health as they can penetrate and depose deep into the respiratory system, and can even enter the bloodstream if sufficiently small [19, 20, 44, 45]. The particles not only irritate the air passages, they also absorb toxic substances, such as heavy metals and combustion by-products (*e.g.*, carcinogenic polycyclic aromatic hydrocarbons), which are introduced in the respiratory system in concentrations exceeding the ambient conditions [45, 46]. Exposure to very small concentrations of inhalable particles was shown to increase the rate of lung cancer, as well as to cause acute and chronic respiratory and cardiovascular diseases, resulting in an average lifespan reduction of 8.6 months in European cities [19, 20, 44, 45]. $\mathrm{PM_{2.5}}$ are also an important component of photochemical smog [19, 44].

Peroxyacetyl nitrate molecules: $\mathbf{NO_x}$ reservoirs

The principal reservoirs of NO_x in the troposphere are long-travelling, peroxyacetyl nitrate (PAN) molecules formed through the reaction [16, 47]:

$$\mathrm{CH_3C(O)OO + NO_2 + M \leftrightarrow \underbrace{CH_3C(O)OONO_2}_{\text{PAN}} + M.} \tag{1.10}$$

The peroxyacetyl radical, $\mathrm{CH_3C(O)OO}$, is primarily formed by photolysis and oxidation reactions of acetaldehyde ($\mathrm{CH_3CHO}$), acetone ($\mathrm{CH_3C(O)CH_3}$), and methylglyoxal ($\mathrm{CH_3COCHO}$), directly emitted in the atmosphere from biogenic and anthropogenic sources, or formed through oxidation of other VOCs [47]. At low-temperatures, characteristic of the upper troposphere or during winter time, the lifetime of the PAN molecules is on the order of months. This allows them to travel long distances before to dissociate (reverse of reaction 1.10), thus spreading the deleterious impacts of

NO_x emissions on a global scale [16]. The principal effect of peroxyacetyl nitrate on humans is to cause eye irritation [15]. However, PAN molecules are toxic to plants at concentrations as low as 5 to 10 ppb [26, 48] and, even if their concentration significantly decreased over the past decades [49, 50], such levels of pollution are still reached in large, polluted cities [48].

1.3 NO formation in flames

Increasingly stringent regulations on nitrogen oxides emissions are being enforced by governments because of their deleterious effects on health and the environment. A detailed discussion on the emission standards that transportation and stationary gas turbine engines must meet is presented in [51]. The U.S. emission standards for on- and off-road vehicles are provided by the United States Environmental Protection Agency [52], and the Canadian regulations are aligned with the U.S. standards [53]. In order to achieve these ever-decreasing emission targets while maintaining or, even better, improving engine efficiency, new combustor architectures must be developed [54, 55]. For that effort, a deeper understanding of NO_x formation is required to develop design tools of sufficient accuracy [54, 56].

Four NO formation routes have been identified in the combustion of fuels with air: thermal (Zel'dovich), prompt (Fenimore), N_2O, and NNH [57–59]. The last two pathways are generally of minor importance in engines [14, 57, 60, 61], and they are omitted in this introduction for the sake of brevity. They will be concisely discussed in the concluding remarks. In addition, NO_x are formed from the fuel-bound nitrogen in solid and liquid fuels, such as coal and oil, but this formation pathway is beyond the scope of the current dissertation.

1.3.1 Thermal (Zel'dovich) formation pathway

The thermal NO formation mechanism was initially proposed by Zel'dovich [62] and consisted of reactions 1.11 and 1.12. The mechanism was supplemented with reaction 1.13 by Lavoie, Heywood, and Keck [63]. This pathway is initiated by the reaction of atomic oxygen with the strongly triple-bonded nitrogen molecules. The resulting nitrogen atoms readily react with molecular oxygen (reaction 1.12) and the hydroxyl radical (reaction 1.13) to form additional NO molecules.

$$\mathrm{N_2 + O \leftrightarrow NO + N} \tag{1.11}$$

$$\mathrm{N + O_2 \leftrightarrow NO + O} \tag{1.12}$$

$$\mathrm{N} + \mathrm{OH} \leftrightarrow \mathrm{NO} + \mathrm{H} \tag{1.13}$$

Reaction 1.11 has a very high activation energy, E_{a}, in comparison to reactions 1.12 and 1.13, which makes it the rate-limiting step of the thermal-NO formation route [57, 59]. In other words, the rate of progress of reaction 1.11 determines the overall rate of thermal-NO formation. The Zel'dovich route is particularly important at high temperatures (> 1800-1850 K [14, 57]), which are required for the reactants to have enough energy to overcome the elevated E_{a} of reaction 1.11, and because the concentration of atomic oxygen rises rapidly with the temperature due to dissociation [57, 59].

In a recent study, Watson, Versailles, and Bergthorson [64] measured NO concentration profiles in axisymmetric, laminar, premixed, stagnation flames of $\mathrm{C_1}$-$\mathrm{C_3}$ alkanes and alcohols using Laser-Induced Fluorescence (LIF). A subset of the experimental data for a stoichiometric, methane-air flame is shown in Figure 1.1. The slope of the NO-LIF profile[2] in the post flame region non-affected by the heat loss to the water-cooled stagnation surface ($2\ \mathrm{mm} < z < 7.5\ \mathrm{mm}$) is determined by the rate of reaction 1.11 and the overall flame burning rate, which governs the residence time [64]. All the thermochemical mechanisms presented in Figure 1.1 were shown to accurately predict the flame speed of stoichiometric, methane-air flames [64]. The discrepancies observed in the post-flame NO-LIF profiles, among the models and against the experimental data, are then caused by inconsistent, inaccurate descriptions of the specific rate of reaction 1.11 that appear too high relative to the experiments. The data for syngas, biogas, and $\mathrm{C_1}$-$\mathrm{C_3}$ alkane and alcohol fuels provided by Watson and co-workers are useful for the optimization and validation of thermal-NO kinetic mechanisms [60, 61, 64].

1.3.2 Prompt (Fenimore) formation route

While the thermal route is generally the dominant formation mechanism in the post-flame region, the prompt route is the source of rapid NO formation through the reaction zone of hydrocarbon flames. It is the dominant NO formation pathway in rich, premixed flames due to the almost complete consumption of oxygen through the flame front, which starves the thermal-NO route and prevents NO production in the post-flame region [69]. The reaction of methylidyne with nitrogen, $\mathrm{CH} + \mathrm{N_2} \rightarrow \mathrm{HCN} + \mathrm{N}$, was initially proposed by Fenimore as the initiation reaction of the prompt-NO route [70]. It was later shown that this reaction is spin-forbidden for reactants and products

[2]The NO-LIF signal, $S_{\mathrm{NO}}/\left(E_{\mathrm{B}} C_{\mathrm{opt}}\right)$, is a surrogate measure of NO concentration. For the low laser irradiance used in [64], and constant temperature, pressure and number density of the collisional quenchers, $S_{\mathrm{NO}}/\left(E_{\mathrm{B}} C_{\mathrm{opt}}\right)$ is linearly proportional to the number density of NO molecules.

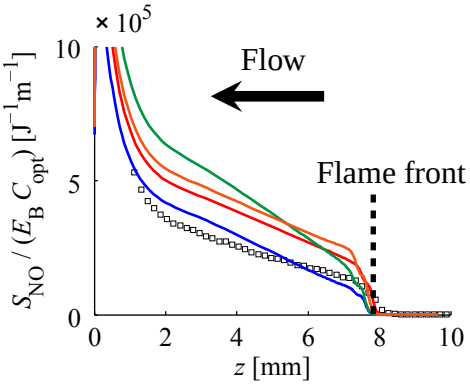

FIGURE 1.1: Experimental NO-LIF profile for a stoichiometric, stagnation, premixed methane-air flame (symbols) superimposed with simulated, 1D NO-LIF profiles obtained with the GRI-Mech 3.0 [65] (red), San Diego [66] (blue), Konnov 0.6 [67] (green), and CRECK [68] (orange) thermochemical mechanisms. The water-cooled stagnation surface is located at $z = 0$ mm. Reproduced with permission [64].

in the ground electronic state [71, 72], which led Moskaleva, Xia, and Lin [73, 74] to propose the more probable, spin-allowed reaction:

$$\mathrm{CH} + \mathrm{N_2} \rightarrow \mathrm{NCN} + \mathrm{H}. \tag{1.14}$$

The NCN molecules are oxidized by O_2, O, and OH to form NO [57, 75]:

$$\mathrm{NCN} + \mathrm{O_2} \leftrightarrow \mathrm{NO} + \mathrm{NCO}, \tag{1.15}$$

$$\mathrm{NCN} + \mathrm{O} \leftrightarrow \mathrm{NO} + \mathrm{CN}, \tag{1.16}$$

$$\mathrm{NCN} + \mathrm{OH} \leftrightarrow \mathrm{NO} + \mathrm{HCN}. \tag{1.17}$$

NCN can also react with atomic hydrogen and carbon to form N, HCN and CN molecules, which contribute to other NO formation pathways. Namely, atomic nitrogen readily forms NO via reactions 1.12 and 1.13 of the thermal route, and HCN and CN are expected to form NCO and subsequently NO [57].

Sutton, Williams, and Fleming [76] measured NCN and NO profiles in low-pressure, McKenna burner-stabilized, premixed $CH_4/O_2/N_2$ flames. The measured NCN layer profiles were consistently observed immediately downstream of the CH layer profiles measured by Berg et al. [77] in an identical burner, and a strong correlation was found between the maximum CH, NCN, and NO concentrations supporting the reaction mechanism of equations 1.14 to 1.17. In a subsequent study

considering C_1-C_4 alkanes [78], the same authors showed that the strong correlation between NCN and NO is preserved as the chain length is increased, but that of CH with NCN weakens. They concluded that there may be another precursor to NCN that becomes increasingly important for longer alkanes.

Watson, Versailles, and Bergthorson [69] used laser-induced fluorescence to measure temperature, CH, and NO concentration profiles, as well as Particle Tracking velocimetry (PTV) to obtain axial velocity profiles, in atmospheric-pressure, premixed, rich ($\phi = 1.3$), stagnation flames of air with all isomers of C_1-C_4 alkanes and alcohols. A subset of the experimental data for the methane-air flame is shown in Figure 1.2. Descriptions of the jet-wall burner, and PTV and CH-LIF techniques are provided in Chapters 2 and 3 of this dissertation.

As shown in Figure 1.2(a), the jet of reactants exiting the burner nozzle decelerates as it flows towards the flame. It then rapidly accelerates due to thermal expansion through the flame front, and decelerates again as it impinges on the water-cooled stagnation surface located at $z = 0$ mm. The strained reference flame speed, S_u, which corresponds to the minimum velocity immediately upstream of the flame front, is a surrogate measure of the laminar flame speed [79–82].

As expected for rich flames, there is a rapid rise of NO concentration through the flame front via the prompt route, which spatially coincides with the CH layer shown in Figure 1.2(c). As shown in Figure 1.2(b), thermal-NO production in the post-flame region is prevented due to the lack of oxygen. The rise in the LIF signal intensity observed for $z < 3$ mm is caused by an increase in NO number density as the heat loss to the water-cooled stagnation surface reduces the temperature of the gas mixture. In such rich flames, the prompt route contributes to ~93% of the NO formation [60, 69]. It is worth noticing that none of the considered thermochemical mechanisms has the ability to accurately predict the flame burning rate, prompt-NO, and maximum CH concentrations altogether.

Figure 1.3(a) presents the maximum CH concentration, $[\mathrm{CH}]_\mathrm{peak}$, measured in each of the C_1-C_4 alkane and alcohol flames. In alkane-air flames, $[\mathrm{CH}]_\mathrm{peak}$ is significantly higher for ethane than methane, but stabilizes for longer straight-chain lengths. In contrast, the peak CH concentration monotonically rises with increasing chain length of normal alcohols. Furthermore, branching of the fuel molecules hinders the formation of methylidyne as observed for the isomers of butane, propanol, and butanol.

Figure 1.3(b) shows the concentration of NO, [NO], obtained 4 mm upstream of the water-cooled stagnation surface (this location is shown as z_NO in Figure 1.2(b)). Remarkably, unlike $[\mathrm{CH}]_\mathrm{peak}$, [NO] does not decrease with the branching of the C_4 fuel molecules, and the NO concentration in ethane and methane flames is identical, within experimental uncertainty. In Figure 1.4(a), showing [NO] against $[\mathrm{CH}]_\mathrm{peak}$, these inconsistencies are observed as experimental data

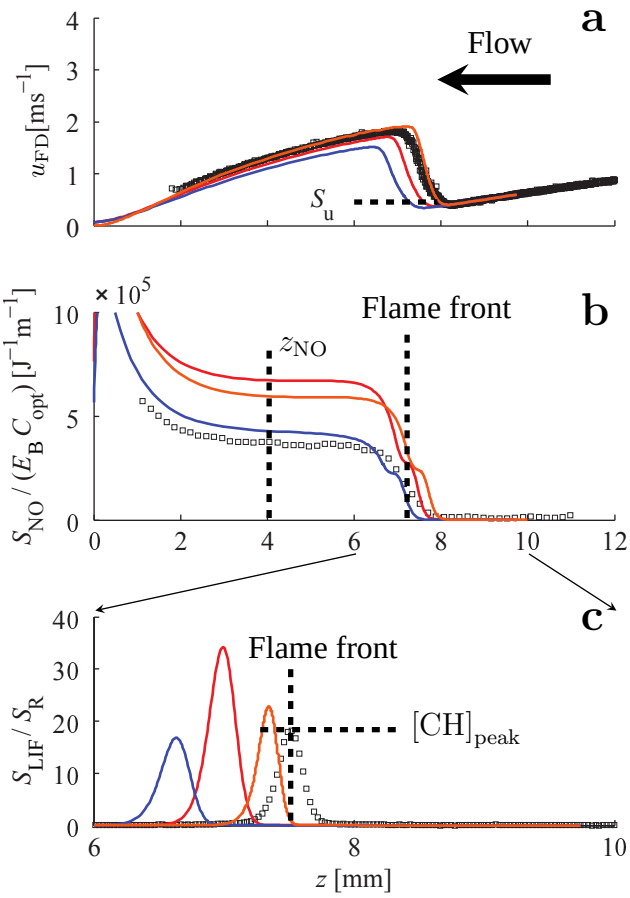

FIGURE 1.2: Experimental particle velocity, u_{FD}, and NO-LIF and CH-LIF profiles for a rich ($\phi = 1.3$), stagnation, premixed methane-air flame (symbols) superimposed with simulated, one-dimensional profiles. Same legend as Figure 1.1. Reproduced with permission [69].

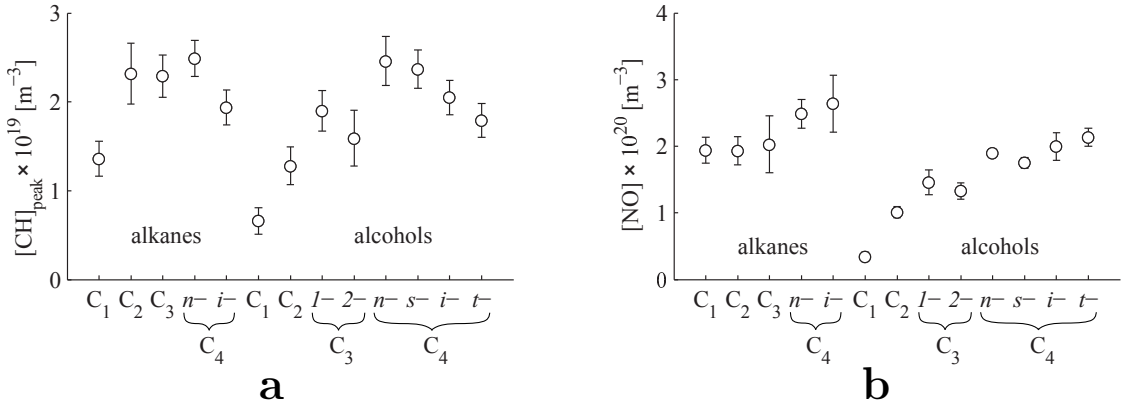

FIGURE 1.3: (a) Experimentally determined, maximum concentration of CH, and (b) concentration of NO obtained 4 mm upstream of the stagnation surface, for all isomers of C_1-C_4 alkanes and alcohols. Reproduced with permission [69].

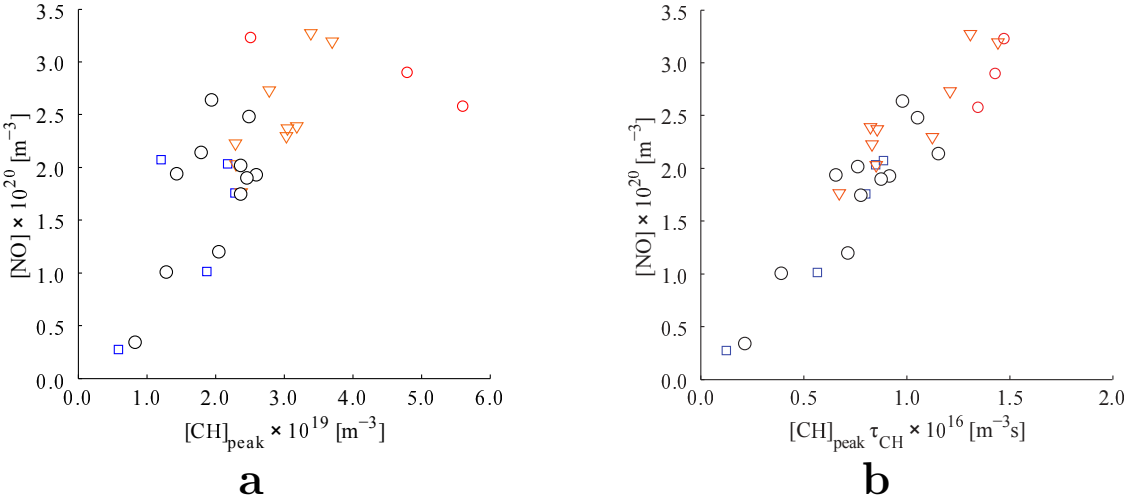

FIGURE 1.4: (a) NO concentration in the post-flame region vs. peak CH concentration in the flame front, and (b) NO concentration in the post-flame region vs. peak CH concentration in the flame front scaled by the residence time within the CH layer. Experiments (black symbols) and simulations (coloured symbols, same legend as Figure 1.1). Reproduced with permission [69].

points located too far to the left in comparison to the others. One could then conclude that precursors other than CH contribute to prompt-NO formation in flames of methane, and branched alkanes and alcohols, as suggested in some past studies of low-pressure flames [75, 76, 83, 84]. However, the sole consideration of $[\mathrm{CH}]_{\mathrm{peak}}$ in attempting to correlate CH and NO formations neglects an important parameter: the duration over which nitrogen molecules can react through reaction 1.14 with the methylidyne radical. The following expression, which represents the time integral of the CH concentration profile, accounts for that effect:

$$\int [\mathrm{CH}(t)]\,\mathrm{d}t = \int \frac{[\mathrm{CH}(z)]}{u(z)}\mathrm{d}z \approx [\mathrm{CH}]_{\mathrm{peak}} \cdot \frac{\delta_{\mathrm{CH}}}{S_{\mathrm{u}}} = [\mathrm{CH}]_{\mathrm{peak}} \cdot \tau_{\mathrm{CH}}. \tag{1.18}$$

A residence time in the CH layer, τ_{CH}, is defined as the ratio of the width of the CH layer taken at half-maximum, δ_{CH}, to the reference flame speed, S_{u}. As shown in Figure 1.4(b), a much-improved correlation, linear within the uncertainty of the experiments,[3] is obtained when reporting $[\mathrm{NO}]$ against $[\mathrm{CH}]_{\mathrm{peak}} \cdot \tau_{\mathrm{CH}}$. This confirms CH as the principal precursor of prompt-NO formation, and highlights the requirement for thermochemical mechanisms to accurately predict the flame reactivity (S_{u}), as well as the concentration profile of methylidyne ($[\mathrm{CH}]_{\mathrm{peak}}$ and δ_{CH}).

As observed by comparing the two plots of Figure 1.4, scaling $[\mathrm{CH}]_{\mathrm{peak}}$ by τ_{CH} results in a

[3]The error bars are omitted in Figure 1.4 for the sake of clarity, but can be found in [69].

better clustering of the simulation data, and yields a fair agreement with the experimentally determined, linear correlation. This suggests that the rate of prompt-NO formation is relatively well-defined in the thermochemical mechanisms considered here, and that inaccuracies in numerical values of [NO] are caused by improper predictions of the CH concentration profile and/or flame burning rate.

1.4 CH formation in flames

The design of reliable, fully constrained thermochemical mechanisms requires a comprehensive set of independently determined experimental data of known, and sufficiently high, accuracy [85, 86]. Significant advances in the measurement of the laminar flame speed, a surrogate measure of the flame reactivity, have been made since the pioneering work of Bunsen [87] and Mallard and Le Chatelier [88]. Whereas important scatter existed in the experimental data prior to the 1980s [89], improvements in experimental methods, namely corrections for the effect of hydrodynamic stretch, resulted in better consistency in the measurements performed in different apparatus, as well as reduced uncertainty in the data [90, 91]. With time, a vast pool of experimentally determined laminar flame speeds was assembled accounting for a variety of operating conditions, types of inert, dilution levels, and fuels [68, 91]. While simple fuels were originally studied, the body of experimental data is now extended to more complex and larger hydrocarbon and oxygenated fuel molecules due to the recent interest in non-conventional, fossil and bio-derived fuels [55, 90].

On the other hand, the body of available experimental data is not as exhaustive when it comes to methylidyne concentration, as summarized in Table 1.1. With few exceptions, experiments were generally performed with methane, or also acetylene owing to its intense formation of CH mitigating the need for highly sensitive diagnostics. To the knowledge of the author, besides the experimental data presented in this dissertation and reported in [92], quantitative [CH] measurements for hydrocarbons longer than acetylene at atmospheric pressure and above are not available in the literature. Furthermore, only a limited number of studies systematically investigated the effect of the equivalence ratio, most of them being devoted to partially, non-premixed, or rich flames.

Proper optimization of thermochemical mechanisms can only be achieved if the experiments can be accurately reproduced numerically. The validation targets, as well as the initial/boundary conditions to the simulations, must be accurate, and their respective uncertainties properly estimated. As shown in Table 1.1, the McKenna burner is the preferred configuration at low pressures as it produces a flat flame stabilized through heat loss to the porous surface. It is conveniently solved in modern numerical combustion models assuming one-dimensionality of the reactive flow,

TABLE 1.1: Summary of CH formation data in laboratory flames.

Burner type	Flame type*	Fuel	$\phi^{\dagger}$	P [atm]	Diagnostic‡	Ref.
McKenna	Pr	CH_4	1.07	0.0332	Lin. LIF + CRDS	[93, 94]
McKenna	Pr	CH_4	0.81,1.07,1.28	0.033, 0.040	Abs. lin. LIF	[77, 95]
McKenna	Pr	CH_4	1.07,1.28	0.033, 0.040	Abs. lin. LIF	[78]
		C_2H_6				
		C_3H_8				
		C_4H_{10}				
McKenna	Pr	C_3H_8	1.15	0.053	Abs. lin. LIF	[94, 96]
McKenna	Pr	C_2H_2	0.6-1.4	0.053, 0.079, 0.13	Laser absorption	[97]
Bunsen	PPr	CH_4	1.36	1	Abs. lin. LIF	[98]
Bunsen	Pr	CH_4	0.85-1.55	1	Rel. sat. LIF	[99]
		C_3H_8				
Bunsen	NPr	CH_4	N/A	1	Abs. lin. LIF	[100]
Counterflow	NPr	CH_4	N/A	1	Abs. lin. LIF	[101]
Counterflow	NPr, PPr	CH_4	1.45,1.6,2.0	1	Lin. LIF + CRDS	[102]
Counterflow	NPr	CH_4	N/A	1	Rel. lin. LIF	[103]
		C_2H_2				
		C_2H_6				
McKenna	Pr	CH_4	1.2	1	CRDS	[104]
Jet-wall	Pr	CH_4	0.69,0.96,1.31	1	Rel. sat. LIF	[79, 80]
Padley-Sugden	Pr	C_2H_2	1.2,1.6,2.0	1	Rel. sat. LIF	[105]
Slot	Pr	C_2H_2	N/Av.	1	Abs. sat. LIF	[106–108]
Torch	Pr	C_2H_2	1.05	1	CRDS	[104]
Wolfard-Parker	NPr	CH_4	N/A	1	CRDS	[109]
Wolfard-Parker	NPr	CH_4	N/A	1	WMS	[110]
		C_2H_2				
Counterflow	NPr, PPr	CH_4	1.45,1.6,2.0	1, 3, 6, 9, 12	Abs. lin. LIF	[111]

* Pr, NPr, and PPr stand for premixed, non-premixed, and partially premixed flames, respectively.
† N/A and N/Av. stand for not applicable, and not available, respectively.
‡ Abs., Rel., Lin., Sat., LIF, CRDS, and WMS correspond to absolute, relative, linear, saturated, laser-induced fluorescence, cavity ring-down spectroscopy, and wavelength modulation absorption spectroscopy, respectively.

and knowing the mixture composition and flow rate, as well as the surface temperature or, alternatively, the axial temperature profile through the flame front [112]. Due to reduced molecular collision rates at low pressures, the thickness of the CH layer generally spans over several millimetres [77]; hence, highly spatially resolved measurements are not required and absorption methods involving laser beams of finite diameter can be used. As the pressure is increased to more practical conditions, the flame stabilizes closer to the porous surface of the McKenna burner, and the thickness of the CH layer decreases. This makes measurements on the reactant side and through the flame front unrealizable, and laser-based diagnostics difficult, due to scattering off the burner surface [113]. Hence, a variety of burners producing partially, non-, and premixed flames are used at higher pressures. While some configurations, such as the counterflow and jet-wall burners, can

be directly simulated invoking quasi-one-dimensionality of the hydrodynamics without significant loss of accuracy [82, 114–116], others are simulated with models not exactly reproducing the experiments (*e.g.*, 1D freely propagating flame approximating a Bunsen flame [99]), or just cannot be simulated using reduced order modelling and, instead, require more complex CFD computations. In these last two situations, thermochemical mechanism validation using experimental data is made difficult, and the relevancy to chemistry modellers reduced.

As CH is a short-lived radical, it prevents the use of diagnostic methods relying on mechanical probes and, rather, requires the use of *in-situ* measurements. Non-intrusive, laser-based techniques are commonly used to measure the concentration of radicals in flames as discussed in [117–119]. As shown in Table 1.1, laser absorption and laser-induced fluorescence are common methods to probe CH concentration in flames. Being spatially resolved, LIF is often preferred to absorption techniques. It consists of exciting the molecules by laser light irradiation and collecting the spontaneous light emission of excited molecules as they return to the ground state. Saturated LIF has the benefit of high signal-to-noise ratio, and is insensitive to the rate of non-radiative collisional quenching of the electronically excited molecules by other species [98]. However, it is plagued with the problem of partial-saturation, both spatially and temporally, due to lower irradiance on the edges of the laser beam and finite rise and fall times of the laser pulse, respectively, causing inaccuracies in the measured CH concentration [98]. Alternatively, linear LIF, operating on weak laser irradiation, can be used at the expense of reduced signal-to-noise ratio; however, the rate of collisional quenching must be taken into account [98, 117, 118]. While the fluorescence intensity is normalized to a nominal case for relative LIF measurements, absolute (quantitative) LIF requires calibration of the optical collection system. Since CH has a short chemical lifetime, it cannot be stored and seeded in known concentrations for calibration purposes as done for NO-LIF [60, 61, 120]. Instead, the CH-LIF signal is generally adjusted to match a quantitative measurement obtained with a different diagnostic technique, such as cavity ring-down spectroscopy (CRDS) [93, 94, 102], or by determining the optical calibration coefficient from Raman [98] or Rayleigh [77, 94–96, 100, 101, 106–108] scattering signals.

1.5 Methodology

Given the current state of knowledge, the objective of this study is to quantify the formation of CH in atmospheric-pressure, premixed flames of C_1-C_4 normal alkanes at equivalence ratios, ϕ, ranging from 0.7 to 1.5 to evaluate the current understanding of CH production, and the modelling capability of a selection of available thermochemical mechanisms.

This dissertation starts with a survey of the jet-wall stagnation flame apparatus, and of the particle tracking velocimetry and planar laser-induced fluorescence methods used in this study. A description and a thorough analysis of the LIF model, which is used to translate the output of flame simulations in units compatible with the experimental data, are presented in Chapter 3. Experimentally determined CH layer thicknesses and maximum concentrations, two scalar values characterizing CH concentration profiles, over a range of equivalence ratios are presented in Chapter 4 for all fuels, and compared to predictions from four thermochemical mechanisms. A detailed analysis of the models is also presented to identify the sources of the significant variability in predictive performance. In Chapter 5, an optimization procedure is applied to the most accurate model to exemplify how the current set of experimental data can be used to improve thermochemical mechanisms, and to provide a model that properly describes CH formation, hence enabling accurate predictions of prompt-NO concentration.

The measurements reported in this investigation are expected to be useful as targets for the development, optimization, and validation of thermochemical mechanisms. Furthermore, the analyses presented in Chapters 4 and 5 highlight the principal rate coefficients that must be improved to better capture the experimental data.

Chapter 2

Methodology

2.1 Jet-wall stagnation burner

The experiments were performed in an atmospheric-pressure, premixed, jet-wall stagnation burner (see Figure 2.1), a configuration extensively used by our research group, as well as many others, to study flame reactivity [80, 81, 121] and NO formation [60, 61, 64, 69, 122] of fossil and bio-derived fuels. This geometry produces stable, compact, lifted flames readily accessible for optical diagnostics and free from influences from the burner boundaries. As such, the burning rate, flame temperature, and species profiles are functions of the fundamental properties of the combustible mixture. Details on the design, performance, and modelling of the jet-wall stagnation burner are found in [79, 82, 123].

2.1.1 Experimental configuration

A combustible jet of premixed fuel and air exits a converging nozzle with a throat diameter of 20 mm, and impinges on a water-cooled stagnation plate located ~25 mm away from the nozzle assembly. The inner jet decelerates as it approaches the stagnation surface, and the flame stabilizes where its propagation speed matches the flow velocity. Figure 2.2 presents a typical axial velocity profile for an atmospheric-pressure, stoichiometric ethane-air flame [64]. Starting from $z = 16$ mm, the flow initially decelerates, then accelerates due to thermal expansion through the flame front, and decelerates again as it travels towards the stagnation plate maintained at ~350 K to prevent condensation and surface reactions [124]. A co-flowing stream of inert gas, nitrogen or helium depending on flame composition, shrouds the inner jet to insulate the flame from the environment and improve its stability [79]. The temperatures of the plate and inner jet, obtained during and following each experimental trial, respectively, are measured with type-K thermocouples, and the mass flow rates of fuel and air are controlled with thermal mass flow controllers (Brooks models 5850S and 5851S). They are calibrated using a DryCal ML-500-44 dry-piston calibrator providing

a total uncertainty of $\pm 0.45\%$ of the measured mass flow rates, leading to a total uncertainty of $\pm 0.64\%$ in terms of equivalence ratio.

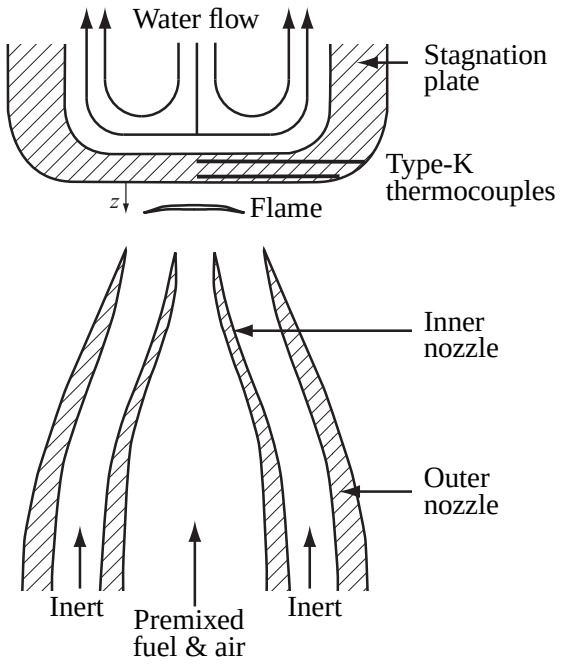

FIGURE 2.1: Jet-wall, stagnation flame burner. Reproduced with permission [69].

2.1.2 Stagnation flame modelling

2.1.2.1 Quasi-one-dimensional, stagnation flame model

The axial symmetry of the jet-wall configuration allows for simplification of the three-dimensional Navier-Stokes, continuity, and energy and species conservation equations to a quasi-1D formulation invoking similarity assumptions [114]. In this steady-state model, the axial flow velocity, temperature, density, and species mole fractions depend on the axial position, z, only. The quasi-1D model provides good agreement with experiments in terms of flow velocity, temperature, and species concentration profiles if the velocity boundary conditions (BC) are obtained through a parabolic fit to the velocity data in the un-reacted, stagnating, cold flow region (see section 2.2.3), if the motion of the tracer particles is modelled, and if the thermochemical mechanism describing the chemical rates, thermodynamic, and transport properties is accurate [60, 81, 82, 125, 126].

Here, the experiments are numerically reproduced with the premixed, stagnation flame reactor of Chemkin-Pro [112]. It solves the 1D axisymmetric model of Kee et al. [114] along with the

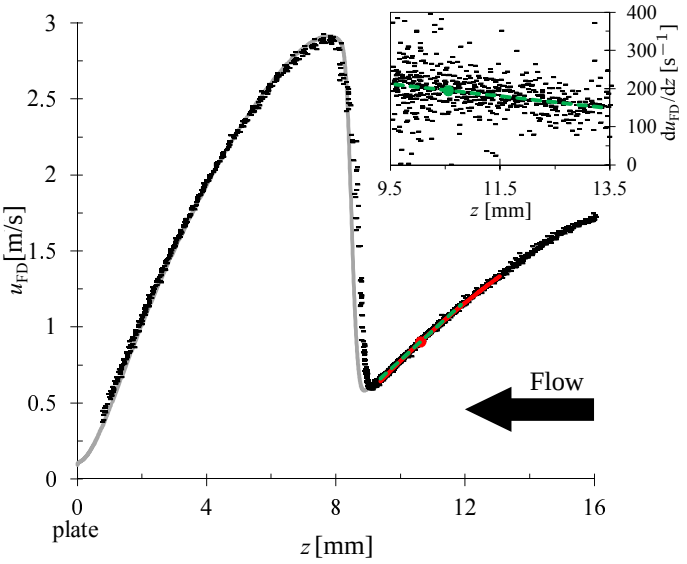

FIGURE 2.2: $u_{\mathrm{FD}}(z)$ and $\mathrm{d}u_{\mathrm{FD}}(z)/\mathrm{d}z$ (inset) for a stoichiometric, ethane-air flame. Legend: the solid black symbols are experimentally measured values, the red curve is the parabolic fit to the cold flow portion of the velocity profile, the red dot is the inlet velocity BC, the green dashed line corresponds to the linear-fit to $\mathrm{d}u_{\mathrm{FD}}(z)/\mathrm{d}z$, the green dot is the inlet velocity gradient BC, and the solid grey curve is the solution of a flame simulation performed with the GRI-Mech 3.0 mechanism [65].

energy and species conservation equations for the following set of boundary conditions: u_{inlet}, $v/r \approx -1/2 \cdot \mathrm{d}u/\mathrm{d}z|_{\mathrm{inlet}}$, T_{inlet}, and $Y_{i,\mathrm{inlet}}$ at the inlet, and T_{plate}, $u = 0$, $\mathrm{d}u/\mathrm{d}z = 0$, and $\rho Y_i(u + V_i) = 0$ at the stagnation surface. The specification of the wall temperature, T_{plate}, accounts for the heat loss to the plate, and the mass transport BC implies no-flux of species at the stagnation surface (surface reactions neglected). The experimentally determined BCs are reported for all test conditions in Table F.1. Mixture-averaged formulation of the diffusion coefficients is used and thermal (Soret) diffusion is neglected. Convergence down to 10^{-5} and 10^{-9} in terms of relative and absolute tolerances, respectively, is obtained on meshes refined to achieve *grad* and *curv* parameters of 0.05 and 0.075, respectively.

2.1.2.2 Thermochemical mechanisms

The predictive capability of four thermochemical mechanisms is studied in this work. GRI-Mech 3.0 (GRI) [65] was assembled to model the combustion of natural gas and is commonly used as a design tool in industry. It consists of 325 reversible and non-reversible reactions involving 53 species. The rates of the reactions were adjusted using a global optimization procedure against an extensive set of ignition delay times measured in shock tubes, species concentrations obtained in reactors, shock tubes and flames, and laminar flame speeds in twin-counterflow and spherically

expanding flames [65]. Of particular interest for the current study, GRI was validated against methylidyne concentrations in low-pressure flames stabilized on McKenna burners [94, 95] and during rich methane oxidation behind shock waves [127].

Another model is the San Diego mechanism (SD) [128] that includes C_1-C_3 hydrocarbon and C_1-C_2 alcohol chemistry. The 2005 version used here has 235 reactions and 46 species, and does not include the optional NO sub-model. This mechanism, optimized for pressures $<$100 atm and temperatures $>$1000 K, was assembled in a hierarchical manner starting with hydrogen chemistry and subsequently extending to CO, C_1, C_2 and C_3 compounds. It differs from the other mechanisms by its design philosophy that aims to include the minimum number of species and reactions to describe the combustion processes of interest. A historical perspective on the development of the SD mechanism is presented in [129]. The validation targets include ignition delay times in shock tubes, laminar flame speeds measured in combustion bombs and stagnation flow configurations, as well as species profiles measured by gas chromatography in counterflow, two-stage flames. It does not appear that the SD model has been validated against experimental CH measurements. However, the mechanism supplemented with NO chemistry was benchmarked against NO_x measurements in counterflow methanol [130], methane [131], and ethanol flames [132].

A third model is USC Mech II (USC) by Wang et al. [133]. This mechanism describes the high-temperature combustion of H_2, CO, and C_1-C_4 hydrocarbons using 111 species and 784 reactions. It was benchmarked against ignition delay times in shock tubes, laminar flame speeds in combustion bombs and stagnation flame burners, as well as species profiles in shock tubes, flow reactors, and low-pressure flames measured by molecular beam mass spectroscopy. Even if comprehensive, the set of species concentrations against which the USC mechanism was validated does not include methylidyne.

Recently, new generation, hierarchical chemical mechanisms were designed to simulate the combustion of a comprehensive set of fuels over a wide range of regimes by including all relevant reaction steps, regardless of their significance [68, 134]. The AramcoMech 1.3 mechanism (NUIG) [134] was constructed in a hierarchical manner, starting with simple, short-chain fuels to more complex C_1 to C_4 hydrocarbon and oxygenated chemistry. This model contains 253 species and 1542 reactions, and has been validated against numerous experimental targets including ignition delay times measured in shock tubes, laminar flame speeds in stagnation-flow configurations and combustion bombs, and species concentrations in jet-stirred and flow reactors, but not against CH measurements. In 2016, the new AramcoMech 2.0 mechanism (NUIG2) [135] was released, but could not be included in the analysis of the models presented in Chapter 4 due to time constraints.

2.1.2.3 Reaction pathway analysis

Reaction Pathway Analysis (RPA) is a useful tool to visualize and understand the complex chemistry included in modern thermochemical models. The RPA outputs a network where the nodes are chemical species linked together by arrows representing the chemical reactions. The RPA method used here is inspired by [136], where a conserved scalar, the flux of element e, is tracked as reactants are made into products. The thickness of the arrows in the network is linearly scaled with the spatially integrated rate of transfer of element e from species s_1 to s_2, $R(e, s_1, s_2)$ [kmol/s], calculated using equation 2.1, where $n_l(e, s_1, s_2)$ is the number of atoms of element e transferred from species s_1 to s_2 through reaction l, $q_l(z)$ [kmol/m^3-s] is the rate of progress variable of reaction l, z [m] is the axial direction, and r_{CV} [m] is the radius of the cylindrical control volume (CV) adjusted to achieve an influx of element e of 1 kmol/s. As such, $R(e, s_1, s_2)$ can be thought of as an absolute flux of element e, or as a fraction of the flux of e-atoms entering the control volume. To prevent molecular transport fluxes across the CV boundaries, z_{in} and z_{out}, the inlet and outlet locations of the control volume, respectively, are taken at the inlet and outlet of the computational domain. Therefore, the net fluxes of element e crossing the boundaries of the CV are determined solely from the mixture composition, velocity, and density data commonly available in the output of freely propagating flame simulations.

$$R(e, s_1, s_2) = \int_{z_{\mathrm{in}}}^{z_{\mathrm{out}}} \sum_{l} n_l(e, s_1, s_2) \cdot q_l(z) \cdot \pi r_{\mathrm{CV}}^2 \, \mathrm{d}z \tag{2.1}$$

Equation 2.1 differs from [136] by the summation over all l reactions being inside the spatial integral. This allows for a significant reduction in the number of numerical integrals performed and, thereby, provides a reduced numerical error in calculating $R(e, s_1, s_2)$. The integral is computed using a Simpson's $1/3$ rule redeveloped in this work to make it applicable to unequally distributed grid points characteristic of refined computational meshes. The details of the method are provided in Appendix A.

2.2 Particle tracking velocimetry

The velocity boundary conditions for the flame simulations discussed in section 2.1.2 are obtained through particle tracking velocimetry. This Lagrangian technique consists of recording the trajectory of individual tracer particles illuminated by a laser source, and subsequently converting

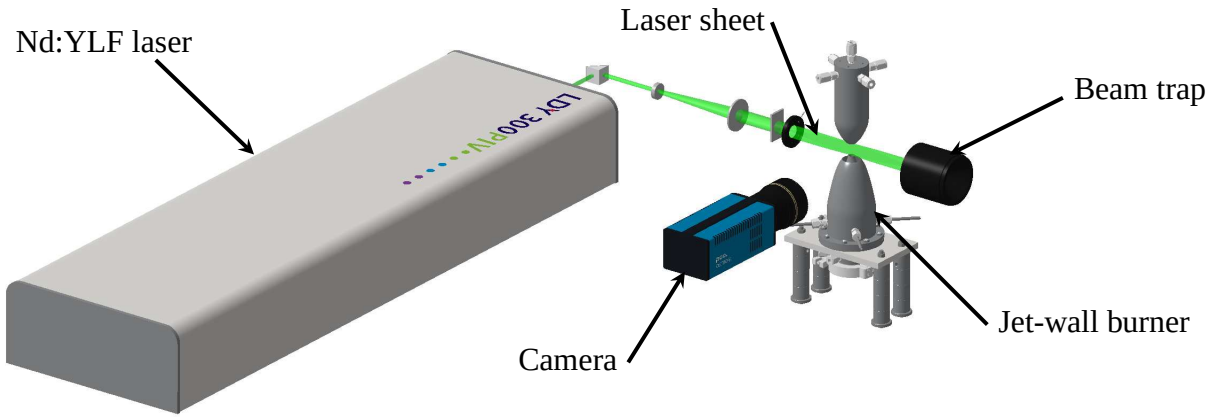

FIGURE 2.3: Integration of the PTV diagnostic technique around the jet-wall burner.

the spatio-temporal information to velocities, and their derivatives. Two- and stereoscopic three-dimensional PTV methods, with particle streaks obtained from single images or a set of consecutive images, have been used to study droplet atomization [137], the geological phenomenon of saltation [138], turbulent flows [139], and laminar combustion [126, 140, 141].

Flame simulations have demonstrated that small-size inert particles act as a diluent in particle-laden premixed flames causing a monotonic reduction of flame temperature and speed as the particle loading is increased [142]. The main benefit of PTV for the current study is to reduce this thermodynamic effect by theoretically requiring a particle loading as much as five orders of magnitude lower than other common techniques, such as Particle Image Velocimetry (PIV). Furthermore, thermal expansion through the flame causes a reduction of particle density affecting the accuracy of PIV unless more intricate image processing methods are adopted (*e.g.*, adaptive interrogation window size [143]). In contrast, PTV readily provides reliable information throughout the spatial domain as the same particle is tracked in a Lagrangian manner.

2.2.1 Experimental implementation

The integration of the PTV diagnostic around the jet-wall burner is shown in Figure 2.3. A minimal amount of refractory scattering particles (1μm diameter Al_2O_3 particles) is seeded into the flow using a miniaturized cyclone aerosol generator [144], and illuminated by a high repetition rate, diode pumped, dual cavity, Nd:YLF laser (Litron LDY 303, $\lambda = 527$ nm, 20 mJ/pulse at 1 kHz). For the current set of experiments, the laser is operated at a repetition rate, f, of 8 kHz adjusted to maximize the resolution of the measurements in the low velocity region immediately upstream of the flame. Using a series of plano-spherical and plano-cylindrical borosilicate (N-BK7) glass lenses, the beam emerging from the laser is made into a sheet, ~1 mm thick, centred on the axis of

the burner. The light scattered by the particles is collected using a 90 mm Tamron $f/2.8$ macro lens, and focused on a 14-bit, monochrome, CCD camera (Cooke PCO.2000, 2048 $\times$ 2048 pixels^2). An exposure time of 150 ms results in series (streaks) of dots, analogous to streamlines, on individually captured images (see Figure 2.4).

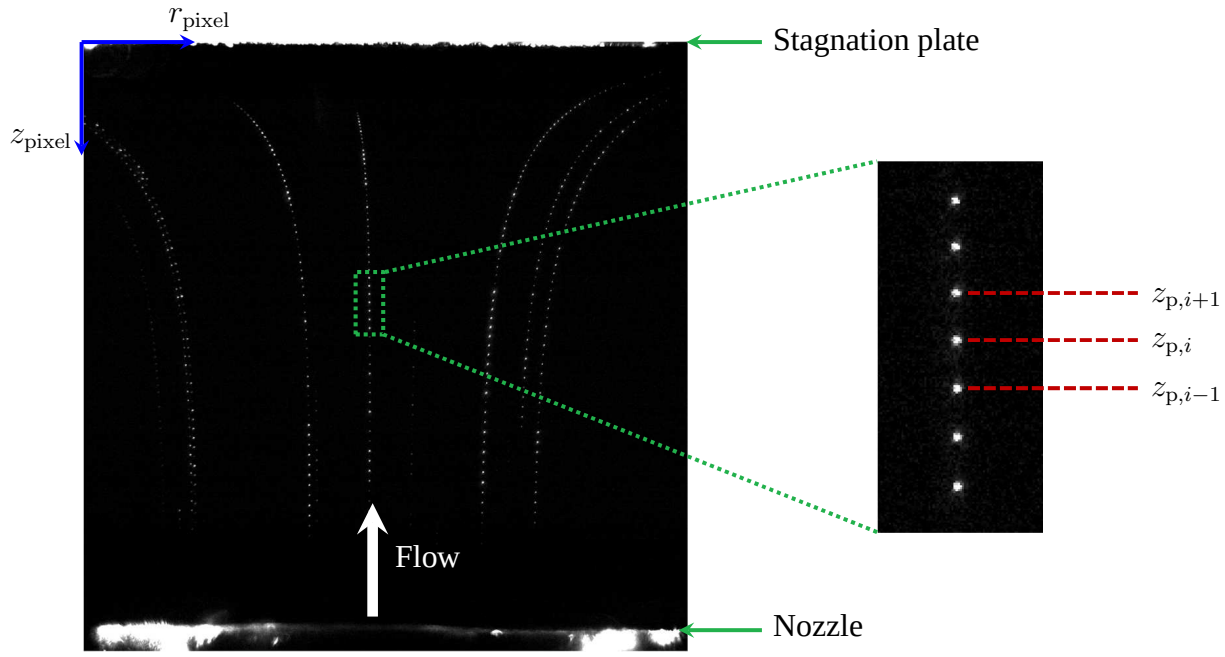

FIGURE 2.4: PTV image obtained in a cold, non-reacting flow. The reference frame of the PTV image is shown by the blue vectors at the top left corner of the picture.

2.2.2 Image processing

The PTV method used in this study extends the measurement technique of Benezech et al. [126, 141]. The axial and radial positions of a given particle (dot) in the image reference frame at time t_i, $z_{\mathrm{p},i}$ [pixel] and $r_{\mathrm{p},i}$ [pixel], respectively, are obtained through a grey scale intensity centroid calculation:

$$z_{\mathrm{p},i} = \frac{\sum_{j=1}^{N} z_{\mathrm{pixel},j} \cdot I_{\mathrm{pixel}}(z_{\mathrm{pixel},j}, r_{\mathrm{pixel},j})}{\sum_{j=1}^{N} I_{\mathrm{pixel}}(z_{\mathrm{pixel},j}, r_{\mathrm{pixel},j})}, \tag{2.2}$$

$$r_{\mathrm{p},i} = \frac{\sum_{j=1}^{N} r_{\mathrm{pixel},j} \cdot I_{\mathrm{pixel}}(z_{\mathrm{pixel},j}, r_{\mathrm{pixel},j})}{\sum_{j=1}^{N} I_{\mathrm{pixel}}(z_{\mathrm{pixel},j}, r_{\mathrm{pixel},j})}, \tag{2.3}$$

where $z_{\mathrm{pixel},j}$ [pixel] and $r_{\mathrm{pixel},j}$ [pixel] are the axial and radial positions of individual pixels, respectively, $I_{\mathrm{pixel}}(z_{\mathrm{pixel},j}, r_{\mathrm{pixel},j})$ [count] is the pixel intensity at position $(z_{\mathrm{pixel},j}, r_{\mathrm{pixel},j})$, and N is the number of pixels in the interrogation box surrounding the dot i. The original script, inherited from [126, 141], required the user to manually select every dot on the images. Several hours were necessary to record the 15 to 30 streaks superimposed to obtain a single one-dimensional velocity profile similar to Figure 2.2. The image processing script was automated for the current study, and requires the user to only select the first two dots of a streak. The program finds the others by establishing a search area knowing the location of the previous dots; the processing script essentially walks along the streaks of dots. One-dimensional velocity profiles are now obtained within approximately 10 minutes with the new image processing method.

Commonly, the origin of stagnation flow fields is placed at the intersection of the centreline axis of the burner with the stagnation plate. The axial and radial positions of a given particle in the burner reference frame at time t_i, z_i [m] and r_i [m], respectively, are made dimensional through the application of a spatial calibration coefficient, C [m/pixel]:

$$z_i = (z_{\mathrm{p},i} - z_{\mathrm{plate}}) \cdot C, \tag{2.4}$$

$$r_i = (r_{\mathrm{p},i} - r_{\mathrm{axis}}) \cdot C, \tag{2.5}$$

where z_{plate} [pixel] and r_{axis} [pixel] are the axial location of the stagnation surface and the radial position of the axis of the burner in the image reference frame, respectively. The calibration coefficient, C, is determined from the image of a dotted target with a 1 mm centre-to-centre grid-spacing (0.5 mm dot-size, see Figure 2.5(a)). The location of the dots on the calibration image (see Figure 2.5(b)) is obtained with the grey scale intensity centroid calculation described above, performed on the negative of the calibration image. C is taken as the average, over all dot-to-dot interstices in the image, of the ratio of the nominal grid-spacing (1 mm) to the dot-separation in pixels.

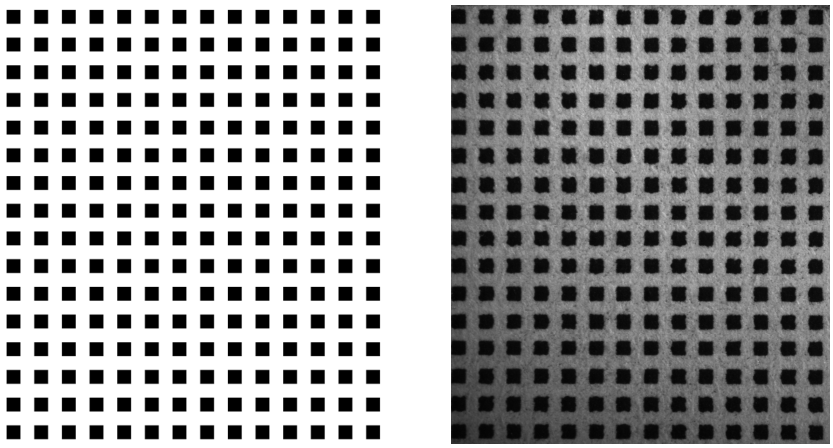

FIGURE 2.5: PTV calibration target. a) Computer-generated target with a 1 mm centre-to-centre grid-spacing, and 0.5 mm dot-size, and b) image of the target recorded with the PCO camera. The images are not to scale.

The axial velocity of the particles is determined using a second-order accurate, central finite difference scheme [145]:

$$\begin{aligned} u_{\mathrm{p}}(z_i, r_i) &= \left.\frac{\mathrm{d}z}{\mathrm{d}t}\right|_{z_i, r_i} \\ &= \underbrace{\frac{z_{\mathrm{p},i+1} - z_{\mathrm{p},i-1}}{2} \cdot f \cdot C}_{u_{\mathrm{FD}}\left(z_i, r_i\right)} + E_{u_{\mathrm{p},i}}, \end{aligned} \tag{2.6}$$

where f [Hz] is the laser repetition rate, $E_{u_{\mathrm{p},i}}$ is the error induced by the finite difference (see section 2.2.3), and $u_{\mathrm{FD}}\left(z_i, r_i\right)$ is the particle velocity estimated with the central finite difference, which is reported in the velocity profiles (see Figure 2.2). The PTV method can be readily extended to provide two-dimensional flow fields by computing the radial particle velocity:

$$\begin{aligned} v_{\mathrm{p}}(z_i, r_i) &= \left.\frac{\mathrm{d}r}{\mathrm{d}t}\right|_{z_i, r_i} \\ &= \frac{r_{\mathrm{p},i+1} - r_{\mathrm{p},i-1}}{2} \cdot f \cdot C + E_{v_{\mathrm{p},i}}. \end{aligned} \tag{2.7}$$

The finite difference scheme made of equations 2.4 and 2.6 yields an improved accuracy over the method of Benezech and co-workers [126, 141]. In their formulation, the axial particle velocity is calculated as the product of the laser repetition rate, f, with the distance travelled by the

particle between two consecutive laser pulses ($u_{\mathrm{FD}} = (z_{i+1} - z_i) \cdot f$). The velocity is placed midway between the dots on the PTV image, *i.e.*, at $z = (z_{i+1} + z_i)/2$. In essence, their method computes the particle velocity using the position of two consecutive dots as with first-order finite differences, but mimics a second-order finite difference scheme by placing the velocity between the dots. However, it can be shown that, unlike the current central finite difference scheme, the method of Benezech and co-workers [126, 141] does not exactly capture quadratic particle trajectories of the form $z(t) = C_0 + C_1 \cdot t + C_2 \cdot t^2$, where C_i are arbitrary constants.

Misfires and/or significant, momentary drops in laser pulse energy lead to missing dots in the PTV images. Referring to equation 2.6, a single missing dot causes an over-prediction of ~50% of the local velocity. To remove such outliers, two 10^{th}-order polynomials, the first extending from the stagnation surface to the flame front, and the second from the flame front to the outlet of the nozzle, are least-squares adjusted to the raw particle velocity profile. Any data point departing by more than 25% of the local value of the polynomial is removed from the velocity profile. Only a small number of outliers remains after a few iterations of this method. They are manually removed by the user through the graphical interface. Once the analysis is completed, a velocity profile, similar to Figure 2.2, is obtained from the superposition of 15 to 30 streaks collected in the vicinity of the centreline axis of the burner.

2.2.3 Boundary conditions and uncertainties

Particle velocimetry methods rely on the assumption that the tracer particles closely track the flow. However, it was shown that high-gradient, high-curvature, chemically reactive flows are plagued by significant particle lag due to the combined effects of the thermophoretic force and particle inertia [125, 146, 147]. In the current study, since the boundary conditions for the simulations are measured 1.5 mm upstream of the reaction zone, the temperature is constant and equal to the inlet (cold) temperature, and the rate of flow deceleration is weak, such that the particles accurately track the flow. In other words, the flow and particle velocities are equal in the cold region upstream of the flame ($u = u_{\mathrm{p}} \approx u_{\mathrm{FD}}$) and, therefore, the boundary conditions are evaluated from the measured particle velocities, u_{FD}, without further corrections for the thermophoretic force and particle inertia.

2.2.3.1 Axial velocity

When simplified by assuming an isothermal fluid, the analytical solution of the quasi-1D hydrodynamic model of Kee et al. [114] is a second-order polynomial of the form of equation 2.8 [79, 80]. The inlet velocity boundary condition, u_{inlet}, shown as a red dot in Figure 2.2, is then obtained

through a least-squares adjustment of a parabola to the cold, constant-temperature portion of the velocity profile (see red curve in Figure 2.2):

$$u_{\mathrm{fit}}(z) = \beta_0 + \beta_1 \cdot z + \beta_2 \cdot z^2, \tag{2.8}$$

evaluated at $z = z_{\mathrm{inlet}}$, *i.e.*, $u_{\mathrm{inlet}} = u_{\mathrm{fit}}(z_{\mathrm{inlet}})$. The coefficients of the quadratic polynomial are calculated as [148]:

$$\boldsymbol{\beta} = \begin{bmatrix} \beta_0 \\ \beta_1 \\ \beta_2 \end{bmatrix} = (\boldsymbol{Z}'\boldsymbol{Z})^{-1}\,\boldsymbol{Z}'\boldsymbol{U}_{\mathbf{p}}, \tag{2.9}$$

where $\boldsymbol{Z}$ is defined as:

$$\boldsymbol{Z} = \begin{bmatrix} 1 & z_1 & z_1^2 \\ 1 & z_2 & z_2^2 \\ \vdots & \vdots & \vdots \\ 1 & z_{n-1} & z_{n-1}^2 \\ 1 & z_n & z_n^2 \end{bmatrix}, \tag{2.10}$$

and $\boldsymbol{U}_{\mathbf{p}}$ as:

$$\boldsymbol{U}_{\mathbf{p}} = \begin{bmatrix} u_{\mathrm{FD},1} \\ u_{\mathrm{FD},2} \\ \vdots \\ u_{\mathrm{FD},n-1} \\ u_{\mathrm{FD},n} \end{bmatrix}. \tag{2.11}$$

In equations 2.10 and 2.11, z_i and $u_{\mathrm{FD},i}$ are the particle locations and velocities for the n data points included in the least-squares adjustment.

The overall error in u_{inlet}, which is the value of u_{fit} calculated 1.5 mm upstream of the velocity minimum, consists of two components: 1) the systematic error in the determination of the particle velocities, u_{p}, and 2) the uncertainty in the least-squares adjustment of equation 2.8 due to the scatter in the experimental data. Inspection of equation 2.6 reveals that the systematic error on u_{p} arises from three sources: 1) the systematic uncertainty on the laser repetition rate, 2) the overall error on the calibration coefficient, and 3) the limited accuracy of the second-order finite difference scheme. It is assumed that the distance between the camera pixels is consistent over the whole CCD sensor, such that the difference $z_{\mathrm{p},i+1} - z_{\mathrm{p},i-1}$ in equation 2.6 is devoid of local systematic errors. The accuracy on f was provided by the laser manufacturer as $< 0.1\%$ of reading [149].

The contribution of the calibration factor to the systematic error in u_p is divided in two, systematic (ΔC_sys) and random (ΔC_rand), components. The former, which accounts for an overall magnification of the calibration grid pattern, *e.g.*, during the printing of the target, was determined by measuring the distance over 17 grid points using a high-precision caliper, and comparing to the expected distance based on the 1 mm grid-spacing. This yielded ${}^{\Delta C_\mathrm{sys}}/_{C} = 0.61\%$. The effect on the calibration coefficient of the misalignment of the camera vertical vector (z_pixel in Figure 2.4) with the flow centreline axis, or the calibration target, was also investigated. It can be shown that it induces a magnification proportional to the cosine of the angle between the camera and the burner/target and, therefore, it has a weak impact on the calibration coefficient. Furthermore, great care was put in properly aligning the burner and the camera, and in performing the calibration, such that these misalignment errors are unimportant. The effect of having the target for the calibration and the laser sheet during the experiments at the two extremes of the focus range (depth of field) of the collection optics (both locations yielding a different magnification ratio) was also considered, but found negligible. The random uncertainty in the calibration coefficient is calculated using the Student's t-distribution [148]:

$$\frac{\Delta C_\mathrm{rand}}{C} = \frac{t_{0.025,n-1}}{C}\frac{\sigma}{\sqrt{n}}, \tag{2.12}$$

where n is the number of samples (number of intervals between two adjacent grid points used to obtain C), $t_{0.025,n-1}$ is the Student's t inverse cumulative distribution function with a 95% interval of confidence, and σ is the standard deviation of the ratio of the nominal grid-spacing (1 mm) to the size of the interstices considered in the computation of C. This random uncertainty is expected to mostly reflect local variations in the grid-spacing on the printed target. The overall uncertainty on the calibration coefficient is computed as:

$$\frac{\Delta C}{C} = \sqrt{\left(\frac{\Delta C_\mathrm{sys}}{C}\right)^2 + \left(\frac{\Delta C_\mathrm{rand}}{C}\right)^2} = 0.74\%. \tag{2.13}$$

As shown in equation 2.6, the axial velocity is approximated with a second-order accurate, central finite difference for which the error term is defined as [145]:

$$E_{u_{\mathrm{p},i}} = \frac{1}{6f^2}\cdot\frac{\mathrm{d}^3 z\left(\epsilon\right)}{\mathrm{d}t^3}. \tag{2.14}$$

The third derivative of the particle position with respect to time is evaluated at an unknown instant, ϵ, comprised in the interval $t_i - {}^1/_f \leq \epsilon \leq t_i + {}^1/_f$, where t_i corresponds to the time at which the particle is recorded at the location z_i. *A priori*, the exact, continuous function $z(t)$ is unknown due

to the discrete nature of the PTV technique. Indeed, only the position of the particles at discrete instants is known. However, as explained above, the stagnation flow in the cold region upstream of the flame is described by a quadratic function of the axial position z. A series of mathematical manipulations, shown in equation 2.17, are applied to transform ${}^{\mathrm{d}^3 z}/_{\mathrm{d}t^3}$ into a function that depends on the axial particle velocity, u_p, and its spatial derivatives. It must be remembered that the particle velocity is defined as:

$$u_\mathrm{p} = \frac{\mathrm{d}z}{\mathrm{d}t}. \tag{2.15}$$

Also, the axial flow velocity and, consequently, the particle velocity in the cold region upstream of the flame, is solely a function of z in a stagnation flow. The chain rule for an arbitrary function $f(z)$, such as $u_\mathrm{p}(z)$, ${}^{\mathrm{d}u_\mathrm{p}(z)}/_{\mathrm{d}z}$, etc., can be written as:

$$\frac{\mathrm{d}f}{\mathrm{d}t} = \frac{\mathrm{d}f}{\mathrm{d}z}\frac{\mathrm{d}z}{\mathrm{d}t} = \frac{\mathrm{d}f}{\mathrm{d}z} \cdot u_\mathrm{p}. \tag{2.16}$$

$$\begin{aligned} \frac{\mathrm{d}^3 z}{\mathrm{d}t^3} = \frac{\mathrm{d}^2}{\mathrm{d}t^2}\left(\frac{\mathrm{d}z}{\mathrm{d}t}\right) &= \frac{\mathrm{d}}{\mathrm{d}t}\left(\frac{\mathrm{d}u_\mathrm{p}}{\mathrm{d}t}\right) \\ &= \frac{\mathrm{d}}{\mathrm{d}t}\left(\frac{\mathrm{d}u_\mathrm{p}}{\mathrm{d}z}u_\mathrm{p}\right) \\ &= u_\mathrm{p}^2\frac{\mathrm{d}^2 u_\mathrm{p}}{\mathrm{d}z^2} + u_\mathrm{p}\left(\frac{\mathrm{d}u_\mathrm{p}}{\mathrm{d}z}\right)^2 \end{aligned} \tag{2.17}$$

Inserting the result of equation 2.17 in equation 2.14, the error induced by the finite difference scheme becomes:

$$E_{u_{\mathrm{p},i}} = \frac{1}{6f^2} \cdot \left[u_\mathrm{p}^2\frac{\mathrm{d}^2 u_\mathrm{p}}{\mathrm{d}z^2} + u_\mathrm{p}\left(\frac{\mathrm{d}u_\mathrm{p}}{\mathrm{d}z}\right)^2\right]\Bigg|_{t=\epsilon}. \tag{2.18}$$

The first and second-order derivatives of u_p with respect to the axial position are estimated using the quadratic equation 2.8. As explained above, ϵ is an unknown instant comprised within $t_i \pm {}^1/_f$. The maximum value of $E_{u_{\mathrm{p},i}}$, calculated over 100 grid points uniformly distributed on the interval $z_\mathrm{inlet} \pm {}^{u_\mathrm{inlet}}/_f$, is taken as a conservative estimation of the error. As the first and second-order velocity derivatives of equation 2.18 are relatively small in the cold flow region, $E_{u_{\mathrm{p},i}}$ at the position z_inlet is generally negligible in comparison to the errors on the calibration coefficient and due to the scatter in the particle velocities (see below).

Random fluctuations in the velocity measurements, which are expected to be primarily caused by 1) variations around the nominal value of the laser repetition rate, 2) random errors in the particle locations due to the finite resolution of the CCD sensor, 3) slight oscillations of the flame causing a transient shift in the axial velocity profile, and 4) minor variations of the axial velocity

over the radius of the stream tube in which the particle streaks are collected, limit the precision of the least-squares adjustment of equation 2.8. The uncertainty in the value of u_{inlet} due to the scatter in the velocity measurements is calculated as [148]:

$$\Delta u_{\text{inlet,rand}} = t_{0.025,n-3}\sqrt{\frac{\boldsymbol{U_p}'\boldsymbol{U_p} - \boldsymbol{\beta}'\boldsymbol{Z}'\boldsymbol{U_p}}{n-3}\boldsymbol{Z_0}'\left(\boldsymbol{Z}'\boldsymbol{Z}\right)^{-1}\boldsymbol{Z_0}}, \tag{2.19}$$

where,

$$\boldsymbol{Z_0} = \begin{bmatrix} 1 \\ z_{\text{inlet}} \\ z_{\text{inlet}}^2 \end{bmatrix}. \tag{2.20}$$

Finally, the overall error in the inlet velocity boundary condition is calculated as:

$$\Delta u_{\text{inlet}} = \sqrt{\left(u_{\text{inlet}}\frac{\Delta C}{C}\right)^2 + \left(u_{\text{inlet}}\frac{\Delta f}{f}\right)^2 + E_{u_{\text{p}},\text{inlet}}^2 + \Delta u_{\text{inlet,rand}}^2}. \tag{2.21}$$

For the current set of experiments, it is principally due to the uncertainty on the calibration coefficient, and the scatter in the experimental particle velocities.

2.2.3.2 Axial velocity gradient

A first attempt to determine ${}^{\mathrm{d}u}/_{\mathrm{d}z}\big|_{\text{inlet}}$ was made through derivation of equation 2.8:

$$\left.\frac{\mathrm{d}u}{\mathrm{d}z}\right|_{\text{inlet}} = \beta_1 + 2\beta_2 \cdot z_{\text{inlet}}, \tag{2.22}$$

and the uncertainty in the velocity gradient was assessed by propagating the error in the β_i values:

$$\Delta\left.\frac{\mathrm{d}u}{\mathrm{d}z}\right|_{\text{inlet}} = \sqrt{\Delta\beta_1^2 + \left(2z_{\text{inlet}}\Delta\beta_2\right)^2}. \tag{2.23}$$

The error on the polynomial coefficients was calculated as [148]:

$$\Delta\beta_i = t_{0.025,n-3}\sqrt{\frac{\boldsymbol{U_p}'\boldsymbol{U_p} - \boldsymbol{\beta}'\boldsymbol{Z}'\boldsymbol{U_p}}{n-3}\left(\boldsymbol{Z}'\boldsymbol{Z}\right)_{ii}^{-1}}, \tag{2.24}$$

where $\left(\boldsymbol{Z}'\boldsymbol{Z}\right)_{ii}^{-1}$ is the element (i,i) of the matrix $\left(\boldsymbol{Z}'\boldsymbol{Z}\right)^{-1}$. While equation 2.22 provided reasonable values of ${}^{\mathrm{d}u}/_{\mathrm{d}z}\big|_{\text{inlet}}$, the errors estimated with equation 2.23 were so large that linear polynomials with slopes corresponding to the uncertainty limits of ${}^{\mathrm{d}u}/_{\mathrm{d}z}\big|_{\text{inlet}}$ were clearly not tangent to the

axial velocity profile at the position z_{inlet}. Therefore, equation 2.23 overestimates the uncertainty in ${}^{\mathrm{d}u}/_{\mathrm{d}z}\big|_{\text{inlet}}$.

Considering the parabolic nature of the flow upstream of the flame [79, 80], an alternative method was developed to determine ${}^{\mathrm{d}u}/_{\mathrm{d}z}\big|_{\text{inlet}}$ from a least-squares linear regression to the individual, experimental values of ${}^{\mathrm{d}u_{\mathrm{p}}}/_{\mathrm{d}z}$ (see the inset of Figure 2.2):

$$\left.\frac{\mathrm{d}u}{\mathrm{d}z}\right|_{\text{inlet}} = \eta_0 + \eta_1 \cdot z_{\text{inlet}}, \tag{2.25}$$

where the polynomial coefficients are calculated as:

$$\boldsymbol{\eta} = \begin{bmatrix} \eta_0 \\ \eta_1 \end{bmatrix} = (\boldsymbol{z}'\boldsymbol{z})^{-1}\,\boldsymbol{z}'\boldsymbol{L_p}, \tag{2.26}$$

$\boldsymbol{z}$ is defined as:

$$\boldsymbol{z} = \begin{bmatrix} 1 & z_1 \\ 1 & z_2 \\ \vdots & \vdots \\ 1 & z_{n-1} \\ 1 & z_n \end{bmatrix}, \tag{2.27}$$

and $\boldsymbol{L_p}$ is:

$$\boldsymbol{L_p} = \begin{bmatrix} {}^{\mathrm{d}u_{\mathrm{FD}}}/_{\mathrm{d}z}\big|_1 \\ {}^{\mathrm{d}u_{\mathrm{FD}}}/_{\mathrm{d}z}\big|_2 \\ \vdots \\ {}^{\mathrm{d}u_{\mathrm{FD}}}/_{\mathrm{d}z}\big|_{n-1} \\ {}^{\mathrm{d}u_{\mathrm{FD}}}/_{\mathrm{d}z}\big|_n \end{bmatrix}. \tag{2.28}$$

The experimental values of the velocity derivative, ${}^{\mathrm{d}u_{\mathrm{FD}}}/_{\mathrm{d}z}\big|_i$, are approximations of ${}^{\mathrm{d}u_{\mathrm{p}}}/_{\mathrm{d}z}$ as shown in equation 2.29, which includes a second-order accurate, central finite difference to approximate the derivative of $\ln(u_{\mathrm{p}})$.

$$\begin{aligned} \frac{\mathrm{d}u_{\mathrm{p}}}{\mathrm{d}z} = \frac{\mathrm{d}u_{\mathrm{p}}}{\mathrm{d}t}\cdot\frac{1}{u_{\mathrm{p}}} = \frac{\mathrm{d}\ln(u_{\mathrm{p}})}{\mathrm{d}t} &= \ln\left[\frac{u_{\mathrm{p}}(t+1/f)}{u_{\mathrm{p}}(t-1/f)}\right]\cdot\frac{f}{2} + E_{\mathrm{d}u_{\mathrm{p}}/\mathrm{d}z} \\ &\approx \underbrace{\ln\left[\frac{u_{\mathrm{FD}}(t+1/f)}{u_{\mathrm{FD}}(t-1/f)}\right]\cdot\frac{f}{2}}_{\frac{\mathrm{d}u_{\mathrm{FD}}}{\mathrm{d}z}} + E_{\mathrm{d}u_{\mathrm{p}}/\mathrm{d}z} \end{aligned} \tag{2.29}$$

The error induced by the finite difference approximation of the derivative is calculated as [145]:

$$E_{\mathrm{d}u_\mathrm{p}/\mathrm{d}z} = \frac{1}{6f^2} \cdot \frac{\mathrm{d}^3 \ln u_\mathrm{p}\left(\epsilon\right)}{\mathrm{d}t^3}. \tag{2.30}$$

As for equation 2.14, the third-order derivative is evaluated at an unknown instant, ϵ, comprised in the time interval $t_i - {}^1\!/_f \leq \epsilon \leq t_i + {}^1\!/_f$, where t_i corresponds to the time at which the particle is recorded at the location z_i. As performed above, the third-order time derivative is transformed (see equation 2.31) to yield a finite-difference error solely dependent on the axial velocity and its derivatives with respect to the axial location, as shown in equation 2.32. It must be noted that since the flow is parabolic upstream of the flame, the third-order spatial derivative in the last term of equation 2.31 equals zero and, therefore, does not appear in equation 2.32.

$$\begin{aligned}
\frac{\mathrm{d}^3 \ln u_\mathrm{p}}{\mathrm{d}t^3} &= \frac{\mathrm{d}^2}{\mathrm{d}t^2}\left(\frac{1}{u_\mathrm{p}}\frac{\mathrm{d}u_\mathrm{p}}{\mathrm{d}t}\right) \\
&= \frac{\mathrm{d}^2}{\mathrm{d}t^2}\left(\frac{\mathrm{d}u_\mathrm{p}}{\mathrm{d}z}\right) \\
&= \frac{\mathrm{d}}{\mathrm{d}t}\left(u_\mathrm{p}\frac{\mathrm{d}^2 u_\mathrm{p}}{\mathrm{d}z^2}\right) \\
&= u_\mathrm{p}\frac{\mathrm{d}u_\mathrm{p}}{\mathrm{d}z}\frac{\mathrm{d}^2 u_\mathrm{p}}{\mathrm{d}z^2} + u_\mathrm{p}^2\frac{\mathrm{d}^3 u_\mathrm{p}}{\mathrm{d}z^3}
\end{aligned} \tag{2.31}$$

$$E_{\mathrm{d}u_\mathrm{p}/\mathrm{d}z} = \frac{1}{6f^2} \cdot \left(u_\mathrm{p}\frac{\mathrm{d}u_\mathrm{p}}{\mathrm{d}z}\frac{\mathrm{d}^2 u_\mathrm{p}}{\mathrm{d}z^2}\right)\Bigg|_{t=\epsilon} \tag{2.32}$$

The maximum value of $E_{\mathrm{d}u_\mathrm{p}/\mathrm{d}z}$, evaluated over 100 grid points uniformly distributed on the interval $z_\mathrm{inlet} \pm {}^{u_\mathrm{inlet}}\!/_f$, is selected as a conservative error estimation. In general, the values of the first and second-order derivatives in equation 2.32 are small, and so is $E_{\mathrm{d}u_\mathrm{p}/\mathrm{d}z}$.

Other than $E_{\mathrm{d}u_\mathrm{p}/\mathrm{d}z}$, the systematic uncertainty in the individual particle velocities can induce an error in ${}^{\mathrm{d}u_\mathrm{p}}\!/_{\mathrm{d}z}$. As discussed above, among the three sources of systematic uncertainty on u_p, the error on the calibration coefficient (${}^{\Delta C}\!/_C$) is the most important; the error incurred by approximating the derivative ${}^{\mathrm{d}z}\!/_{\mathrm{d}t}$ with the second-order finite difference scheme, $E_{u_{\mathrm{p},i}}$, is generally more than two orders of magnitude smaller than ${}^{\Delta C}\!/_C$ in the vicinity of z_inlet and is, therefore, negligible. However, both velocities in the natural logarithm of equation 2.29 are scaled by the calibration factor (C) and the laser repetition rate (f), which then simplify in the ratio ${}^{u_\mathrm{FD}(t+1/f)}\!/_{u_\mathrm{FD}(t-1/f)}$. It follows that the systematic uncertainty on the particle velocities does not significantly contribute to the systematic error on the individual values of ${}^{\mathrm{d}u_\mathrm{p}}\!/_{\mathrm{d}z}$, which is then mostly caused by $E_{\mathrm{d}u_\mathrm{p}/\mathrm{d}z}$ (see equation 2.32).

The main contributor to the uncertainty in ${}^{\mathrm{d}u}\!/_{\mathrm{d}z}\big|_\mathrm{inlet}$ is the error caused by the scatter in the

values of ${}^{\mathrm{d}u_{\mathrm{FD}}}/_{\mathrm{d}z}$, which limits the precision of the linear, least-squares regression of equation 2.25. This error is calculated as [148]:

$$\Delta\, {}^{\mathrm{d}u}/_{\mathrm{d}z}\big|_{\mathrm{inlet,rand}} = t_{0.025,n-2}\sqrt{\frac{\boldsymbol{L_p}'\boldsymbol{L_p} - \boldsymbol{\eta}'\boldsymbol{z}'\boldsymbol{L_p}}{n-2}\boldsymbol{z_0}'\left(\boldsymbol{z}'\boldsymbol{z}\right)^{-1}\boldsymbol{z_0}}, \tag{2.33}$$

where n is the number of data points included in the adjustment, and $\boldsymbol{z_0}$ is:

$$\boldsymbol{z_0} = \begin{bmatrix} 1 \\ z_{\mathrm{inlet}} \end{bmatrix}. \tag{2.34}$$

The overall error in the velocity gradient at z_{inlet} is finally calculated as:

$$\Delta\, {}^{\mathrm{d}u}/_{\mathrm{d}z}\big|_{\mathrm{inlet}} = \sqrt{\Delta\, {}^{\mathrm{d}u}/_{\mathrm{d}z}\big|^2_{\mathrm{inlet,rand}} + E^2_{{}^{\mathrm{d}u_{\mathrm{p}}}/_{\mathrm{d}z}}}. \tag{2.35}$$

This method yields a smaller uncertainty than calculating the inlet velocity gradient based on the quadratic polynomial adjusted to the velocity data points (equations 2.8 and 2.22). Linear polynomials with slopes set to the uncertainty limits of ${}^{\mathrm{d}u}/_{\mathrm{d}z}\big|_{\mathrm{inlet}}$ are more consistent with the experimentally determined particle velocities in the vicinity of z_{inlet}. The velocity boundary conditions (u_{inlet} and ${}^{\mathrm{d}u}/_{\mathrm{d}z}\big|_{\mathrm{inlet}}$), and related uncertainties, are reported in Table F.1.

2.3 Two-dimensional, planar CH laser-induced fluorescence

The integration of the CH-LIF diagnostic around the jet-wall burner is shown in Figure 2.6. The third harmonic (355 nm) of a Nd:YAG Laser (Spectra-Physics Quanta-Ray Pro-230) firing at 10 Hz pumps a wavelength-tunable dye laser (Sirah Cobra-Stretch SL) filled with Stilbene 420 dye. A fairly homogeneous portion of the emerging beam is passed through a pinhole iris followed by Powell and plano-cylindrical lenses to form an unfocused, quasi-homogeneous, laser sheet of ~20 mm by ~6 mm centred on the axis of the burner. The average energy of the laser sheet is ~0.137 mJ spread over a pulse duration of 8.5 ns. Linearity of the LIF response is ensured by comparison of experimentally realized excitation spectra to theoretically determined ones in LIFBASE [150] (see Figure 2.7), and by noting that the spectral irradiance ($I_\nu \approx 3.9 \cdot 10^4\ \mathrm{W/(cm^2 cm^{-1})}$) is approximately one order of magnitude lower than the value of I_ν at which saturation effects appear [106].

Similarly to other studies [100, 106], the dye laser wavelength is adjusted to ~426.93 nm to

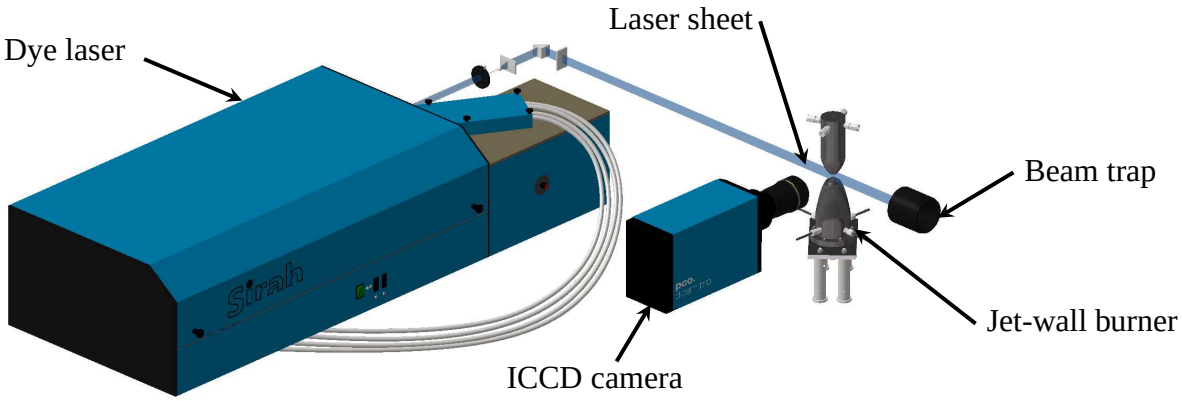

FIGURE 2.6: Integration of the CH-PLIF diagnostic technique around the jet-wall burner. Note: the Nd:YAG laser, which pumps the dye laser, is not shown on this figure.

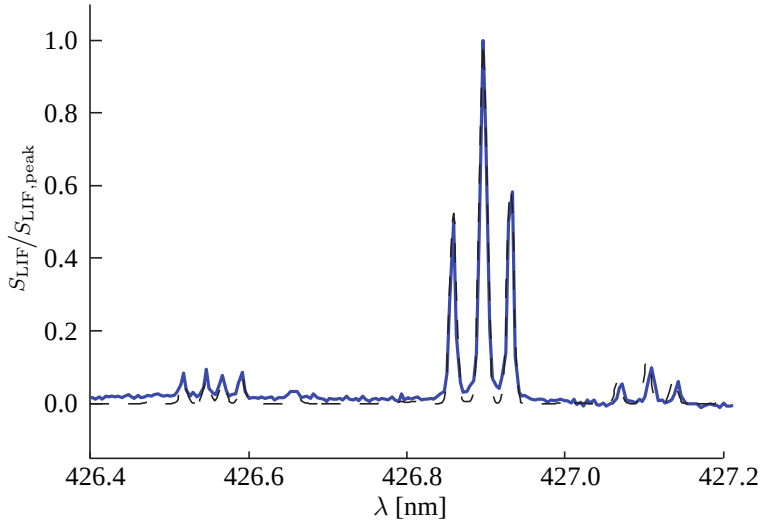

FIGURE 2.7: CH excitation spectra obtained with a laser spectral resolution of 0.00412 nm in a rich, $\phi = 1.3$, methane-air flame. The blue curve corresponds to the measured spectrum, and the black dashed curve to a numerical, linear CH-LIF excitation spectrum simulated with LIFBASE [150].

excite the R(7) ($N'' = 7$,$N' = 8$) transition of the $A^2\Delta$-$X^2\Pi$ ($v'' = 0,\ v' = 0$) electronic system. Λ-doubling and spin-splitting, related to the two possible orientations of the projection of the orbital and spin angular momenta on the internuclear axis, make the ground and electronically excited states degenerate leading to multiple allowed transitions between the two electronic energy levels [106]. Figure 2.8 shows the absorption spectrum of the R(7) $A^2\Delta$-$X^2\Pi$ ($v'' = 0, v' = 0$) system as obtained from LIFBASE for a thermalized population distribution at 1800 K (e and f refer to Λ-doubling, and 1 and 2 to spin-splitting). The spectrum includes the effects of Doppler and collisional line-broadening through convolutions of Gaussian and Lorentzian distributions, respectively, with the non-broadened absorption spectrum. Doppler broadening is readily described as it depends only on the gas temperature and molecular mass of the probed species [117, 150]. In contrast, the width of the Lorentzian distribution, calculated using equation 2.36 where P_i [atm] is the partial pressure of the broadening species i, and $2\gamma_{\mathrm{CH}-i}$ $[\mathrm{cm}^{-1}/\mathrm{atm}]$ is the collisional broadening parameter [151], depends on the local gas composition, temperature and pressure. Functions describing $2\gamma_{\mathrm{CH}-i}(T)$ for various broadening species are sparse. Vasudevan et al. [152] measured $2\gamma_{\mathrm{CH}-\mathrm{N}_2}(2312\mathrm{K}) = 0.044\ \mathrm{cm}^{-1}/\mathrm{atm}$ in an ethane-nitrogen mixture heated by a shock wave. Noting that the mixtures consist mostly of nitrogen in the current set of experiments, and applying the temperature dependence of $2\gamma_{\mathrm{OH}-\mathrm{N}_2}(T)$ [151] as performed in [152], the width of the Lorentzian distribution is approximated as $\Delta\nu_c \approx 2\gamma_{\mathrm{CH}-\mathrm{N}_2}(T) \cdot P \approx 0.044 \cdot (\frac{2312}{T})^{0.72} \cdot P$. At 1800 K and 1 atm, this yields $\Delta\nu_c = 0.053\ \mathrm{cm}^{-1}$, which is in fair agreement with reported values ranging from 0.03 cm^{-1} to 0.1 cm^{-1} at atmospheric-pressure conditions [98, 117].

$$\Delta\nu_c = \sum_i 2\gamma_{\mathrm{CH}-i}(T) \cdot P_i \tag{2.36}$$

Also shown in Figure 2.8 is the laser line profile approximated by a Voigt distribution. It was obtained via a least-squares adjustment of a virtual excitation spectrum, made through a convolution of an adjustable Voigt line-shape profile with a theoretical excitation spectrum extracted from LIFBASE including the Doppler and collisional line-broadening mechanisms, to an experimentally measured excitation spectrum. Given the thin line width (0.34 cm^{-1}) of the dye laser, the current LIF excitation scheme targets only one spectral feature that includes the $R_{1e}(7)$ and $R_{2f1e}(7)$ transitions. It must be noted that the Einstein coefficient for stimulated absorption, B_{12}, is approximately 50 times larger for the $R_{1e}(7)$ transition.

An off-resonance signal (Figure 2.9(b)), measured at a theoretical absorption minimum at 427 nm, is subtracted from the on-resonance signal (Figure 2.9(a)) to remove the effects of Rayleigh scattering, ambient luminosity, camera dark noise, and flame chemiluminescence (see net LIF

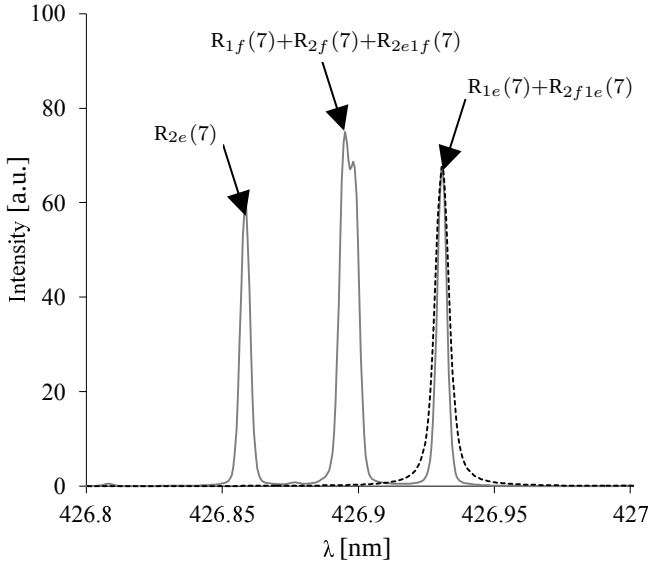

FIGURE 2.8: Absorption spectrum of CH at 1800 K assuming a thermalized Boltzmann population distribution and accounting for Doppler and collisional line-broadening (solid grey curve), superimposed with the laser line profile (black dashed curve).

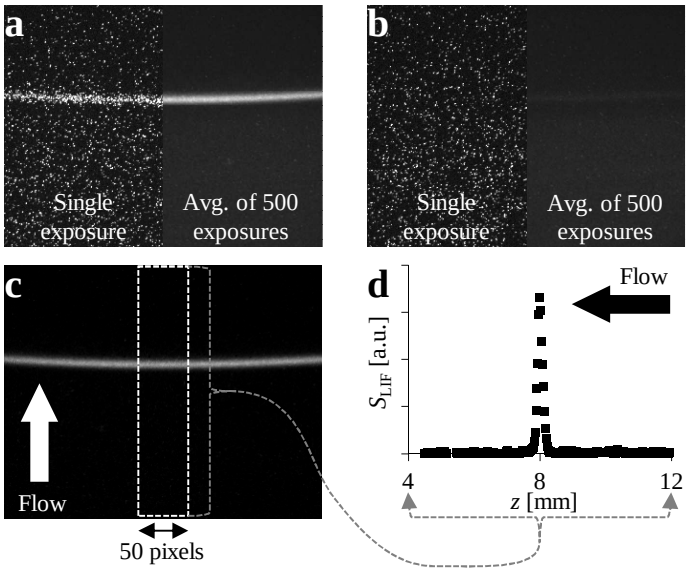

FIGURE 2.9: (a) On-resonance PLIF, (b) off-resonance PLIF, (c) net (on − off-resonance) PLIF, and (d) resulting 1D CH-LIF profile. In images (a) and (b), the left and right sides show a single image and the average of 500 exposures, respectively.

signal in Figure 2.9 (c)). Both signals pass through a 10 nm bandpass filter centred at 430 nm (Andover Optics 430FS10-50), and are collected using a 90 mm Tamron $f/2.8$ macro lens mounted on extension tubes for improved spatial resolution. The signals are recorded using an intensified CCD

camera (Dicam Pro, GaAsP photocathode) binned 4 by 4 for increased signal-to-noise ratio (S/N), which results in a projected pixel resolution of 0.029 mm/pixel. Five hundred images are exposed for 30 ns, a gate time longer than the fluorescence duration but short enough to minimize noise, again in an attempt to boost S/N. One-dimensional profiles of LIF signal intensity are obtained by averaging, at each axial location, the intensity of 50 pixels in the radial direction (see Figure 2.9 (c & d)).

As shown in equation 2.37, the experimental LIF signal recorded by the camera, S_{LIF}, is determined by many variables: the number density of CH molecules, $N_{0,\mathrm{CH}}$ [m^{-3}], the fraction of CH molecules in the ground rotational state excited by the laser, $f_{\mathrm{B},N_{1a}}$, the laser irradiance, I [W/m^2], the spectral laser line width, $\Delta\nu_{\mathrm{L}}$ [cm^{-1}], the laser pulse duration, τ_{Laser} [s], the dimensionless overlap fraction, Γ, the Einstein absorption and stimulated emission coefficients, B_{12} and B_{21} [m^2/J-s], respectively, the Einstein rate constant of spontaneous emission, A_{21} [s^{-1}], the rate constant of collisional quenching, Q_{21} [s^{-1}], and the average transmissivity of the bandpass filter over the CH emission spectrum, $\tau_{\lambda,\mathrm{LIF}}$ [60, 64, 117]. These values can be directly measured, calculated, or obtained from databases. Their dependence on the local temperature (T), pressure (P), and mixture composition (X_j) is also shown in equation 2.37. The function f_{LIF}, which corresponds to the number of photons emitted in all directions per unit volume and solid angle, is *a priori* unknown. As discussed in Chapter 3, it must be simulated using a LIF model in order to relate the number density of CH molecules to the measured LIF signal. S_{LIF} also depends on the solid angle, Ω [sr], which determines the fraction of all emitted photons that are captured by the collection optics, the probe volume, V [m^3], and the optical collection constant, C_{opt} [count/photon], that relates the fluorescence intensity reported in counts on the images to the number of photons collected. Ω, V, and C_{opt} cannot be readily measured nor calculated and, therefore, must be calibrated.

$$\begin{aligned} S_{\mathrm{LIF}} =& f_{\mathrm{LIF}}[N_{0,\mathrm{CH}}, f_{\mathrm{B},N_{1a}}(T), I, \Delta\nu_{\mathrm{L}}, \tau_{\mathrm{Laser}}, \Gamma(T,P,X_j), \\ & B_{12}, B_{21}, A_{21}, Q_{21}(T,P,X_j)] \cdot \tau_{\lambda,\mathrm{LIF}} \cdot \underbrace{\Omega \cdot V \cdot C_{\mathrm{opt}}}_{\substack{\text{Optical parameters} \\ \text{to calibrate}}} \end{aligned} \tag{2.37}$$

To yield quantitative data, the net LIF signal is calibrated by the Rayleigh scattering signal of nitrogen, S_{R}, measured at the on-resonance laser wavelength using the exact same optical collection configuration. A signal, $S_{\mathrm{N_2}}$, is first recorded with cold nitrogen gas flowing in the apparatus. Taking advantage that the Rayleigh scattering cross-section of helium is only ~1.3% that of nitrogen at room temperature and pressure, a Rayleigh scattering signal measured with He is deducted from $S_{\mathrm{N_2}}$ to remove the effects of ambient luminosity and camera dark noise (*i.e.*, $S_{\mathrm{R}} = S_{\mathrm{N_2}} - S_{\mathrm{He}}$).

To minimize the impact of Mie scattering, the calibration gases are passed through an ultra-high-purity particulate filter (Swagelok SS-SCF3-VR4-P-30). As shown in equation 2.38, the experimental Rayleigh scattering signal is influenced by the Rayleigh scattering cross-sections of nitrogen and helium, $\left(\frac{\partial\sigma}{\partial\Omega}\right)_{\mathrm{N_2}}$ [m^2/sr] and $\left(\frac{\partial\sigma}{\partial\Omega}\right)_{\mathrm{He}}$ [m^2/sr], respectively, the number density, N [m^{-3}], the laser irradiance, the laser pulse duration, the laser wavelength, λ [m], and the transmissivity of the bandpass filter at the wavelength of the Rayleigh scattering signal (on-resonance wavelength), $\tau_{\lambda,\mathrm{R}}$. As for the LIF signal, S_{R} depends on the solid angle, the probe volume, and the optical collection constant.

$$\begin{aligned} S_{\mathrm{R}} =& f_{\mathrm{R}}\left[\left(\frac{\partial\sigma}{\partial\Omega}\right)_{\mathrm{N_2}}(P,T,\lambda), \left(\frac{\partial\sigma}{\partial\Omega}\right)_{\mathrm{He}}(P,T,\lambda), N(P,T), I, \tau_{\mathrm{Laser}}, \lambda\right] \\ & \cdot \tau_{\lambda,\mathrm{R}} \cdot \underbrace{\Omega \cdot V \cdot C_{\mathrm{opt}}}_{\substack{\text{Optical parameters} \\ \text{to calibrate}}} \end{aligned} \tag{2.38}$$

Traditionally (*e.g.*, [100]), the optical parameters are obtained by applying a model for the function f_{R}, and inserting an experimentally measured Rayleigh scattering signal (S_{R}) in equation 2.38. The product $\Omega \cdot V \cdot C_{\mathrm{opt}}$ is then transferred to equation 2.37 to extract a CH number density by inserting an experimentally determined value of S_{LIF}, and applying a model for f_{LIF}. However, this methodology has drawbacks. Namely, the accuracies of the optical calibration and of the conversion of LIF signal intensities into number densities are limited by the accuracy of the models used (f_{LIF} and f_{R}), and of the temperature and species concentration data they require. In addition, if these models (f_{LIF} and f_{R}) are proven inadequate or improved, it makes the experimental data obsolete even if the methodology is formally correct. To avoid these issues, the approach proposed by Connelly et al. [153] is employed in which relatively raw experimental signals are directly compared to modelled LIF and Rayleigh scattering signal intensities. Experimental and computational parameters are then segregated, removing uncertainties related to the LIF and Rayleigh models from the experimental data. In this work, the LIF signal is normalized by the Rayleigh scattering signal, such that the solid angle, probe volume, and optical coefficient cancel out as shown in equation 2.39. Therefore, the ratio $S_{\mathrm{LIF}}/S_{\mathrm{R}}$ is a quantitative, surrogate measure of the CH number density. Numerical values of LIF-to-Rayleigh ratio, $\left(S_{\mathrm{LIF}}/S_{\mathrm{R}}\right)_{\mathrm{num}}$, are obtained by inserting the solution of flame simulations into a proper LIF model (f_{LIF}), and calculating the Rayleigh scattering signal using a model for f_{R}. The generation of $\left(S_{\mathrm{LIF}}/S_{\mathrm{R}}\right)_{\mathrm{num}}$, based on flame simulations, is

the topic of Chapter 3.

$$\underbrace{\frac{S_{\mathrm{LIF}}}{S_{\mathrm{R}}}}_{\substack{\text{Experimental data}\\ (S_{\mathrm{LIF}}/S_{\mathrm{R}})_{\mathrm{exp}}}} = \frac{f_{\mathrm{LIF}}}{f_{\mathrm{R}}}\frac{\tau_{\lambda,\mathrm{LIF}}}{\tau_{\lambda,\mathrm{R}}}\underbrace{\frac{\Omega\cdot V\cdot C_{\mathrm{opt}}}{\Omega\cdot V\cdot C_{\mathrm{opt}}}}_{=1} = \underbrace{\frac{f_{\mathrm{LIF}}}{f_{\mathrm{R}}}\frac{\tau_{\lambda,\mathrm{LIF}}}{\tau_{\lambda,\mathrm{R}}}}_{\substack{\text{Numerical data}\\ (S_{\mathrm{LIF}}/S_{\mathrm{R}})_{\mathrm{num}}}} \tag{2.39}$$

Chapter 3

Laser-induced fluorescence modelling

Being non-intrusive, laser-induced fluorescence is a widely used diagnostic technique to obtain spatially resolved fields of species concentration in flames [117–119]. A model replicating the LIF process (f_{LIF} in equation 2.37) is required to convert the output of flame simulations into units compatible with the experimentally determined profiles of fluorescence intensity. Models with various degrees of sophistication are reported in the literature. For data reduction of CH-LIF in the A-X electronic system, it is common practice to apply models with two electronic energy levels, either in the linear [100, 101] or saturated [106, 108] regimes, motivated by their relative simplicity. Such two-level models accurately characterize the LIF process of atoms as they are devoid of rotational and vibrational energy modes [117]. There are claims that for such models to adequately describe the LIF process of molecules, collisional energy transfer within the ground and electronically excited states must be either frozen, or extremely fast [117]. However, at atmospheric pressure and beyond, most molecules feature non-negligible rates of collisional energy transfer within given electronic states [98, 117, 118, 154–156], and it is believed that these processes must be modelled [117]. As an example, Luque et al. [98] developed a steady-state, four-level LIF model to describe the laser-induced fluorescence of methylidyne excited to the highly predissociative $\mathrm{B}^2\Sigma^-(v' = 1, N' = 8)$ energy level, and found that it is necessary to include the effects of rotational energy transfer (RET) in the ground and electronically excited states. In contrast, Naik and Laurendeau [157] assembled a five-level LIF model including rotational and vibrational energy transfers to describe NO-LIF in the $\mathrm{A}^2\Sigma$-$\mathrm{X}^2\Pi$ system, and observed that the effects of RET are negligible under weak laser irradiation. Such a detailed model does not exist for CH-LIF in the $\mathrm{A}^2\Delta$-$\mathrm{X}^2\Pi$ ($v'' = 0, v' = 0$) system, and it is unclear if the effects of collisional energy transfer within the ground and electronically excited states can be neglected.

Furthermore, with the intent to develop a simple, algebraic expression relating the number density of the probed species to the LIF signal intensity, the achievement of steady-state populations in the various energy levels is often hypothesized [98, 100, 101, 107, 158]. While this assumption can be accurate for long laser pulses or for systems rapidly achieving steady-state, *e.g.*, saturated

LIF, it cannot be considered *a priori* correct for short duration laser pulses, weak laser irradiation, and LIF systems with slow transitional rates [117]. Thus far, CH $A^2\Delta$-$X^2\Pi$ LIF measurements in the linear regime were processed with steady-state models, without properly verifying the validity of this assumption [100, 101].

In this chapter, a detailed, time-resolved, four-level LIF model is presented. Along with simpler, two-level LIF models assuming 1) negligible rates of RET, 2) infinitely fast rotational energy transfer, and 3) weak laser irradiation, it is used to analyze the commonly made assumptions in CH-LIF data processing. Namely, the temporal evolution of the populations in the ground and electronically excited states, the effect of RET on the LIF signal predictions, the impact of the temporal profile of laser irradiance, and the interactions of the flame chemistry with the LIF system are investigated. The methodology to translate the output of flame simulations into LIF signal intensities compatible with the experimental data is then presented, as well as an uncertainty analysis of the time-resolved, four-level LIF model performed to quantify the error in the modelled LIF signals. All LIF simulations in this chapter are performed at the location of maximum CH concentration in an unstrained, adiabatic flame freely propagating in a stoichiometric mixture of methane and air initially at 300 K and 1 atm simulated with the SD mechanism.

3.1 Laser-induced fluorescence models

3.1.1 Four-level LIF model

The four-level LIF model is shown in Figure 3.1. It includes two electronic energy levels, each containing a rotational energy level directly coupled to laser irradiation (state a) and a manifold within which all the other energy levels lie (state b). Transitions relating to photon absorption (b_{12}), stimulated emission (b_{21}), spontaneous emission (A_{2i1j}), non-radiative collisional quenching (Q_{2i1j}), and rotational energy transfer (R_{kakb} and R_{kbka}) are included in the model. Vibrational energy transfer ($v' = 0 \rightarrow v' = 1, 2,$ etc.) is neglected consistent with the lack of fluorescence observed from vibrational levels other than the laser-populated one in the LIF experiments of Garland and Crosley [154] performed in atmospheric-pressure flames. Also, the rate of electronic energy transfer from the $A^2\Delta$ to the $B^2\Sigma^-$ electronic energy levels is more than two orders of magnitude slower than the rate of RET for CH molecules initially in the $A^2\Delta$ ($v' = 0,\ N' = 2,\ 6,\ 10,$ and 15) levels [154]. Therefore, electronic energy transfer is not considered here. Furthermore, predissociation is neglected as, unlike the $B^2\Sigma^-$ and $C^2\Sigma^+$ electronic energy levels, the $A^2\Delta$ level does

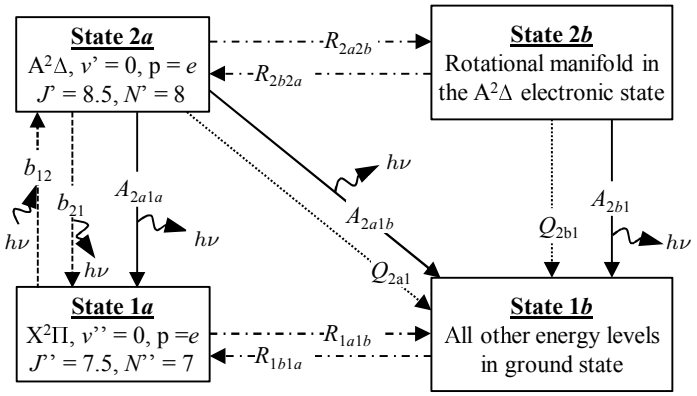

FIGURE 3.1: Four-level LIF model.

not present a declining potential energy for increasing, large internuclear distances (r, see Figure 3.2), which would repel and dissociate the carbon and hydrogen atoms[1]. Photo-ionization ($\mathrm{CH} + h\nu \rightarrow \mathrm{CH}^+ + \mathrm{e}^-$) is also omitted as the ionization energy of methylidyne (10.64 eV = 85 817.34 cm^{-1} [160]) is 3.7 times higher than the energy required to excite the molecules from the ground state to the $\mathrm{A}^2\Delta$ electronic level (T_e = 2.88 eV = 23 189.8 cm^{-1} [160]).

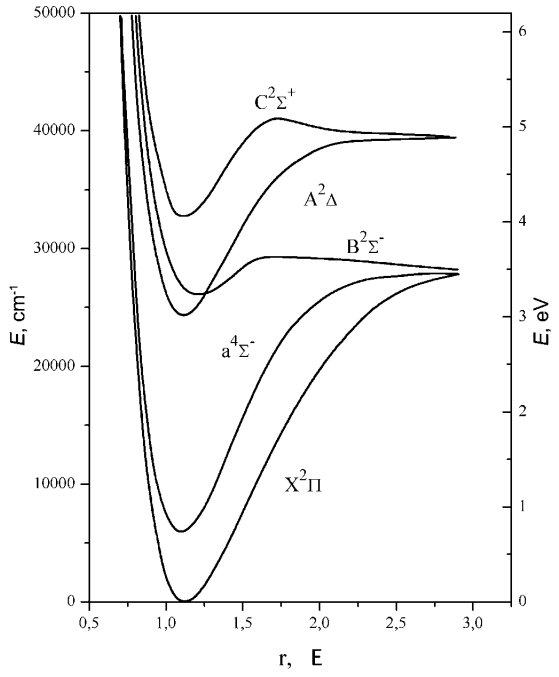

FIGURE 3.2: Potential energy curves for the first five electronic energy levels of CH. Reproduced with permission [161].

[1]The force, F, in a conservative system relates to the potential energy, E, through $F = -{}^{dE}/_{dr}$ [159]. Hence, if the potential energy decreases with r, then ${}^{dE}/_{dr} < 0$, the force F is positive and works to dissociate the molecule.

Under weak laser irradiation, collisional quenching is the principal transitional process depleting the electronically excited levels ($2a$ and $2b$). However, the distribution of the quenched molecules into the various ground state energy levels is uncertain, and different assumptions are made in the literature [98, 118, 162]. For OH, Daily [118] assumes that the molecules are quenched to the same rotational level by analogy to the conservation of the vibrational state suggested by Paul [163], a hypothesis contradicted in [164–166]. In contrast, Laurendeau and co-workers, in their models for saturated OH-LIF [162] and linear NO-LIF [157], assume that the molecules quenched from a given rotational energy level in the electronically excited state are evenly distributed among the 20 distinct rotational levels considered in the ground state. Given the lack of a consistent description for the distribution of the quenched molecules among the ground state rotational energy levels, the current LIF model assumes that all molecules are transferred to the manifold (state $1b$) as in the pre-dissociative CH-LIF model of Luque et al. [98]. Similarly, all molecules undergoing spontaneous emission from the rotational manifold in the $\mathrm{A}^2\Delta$ electronic level (state $2b$) are sent to the $1b$ state. Otherwise, it would be necessary to resolve the rotational levels in the excited state manifold in order to discriminate the fractions of molecules transferred to the $1a$ and $1b$ states. This would make the model more complex, but would not significantly change the populations in the $1a$ and $1b$ levels as spontaneous emission occurs at a much slower rate than collisional quenching and RET (and stimulated emission for LIF in the saturated regime), which proceed in parallel and, therefore, determine the populations.

Invoking species conservation, a set of ordinary differential equations (ODE), which describe the rate of change of the population in each of the energy levels, is developed:

$$\frac{\mathrm{d}N_{1a}}{\mathrm{d}t} = \dot{N}_{1a} = -N_{1a} \cdot b_{12} + N_{2a}\left(b_{21} + A_{2a1a}\right) - N_{1a} \cdot R_{1a1b} + N_{1b} \cdot R_{1b1a}, \tag{3.1}$$

$$\frac{\mathrm{d}N_{1b}}{\mathrm{d}t} = \dot{N}_{1b} = N_{2a} \cdot \left(A_{2a1b} + Q_{2a1}\right) + N_{2b} \cdot \left(A_{2b1} + Q_{2b1}\right) + N_{1a} \cdot R_{1a1b} - N_{1b} \cdot R_{1b1a}, \tag{3.2}$$

$$\frac{\mathrm{d}N_{2a}}{\mathrm{d}t} = \dot{N}_{2a} = N_{1a} \cdot b_{12} - N_{2a} \cdot \left(b_{21} + A_{2a1a} + A_{2a1b} + Q_{2a1} + R_{2a2b}\right) + N_{2b} \cdot R_{2b2a}, \tag{3.3}$$

$$\frac{\mathrm{d}N_{2b}}{\mathrm{d}t} = \dot{N}_{2b} = -N_{2b} \cdot \left(A_{2b1} + Q_{2b1} + R_{2b2a}\right) + N_{2a} \cdot R_{2a2b}, \tag{3.4}$$

where N_{ki} [m^{-3}] is the number density in the electronic level k and energy state i, b_{12} [s^{-1}] is the rate constant of photon absorption by the ground state molecules, b_{21} [s^{-1}] is the rate constant of stimulated emission, A_{2i1j} [s^{-1}] is the rate constant of spontaneous emission from the $2i$ to the $1j$ states, R_{kakb} and R_{kbka} are the forward and backward rate constants of rotational energy

transfer in the electronic level k, respectively, and Q_{2i1} is the rate constant of collisional quenching from state $2i$. As shown in Figure 3.1, the LIF model is isolated; no molecules are gained or lost to the environment. Hence, it would be possible to solve only three ODEs and obtain the population in the remaining state by invoking conservation of the total number of CH molecules ($N_{0,\mathrm{CH}} = \sum N_{ki}$). However, the complete set of ODEs is implemented to conserve the ability to solve processes incurring net gain/loss of molecules, such as chemical reactions.

In equations 3.1 and 3.3, the rate constant of absorption, b_{12}, is defined as [117]:

$$b_{12} = \frac{B_{12}}{c} \cdot \frac{I}{\Delta\nu_{\mathrm{L}}} \cdot \Gamma, \tag{3.5}$$

where B_{12} [m^2/J-s] is the Einstein absorption coefficient for the $R_{1e}(7)$ transition obtained from LIFBASE [150], c [cm/s] is the speed of light, I [W/m^2] is the irradiance, $\Delta\nu_{\mathrm{L}}$ [cm^{-1}] is the spectral laser line width, and Γ is the dimensionless overlap fraction. Γ is defined in equation 3.6, where $L(\nu)$ is the laser spectral distribution normalized such that its integral over the frequency ν is equal to $c \cdot \Delta\nu_{\mathrm{L}}$, and $g(\nu)$ is the spectral shape of the absorption line normalized to unity [167].

$$\Gamma = \int_{\nu} L(\nu) g(\nu) d\nu \tag{3.6}$$

The irradiance is defined as:

$$I = \frac{E_{\mathrm{B}} \cdot \tau_{\mathrm{B}}}{A_{\mathrm{B}} \cdot \tau_{\mathrm{Laser}}}, \tag{3.7}$$

where E_{B} [J] is the average laser energy per pulse, τ_{B} is the transmissivity of the beam shaping optics downstream of the laser energy measurement point, A_{B} [m^2] is the laser sheet cross-sectional area, and τ_{Laser} [s] is the laser pulse duration. The rate constant of stimulated emission, b_{21}, is calculated by multiplying b_{12} by the ratio of the degeneracies in the ground and electronically excited levels [117, 118, 159] which, owing to identical effective electronic degeneracies in the two electronic states ($\omega_{\mathrm{el,eff}}$, see Table 3.2), simplifies to [150]:

$$b_{21} = b_{12} \cdot \frac{2 \cdot J'' + 1}{2 \cdot J' + 1}. \tag{3.8}$$

As shown in Figure 3.1, three spontaneous emission transitions are considered in the current LIF model. A_{2a1a} relates to photon emission through the $R_{1e}(7)$ transition, which occurs at a rate constant of $6.087 \cdot 10^5$ s^{-1} [150]. A_{2a1b} accounts for all spontaneous emission transitions originating from the $2a$ state other than through the $R_{1e}(7)$ line. Included in A_{2a1b} are the $Q_1(8)$, $Q_{12}(8)$, $P_1(9)$, $P_{12}(9)$, and $O_{12}(10)$ transitions [150]. Through summation of the individual rate constants, a value

of $1.209 \cdot 10^6$ s^{-1} is obtained for A_{2a1b}. A_{2b1} is calculated using equation 3.9, where the first right-hand side term combines all spontaneous emission transitions originating from the $2i$ states, and the second term removes the contributions of A_{2a1a} and A_{2a1b}.

$$\begin{aligned} A_{2b1} = & \frac{\sum_{N'=1}^{27} \sum_{S'=-1/2}^{1/2} \sum_{\mathrm{p}=e,f} A(J'=N'+S', N', \mathrm{p}) \cdot f_{\mathrm{B}}(J'=N'+S', N', \mathrm{p})}{1 - f_{\mathrm{B}}(J'=8.5, N'=8, e)} \\ & - \frac{(A_{2a1a} + A_{2a1b}) \cdot f_{\mathrm{B}}(J'=8.5, N'=8, e)}{1 - f_{\mathrm{B}}(J'=8.5, N'=8, e)} \end{aligned} \tag{3.9}$$

In equation 3.9, p is the parity (e or f), S' is the electron spin quantum number, and $A(J' = N' + S', N', \mathrm{p})$ [s^{-1}] is the rate constant of spontaneous photon emission from the $\mathrm{A}^2\Delta$, J', N', p state, which consists of an amalgam of A-X transitions in the O, P, Q, R and S branches. The Boltzmann fraction, f_{B}, is calculated for each (J', N', p) set assuming a rotationally thermalized system in the $\mathrm{A}^2\Delta$ ($v' = 0$) state at $T = 1800$ K. This yields $A_{2b1} = 1.770 \cdot 10^6$ s^{-1}.

With regards to collisional processes, Bülter et al. [168] estimated a variation in the rate constant of collisional quenching of ~15% over the rotational levels $N' = 12$ to $N' = 2$ based on CH A-X radiative lifetime measurements performed in atmospheric, rich, premixed methane-oxygen and acetylene-oxygen flames. In the current study, as most of the electronically excited species are expected to lie within the $N' = 8$ rotational level, or its neighbouring levels owing to the limited rate of RET, variations in the quenching rate constant with the rotational quantum number are disregarded. As such, Q_{2b1} and Q_{2a1} are assumed equal ($Q_{2b1} = Q_{2a1} = Q_{21}$). Knowing the major species and temperature profiles from the flame simulations, the quenching rate constant, Q_{21}, is calculated based on the parameters specified in [169] along with the improved cross-sections of quenching for H_2, H_2O and N_2 specified in [170].

The rate constant of RET is commonly defined relative to the rate constant of quenching [98, 154–156]. Analyses of collisional energy transfer in studies on CH $\mathrm{A}^2\Delta$-$\mathrm{X}^2\Pi$ LIF in low and atmospheric-pressure, methane-air and oxygen-acetylene flames demonstrated that the rate constant of RET is ~2.4 to ~4.1 times faster than the rate constant of quenching [154–156]. Here, the ratio R_{2a2b}/Q_{21} is approximated as 2.83 by linearly interpolating the data of Garland and Crosley [154] for methane-air flames at atmospheric pressure. It must be noted that their data only consider collisional energy transfer over different rotational levels of the $\mathrm{A}^2\Delta$ electronic state, *i.e.*, with $\Delta N' \neq 0$. Based on emission spectra, they obtained the rate of RET by comparing the emission of photons from the laser-pumped rotational level to that of all other rotational levels. While the line width of their laser was sufficiently thin to excite a single feature of the fine structure induced by Λ-doubling and spin-splitting, the relatively low resolution of their monochromator only

allowed to separate fluorescence from individual rotational levels. Therefore, collisional transfer of energy within the laser-populated rotational level, *i.e.*, with $\Delta N' = 0$, was not considered in their assessment of the RET rate constant. However, experiments performed at low pressures and room temperature revealed that the rate at which the laser-pumped state is depopulated to other states within a given rotational energy level (with a different parity and/or spin quantum number) due to collisions of CH $A^2\Delta$ with CO_2, N_2, and Ar is significant [171], and has a magnitude similar to, but smaller than, the rate at which molecules shift to other rotational energy levels [172]. Given the lack of data at atmospheric flame conditions, the value of R_{2a2b} extracted from the data of Garland and Crosley [154] is used, while keeping in mind that it is likely underestimated. For that reason, a wide range of uncertainty is applied on the values of R_{2a2b} and R_{1a1b} in the error analysis presented in section 3.4. Following Luque et al. [98] and Driscoll et al. [173], R_{1a1b} is set equal to R_{2a2b}. To obtain the backward rate of rotational energy transfer, R_{kbka}, an analogy to chemical equilibrium is made invoking the similar collisional nature of both processes. Upon equilibrium, the rate at which CH molecules are transferred from the a to b states must be balanced by the rate at which CH molecules from the manifold (b state) are fed into the a state, such that the population in each state remains unchanged. This equilibrium hypothesis can be written as:

$$N_{kb} \cdot R_{kbka} = N_{ka} \cdot R_{kakb}. \tag{3.10}$$

Recognizing that at equilibrium $N_{ka} = f_{\mathrm{B},N_{ka}} \cdot N_k$ and $N_{kb} = (1 - f_{\mathrm{B},N_{ka}}) \cdot N_k$, where N_k is the total number density of CH molecules in the electronic level k, it follows that:

$$R_{kbka} = R_{kakb} \cdot \frac{f_{\mathrm{B},N_{ka}}}{1 - f_{\mathrm{B},N_{ka}}}. \tag{3.11}$$

Typically, this yields a backward rate constant of RET approximately 40 to 50 times slower than R_{kakb} in the ground and electronically excited states.

The population in each of the four states is obtained by solving equations 3.1 to 3.4 with the Runge-Kutta $4^{\mathrm{th}}/5^{\mathrm{th}}$ order solver (ode45) of Matlab for relative and absolute tolerances of 10^{-8} and 10^{-15}, respectively, and using the values for the various parameters of the LIF model reported in Table 3.1. The laser pulse is modelled as a boxcar function with a time interval equal to the laser pulse temporal width (τ_{Laser}). Assuming thermal equilibrium of the internal energy modes, a hypothesis generally valid for subsonic combustion processes [118], the initial conditions, *i.e.*, the initial population in each state (N_{1a}, N_{1b}, N_{2a}, N_{2b}), are computed using the Boltzmann distribution yielding ($N_{0,\mathrm{CH}} \cdot f_{\mathrm{B},N_{1a}}$, $N_{0,\mathrm{CH}} \cdot (1 - f_{\mathrm{B},N_{1a}})$, 0, 0), where $N_{0,\mathrm{CH}}$ [m^{-3}] is the total number density of CH molecules as predicted by flame simulations. The initial concentration of molecules in the $A^2\Delta$

TABLE 3.1: Time-resolved, four-level LIF model parameters.

Parameter	Function	Constants				Units
		c_1	c_2	c_3	c_4	
B_{12}		$1.072 \cdot 10^{10}$				$[\mathrm{m^2J^{-1}s^{-1}}]$
B_{21}	$B_{12} \cdot c_1$	0.889				$[\mathrm{m^2J^{-1}s^{-1}}]$
I		$1.34 \cdot 10^8$				$[\mathrm{Wm^{-2}}]$
$\Delta\nu_\mathrm{L}$		0.34				$[\mathrm{cm^{-1}}]$
Γ		0.583				
A_{2a1a}		$6.087 \cdot 10^5$				$[\mathrm{s^{-1}}]$
A_{2a1b}		$1.209 \cdot 10^6$				$[\mathrm{s^{-1}}]$
A_{21b}		$1.770 \cdot 10^6$				$[\mathrm{s^{-1}}]$
R_{kakb}/Q_{21}		2.83				
R_{kbka}	$R_{kakb} \cdot \frac{f_{\mathrm{B},N_{ka}}}{1-f_{\mathrm{B},N_{ka}}}$					$[\mathrm{s^{-1}}]$
$f_{\mathrm{B},N_{1a}}$	$c_1 \cdot e^{c_2/T} + c_3 \cdot e^{c_4/T}$	0.1683	-929.0	-0.1822	-1498	
$f_{\mathrm{B},N_{2a}}$	$c_1 \cdot e^{c_2/T} + c_3 \cdot e^{c_4/T}$	2.608	-1402	-2.609	-1438	
τ_cam		$30 \cdot 10^{-9}$				[s]
$\left(\frac{\partial\sigma}{\partial\Omega}\right)$	$f(T_\mathrm{R})$	ref. [174]				
T_R		296				[K]
$\tau_{\lambda,\mathrm{LIF}}$		0.376				
$\tau_{\lambda,\mathrm{R}}$		0.166				
δ_PSF		0.124				[mm]
Quenching coefficients are from [169]:						
Q_{21}	$\sum Q_j \cdot \frac{PX_j}{RT}$					$[\mathrm{s^{-1}}]$
$Q_{\mathrm{H_2}}$	$c_1\sigma_{\mathrm{H_2}}T^{c_2}$	11.02	0.5			$[10^{-13}\mathrm{cm^3s^{-1}}]$
Q_H	$c_1\sigma_\mathrm{H}T^{c_2}$	15.09	0.5			$[10^{-13}\mathrm{cm^3s^{-1}}]$
$Q_{\mathrm{H_2O}}$	$c_1\sigma_{\mathrm{H_2O}}T^{c_2}$	5.30	0.5			$[10^{-13}\mathrm{cm^3s^{-1}}]$
$Q_{\mathrm{O_2}}$	$c_1\sigma_{\mathrm{O_2}}T^{c_2}$	4.79	0.5			$[10^{-13}\mathrm{cm^3s^{-1}}]$
Q_OH	$c_1\sigma_\mathrm{OH}T^{c_2}$	5.36	0.5			$[10^{-13}\mathrm{cm^3s^{-1}}]$
$Q_{\mathrm{CH_4}}$	$c_1\sigma_{\mathrm{CH_4}}T^{c_2}$	5.43	0.5			$[10^{-13}\mathrm{cm^3s^{-1}}]$
Q_CO	$c_1\sigma_\mathrm{CO}T^{c_2}$	4.88	0.5			$[10^{-13}\mathrm{cm^3s^{-1}}]$
$Q_{\mathrm{CO_2}}$	$c_1\sigma_{\mathrm{CO_2}}T^{c_2}$	4.59	0.5			$[10^{-13}\mathrm{cm^3s^{-1}}]$
$Q_{\mathrm{N_2}}$	$c_1\sigma_{\mathrm{N_2}}T^{c_2}$	4.88	0.5			$[10^{-13}\mathrm{cm^3s^{-1}}]$
Quenching cross-sections are from [169], with updates from [170]:						
$\sigma_{\mathrm{H_2}}$	$c_1T^{c_2}e^{-c_3/T}$	6.1	0.0	686		$[\mathrm{Å^2}]$
σ_H	$c_1T^{c_2}e^{-c_3/T}$	221	-0.5	686		$[\mathrm{Å^2}]$
$\sigma_{\mathrm{H_2O}}$	$c_1T^{c_2}e^{-c_3/T}$	9.6	0.0	0.0		$[\mathrm{Å^2}]$
$\sigma_{\mathrm{O_2}}$	$c_1T^{c_2}e^{-c_3/T}$	$8.61 \cdot 10^{-6}$	1.64	-867		$[\mathrm{Å^2}]$
σ_OH	$c_1T^{c_2}e^{-c_3/T}$	221	-0.5	686		$[\mathrm{Å^2}]$
$\sigma_{\mathrm{CH_4}}$	$c_1T^{c_2}e^{-c_3/T}$	52.8	-0.5	84		$[\mathrm{Å^2}]$
σ_CO	$c_1T^{c_2}e^{-c_3/T}$	8.31	0.0	0.0		$[\mathrm{Å^2}]$
$\sigma_{\mathrm{CO_2}}$	$c_1T^{c_2}e^{-c_3/T}$	$8.67 \cdot 10^{-13}$	3.8	-854		$[\mathrm{Å^2}]$
$\sigma_{\mathrm{N_2}}$	$c_1T^{c_2}e^{-c_3/T}$	$1.53 \cdot 10^{-4}$	1.23	552.1		$[\mathrm{Å^2}]$

electronic energy level is assumed negligible. As shown by the equilibrium distribution presented in the last column of Table 3.2, this is a reasonable hypothesis when assuming thermal equilibrium at a typical temperature of 1850 K. However, in hydrocarbon flames, chemical reactions can induce concentrations of electronically excited species several orders of magnitude larger than observed at thermal equilibrium [175]. Neglecting the initial population in the $A^2\Delta$ state can therefore impact the accuracy of the LIF model [98]. The effects of chemical reactions on the initial concentration of electronically excited CH molecules, and on the dynamics of the LIF system, will be investigated in section 3.2.4, as per the recommendation of Daily [118].

TABLE 3.2: Methylidyne electronic energy levels and properties (ϕ_Λ is the Λ-doubling factor, $2S+1$ the multiplicity (spin-splitting factor), $\omega_{\text{el,eff}} = \phi_\Lambda \cdot (2S+1)$ the effective electronic degeneracy, and T_e the electronic energy measured at the minimum of the Morse potential), along with the equilibrium particle distribution, $N_i/N = \omega_{\text{el,eff}} \cdot \exp\left(-\frac{T_e}{k_\text{B}T}\right)/Z_\text{el}$, where $Z_\text{el} = \sum \omega_{\text{el,eff}} \cdot \exp\left(-\frac{T_e}{k_\text{B}T}\right) = 4.04248$, calculated at $T = 1850$ K. Properties are from [159, 160].

Level	ϕ_Λ	$2S+1$	$\omega_{\text{el,eff}}$	T_e [cm^{-1}]	$\omega_{\text{el,eff}} \cdot \exp\left(-\frac{T_e}{k_\text{B}T}\right)$	N_i/N
$X^2\Pi$	2	2	4	0	4	0.9895
$a^4\Sigma^-$	1	4	4	5844	0.04248	0.01051
$\mathbf{A^2\Delta}$	**2**	**2**	**4**	**23189.8**	$\mathbf{5.882 \cdot 10^{-8}}$	$\mathbf{1.455 \cdot 10^{-8}}$
$B^2\Sigma^-$	1	2	2	26044	$3.195 \cdot 10^{-9}$	$7.903 \cdot 10^{-10}$
$C^2\Sigma^+$	1	2	2	31801.5	$3.629 \cdot 10^{-11}$	$8.978 \cdot 10^{-12}$
$D^2\Pi$	2	2	4	60394	$1.598 \cdot 10^{-20}$	$3.952 \cdot 10^{-21}$
$E^2\Pi$	2	2	4	65625	$2.733 \cdot 10^{-22}$	$6.761 \cdot 10^{-23}$
$F^2\Sigma^+$	1	2	2	65945	$1.065 \cdot 10^{-22}$	$2.636 \cdot 10^{-23}$

3.1.2 Two-level LIF models

Three simpler, two-level LIF models are assembled, which assume 1) negligible rates of RET, 2) infinitely fast rotational energy transfer, and 3) weak laser irradiation. The typical model, shown in Figure 3.3, includes photon absorption (b_{12}), stimulated emission (b_{21}), spontaneous emission (A_{21}), and non-radiative collisional quenching (Q_{21}) [117]. The simplicity of the two-level models allows to more easily identify the dominant time scales in the LIF process, and helps in assessing the effects of RET. The three models are briefly presented in sections 3.1.2.1 to 3.1.2.3, and the parameters required to compute the populations are those provided in Table 3.1, unless explicitly stated.

3.1.2.1 Model with frozen rotational energy transfer

Frozen rotational energy transfer, *i.e.*, $R_{kakb} = 0\ \mathrm{s}^{-1}$, implies that the ground and electronically excited states (states 1 and 2 in Figure 3.3, respectively) solely comprise energy levels directly coupled to laser irradiation, *i.e.*, $v' = v'' = 0$, $J'' = 7.5$, $N'' = 7$, $J' = 8.5$, $N' = 8$, and $\mathrm{p} = e$. It is also customary to assume that all electronically excited species are quenched to the $\mathrm{X}^2\Pi, v'' = 0, J'' = 7.5, N'' = 7, \mathrm{p} = e$ state [100, 117]. The system is therefore isolated from the other vibrational, electronic, and rotational energy levels. It follows that the total number density of CH molecules in the system is equal to the initial population in state 1 (it is assumed that $N_2(0) = 0$):

$$N_2(t) + N_1(t) = N_1(0) = N_{0,\mathrm{CH}} \cdot f_{\mathrm{B},N_{1a}}, \tag{3.12}$$

where $N_{0,\mathrm{CH}}$ is the overall CH number density predicted by the flame simulations, and $f_{\mathrm{B},N_{1a}}$ is the Boltzmann fraction of molecules in the $\mathrm{X}^2\Pi, v'' = 0, J'' = 7.5, N'' = 7, \mathrm{p} = e$ state at thermal equilibrium. The ODE representing the rate of change of N_2 is obtained by invoking species conservation, and using equation 3.12:

$$\begin{aligned} \frac{\mathrm{d}N_2}{\mathrm{d}t} = \dot{N}_2 &= N_1 \cdot b_{12} - N_2 \cdot (b_{21} + A_{21} + Q_{21}) \\ &= N_{0,\mathrm{CH}} \cdot f_{\mathrm{B},N_{1a}} \cdot b_{12} - N_2 \cdot (b_{12} + b_{21} + A_{21} + Q_{21})\,. \end{aligned} \tag{3.13}$$

Equation 3.13 is a first-order, linear, ordinary differential equation conveniently solved analytically through separation of variables [176]:

$$N_{2,\mathrm{on}}(t) = \frac{b_{12} \cdot N_{0,\mathrm{CH}} \cdot f_{\mathrm{B},N_{1a}}}{b_{21} + b_{12} + A_{21} + Q_{21}} \cdot (1 - e^{-(b_{21}+b_{12}+A_{21}+Q_{21})\cdot t}) \qquad 0 \leq t \leq \tau_{\mathrm{Laser}}, \tag{3.14}$$

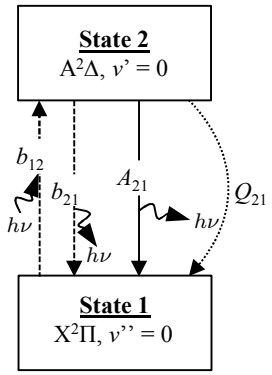

FIGURE 3.3: Two-level LIF model [117].

and,

$$N_{2,\mathrm{off}}(t) = N_{2,\mathrm{on}}(\tau_{\mathrm{Laser}}) \cdot e^{-(A_{21}+Q_{21})\cdot(t-\tau_{\mathrm{Laser}})} \qquad \tau_{\mathrm{Laser}} < t \leq \tau_{\mathrm{cam}}, \tag{3.15}$$

where $N_{2,\mathrm{on}}(t)$ and $N_{2,\mathrm{off}}(t)$ correspond to the number density in state 2 during and following laser irradiation, respectively, and the rate constant of spontaneous emission, A_{21}, is taken as the sum of A_{2a1a} and A_{2a1b} reported in Table 3.1. At the location of maximum CH concentration in the freely propagating, premixed methane-air flame discussed above, ${Q_{21}}/{(A_{2a1a}+A_{2a1b})} \approx 150$ and, therefore, the time constant of the exponential decay of the population in state 2 after the laser pulse is mainly determined by the rate constant of collisional quenching.

3.1.2.2 Model with infinitely fast rotational energy transfer

Infinitely fast rotational energy transfer, *i.e.*, $R_{kakb} \rightarrow \infty$, results in fully equilibrated population distributions in both, ground and electronically excited, states. In this case, $N_2(t)$ represents all energy levels in the $\mathrm{A}^2\Delta$ state, while the whole population in the ground state corresponds to $N_1(t) = [N_{0,\mathrm{CH}} - N_2(t)]$. The fraction of the ground state molecules available for excitation by the laser is calculated as:

$$N_{1,\mathrm{exc}}(t) = N_1(t) \cdot f_{\mathrm{B},N_{1a}} = [N_{0,\mathrm{CH}} - N_2(t)] \cdot f_{\mathrm{B},N_{1a}}. \tag{3.16}$$

Equation 3.17, which describes the rate of change of population in the electronically excited state, is obtained through species conservation and invoking equation 3.16. It must be noted that the rate constant of stimulated emission, b_{21}, must be multiplied by the Boltzmann fraction of CH molecules in the $\mathrm{A}^2\Delta, v' = 0, J' = 8.5, N' = 8, \mathrm{p} = e$ state, $f_{\mathrm{B},N_{2a}}$, as only these molecules can undergo stimulated emission through the $R_{1e}(7)$ transition.

$$\begin{aligned} \frac{\mathrm{d}N_2}{\mathrm{d}t} = \dot{N}_2 &= N_{1,\mathrm{exc}} \cdot b_{12} - N_2 \cdot (b_{21} \cdot f_{\mathrm{B},N_{2a}} + A_{21} + Q_{21}) \\ &= N_{0,\mathrm{CH}} \cdot f_{\mathrm{B},N_{1a}} \cdot b_{12} - N_2 \cdot (b_{12} \cdot f_{\mathrm{B},N_{1a}} + b_{21} \cdot f_{\mathrm{B},N_{2a}} + A_{21} + Q_{21}) \end{aligned} \tag{3.17}$$

As previously, equation 3.17 is solved through separation of variables, which yields [176]:

$$\begin{aligned} N_{2,\mathrm{on}}(t) = &\frac{b_{12} \cdot N_{0,\mathrm{CH}} \cdot f_{\mathrm{B},N_{1a}}}{b_{21} \cdot f_{\mathrm{B},N_{2a}} + b_{12} \cdot f_{\mathrm{B},N_{1a}} + A_{21} + Q_{21}} \\ &\cdot (1 - e^{-(b_{21}\cdot f_{\mathrm{B},N_{2a}} + b_{12}\cdot f_{\mathrm{B},N_{1a}} + A_{21} + Q_{21})\cdot t}) \qquad 0 \leq t \leq \tau_{\mathrm{Laser}}. \end{aligned} \tag{3.18}$$

The decaying part of the LIF process is described by equation 3.15. A_{21} is assumed identical to the two-level LIF model with ${R_{kakb}}/{Q_{21}} = 0$, as the rate constants of spontaneous emission out of

states $2a$ and $2b$ in the four-level LIF model are similar, as shown in Table 3.1.

3.1.2.3 Model assuming weak laser irradiation (linear LIF regime)

Weak laser irradiation (linear LIF regime) is often assumed in the development of simple, algebraic LIF models. This hypothesis implies that the rate constants of photon absorption and stimulated emission are negligible in comparison to the rate constants of quenching and spontaneous emission, *i.e.*, $b_{12} + b_{21} \ll Q_{21} + A_{21}$ for equation 3.14, and $b_{21} \cdot f_{\mathrm{B},N_{2a}} + b_{12} \cdot f_{\mathrm{B},N_{1a}} \ll Q_{21} + A_{21}$ for equation 3.18. Both equations become identical when the laser-coupled terms (b_{12} and b_{21}) are removed from the denominator and the exponential term:

$$N_{2,\mathrm{on}}(t) = \frac{b_{12} \cdot N_{0,\mathrm{CH}} \cdot f_{\mathrm{B},N_{1a}}}{A_{21} + Q_{21}} \cdot (1 - e^{-(A_{21}+Q_{21})\cdot t}) \qquad 0 \leq t \leq \tau_{\mathrm{Laser}}, \tag{3.19}$$

which suggests that RET plays a negligible role for low irradiance levels.

3.2 Adequacy of the principal assumptions invoked in the development of LIF models

In this section, four assumptions commonly invoked in the development of LIF models are reviewed: 1) the populations in the ground and electronically excited states achieve steady-state over the duration of the laser pulse; 2) rotational energy transfer can be neglected; 3) the temporal shape of the laser pulse has a minimal impact on the predicted LIF signal; and 4) the LIF process and the flame chemistry are decoupled.

3.2.1 Steady-state assumption

Figure 3.4 shows the temporal evolution of the population in each of the energy levels computed with the four-level LIF model. The curves correspond to the solution obtained with the Runge-Kutta solver of Matlab, while the dots are calculated using the analytical solution of the LIF model presented in Appendix B. The remarkable agreement between both sets of data confirms the accuracy of the numerical ODE solver. Laser irradiation depopulates the $1a$ state and excites the methylidyne molecules to the $2a$ state. In the ground electronic energy level, a net transfer of molecules from the $1b$ to the $1a$ states is induced by RET, which decreases the number density in the former. In the electronically excited state, RET occurs in the opposite direction, *i.e.*, from the laser-coupled level ($2a$) to the rotational manifold ($2b$). Once the laser is turned off, the populations in the $2a$ and $2b$ states decay, and the two states in the ground electronic energy level are

replenished. As expected, the total number density in the system, $\sum N_{ki}$, remains constant over the whole process as shown in Figure 3.4(a).

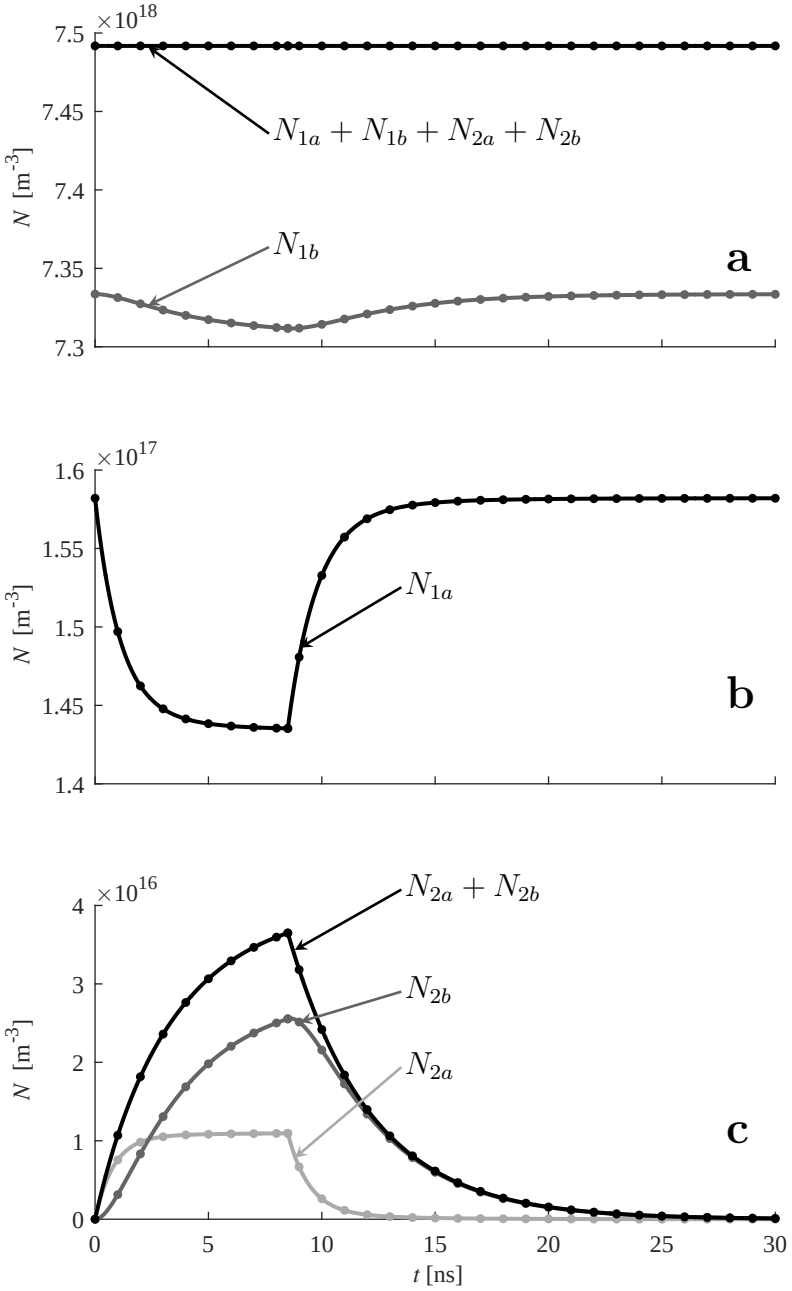

FIGURE 3.4: Predicted populations by the four-level LIF model at the location of maximum CH concentration in a freely propagating, stoichiometric, premixed flame of methane and air simulated with the SD mechanism. The curves correspond to the solution provided by the Runge-Kutta solver of Matlab, while the superimposed, solid dots are obtained using the analytical solution presented in Appendix B.

Over the 8.5 ns of the laser pulse, the populations in the laser-coupled states ($1a$ and $2a$) almost reach steady-state (SS) conditions, *i.e.*, ${}^{\mathrm{d}N_{ki}}/_{\mathrm{d}t} = 0$. However, state $2b$, out of which most (~72%) of the photons originate, only achieves ~88% of its SS number density. This causes the total population in the electronically excited level ($N_{2a} + N_{2b}$) to only attain ~91% of the number density at SS conditions. For the steady-state assumption to be adequate, the populations should not only reach their SS concentration, but also maintain it for a sufficiently long duration such that the transient behaviours at the beginning and after the laser pulse are of negligible importance. Consistent with the estimated time to reach SS reported in [117], the LIF process is undoubtedly transient for laser pulses of a few nanoseconds.

Nevertheless, the steady-state assumption is often invoked in the processing of experimental, linear, nanosecond LIF signals, *e.g.*, [100, 101], most of the time implicitly, *i.e.*, by blindly using the solution of a two-level, steady-state model provided in a reference book or a review paper [117, 118, 159]. In this case, the number of photons emitted per unit volume is calculated as[2]:

$$N_{\mathrm{p}} = A_{21} \cdot N_{2,\mathrm{on,SS}} \cdot \tau_{\mathrm{Laser}}, \tag{3.20}$$

where $N_{2,\mathrm{on,SS}}$ corresponds to the steady-state number density of CH molecules in the electronically excited state obtained by evaluating equation 3.19 with $t \to \infty$:

$$N_{2,\mathrm{on,SS}} = \frac{b_{12} \cdot N_{0,\mathrm{CH}} \cdot f_{\mathrm{B},N_{1a}}}{A_{21} + Q_{21}}. \tag{3.21}$$

Although, at the first glance, it could be concluded that these datasets are flawed, the mathematical demonstration performed in Appendix C reveals that equation 3.20 provides accurate values of N_{p} in the linear LIF regime (weak laser irradiation) if the camera exposure time is sufficiently long to collect most of the LIF signal. This does not mean that the steady-state assumption is valid; it is instead a fortuitous behaviour caused by the similar characteristic time scales of the exponential rise and decay of the overall population in the electronically excited energy level, both determined by the rate constant of quenching, Q_{21}, in the linear LIF regime. The deficit in terms of emitted photons of the transient solution in comparison to the steady-state case as the laser irradiates the CH molecules is exactly compensated by the emission of photons during the exponential decay of the $\mathrm{A}^2\Delta$ electronic state once the laser is turned off (see Figure C.1). Therefore, extending the value of τ_{Laser} in equation 3.20 by ${}^{1}/_{Q_{21}}$ to account for the photons emitted after the laser pulse, as performed by Gibaud et al. [101], is erroneous. Considering their reported values for the laser pulse duration (3 ns), and ${}^{1}/_{Q_{21}}$ (3.6 ns), it follows that their concentration dataset has a systematic

[2]The LIF signal, S_{LIF}, collected on the camera detector is proportional to N_{p} as discussed in section 3.3.

error (underestimation) of ~55%, significantly beyond the stated uncertainty in their measurements. Using a steady-state formulation with such a correction ($^1/_{Q_{21}}$) for the photons emitted after the laser pulse would be appropriate in the saturated LIF regime where the exponential rise is almost instantaneous due to the large values of b_{12} and b_{21} (see equations 3.14 and 3.18), while the decay of the electronically excited state population is still determined by the rate constant of collisional quenching (see equation 3.15). Between these two asymptotic regimes (linear and saturated), the transient nature of the LIF process must be considered, and a time-resolved formulation needs to be used.

The main benefit of using two-level, steady-state LIF models is that they provide a simple, algebraic equation relating the LIF signal to the number density of CH molecules, which can be easily inverted to extract concentrations based on experimental LIF signal values. Here, as the comparison to experiments is instead performed using LIF signals derived from flame simulations, this advantage is not as relevant. Furthermore, the computational cost of calculating N_p based on a transient LIF model is not sufficiently high to justify the usage of steady-state formulations, whose validity is coincidental and limited to the asymptotic linear and saturated regimes. Also, as discussed below, the finite rate constant of RET, which is only included in the four-level LIF model, must be considered for typical values of laser irradiance used in experiments.

3.2.2 Negligible impact of rotational energy transfer on the LIF process

As shown by equation 3.19, the solutions of the two-level LIF models with negligible and infinitely fast RET, equations 3.14 and 3.18, respectively, are identical under very weak laser irradiation, which suggests that rotational energy transfer does not impact the LIF process. This negligible effect of the rate of RET in the linear LIF regime is confirmed in Figure 3.5(a) where the overall populations in the upper electronic level predicted by both two-level models and the four-level LIF model ($N_{2a} + N_{2b}$) almost perfectly agree for a low absorption rate constant, $b_{12} = 1 \cdot 10^6\ \mathrm{s}^{-1}$. This is explained by the fact that, under very weak laser irradiation, the rate of photon absorption is very slow, such that the number density in the laser-coupled ground state remains almost unchanged. That is, the thermal equilibrium among the energy levels in the ground state is relatively unperturbed, such that the rate of RET in the ground state has virtually no impact on the LIF process. In the electronically excited state, the four-level LIF model predicts that a significant fraction of the molecules initially excited to the $2a$ state (dotted curve in Figure 3.5(a)) is transferred to the $2b$ state (dashed curve in Figure 3.5(a)). However, since the main mechanism depopulating the upper electronic level is collisional quenching, and that it depletes the $2a$ and $2b$ states at the same rate constant (Q_{21}), it follows that the actual distribution of molecules between both states, which

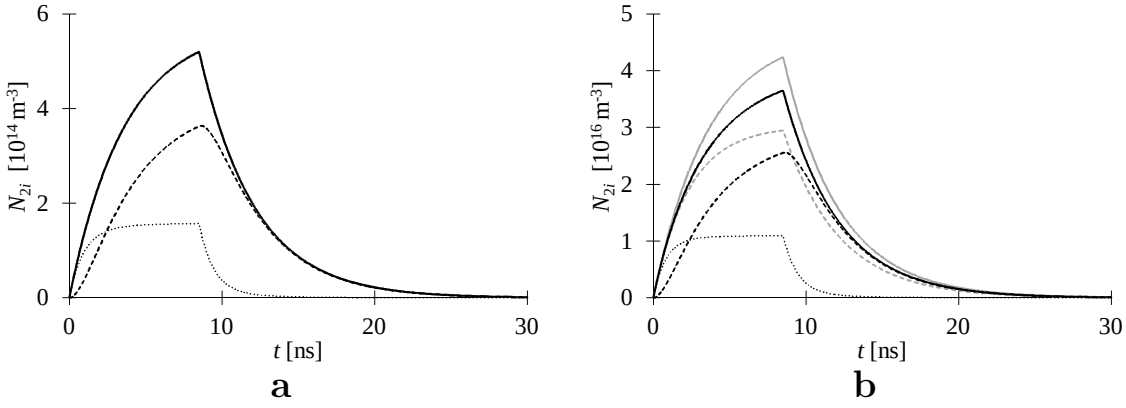

FIGURE 3.5: Electronically excited state populations as a function of time for absorption rate constants, b_{12}, of (a) $1 \cdot 10^6$ s^{-1}, and (b) $8.21 \cdot 10^7$ s^{-1}. Legend: two-level LIF model with $R_{kakb} = 0$ s^{-1} (dashed grey curve), two-level LIF model with $R_{kakb} \to \infty$ (solid grey curve), and states $2a$ (dotted black curve), $2b$ (dashed black curve) and total electronically excited state population (solid black curve) computed with the four-level, LIF model.

is determined by the rate constant of RET, does not impact the total number of molecules in the $A^2\Delta$ state ($N_{2a} + N_{2b}$). Since the rate constants of spontaneous emission from states $2a$ and $2b$ are very similar as presented in Table 3.1, it follows that the total number of emitted photons per unit volume, N_p, calculated with equation 3.22 where τ_cam is the camera exposure time, is also negligibly impacted by the rate of RET.

$$N_\mathrm{p} = \int_0^{\tau_\mathrm{cam}} \sum_{i,j} N_{2i}(t) \cdot A_{2i1j} \, \mathrm{d}t \tag{3.22}$$

Figure 3.6 presents the total number of emitted photons per unit volume obtained with the models discussed in section 3.1. As expected, they agree very well with one another at low laser pulse energies ($b_{12} \propto E_\mathrm{B}$). As b_{12} increases, the predictions of the LIF models including all laser-coupled terms (referred to as complete models in the following) transition into the saturated LIF regime where N_p becomes independent of b_{12}. The onset of saturation is characterized by the saturation irradiance, I_sat, which is the irradiance calculated at the intercept of the solution of the linear LIF model (equation 3.19, dotted grey line in Figure 3.6) with the value of N_p at saturation ($b_{12} \to \infty$). This condition is shown with symbols for the three complete LIF models in Figure 3.6. The principal effect of RET is to delay the transition to saturation, thus yielding higher values of N_p for larger rate constants of RET. This behaviour is consistent with the necessity to consider RET in the processing of saturated LIF signals discussed in [117].

Figure 3.5(b) presents the populations in the upper electronic level predicted by the complete

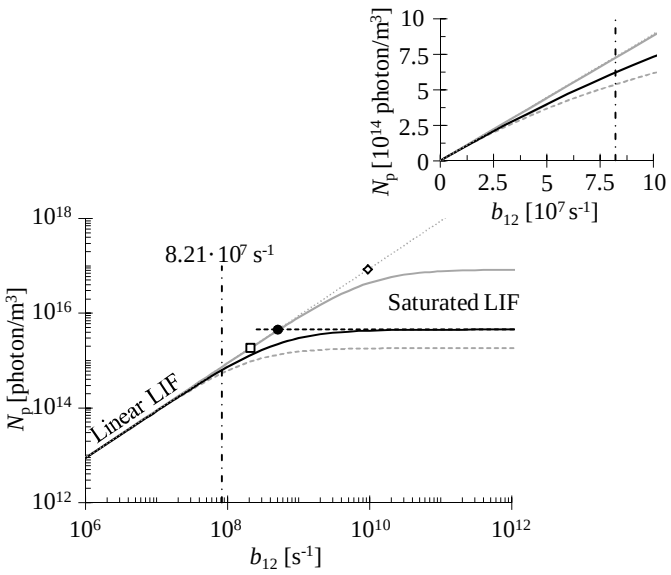

FIGURE 3.6: Number of emitted photons per unit volume as a function of the rate constant of absorption. Note the logarithmic scale on the principal plot, and the linear scale in the inset. Legend: two-level LIF model with $R_{kakb} = 0\ \mathrm{s}^{-1}$ (dashed grey curve), two-level LIF model with $R_{kakb} \to \infty$ (solid grey curve), four-level LIF model (solid black curve), two-level linear LIF model (dotted grey curve), and absorption rate constant for the current experimental configuration (dashed-dotted black line). The saturation irradiance (symbols) is determined at the intercept of the dashed black and grey-dotted lines for the four-level LIF model.

LIF models presented in section 3.1 for the rate constant of photon absorption used in the current study, which is approximately 6.2 times smaller than the saturation limit predicted by the four-level LIF model (black dot in Figure 3.6). At all times, the models including rotational energy transfer predict a larger overall number density of electronically excited molecules. In the ground electronic energy level, RET replenishes the laser-coupled ($1a$) state, which is significantly depopulated (see Figure 3.4(b)) due to the non-negligible value of the rate constant of absorption (b_{12}). A larger number density of molecules is then available for excitation, which raises the rate of photon absorption ($N_{1a} \cdot b_{12}$) and, consequently, the number density of electronically excited molecules. In the $\mathrm{A}^2\Delta$ electronic state, although bidirectional, RET induces a net transfer of molecules from the laser-coupled energy level (state $2a$) to the rotational manifold (state $2b$). This reduces the rate at which the upper electronic level is depleted as, unlike state $2b$ that is mainly affected by collisional quenching, a non-negligible level of stimulated emission depopulates the $2a$ state in addition to Q_{21}. The faster is the rate constant of RET, the lower is the contribution of b_{21} in depleting the upper electronic level, and the higher is the total number density in the $\mathrm{A}^2\Delta$ electronic level. As shown in Figure 3.6, this causes the two-level LIF model with infinitely fast RET to predict the largest values of N_p over the considered range of absorption rate constants, followed by the

four-level LIF model, and the two-level LIF model with $R_{kakb}/Q_{21} = 0$.

Interestingly, the solution of the linear LIF model (dotted grey line in Figure 3.6) is an asymptote that the complete LIF models approach as the laser irradiance is reduced. The linear LIF model consistently over-predicts N_p in comparison to the more detailed four-level LIF model, while the two-level LIF models with infinitely fast and frozen RET overestimates and underestimates N_p, respectively. The lower is the value of b_{12}, the smaller is the error incurred by using one of the two-level LIF models (see the inset of Figure 3.6). The rate constant of photon absorption at which the current experiments are performed, $b_{12} = 8.21 \cdot 10^7$ s^{-1}, is shown by the black dashed-dotted line in Figure 3.6. As in [100], this value is approximately one order of magnitude lower than the experimental saturation limit reported in [106], and yields experimental excitation spectra agreeing with theoretical ones produced assuming LIF in the linear regime (see Figure 2.7). However, even if the rate constant b_{12} used in this study is much lower than the saturation limit, there is a non-negligible difference in the values of N_p predicted by the various LIF models as shown in the inset of Figure 3.6; the two-level linear model and the two-level model with infinitely fast RET over-predict by ~18%, and the two-level model with negligible RET underestimates by ~13%, the value of N_p provided by the four-level LIF model. That is, using the common two-level linear LIF model at the current laser energy would cause a systematic error of ~18%. For the linear LIF model to agree within 5% with the four-level LIF model, the laser irradiance would need to be reduced by a factor of ~5.2. This would cause a significant decrease in the LIF signal recorded by the camera, and a corresponding reduction in the signal-to-noise ratio restricting the range of operating conditions that can be investigated. Instead, the four-level LIF model is used, which considers the finite rate of RET in the ground and electronically excited states and, consequently, properly accounts for the continuous transition from the linear to the saturated LIF regimes. Unless the experimental conditions allow to operate at laser irradiance levels ~30 to ~50 times lower than the saturation limit, the detailed four-level LIF model should be preferred over the two-level models[3].

3.2.3 Impact of laser temporal energy profile

It is common practice to assume that the irradiance is constant throughout the laser pulse and, therefore, that the rate constant of absorption does not vary with time [94, 98, 100, 101]. The exact temporal energy profile of the beam exiting the dye laser could not be measured in the current

[3]For the linear LIF model to agree within 5% with the four-level LIF model, the laser energy would need to be reduced by a factor of ~5.2. Considering that the saturation limits determined with the four-level LIF model, and obtained from [106], are approximately 6.2 and 10 times higher, respectively, than the rate constant of absorption at which the current set of experiments is performed, it is established that the linear LIF model is only valid for laser irradiance levels ~30 to ~50 times lower than the saturation irradiance.

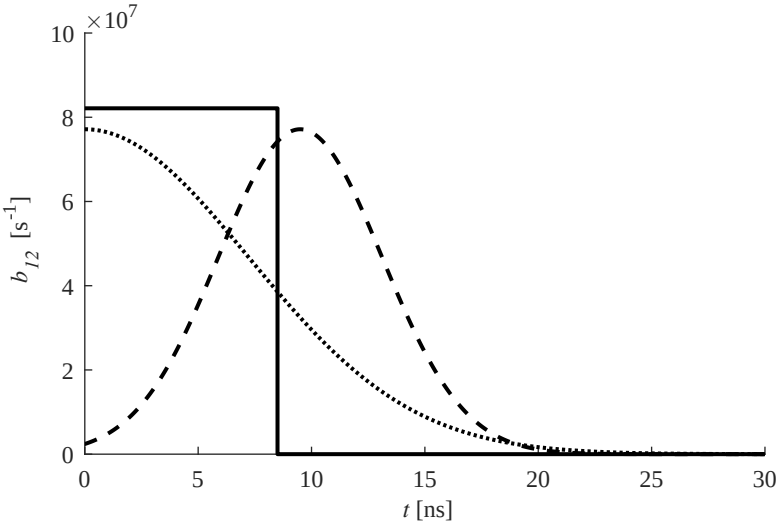

FIGURE 3.7: Temporal variation in the rate constant of absorption. Legend: boxcar (solid lines), half-normal (dotted curve), and Gaussian (dashed curve) laser pulse shapes.

study as a sensor with a sufficiently fast response, and a measuring instrument with a sufficiently high sampling rate, were not available. However, it is likely that the temporal energy profile of the laser pulse departs from a boxcar function [177]. To investigate its effect on the predicted LIF signal, the time-resolved, four-level LIF model is solved with two transient profiles of b_{12} shown in Figure 3.7: 1) a half-normal distribution (dotted curve), and 2) a Gaussian distribution (dashed curve). Both profiles have the same duration, $\tau_{\mathrm{Laser}} = 8.5$ ns (full width at half maximum), and overall energy, E_{B}, as the boxcar laser pulse. Therefore, the integral $\int_{-\infty}^{\infty} b_{12}\mathrm{d}t$ for the three laser pulse shapes is equal.

The populations in the $\mathrm{A}^2\Delta$ electronic energy level are shown in Figure 3.8 for the boxcar (a), Gaussian (b), and half-normal (c) laser pulses. As expected, the shape of the laser pulse impacts the populations in states $2a$ and $2b$. Namely, the Gaussian and half-normal distributions lead to lower maximum number densities in comparison to the boxcar laser pulse, but non-negligible values of N_{2a} and N_{2b} are observed over longer periods of time due to their flared wings. However, as discussed in section 3.3, the LIF signal is proportional to the number of photons emitted per unit volume computed with equation 3.22. The Gaussian and half-normal laser pulse shapes lead to overestimations of ~3% and ~4%, respectively, in the predicted value of N_{p} in comparison to the boxcar energy profile. Hence, for the irradiance level used in this study, the temporal energy profile of the laser pulse has only a minor effect on the predicted LIF signal.

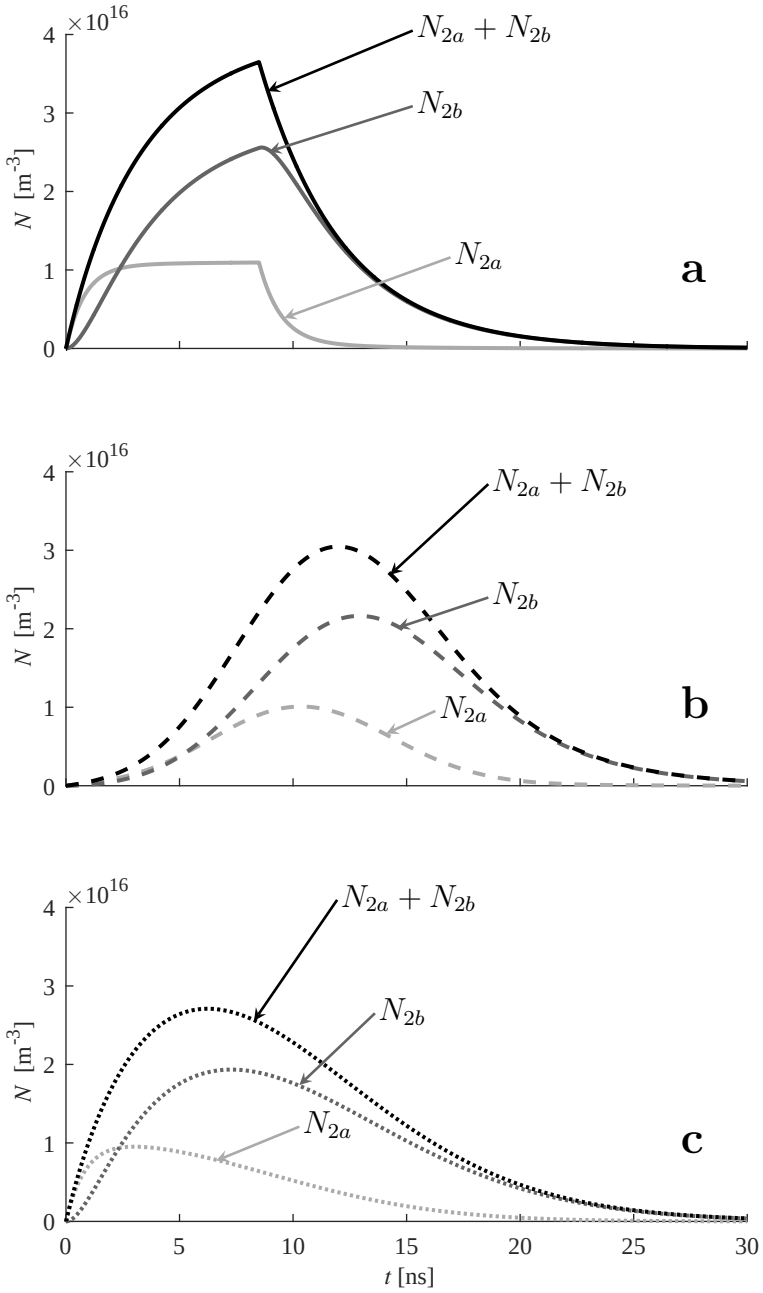

FIGURE 3.8: Electronically excited state populations predicted by the time-resolved, four-level LIF model for three laser pulse temporal shapes: (a) boxcar, (b) Gaussian, and (c) half-normal distributions.

3.2.4 Interactions of the flame chemistry with the LIF system

In LIF data analysis, it is customary to neglect chemical interactions of the ground and electronically excited energy levels with the flame chemistry [77, 94, 100, 101]. This is a reasonable assumption for species with relatively slow chemical rates in comparison to the principal processes in the LIF system [98]. However, fast chemical reactions can alter the LIF signal by replenishing the depopulated ground state, or by consuming the laser-excited molecules thus preventing them from undergoing spontaneous emission [98, 118]. Furthermore, as witnessed from the typical blue chemiluminescence of hydrocarbon flames, chemical reactions produce a non-negligible concentration of electronically excited CH molecules, which emit photons through spontaneous emission [178, 179]. Therefore, the adequacy of the previously made assumptions regarding the negligible initial populations in the $2a$ and $2b$ states, and the absence of interactions between the LIF model and the flame chemistry, must be verified and their effects on the LIF signal predictions assessed.

3.2.4.1 Replenishment of the ground energy level by chemical reactions

For steady flames, the rate of accumulation of a given species ($\partial Y_j/\partial t$, where Y_j is the mass fraction of species j) is null throughout the computational domain. Locally, the net production rate of the species, *i.e.*, the difference between the rates of production and consumption (see equation 3.23), must then be balanced by the convective and diffusive fluxes [180]. To fully capture the coupling between the LIF system and the flame chemistry, it would be necessary to include the four levels of the LIF model, as well as the rate descriptions for all transitional processes, in a transient flame solver, which is a fairly intricate task. Instead, for the current assessment, terms to be added to the system of ODEs of the time-resolved, four-level LIF model are derived taking advantage that CH is in quasi-steady state within the front of hydrocarbon flames [92].

The overall production rate of CH, q_{CH}, is described by equation 3.23, where R_{in} and R_{out} are the numbers of reactions producing/consuming CH, $N_{r,i}$ and $N_{r,k}$ are the numbers of reactants in the reactions producing/consuming CH, k is the specific rate, $[\mathrm{M}_j]$ is the concentration of species

j, and ν is the stoichiometric coefficient[4].

$$\begin{aligned} q_{\mathrm{CH}} = & \underbrace{\sum_{i=1}^{R_{\mathrm{in}}} k_i \prod_{j=1}^{N_{r,i}} [\mathrm{M}_j]^{\nu'_j}}_{\text{rate of production, } q_{f,\mathrm{CH}}} - \underbrace{\sum_{k=1}^{R_{\mathrm{out}}} k_k [\mathrm{CH}] \prod_{l=1,\mathrm{M}_l \neq \mathrm{CH}}^{N_{r,k}} [\mathrm{M}_l]^{\nu'_l}}_{\text{rate of consumption, } q_{c,\mathrm{CH}}} \\ = q_{f,\mathrm{CH}} - [\mathrm{CH}] & \underbrace{\sum_{k=1}^{R_{\mathrm{out}}} k_k \prod_{l=1,\mathrm{M}_l \neq \mathrm{CH}}^{N_{r,k}} [\mathrm{M}_l]^{\nu'_l}}_{\text{rate constant of consumption}} \end{aligned} \tag{3.23}$$

The overall (net) production rate of CH, q_{CH}, and the rates of production and consumption of CH, $q_{f,\mathrm{CH}}$ and $q_{c,\mathrm{CH}}$, respectively, are shown in Figure 3.9 for the freely propagating methane-air flame discussed above. Through the flame front, $q_{f,\mathrm{CH}}$ and $q_{c,\mathrm{CH}}$ are almost equal, such that CH is assumed to be in quasi-steady state, *i.e.*, $q_{\mathrm{CH}} \approx 0$. Inserting $q_{\mathrm{CH}} = 0$ in equation 3.23 and rearranging yields the following description for the rate constant of consumption:

$$\underbrace{\sum_{k=1}^{R_{\mathrm{out}}} k_k \prod_{l=1,\mathrm{M}_l \neq \mathrm{CH}}^{N_{r,k}} [\mathrm{M}_l]^{\nu'_l}}_{\text{rate constant of consumption}} = \frac{q_{f,\mathrm{CH}}}{[\mathrm{CH}]} = \frac{q_{f,\mathrm{CH}} \cdot N_{\mathrm{A}}}{N_{0,\mathrm{CH}}}, \tag{3.24}$$

where $N_{0,\mathrm{CH}}$ is the number density of CH molecules predicted by the flame simulation, and N_{A} is the Avogadro constant. As shown in Figure 3.4, laser excitation of the CH molecules depletes the ground electronic state, but only slightly; at the end of the laser pulse, the overall population in the ground state ($N_{1a} + N_{1b}$) is 0.49% lower than its initial value. Such a small perturbation of the CH concentration is assumed to have a negligible impact on the concentration of the other species involved in the flame chemical reactions. Therefore, it is hypothesized that the rate constant of consumption defined in equation 3.24 is constant throughout the LIF process, and so is $q_{f,\mathrm{CH}}$.

A formula for the overall (net) rate of production of CH to be included in the LIF model,

[4]This formulation assumes that the stoichiometric coefficient of CH is 1 in all reactions.

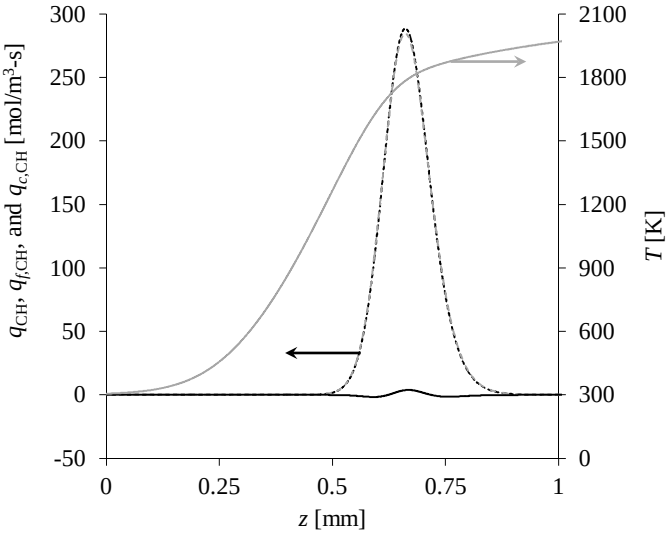

FIGURE 3.9: Net rate of production (solid black curve), rates of production (black dashed curve) and consumption (grey dashed curve) of methylidyne, and temperature (solid grey curve) in a freely propagating, laminar, premixed CH_4-air flame at stoichiometric conditions.

$q_{\mathrm{LIF,CH}}$, is derived by inserting equation 3.24 in equation 3.23, and recognizing that the instantaneous concentration of CH in the ground state corresponds to ${}^{[N_{1a}(t)+N_{1b}(t)]}/_{N_\mathrm{A}}$:

$$
\begin{aligned}
q_{\mathrm{LIF,CH}} &= q_{f,\mathrm{CH}} - [\mathrm{CH}] \underbrace{\sum_{k=1}^{R_{\mathrm{out}}} k_k \prod_{l=1,\mathrm{M}_l\neq\mathrm{CH}}^{N_{r,k}} [\mathrm{M}_l]^{\nu'_l}}_{\text{rate constant of consumption}} \\
&= q_{f,\mathrm{CH}} - [\mathrm{CH}] \cdot \frac{q_{f,\mathrm{CH}} \cdot N_\mathrm{A}}{N_{0,\mathrm{CH}}} \\
&= q_{f,\mathrm{CH}} \cdot \left(1 - \frac{N_{1a} + N_{1b}}{N_{0,\mathrm{CH}}}\right) \\
&= \underbrace{q_{f,\mathrm{CH}} \cdot \left(f_{\mathrm{B},N_{1a}} - \frac{N_{1a}}{N_{0,\mathrm{CH}}}\right)}_{\text{added to equation 3.1}} + \underbrace{q_{f,\mathrm{CH}} \cdot \left[(1 - f_{\mathrm{B},N_{1a}}) - \frac{N_{1b}}{N_{0,\mathrm{CH}}}\right]}_{\text{added to equation 3.2}},
\end{aligned}
\tag{3.25}
$$

where $q_{f,\mathrm{CH}} = 1.686 \cdot 10^{26}$ m^{-3}·s^{-1} is obtained at the location of maximum CH concentration for the freely propagating, premixed methane-air flame discussed above. It must be noted that prior to the laser pulse, the terms added to equations 3.1 and 3.2 are null. They become positive, therefore producing CH molecules, when the populations in the $1a$ and $1b$ states decrease from their concentration at thermal equilibrium.

Figure 3.10 presents the solutions obtained with the four-level LIF model without (solid curves) and with (dashed curves) chemical reactions interacting with the ground state, $1a$ and $1b$, levels. For the first few nanoseconds, both solutions are nearly identical but, for larger values of t, the chemical reactions produce CH molecules yielding higher number densities in the $1a$ and $1b$ levels. After the laser pulse, the $A^2\Delta$ state decays and refills the ground state levels. As the number densities in states $1a$ and $1b$ reach values higher than the initial conditions (thermal equilibrium), the chemical reactions start consuming CH molecules. It is noted that N_{1a}, N_{1b}, and $\sum N_{ki}$ do not return to their initial value over the 30 ns of the simulation due to the limited value of $q_{\mathrm{LIF,CH}}$. It was verified that the system comes back to the initial conditions if given sufficient time.

The chemical reactions do not produce a significant number of CH molecules. In fact, the overall number density ($\sum N_{ki}$) deviates by less than 0.083% from its original value. This is because $q_{\mathrm{LIF,CH}}$ only achieves relatively small values ($7.218 \cdot 10^{23}$ m^{-3}·s^{-1} at maximum). By integrating $q_{\mathrm{LIF,CH}}$ over the duration of the laser pulse, the number density of molecules produced by the chemical reactions is found to be $4.510 \cdot 10^{15}$ m^{-3}, of which $2.356 \cdot 10^{15}$ m^{-3} are provided to state $1a$ and $2.154 \cdot 10^{15}$ m^{-3} to state $1b$. These values are relatively small in comparison to the number densities of CH molecules in the ground electronic state at the end of the laser pulse: $N_{1a} = 1.440 \cdot 10^{17}$ m^{-3}, $N_{1b} = 7.316 \cdot 10^{18}$ m^{-3}, and $N_{1a} + N_{1b} = 7.460 \cdot 10^{18}$ m^{-3}. Consequently, the chemical reactions have a minimal impact on the ground state populations, and on the LIF system.

For sufficiently long laser pulses, it can be shown that the chemical reactions would replenish the ground electronic state ($N_{1a} + N_{1b}$) to its initial value of number density, $N_{0,\mathrm{CH}}$[5]. However, because of the low value of $q_{\mathrm{LIF,CH}}$, this process occurs on a time scale of a few hundreds of nanoseconds, while the laser pulse lasts 8.5 ns. Therefore, the minimal impact of the chemical reactions is caused by two factors: the slow overall rate of CH production, and the limited value of τ_{Laser}. On its own, the rate of production of CH, $q_{f,\mathrm{CH}} = 1.686 \cdot 10^{26}$ m^{-3}·s^{-1}, which once integrated over the duration of the laser pulse yields $1.433 \cdot 10^{18}$ m^{-3}, would be sufficiently fast to interact with the LIF process as suspected in [98]. However, because it is counterbalanced by the rate of consumption of CH molecules, this results in an overall (net) rate of production of CH, $q_{\mathrm{LIF,CH}}$, too small to significantly impact the LIF system over the duration of the laser pulse. Furthermore, it must be noted that because the current set of experiments is performed at a relatively low level of irradiance, state $1a$ is only weakly depopulated during laser irradiation.

[5]Applying the conservation of CH molecules to the complete LIF system, the ODE describing the rate of change of the total number density, $N_{\mathrm{T}} = \sum N_{ki}$, is $\mathrm{d}N_{\mathrm{T}}/\mathrm{d}t = q_{\mathrm{LIF,CH}} = q_{f,\mathrm{CH}} \cdot (1 - (N_{1a}+N_{1b})/N_{0,\mathrm{CH}})$. Assuming that the laser pulse is sufficiently long for the total population to achieve steady-state, *i.e.*, $\mathrm{d}N_{\mathrm{T}}/\mathrm{d}t = 0$, it follows that $q_{f,\mathrm{CH}} \cdot (1 - (N_{1a}+N_{1b})/N_{0,\mathrm{CH}}) = 0$ and, consequently, $N_{1a} + N_{1b} = N_{0,\mathrm{CH}}$.

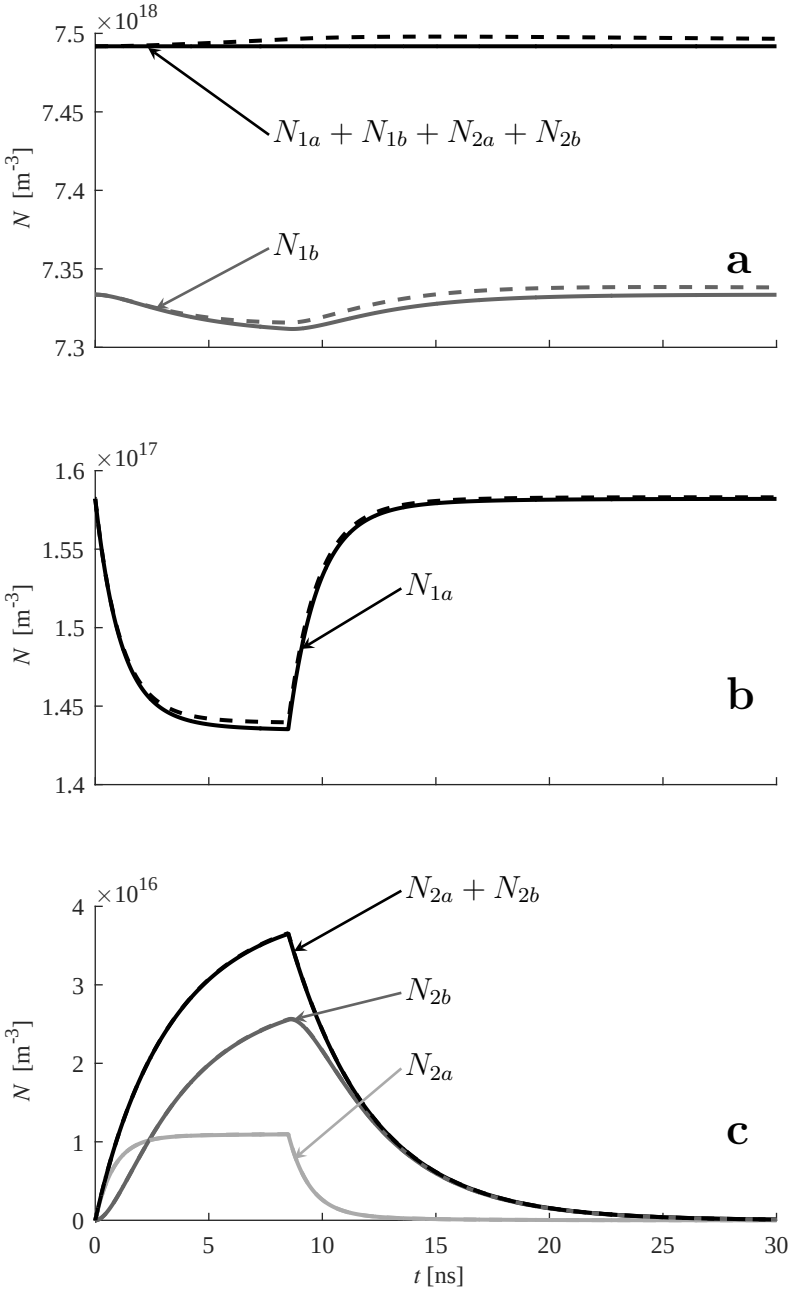

FIGURE 3.10: Predicted populations by the four-level LIF model isolated from the flame chemistry (solid curves), and supplemented with chemical reactions interacting with the ground electronic state (dashed curves).

Therefore, having very fast chemical reactions that would almost instantaneously replenish states $1a$ and $1b$, hence maintaining their initial number density, would have a limited impact on the number of emitted photons per unit volume, which would increase by ~8.5%.

As shown in Figure 3.10, the populations in the $\mathrm{A}^2\Delta$ state are almost unchanged in comparison

to the solution of the LIF model without chemical reactions. This causes a limited increase of ~0.2% in the number of photons emitted per unit volume, N_{p}. Therefore, it is concluded that chemical reactions interacting with the ground state, $1a$ and $1b$, levels have a negligible impact on the predicted LIF signal.

3.2.4.2 Interactions of the electronically excited state with the flame chemistry

Generally, the set of species considered in thermochemical mechanisms does not include CH in the $\mathrm{A}^2\Delta$ state (CH^*) as it is not expected to impact the predictions of the main combustion properties. However, the chemistry of CH^* received some attention in the literature as CH chemiluminescence, emitted when electronically excited methylidyne formed by chemical reactions undergoes spontaneous emission, found applications as a non-intrusive flame diagnostic technique to characterize the heat release, equivalence ratio, and flame location [181, 182]. The effects on the response of the four-level LIF model of non-null, initial concentrations of molecules in the $\mathrm{A}^2\Delta$ state, as well as the impacts of chemical reactions interacting with levels $2a$ and $2b$, are investigated in this section.

The principal reactions expected to form electronically excited methylidyne are presented in equations 3.26 to 3.29. As shown in Table 3.3, significant disagreements in the rate coefficients exist in the literature [135, 178, 179, 181, 183–188]. This causes variations of a few orders of magnitude in the values of the specific rates calculated at a typical temperature of 1850 K, $k(T = 1850\ \mathrm{K})$. There is a consensus that CH^* is primarily consumed via non-radiative collisional quenching, and the rate coefficients provided by Tamura et al. [169] are generally used.

$$\mathrm{C_2 + OH \leftrightarrow CH^* + CO} \tag{3.26}$$

$$\mathrm{C_2H + O \leftrightarrow CH^* + CO} \tag{3.27}$$

$$\mathrm{C_2H + O_2 \leftrightarrow CH^* + CO_2} \tag{3.28}$$

$$\mathrm{C + H + M \leftrightarrow CH^* + M} \tag{3.29}$$

Given the lack of a single, consistent set of chemical reactions and rate coefficients, four CH^* chemical sub-mechanisms, which include for reactions 3.26 to 3.29 the recommended rate coefficients of 1) Zhou et al. [135]; 2) Petersen et al. [181, 183, 184]; 3) Bozkurt, Fikri, and Schulz [185]; or 4) Smith et al. [178, 179] and Kathrotia et al. [186], are assembled. The rate coefficients

TABLE 3.3: Elementary reactions reported in the literature to produce CH^* along with their Arrhenius rate coefficients and specific rate evaluated at 1850 K, $k(T = 1850\ \mathrm{K})$.

Reaction	A [cm^3, mol, s]	n	E_a [cal/mol]	$k(T = 1850\ \mathrm{K})$ [cm^3, mol, s]	Ref.
$C_2 + OH \leftrightarrow CH^* + CO$	$2.00 \cdot 10^{14}$	0	0	$2.00 \cdot 10^{14}$	[181, 183–185]
	$1.11 \cdot 10^{13}$	0	0	$1.11 \cdot 10^{13}$	[178, 186]
$C_2H + O \leftrightarrow CH^* + CO$	$5.20 \cdot 10^{11}$	0	2600	$2.56 \cdot 10^{11}$	[181, 183, 184]
	$3.64 \cdot 10^{12}$	0	2605	$1.79 \cdot 10^{12}$	[185]
	$6.20 \cdot 10^{12}$	0	0	$6.20 \cdot 10^{12}$	[135, 178]
	$6.02 \cdot 10^{12}$	0	457	$5.32 \cdot 10^{12}$	[187]
	$2.50 \cdot 10^{12}$	0	0	$2.50 \cdot 10^{12}$	[179, 186]
	$1.08 \cdot 10^{13}$	0	0	$1.08 \cdot 10^{13}$	[188]
$C_2H + O_2 \leftrightarrow CH^* + CO_2$	0	0	0	0	[181, 183–185]
	$4.10 \cdot 10^{13}$	0	4500	$1.21 \cdot 10^{13}$	[178]
	$6.02 \cdot 10^{-4}$	4.4	-2285	$2.66 \cdot 10^{11}$	[187]
	$2.17 \cdot 10^{10}$	0	0	$2.17 \cdot 10^{10}$	[135, 188]
	$3.20 \cdot 10^{11}$	0	1600	$2.07 \cdot 10^{11}$	[179, 186]
$C + H + M \leftrightarrow CH^* + M$	$3.63 \cdot 10^{13}$	0	0	$3.63 \cdot 10^{13}$	[178, 181, 183, 184, 186]
	$6.00 \cdot 10^{14}$	0	6940	$9.08 \cdot 10^{13}$	[135]

of non-radiative collisional quenching are calculated using the parameters provided in [169, 170]. Reactions 3.26 to 3.29 involve the C and C_2 species, which are not included in the SD mechanism. Additional reactions accounting for their formation and consumption, obtained from [65] for C reactions and [178, 181, 183, 184] for C_2 reactions, are included in the CH^* chemical sub-mechanisms. The database of transport properties of the SD mechanism only missed data for CH^*, which are set equal to those for ground state CH. Thermodynamic properties are also required for C_2 and CH^*, and are taken from [189] and [135], respectively. The rate coefficients and reactions included in the sub-mechanisms are summarized in Table 3.4.

Table 3.5 presents the mole fraction, X_{CH^*}, number density, N_{0,CH^*}, and rate of production, q_{f,CH^*}, of CH^* at the location of maximum CH concentration in the freely propagating, premixed methane-air flame simulated with the SD mechanism supplemented with the four CH^* sub-mechanisms. Predictions of number density and rate of production vary over more than one order of magnitude. The sub-mechanism of Smith et al. [178, 179] and Kathrotia et al. [186] is used for the current assessment as it provides the largest values of N_{0,CH^*} and q_{f,CH^*}, which should have the most significant impact on the LIF process.

As in section 3.2.4.1, simple, algebraic terms are sought to be added to the set of ODEs of the

TABLE 3.4: Elementary reactions and corresponding Arrhenius rate coefficients added to the San Diego mechanism [128] to predict [CH^*].

Reaction	A [cm^3, mol, s]	n	E_a [cal/mol]	Ref.
C reactions				
$H + CH \leftrightarrow C + H_2$	$1.650 \cdot 10^{14}$	0	0	[65]
$C + O_2 \leftrightarrow O + CO$	$5.800 \cdot 10^{13}$	0	576.0	[65]
$C + CH_2 \leftrightarrow H + C_2H$	$5.000 \cdot 10^{13}$	0	0	[65]
$C + CH_3 \leftrightarrow H + C_2H_2$	$5.000 \cdot 10^{13}$	0	0	[65]
$OH + C \leftrightarrow H + CO$	$5.000 \cdot 10^{13}$	0	0	[65]
C_2 reactions				
$C_2 + H_2 \leftrightarrow C_2H + H$	$4.000 \cdot 10^{5}$	2.40	1000	[178, 181, 183, 184]
$CH + CH \leftrightarrow C_2 + H_2$	$5.000 \cdot 10^{12}$	0	0	[178, 181, 183, 184]
$C + C + M \leftrightarrow C_2 + M$	$3.000 \cdot 10^{14}$	0	−1000	[178, 181, 183, 184]
$C + CH \leftrightarrow C_2 + H$	$5.000 \cdot 10^{13}$	0	0	[178, 181, 183, 184]
$O + C_2 \leftrightarrow C + CO$	$5.000 \cdot 10^{13}$	0	0	[178, 181, 183, 184]
$C_2 + O_2 \leftrightarrow CO + CO$	$9.000 \cdot 10^{12}$	0	980.0	[178, 181, 183, 184]
CH^* reactions				
$C_2H + O \leftrightarrow CO + CH^*$	—	—	—	see Table 3.3
$C + H + M \leftrightarrow CH^* + M$	—	—	—	see Table 3.3
$C_2 + OH \leftrightarrow CO + CH^*$	—	—	—	see Table 3.3
$C_2H + O_2 \leftrightarrow CO_2 + CH^*$	—	—	—	see Table 3.3
Non-radiative, collisional quenching				
$CH^* + H_2O \leftrightarrow CH + H_2O$	$3.064 \cdot 10^{12}$	0.50	0	[170]
$CH^* + CO \leftrightarrow CH + CO$	$2.440 \cdot 10^{12}$	0.50	0	[169]
$CH^* + CO_2 \leftrightarrow CH + CO_2$	$2.410 \cdot 10^{-1}$	4.30	−1694	[169]
$CH^* + O_2 \leftrightarrow CH + O_2$	$2.480 \cdot 10^{06}$	2.14	−1720	[169]
$CH^* + H_2 \leftrightarrow CH + H_2$	$4.048 \cdot 10^{12}$	0.50	1363	[170]
$CH^* + CH_4 \leftrightarrow CH + CH_4$	$1.730 \cdot 10^{13}$	0	167.0	[169]
$CH^* + N_2 \leftrightarrow CH + N_2$	$4.496 \cdot 10^{07}$	1.73	1038	[170]
Spontaneous emission				
$CH^* \leftrightarrow CH + h\nu$	$1.818 \cdot 10^{06}$	0	0	This study with [150]

four-level LIF model. Figure 3.11 presents the overall (net) rate of production, and the rates of production and consumption of electronically excited methylidyne. The profiles of q_{f,CH^*} and q_{c,CH^*} almost exactly agree and, therefore, CH^* can be assumed in quasi-steady state. As per the mathematical development presented in equations 3.23 to 3.25, the terms $q_{f,CH^*} \cdot (f_{B,N_{2a}} - {}^{N_{2a}}/_{N_{0,CH^*}})$ and $q_{f,CH^*} \cdot (1 - f_{B,N_{2a}} - {}^{N_{2b}}/_{N_{0,CH^*}})$ are added to the ODEs describing the rate of change of number density in levels $2a$ and $2b$, respectively, to account for the interactions of the flame chemistry

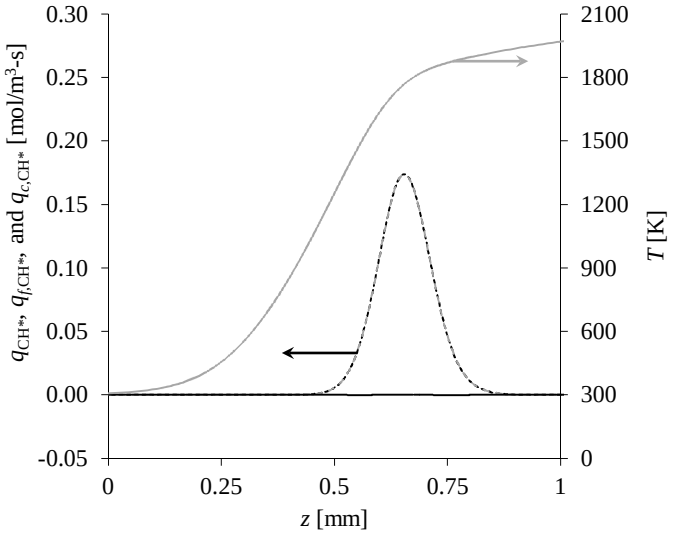

FIGURE 3.11: Net rate of production (solid black curve), rates of production (black dashed curve) and consumption (grey dashed curve) of electronically excited methylidyne, and temperature (solid grey curve) in a freely propagating, laminar, premixed CH_4-air flame at stoichiometric conditions.

with the electronically excited state:

$$\begin{aligned}\frac{\mathrm{d}N_{2a}}{\mathrm{d}t} = \dot{N}_{2a} =& N_{1a} \cdot b_{12} - N_{2a} \cdot (b_{21} + R_{2a2b}) + N_{2b} \cdot R_{2b2a} \\ &+ \boldsymbol{q_{f,\mathrm{CH^*}}} \cdot \left(\boldsymbol{f_{\mathrm{B},N_{2a}}} - \frac{\boldsymbol{N_{2a}}}{\boldsymbol{N_{0,\mathrm{CH^*}}}} \right),\end{aligned} \tag{3.30}$$

and,

$$\frac{\mathrm{d}N_{2b}}{\mathrm{d}t} = \dot{N}_{2b} = - N_{2b} \cdot R_{2b2a} + N_{2a} \cdot R_{2a2b} + \boldsymbol{q_{f,\mathrm{CH^*}}} \cdot \left(\mathbf{1} - \boldsymbol{f_{\mathrm{B},N_{2a}}} - \frac{\boldsymbol{N_{2b}}}{\boldsymbol{N_{0,\mathrm{CH^*}}}} \right). \tag{3.31}$$

Because laser irradiation increases the number density in levels $2a$ and $2b$, it follows that these

TABLE 3.5: Mole fraction, $X_{\mathrm{CH^*}}$, number density, $N_{0,\mathrm{CH^*}}$, and rate of production of CH*, $q_{f,\mathrm{CH^*}}$, predicted by the four sub-mechanisms at the location of maximum CH mole fraction.

CH* sub-mechanism	$X_{\mathrm{CH^*}}$ [ppb]	$N_{0,\mathrm{CH^*}}$ [$\mathrm{m^{-3}}$]	$q_{f,\mathrm{CH^*}}$ [$\mathrm{m^{-3}s^{-1}}$]
Zhou et al. [135]	63.9	$2.61 \cdot 10^{14}$	$7.33 \cdot 10^{22}$
Petersen et al. [181, 183, 184]	6.34	$2.59 \cdot 10^{13}$	$7.08 \cdot 10^{21}$
Bozkurt, Fikri, and Schulz [185]	20.9	$8.52 \cdot 10^{13}$	$2.30 \cdot 10^{22}$
Smith et al. [178, 179] and Kathrotia et al. [186]	87.9	$3.59 \cdot 10^{14}$	$9.87 \cdot 10^{22}$

terms are negative, *i.e.*, $\mathrm{CH^*}$ molecules are consumed, during the LIF process. It must be noted that the terms related to spontaneous emission (A_{2a1a}, A_{2a1b} and A_{2b1}) and non-radiative collisional quenching (Q_{21}) do not appear in equations 3.30 and 3.31. As these processes are now included in the flame simulation, they are actually accounted for in the terms added to the ODEs.

The principal assumption made in section 3.2.4.1 to develop these additional terms is that the concentrations of the collisional partners in the reactions consuming and forming the species of interest, here $\mathrm{CH^*}$, are constant throughout the LIF process. At the end of the laser pulse, the four-level LIF model without chemical reactions predicts a total number density in the electronically excited state $(N_{2a} + N_{2b})$ of $3.65 \cdot 10^{16}\ \mathrm{m^{-3}}$, which is ~100 times higher than the number density of $\mathrm{CH^*}$ predicted by the flame simulation ($N_{0,\mathrm{CH^*}} = 3.59 \cdot 10^{14}\ \mathrm{m^{-3}}$). Such an increase could be expected to cause a significant change in the concentration of other species involved in the formation and consumption of electronically excited methylidyne.

$\mathrm{CH^*}$ is principally consumed via quenching through collisions with major species, *e.g.*, $\mathrm{H_2O}$, $\mathrm{N_2}$, $\mathrm{CO_2}$, $\mathrm{O_2}$, etc., and a change, even important, in the number density of a very minor species, such as $\mathrm{CH^*}$, will not impact their concentration to any significant extent. Also, inspection of the output of the flame simulation revealed that the reaction $\mathrm{C + H + M \leftrightarrow CH^* + M}$ is actually consuming $\mathrm{CH^*}$ molecules. In this case, $\mathrm{CH^*}$ is dissociated through collisions with any other species, and the concentration [M] in the calculation of the reaction rate is that of the mixture, which is independent of its composition.

$\mathrm{CH^*}$ is produced by reactions 3.26, 3.27, and 3.28, accounting for ~0.5%, ~27%, and ~72.5% of its total rate of production, respectively. To assess if an increase of two orders of magnitude in $[\mathrm{CH^*}]$ under laser irradiation could significantly raise the concentrations of $\mathrm{C_2}$ and $\mathrm{C_2H}$, the overall (net) production rate of these two species is compared to the backward rate of reactions 3.26 to 3.28, $\omega_{\mathrm{b},i}$, magnified by a factor of 100 in Table 3.6. For the reactions 3.27 and 3.28, $\omega_{\mathrm{b},i} \cdot 100$ is 237 and 1878 times smaller, respectively, than the overall production rate of $\mathrm{C_2H}$, $q_{\mathrm{C_2H}}$, which is the source term in the species conservation equation [180, 190, 191]. Therefore, it is very unlikely that the increase in $[\mathrm{CH^*}]$, leading to a rise in the backward rate of reactions 3.27 and 3.28, would cause a significant change in the concentration of $\mathrm{C_2H}$. In contrast, $\omega_{\mathrm{b},i} \cdot 100$ for reaction 3.26 is only 7 times smaller than $q_{\mathrm{C_2}}$. Consequently, the increase in the concentration of electronically excited methylidyne during laser irradiation could lead to a moderate, but non-negligible, rise in the concentration of $\mathrm{C_2}$, which would raise the forward rate of reaction 3.26. However, since it only contributes to ~0.5% of the total rate of production of $\mathrm{CH^*}$, a slight increase in the forward rate of this reaction should not significantly change the value $q_{f,\mathrm{CH^*}} = 9.87 \cdot 10^{22}\ \mathrm{m^{-3} \cdot s^{-1}}$ used in this assessment.

Equation 3.32 presents the ODE describing the rate of change of the population in state $1a$. It

TABLE 3.6: Comparison of the overall production rates of C_2H and C_2, q_j, to the backward rate of the reactions 3.26, 3.27, and 3.28, magnified by a factor of 100 ($\omega_{\mathrm{b},i} \cdot 100$).

Species j	q_j [mol·m^{-3}·s^{-1}]	Reaction i	$\omega_{\mathrm{b},i} \cdot 100$ [mol·m^{-3}·s^{-1}]
C_2H	$3.08 \cdot 10^{-1}$	$C_2H + O_2 \leftrightarrow CO_2 + CH^*$ (3.28)	$1.64 \cdot 10^{-4}$
		$C_2H + O \leftrightarrow CO + CH^*$ (3.27)	$1.30 \cdot 10^{-3}$
C_2	$6.53 \cdot 10^{-4}$	$C_2 + OH \leftrightarrow CH^* + CO$ (3.26)	$9.31 \cdot 10^{-5}$

consists of equation 3.1, supplemented with the term accounting for chemical reactions replenishing the ground state (first bold term, see equation 3.25). Prior to the laser pulse, the chemically produced CH^* molecules in state $2a$ undergo spontaneous emission (A_{2a1a}) and fill state $1a$. In order for the number density not to build up, an additional term consuming CH molecules in the $1a$ state must be added to equation 3.32 (second bold term). It is assumed that CH is consumed through bimolecular reactions with other species, such that this additional term is linearly dependent on N_{1a}. As shown in equation 3.32, N_{1a} is multiplied by an invariable rate constant defined as the ratio of the rate of transfer per unit volume of molecules from levels $2a$ to $1a$ via spontaneous emission prior to the laser pulse (*i.e.*, the initial number density in level $2a$ multiplied by A_{2a1a}), to the initial number density in state $1a$. This formulation assumes that the concentration of the reaction partners and the specific rate of the reactions consuming CH are constant during the LIF process. This additional term in equation 3.32 ensures that $\dot{N}_{1a}$ is null prior to, and a long time after, the laser pulse; it exactly compensates for the term $N_{2a} \cdot A_{2a1a}$, which is non-zero initially as molecules are provided to level $2a$, even without laser irradiation, through chemical reactions.

$$\begin{aligned}\frac{\mathrm{d}N_{1a}}{\mathrm{d}t} = \dot{N}_{1a} = &- N_{1a} \cdot b_{12} + N_{2a}\,(b_{21} + A_{2a1a}) - N_{1a} \cdot R_{1a1b} + N_{1b} \cdot R_{1b1a} \\ &+ \boldsymbol{q_{f,\mathrm{CH}} \cdot \left(f_{\mathrm{B},N_{1a}} - \frac{N_{1a}}{N_{0,\mathrm{CH}}} \right)} \\ &- \boldsymbol{N_{1a} \cdot \underbrace{\frac{N_{0,\mathrm{CH^*}} \cdot f_{\mathrm{B},N_{2a}} \cdot A_{2a1a}}{f_{\mathrm{B},N_{1a}} \cdot N_{0,\mathrm{CH}}}}_{\text{rate constant [s}^{-1}\text{]}}}\end{aligned} \tag{3.32}$$

The ODE describing the rate of change of number density in level $1b$ is shown in equation 3.33. It consists of equation 3.2 to which the term accounting for chemical reactions replenishing the ground state (see equation 3.25) is added, as well as a consumption term that accounts for the filling of state $1b$ induced by spontaneous emission and collisional quenching from states $2a$ and $2b$ populated, even without laser irradiation, by chemical reactions. As in equation 3.32, this

additional term is made of an invariable rate constant, which is multiplied by N_{1b}. It ensures that $\dot{N}_{1b}$ is null at $t = 0$, and at the limit $t \to \infty$.

$$\begin{aligned}\frac{\mathrm{d}N_{1b}}{\mathrm{d}t} = \dot{N}_{1b} =& N_{2a} \cdot (A_{2a1b} + Q_{2a1}) + N_{2b} \cdot (A_{2b1} + Q_{2b1}) + N_{1a} \cdot R_{1a1b} - N_{1b} \cdot R_{1b1a} \\ &+ \boldsymbol{q_{f,\mathrm{CH}}} \cdot \left[(\mathbf{1} - \boldsymbol{f_{\mathrm{B},N_{1a}}}) - \frac{\boldsymbol{N_{1b}}}{\boldsymbol{N_{0,\mathrm{CH}}}} \right] \\ -\boldsymbol{N_{1b}} \cdot & \underbrace{\frac{[\boldsymbol{N_{0,\mathrm{CH^*}}} \cdot \boldsymbol{f_{\mathrm{B},N_{2a}}} \cdot (\boldsymbol{A_{2a1b}} + \boldsymbol{Q_{2a1}}) + \boldsymbol{N_{0,\mathrm{CH^*}}} \cdot (\mathbf{1} - \boldsymbol{f_{\mathrm{B},N_{2a}}}) \cdot (\boldsymbol{A_{2b1}} + \boldsymbol{Q_{2b1}})]}{(\mathbf{1} - \boldsymbol{f_{\mathrm{B},N_{1a}}}) \cdot \boldsymbol{N_{0,\mathrm{CH}}}}}_{\text{rate constant [s}^{-1}\text{]}}\end{aligned} \tag{3.33}$$

The set of ODEs of equations 3.30 to 3.33 is solved with the Runge-Kutta solver of Matlab. The initial conditions on (N_{1a}, N_{1b}, N_{2a}, N_{2b}) are $(N_{0,\mathrm{CH}} \cdot f_{\mathrm{B},N_{1a}},\ N_{0,\mathrm{CH}} \cdot (1 - f_{\mathrm{B},N_{1a}}), N_{0,\mathrm{CH^*}} \cdot f_{\mathrm{B},N_{2a}}$, $N_{0,\mathrm{CH^*}} \cdot (1 - f_{\mathrm{B},N_{2a}}))$. The value of $N_{0,\mathrm{CH}}$ is the same as in the previous sections. Figure 3.12 presents the population in the four levels, along with the solution of the four-level LIF model without chemical reactions.

Comparing to Figure 3.10, the effects of the $\mathrm{CH^*}$ chemistry on the ground state populations are negligible. In fact, when drawn on the same figure, the populations predicted by the four-level LIF model only including chemical reactions in the ground state, and in both, $\mathrm{A^2\Delta}$ and $\mathrm{X^2\Pi}$, electronic energy levels are almost undistinguishable (not shown in Figure 3.12 for the sake of clarity). The main, but limited, effect of the $\mathrm{CH^*}$ chemistry is to increase the number density in levels $2a$ and $2b$, which leads to a rise in the number of emitted photons per unit volume, N_p, of ~3% ($6.39 \cdot 10^{14}\ \mathrm{m^{-3}}$ vs. $6.21 \cdot 10^{14}\ \mathrm{m^{-3}}$ for the LIF model excluding chemical reactions). However, as discussed in section 2.3, a fluorescence signal measured at an off-resonance laser wavelength is subtracted from the on-resonance LIF signal during the experiments to remove, among others, the effect of flame chemiluminescence. Integrated over the camera gate time of 30 ns, the initial population in the $\mathrm{A^2\Delta}$ state is predicted to emit a total number of photons of $1.91 \cdot 10^{12}\ \mathrm{m^{-3}}$ via chemiluminescence. It follows that the net number of photons emitted per unit volume is $N_\mathrm{p} = 6.39 \cdot 10^{14} - 1.91 \cdot 10^{12} = 6.20 \cdot 10^{14}\ \mathrm{m^{-3}}$, which agrees within ~$0.1\%$ with the value of N_p obtained with the four-level LIF model excluding chemical reactions. Consequently, the interactions of the LIF model with the flame chemistry in both, $\mathrm{X^2\Pi}$ and $\mathrm{A^2\Delta}$, states can be neglected for the current study. In the remainder, the time-resolved, four-level LIF model is employed to process the output of flame simulations into numerical LIF signals using the methodology presented in the next section.

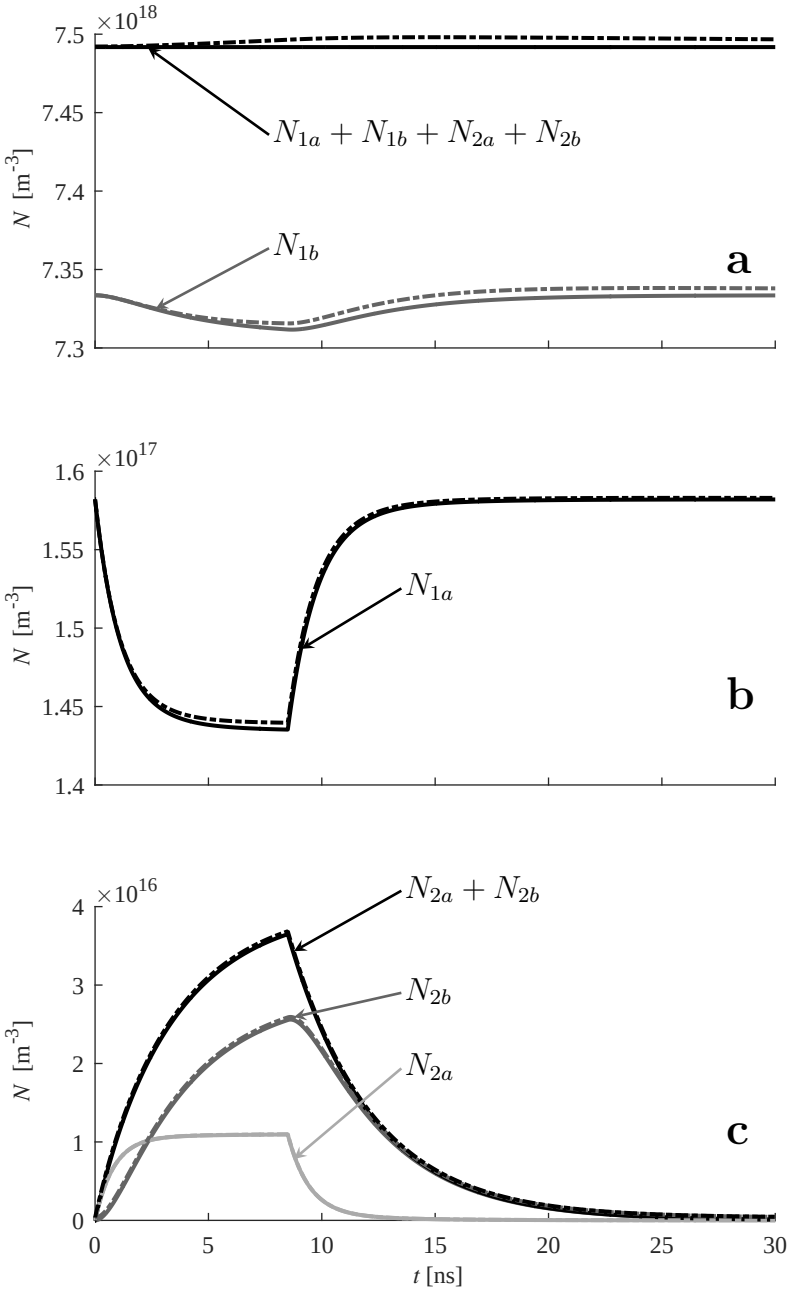

FIGURE 3.12: Predicted populations by the four-level LIF model isolated from the flame chemistry (solid curves), and supplemented with chemical reactions interacting with the ground and electronically excited states (dashed-dotted curves).

3.3 LIF signal prediction using the time-resolved, four-level LIF model

For each grid point of the flame simulations, the temporal evolution of the population in each of the four levels is computed by solving the set of ODEs of equations 3.1 to 3.4. The modelled LIF signal, S_{LIF} [count], is obtained by inserting $N_{2a}(t)$ and $N_{2b}(t)$ in equation 3.34 developed based on the theory presented in [117], where τ_{cam} [s] is the camera exposure time, Ω [sr] is the solid angle, V [m^3] is the probe volume, C_{opt} [count/photon] is the optical collection constant, and $\tau_{\lambda,\mathrm{LIF}}$ is the average transmissivity of the bandpass filter over the emission spectrum.

$$S_{\mathrm{LIF}} = \underbrace{\int_0^{\tau_{\mathrm{cam}}} \sum_{i,j} N_{2i}(t) \cdot A_{2i1j}\, \mathrm{d}t}_{N_{\mathrm{p}},\ \text{see equation 3.22}} \cdot \frac{\Omega}{4\pi} \cdot V \cdot C_{\mathrm{opt}} \cdot \tau_{\lambda,\mathrm{LIF}} \tag{3.34}$$

$\tau_{\lambda,\mathrm{LIF}}$ is provided by equation 3.35, where $\tau_{\mathrm{Filter}}(\lambda)$ is the wavelength-resolved filter transmissivity (maximum transmissivity normalized to 1), and $Y_{\mathrm{E}}(\lambda)$ is the spontaneous emission spectrum normalized such that its integral is unity. A filter transmissivity curve, measured using a Varian Cary 500 spectrophotometer, was provided by the manufacturer. In this work, it was compared to a second curve obtained using an Agilent Cary 5000 spectrophotometer. The trend of both curves is similar, but slight variations in the absolute values of τ_{Filter} are observed. The transmissivity curve in equation 3.35 is taken as the average of the two sets of measurements. Through the LIF process, the population distribution in the $\mathrm{A}^2\Delta$ electronic energy level changes from being mostly in the $2a$ rotational state for small values of t, to a partially distributed population between the $2a$ and $2b$ states. The emission spectrum, $Y_{\mathrm{E}}(\lambda)$, is then extracted from LIFBASE assuming a bulk gas temperature of 1800 K, 32% of the electronically excited molecules in the $2a$ state (a fraction calculated near the end of the laser pulse), and a fully equilibrated population distribution within the $2b$ rotational manifold. This yields $\tau_{\lambda,\mathrm{LIF}} = 37.6\%$ for the current experimental configuration.

$$\tau_{\lambda,\mathrm{LIF}} = \int_{-\infty}^{\infty} \tau_{\mathrm{Filter}}(\lambda) \cdot Y_{\mathrm{E}}(\lambda) d\lambda \tag{3.35}$$

As explained in Chapter 2, the LIF signal is normalized by the Rayleigh scattering signal of nitrogen, S_{R}, to yield a surrogate, quantitative measurement of CH number density. At each grid point of the flame computational domain, S_{LIF} (equation 3.34) is divided by S_{R} [count], which is

modelled as:

$$S_{\mathrm{R}} = \left[\left(\frac{\partial \sigma}{\partial \Omega} \right)_{\mathrm{N_2}} - \left(\frac{\partial \sigma}{\partial \Omega} \right)_{\mathrm{He}} \right] \cdot N \cdot \frac{I \cdot \tau_{\mathrm{R}}}{h\nu} \cdot \Omega \cdot V \cdot C_{\mathrm{opt}} \cdot \tau_{\lambda,\mathrm{R}}, \tag{3.36}$$

where $\left(\frac{\partial \sigma}{\partial \Omega}\right)$ [m^2/sr] is the Rayleigh scattering cross-section calculated according to [174], N [m^{-3}] is the number density, I [W/m^2] is the irradiance, τ_{R} [s] is the duration of the Rayleigh scattering signal corresponding in practice to the laser pulse temporal width, $h\nu$ [J] is the energy of a photon, and $\tau_{\lambda,\mathrm{R}}$ is the transmissivity of the bandpass filter at the on-resonance wavelength. Ω, V, and C_{opt} are equal in equations 3.34 and 3.36, which implies that these optical parameters do not appear in the modelled $S_{\mathrm{LIF}}/S_{\mathrm{R}}$ ratios. In the end, an axial profile of $S_{\mathrm{LIF}}/S_{\mathrm{R}}$ is obtained. Examples are provided in Figure 3.13 (see the grey-dashed curves) for lean *n*-butane, stoichiometric methane, and rich ethane stagnation flames simulated with the USC and SD thermochemical mechanisms.

The numerical, axial profiles of LIF-to-Rayleigh ratio cannot be directly compared to the experimental data. At atmospheric pressure, CH exists in a thin, sub-millimetric layer (see the experimental data points in Figure 3.13). Due to the effects of diffraction and possible aberrations introduced by the collection optics [192], the measured width of the CH-LIF profile is generally larger than the actual CH layer thickness [79, 80, 101]. To account for imaging-system blur, the simulated LIF profiles are corrected through convolution with a point-spread function (PSF), which is an intrinsic property of the light collection setup [192]. The PSF is theoretically described by the Airy distribution, which can be accurately approximated using a Gaussian distribution [193] normalized so as to conserve the radiative energy of the LIF signal. The full width at half maximum of the PSF ($\delta_{\mathrm{PSF}} = 0.124 \pm 0.009$ mm) is determined by taking the average of the width of the Gaussian PSF-distributions needed to reconcile the CH-LIF layer thicknesses predicted by the four mechanisms (SD, USC, NUIG, and GRI) with the experimental data obtained in the same apparatus for the stoichiometric, preheated ($T_{\mathrm{inlet}} = 355$ K), $\mathrm{CH_4}$-air flame presented in [64]. This methodology assumes that the thermochemical mechanisms accurately predict the width of the CH layer, hence the reaction zone thickness, of stoichiometric methane-air flames. From flame theory [190], the reaction zone thickness (l_{R}) is known to be directly and inversely proportional to the thermal diffusivity (α) and flame speed (S_{L}), respectively ($l_{\mathrm{R}} \propto \alpha / S_{\mathrm{L}}$). Considering the demonstrated adequacy of most modern thermochemical mechanisms at predicting the flame speed of stoichiometric $\mathrm{CH_4}$-air mixtures [68, 90, 134], it is expected that both, S_{L} and α, are properly modelled, and that the CH layer thickness is accurately predicted for methane-air flames at $\phi = 1$.

Figure 3.13 presents raw (uncorrected, grey dashed curves) and PSF-corrected (solid grey

curves) numerical $S_{\mathrm{LIF}}/S_{\mathrm{R}}$ profiles for lean *n*-butane, stoichiometric methane, and rich ethane-air flames obtained with the USC and SD mechanisms. Absolute LIF profiles are shown in the upper part of the figure (plots a-c), and profiles normalized by the maximum value of $S_{\mathrm{LIF}}/S_{\mathrm{R}}$ are shown in the lower row (plots d-f) to better assess their shape. The consistent under-prediction of the LIF profile thickness is clearly observed in Figure 3.13 (d-f) where the uncorrected simulated data lie within the experimentally measured profile (solid squares) for all considered flames. Correcting for the blurring effect induced by the collection optics significantly improves the numerical predictions with the PSF-corrected profiles almost perfectly agreeing with the experimental data.

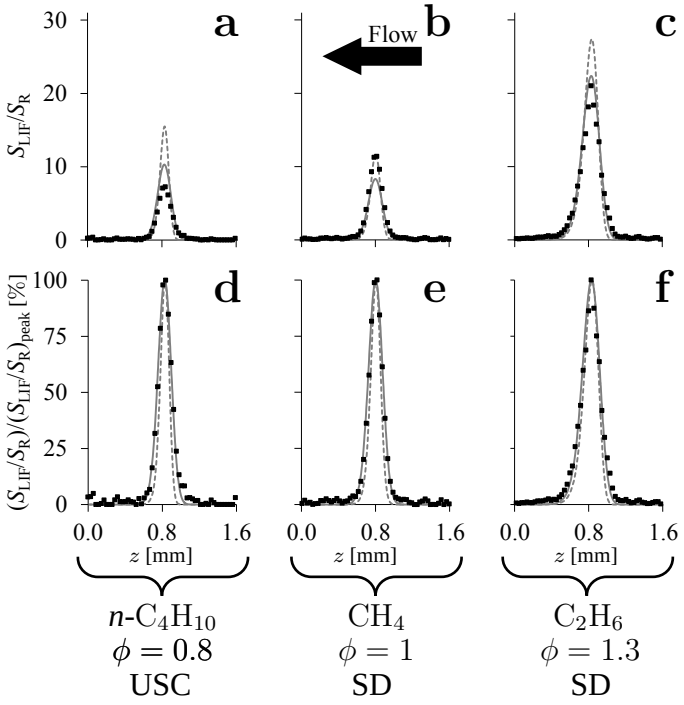

FIGURE 3.13: Absolute (top) and normalized (bottom) axial profiles of LIF-to-Rayleigh ratio for $\phi = 0.8$ *n*-butane, $\phi = 1.0$ methane, and $\phi = 1.3$ ethane stagnation flames simulated with the USC and SD mechanisms. Flow from right to left. Legend: ■ exp., ------ PSF-uncorrected (raw) numerical profiles, and —— PSF-corrected numerical profiles.

In addition to its broadening effect, the PSF-correction reduces the amplitude of the $S_{\mathrm{LIF}}/S_{\mathrm{R}}$ profiles as shown in Figure 3.13 (a-c). The effect is particularly pronounced for thin flames; the thinner the flame, the larger the relative reduction in the peak value of $S_{\mathrm{LIF}}/S_{\mathrm{R}}$ induced by the PSF correction. For the lean-butane and rich-ethane flames (plots a & c), including the point-spread function brings the simulated profiles in closer and almost perfect agreement with the experiments, respectively. For the stoichiometric methane case, it could be concluded from the uncorrected data that the SD mechanism exactly predicts CH formation. However, the PSF-corrected profile instead

indicates that this model slightly under-predicts the maximum value of $S_{\mathrm{LIF}}/S_{\mathrm{R}}$ in comparison to the experiments. These results demonstrate the absolute necessity to perform the PSF-correction in the reduction of flame simulations into LIF signals to properly assess the predictive capability of thermochemical mechanisms. This is true not only on a quantitative basis, but also in terms of the relative trend of $S_{\mathrm{LIF}}/S_{\mathrm{R}}$ vs. ϕ as the amplitude of the correction depends on the flame thickness, which varies with the equivalence ratio as shown and discussed in Chapter 4.

3.4 Uncertainty analysis of the time-resolved, four-level LIF model

The error in the predicted, PSF-corrected, LIF-to-Rayleigh ratios has four main contributors: the error in the [CH] predictions by the flame simulations caused by improper Arrhenius rate coefficients, the error in the BCs of the flame simulations propagated through the flame and LIF models, the uncertainty in the PSF correction, and inaccuracies in the LIF model. To allow for an optimization of the thermochemical models, the uncertainties in the experimentally measured data and in the response of the LIF model must be of minor importance in comparison to the error induced by the uncertain Arrhenius rate coefficients included in the mechanisms. The current section aims to provide an estimation of the uncertainty related to the time-resolved, four-level LIF model. It is expected to properly reproduce the physics of the LIF process, and the overall uncertainty is assumed to be only related to inaccurate descriptions of the parameters. In the following, a sensitivity analysis is presented to identify the principal factors influencing the response of the LIF model. Then, uncertainties are attributed to the parameters and, along with a 50,000 samples Monte-Carlo analysis, provide the estimated accuracy of the LIF model. The analysis is based on the solution, at the location of maximum CH concentration, of the freely propagating, premixed, methane-air flame simulated with the SD model described above.

The logarithmic sensitivity of $S_{\mathrm{LIF}}/S_{\mathrm{R}}$ to a given parameter of the LIF model with a nominal value x_j is defined by equation 3.37. For each parameter, a population of 1,000 samples is assembled by computing $S_{\mathrm{LIF}}/S_{\mathrm{R}}$ for uniformly distributed values $\pm 30\%$ around x_j. The derivative of a 7^{th}-order polynomial, adjusted through a least-squares procedure to the response of the LIF model, provides the value for the partial derivative in the right-hand-side term of equation 3.37. The computed L.S. values are reported in Figures 3.14 and 3.15 presenting parameters independent

and dependent, respectively, on experimental procedures performed in the current work.

$$\text{L.S.}(x_j) = \frac{\partial \ln(\frac{S_{\text{LIF}}}{S_{\text{R}}})}{\partial \ln(x_j)} = \frac{\partial(\frac{S_{\text{LIF}}}{S_{\text{R}}})}{\partial x_j} \cdot \frac{x_j}{\frac{S_{\text{LIF}}}{S_{\text{R}}}} \tag{3.37}$$

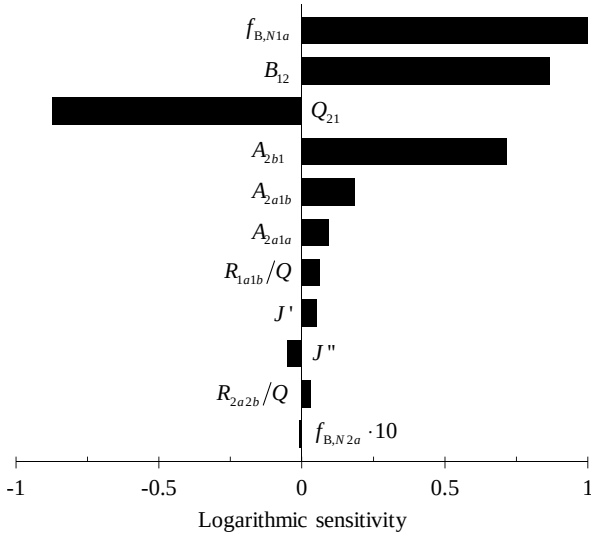

FIGURE 3.14: Logarithmic sensitivity to the experiment-independent model parameters.

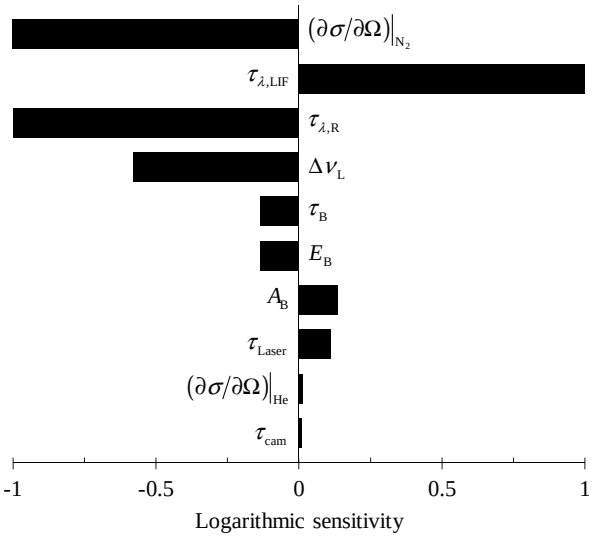

FIGURE 3.15: Logarithmic sensitivity to the experiment-dependent model parameters.

Considering the experiment-independent parameters, $S_{\text{LIF}}/S_{\text{R}}$ is most sensitive to the Boltzmann fraction in the laser-coupled ground state as the initial number density in state $1a$ is directly proportional to f_{B,N_1a}. It is followed by parameters relating to stimulated absorption, collisional quenching, and spontaneous emission. Taken separately, R_{1a1b} and R_{1b1a} have a significant influence on the response of the LIF model. However, as explained previously, they are linked together through equilibrium (see equation 3.11), which causes $S_{\text{LIF}}/S_{\text{R}}$ to be only weakly dependent on R_{1a1b}/Q_{21} as shown in Figure 3.14. The rate constant of RET in the electronically excited state (R_{2a2b}) also has a minor influence on the numerical fluorescence intensity.

As presented in Figure 3.15, $S_{\text{LIF}}/S_{\text{R}}$ is highly sensitive to the Rayleigh scattering cross-section of N_2, but not much to that of helium. This is caused by the Rayleigh cross-section of helium being only ~1.3% that of nitrogen, making $\left(\frac{\partial\sigma}{\partial\Omega}\right)_{\text{N}_2}$ the dominant parameter in the bracketed term of equation 3.36. S_{LIF} and S_{R} are directly proportional to the transmissivity of the bandpass filter over the emission spectrum, $\tau_{\lambda,\text{LIF}}$, and at the online laser wavelength, $\tau_{\lambda,\text{R}}$, respectively, which causes $\text{L.S.} \approx 1$ for these terms (-1 for $\tau_{\lambda,\text{R}}$ as it appears in the denominator of $S_{\text{LIF}}/S_{\text{R}}$). Raising $\Delta\nu_{\text{L}}$ results in an increase of the dimensionless overlap fraction, Γ, which is largely compensated by a lower spectral irradiance reducing the rate constant of photon absorption (see equation 3.5). This

is reflected by a L.S. to $\Delta\nu_{\mathrm{L}}$ of -0.58. In decreasing order of L.S. are then found the parameters related to the irradiance, I. As shown in equation 3.36, the Rayleigh scattering signal is linearly proportional to the irradiance. On the other hand, as discussed previously, S_{LIF} ($\propto N_{\mathrm{p}}$) is linearly proportional to I (or b_{12}) under very weak laser irradiation, and transitions as the irradiance is raised to become independent of I in the saturated LIF regime. It follows that at the two asymptotic limits of low and high laser energy, the logarithmic sensitivity of $S_{\mathrm{LIF}}/S_{\mathrm{R}}$ to the irradiance is 0 and -1, respectively. Therefore, the small L.S. values for the parameters related to I indicate a slightly non-linear response of S_{LIF} to changes in the irradiance. Finally, the model is relatively insensitive to the camera exposure time as it was made sufficiently long to capture the entire LIF signal during the experiments.

Figures 3.16 and 3.17 present the uncertainty of each parameter considered in the sensitivity analysis. The Boltzmann fractions and degeneracies extracted from LIFBASE [150] are assumed exact. As in [98, 101], an uncertainty of 5% is applied on the spectroscopic rate constants obtained from LIFBASE (B_{12}, A_{2a1a}, A_{2a1b}, and A_{2b1}). Calculations of A_{2b1} (see equation 3.9) with thermalized and non-thermalized electronically excited state populations at different temperatures (1500K, 1800K and 1900K) revealed that the error induced by the assumed distribution is negligible in comparison to the stated 5% uncertainty on the spectroscopic coefficients. An error range of $[-26.5\%; 33\%]$[6] is estimated for Q_{21} from the data of Renfro, Venkatesan, and Laurendeau [170] that compared computed quenching rate constants to experimentally measured ones in 77 counterflow, diffusion flames of methane. For the simulated, freely propagating flame discussed above, it was verified, at the location of maximum [CH], that more than 90% of the quenching rate constant is produced by species having a mole fraction within the range covered by the 77 flames in [170]. The lower bound of relative uncertainty in the ratio of RET to quenching rate constants in the ground and electronically excited states is taken as the maximum absolute experimental uncertainty in R_{kakb}/Q_{21} for various rotational levels in the $\mathrm{A}^2\Delta(v'=0)$ system [154] normalized by the nominal value used in this study ($R_{kakb}/Q_{21} = 2.83$). As explained above, the values of RET rate constant provided in [154] are likely significantly underestimated and, as such, an upper bound of uncertainty of 100% is applied on R_{1a1b} and R_{2a2b}.

The uncertainties in the experiment-dependent parameters presented in Figure 3.17 consider solely systematic errors. Random uncertainties are instead reflected by scatter in the experimental data reported using error bars in Figure 4.1. Data provided by manufacturers are assumed exact unless explicitly stated. Errors in the Rayleigh scattering cross-sections are caused by uncertainties

[6]The value of 33% is reported in Figure 3.16.

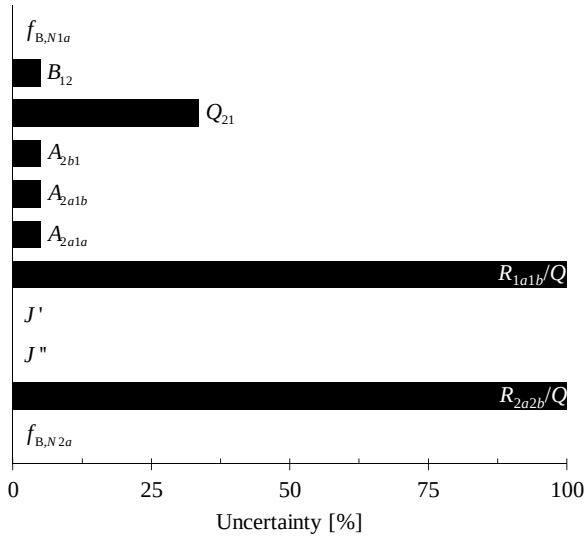

FIGURE 3.16: Uncertainty of the experiment-independent model parameters.

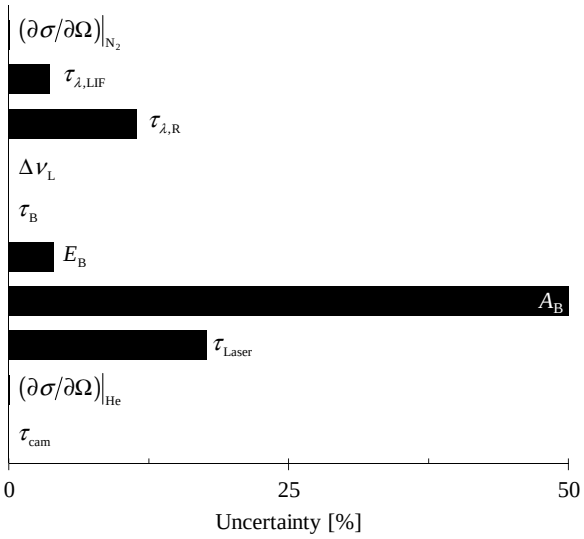

FIGURE 3.17: Systematic uncertainty of the experiment-dependent parameters.

in the refractive index of N_2 and He provided in [194], and by the error in interpolating the experimentally determined depolarization ratio of N_2 reported in [174], both contributions being very small. As discussed previously, the filter transmissivity curve, $\tau_{\mathrm{Filter}}(\lambda)$, is taken as the average of two sets of measurements obtained using Varian Cary 500 and Agilent Cary 5000 spectrophotometers. A relative uncertainty of 2.3% on the average transmissivity values allows to encompass the curves obtained using both devices. $\tau_{\lambda,\mathrm{R}}$ is obtained in an area of the filter transmissivity curve where $\tau_{\mathrm{Filter}}(\lambda)$ is rising. It follows that the uncertainty in the wavelength of the filter transmissivity curve amplifies the error estimation for $\tau_{\lambda,\mathrm{R}}$. Combined with the relative error on $\tau_{\mathrm{Filter}}(\lambda)$, this yields an uncertainty on $\tau_{\lambda,\mathrm{R}}$ of 11.5%. The uncertainty in $\tau_{\lambda,\mathrm{LIF}}$ has three contributors: the uncertainty on the wavelength of the filter transmissivity curve, the relative error of 2.3% on the values of $\tau_{\mathrm{Filter}}(\lambda)$, as well as the uncertainty related to the assumed emission spectrum in equation 3.35. The former is much less important than for $\tau_{\lambda,\mathrm{R}}$ as fluorescence is emitted at wavelengths covering the whole filter transmissivity curve, *i.e.*, in areas where $\tau_{\mathrm{Filter}}(\lambda)$ is stable, rising, and decreasing. The latter is estimated by inserting in equation 3.35 emission spectra corresponding to various population distributions in the electronically excited state, going from a thermalized system to all molecules in the $N' = 8$ rotational level. Taking the sum of squares of these three contributions provides an uncertainty on $\tau_{\lambda,\mathrm{LIF}}$ of 3.61%. The systematic error in the average laser energy per pulse, E_{B}, is taken as the arithmetical sum of the uncertainty in the detector calibration and the meter systematic error. As per Sirah Lasertechnik [195], the laser pulse duration remains unchanged through the dye laser and, as such, the error in τ_{Laser} is calculated from the specifications provided

by Spectra-Physics for the pumping, Quanta-Ray Pro-230 Nd:YAG laser. During the experiments, the beam area was measured by observing the light scattered by a graduated sheet of paper. Due to the diffuse edges of the laser sheet, the area could not be measured to a great level of accuracy, hence the systematic error estimation of 50%. Due to the resonant nature of photon absorption, the wavelength at which the laser is set, λ, has a very pronounced effect on the fluorescence signal. For that reason, the proper alignment of the laser wavelength to the $R_{1e}(7)$ transition was verified on a daily basis, such that the related systematic error is neglected. The dye laser adjustment has a limited repeatability (< 2 picometres), which induces random errors in λ because of the frequent back-and-forth shifts between the on- and off-resonance transition wavelengths. This is reflected by the scatter in the experimental data.

To determine the uncertainty of the LIF model, the value of $S_{\mathrm{LIF}}/S_{\mathrm{R}}$ at the location of maximum CH concentration predicted by the SD mechanism for the freely propagating flame discussed previously is calculated 50,000 times with the values of the parameters uniformly distributed over the ranges of uncertainty specified above. The histogram of Figure 3.18(a) presents the relative frequency of $S_{\mathrm{LIF}}/S_{\mathrm{R}}$, and Figure 3.18(b) the cumulative distribution, f. The $S_{\mathrm{LIF}}/S_{\mathrm{R}}$ ratios corresponding to $f = 2.5\%$ and $f = 97.5\%$, shown by the dashed red lines in Figure 3.18, are taken as the uncertainty limits. Normalized by the nominal value of LIF-to-Rayleigh ratio (red lines in Figure 3.18), this yields an accuracy for the LIF model, for an interval of confidence of 95%, of $[-26\%; 40\%]$, a range considered typical for the predictions presented in this work.

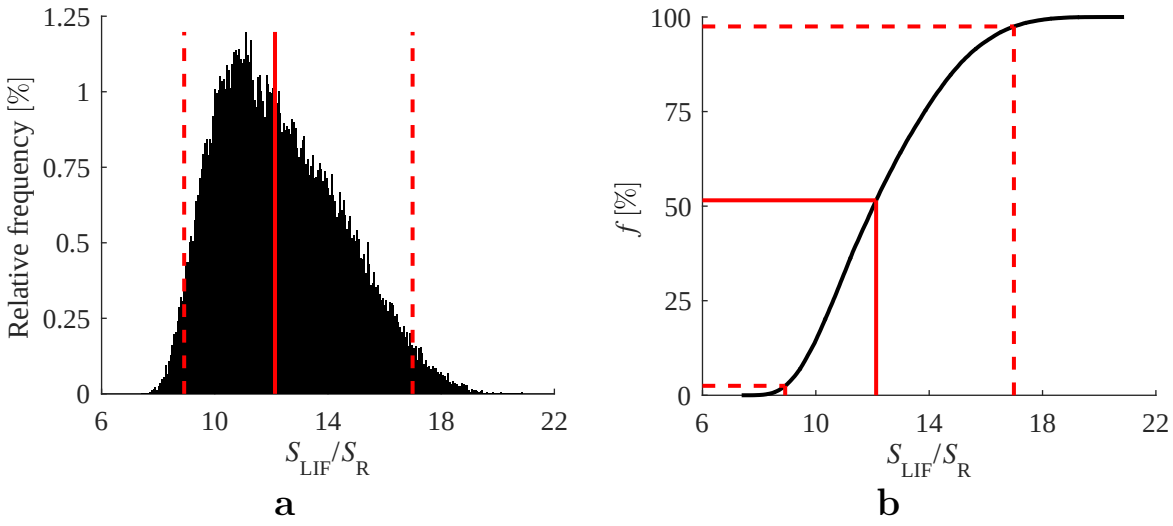

FIGURE 3.18: (a) Relative frequency of $S_{\mathrm{LIF}}/S_{\mathrm{R}}$, and (b) cumulative distribution function, f, obtained with the Monte-Carlo analysis. Legend: nominal LIF-to-Rayleigh ratio (solid red lines) and uncertainty limits (dashed red lines).

Chapter 4

Experimental results and comparison to flame simulations

4.1 Methylidyne concentration measurements

The Rayleigh-calibrated LIF diagnostic allows for an assessment of the accuracy of different thermochemical mechanisms in predicting CH formation. Although spatial profiles are measured and simulated (see Figure 3.13), it is more convenient to make the comparison using a single scalar value obtained from the CH-LIF profiles. Here, the maximum signal intensity is selected as a measure of CH production.

Figure 4.1 presents measured and predicted $S_{\mathrm{LIF}}/S_{\mathrm{R}}$ ratios (note the logarithmic scale). The error bars, obtained using the Student's t-distribution, correspond to a 95% interval of confidence for the variability in the measurements. CH production has a similar dependence on equivalence ratio for the four fuels considered in this study, suggesting that fuel-independent elementary reactions dominate CH production in these flames. For all fuels, the LIF signal reaches its maximum at $\phi = 1.2$, and monotonically decreases on both sides of the peak. The models generally capture the relative trend of the data, but predict a larger drop in $S_{\mathrm{LIF}}/S_{\mathrm{R}}$ as the stoichiometry is shifted to lean mixtures (except USC for $\mathrm{CH_4}$-air flames) as also observed in [79, 99]. Through saturated, relative LIF measurements in an atmospheric-pressure Bunsen burner, Sutton and Driscoll [99] found that the maximum CH-LIF signal for methane-air premixed flames occurs at $\phi = 1.25$, which is consistent with the current set of data. In contrast, they observed the peak CH-LIF signal intensity at $\phi = 1.35$ for propane-air flames. Considering the width of the error bars reported with their measurements, it is possible that the maximum LIF intensity occurs at $\phi = 1.25$, in better agreement with the present work.

For all fuels and equivalence ratios, there is significant variability in the predictions of the thermochemical mechanisms. The simulated values of $S_{\mathrm{LIF}}/S_{\mathrm{R}}$ are spread over more than an

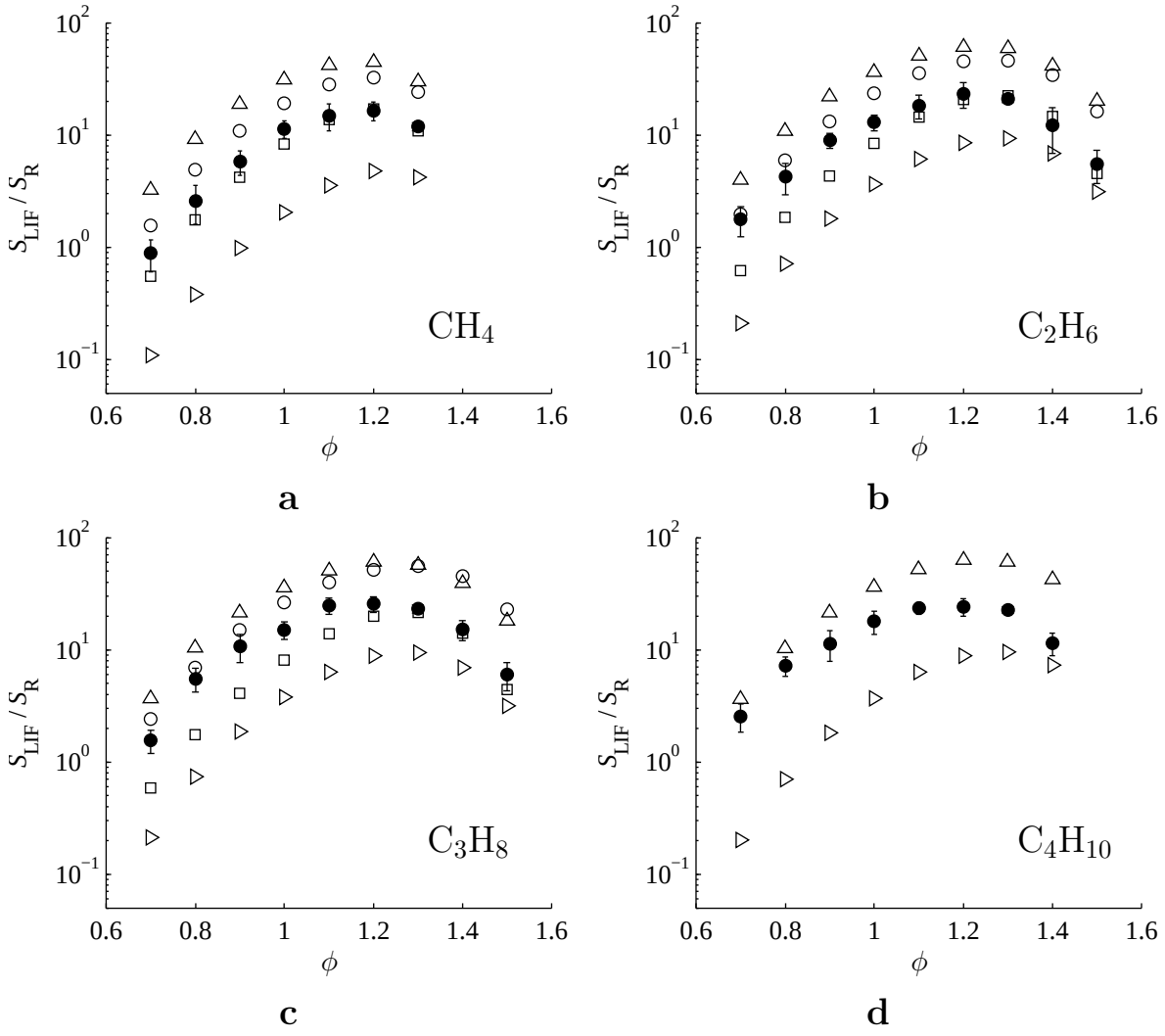

FIGURE 4.1: Measured and simulated values of maximum $S_{\mathrm{LIF}}/S_{\mathrm{R}}$ for (a) methane, (b) ethane, (c) propane, and (d) *n*-butane flames. Legend: • exp., ○ GRI, □ SD, △ USC, and ▷ NUIG.

order of magnitude indicating substantial differences in the chemistry (rate coefficients and/or included reactions) of the models. In increasing order of LIF-to-Rayleigh ratio, the mechanisms are generally sorted as NUIG, SD, GRI and USC, no matter the fuel. The kinetic rates governing this ordering, hence the variability in the predictions, must then be related to fuel-independent elementary reactions.

To assess the agreement of the simulations with the experiments, Figure 4.2 shows the simulated LIF-to-Rayleigh ratio normalized by its experimental counterpart at each equivalence ratio. Exact agreement of the numerical predictions with the experimental data would yield a value

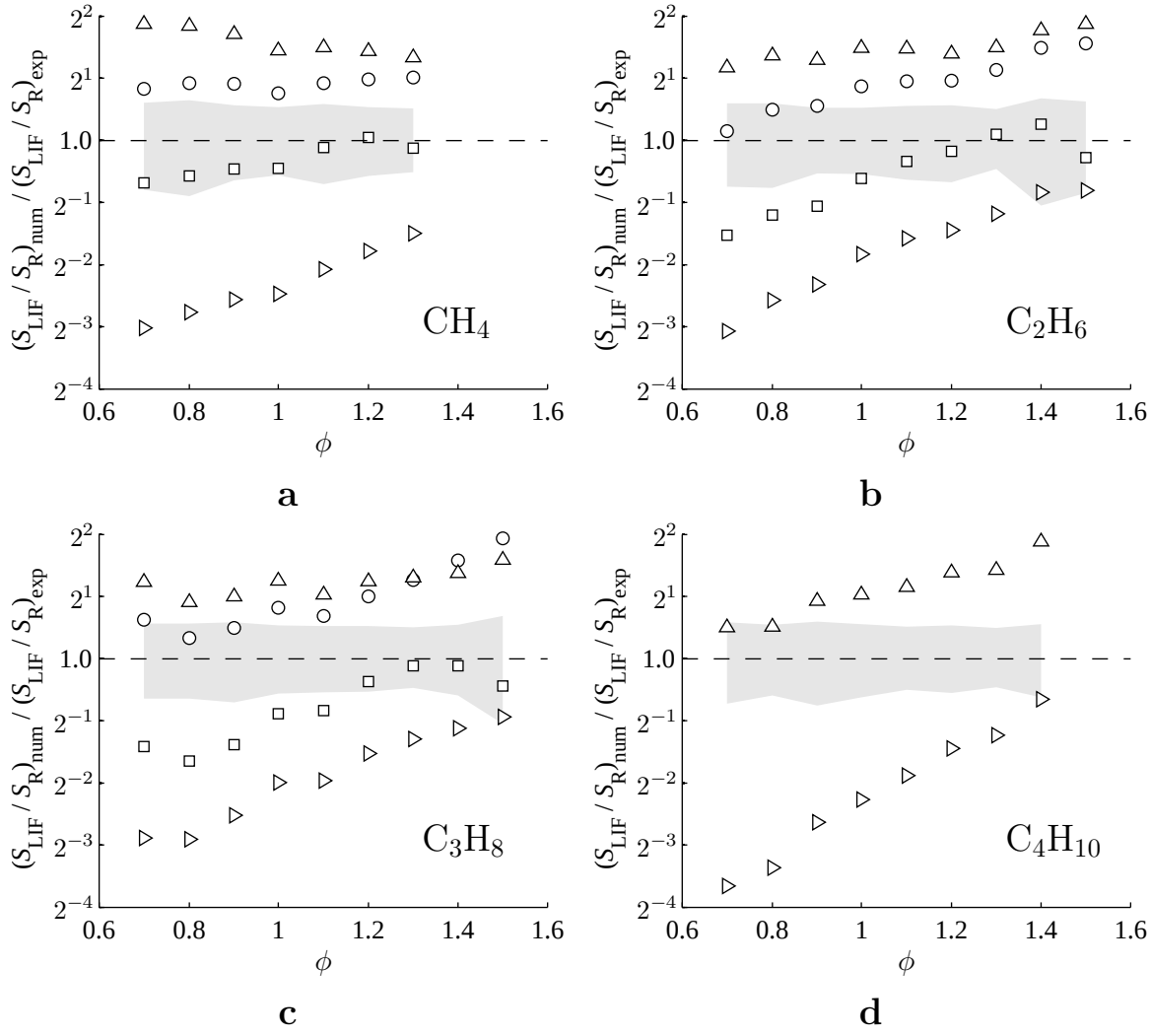

FIGURE 4.2: Numerical $S_{\mathrm{LIF}}/S_{\mathrm{R}}$ normalized by the experimental value for (a) methane, (b) ethane, (c) propane, and (d) *n*-butane flames. $(S_{\mathrm{LIF}}/S_{\mathrm{R}})_{\mathrm{num}} \,/\, (S_{\mathrm{LIF}}/S_{\mathrm{R}})_{\mathrm{exp}} = 1$ shown by dashed lines indicates exact agreement of the predictions with the experimental data. The shaded grey bands present the uncertainty resulting from the LIF model, δ_{PSF}, flame boundary conditions and scatter in the measurements. Same legend as Figure 4.1.

of $(S_{\mathrm{LIF}}/S_{\mathrm{R}})_{\mathrm{num}} \,/\, (S_{\mathrm{LIF}}/S_{\mathrm{R}})_{\mathrm{exp}}$ equal to unity (dashed lines). The shaded grey area superimposed on Figure 4.2 corresponds to the uncertainty in $(S_{\mathrm{LIF}}/S_{\mathrm{R}})_{\mathrm{num}} \,/\, (S_{\mathrm{LIF}}/S_{\mathrm{R}})_{\mathrm{exp}} = 1$, and accounts for the scatter in the experimental data ($\sigma_{(S_{\mathrm{LIF}}/S_{\mathrm{R}})_{\mathrm{exp}}}$, also presented in Figure 4.1 as error bars), the error in the LIF model ($\sigma_{(S_{\mathrm{LIF}}/S_{\mathrm{R}})_{\mathrm{num}},\mathrm{LIF\ model}}$, see section 3.4), as well as the error induced in the LIF response by the uncertainties in the PSF-width and in the experimentally measured boundary conditions ($\sigma_{(S_{\mathrm{LIF}}/S_{\mathrm{R}})_{\mathrm{num}},\mathrm{BC}+\delta_{\mathrm{PSF}}}$, see sections 2.1.2.1 and 3.3). The uncertainties in the PSF-width and in each of the BCs are assumed to be statistically independent, and

their combined contribution to the uncertainty of $\left(S_{\mathrm{LIF}}/S_{\mathrm{R}}\right)_{\mathrm{num}}$ is taken as $\sigma_{\left(S_{\mathrm{LIF}}/S_{\mathrm{R}}\right)_{\mathrm{num}},\mathrm{BC}+\delta_{\mathrm{PSF}}} = \sqrt{\sum\left[\mathrm{L.S.}(x_j)\cdot\sigma_{x_j}\right]^2}$, where $\mathrm{L.S.}(x_j)$ corresponds to the logarithmic sensitivity of $\left(S_{\mathrm{LIF}}/S_{\mathrm{R}}\right)_{\mathrm{num}}$ to the parameter x_j obtained through brute-force sensitivity analysis, and σ_{x_j} is the uncertainty in the parameter x_j. Again assuming statistical independence of the individual uncertainties, the overall error in $\left(S_{\mathrm{LIF}}/S_{\mathrm{R}}\right)_{\mathrm{num}} / \left(S_{\mathrm{LIF}}/S_{\mathrm{R}}\right)_{\mathrm{exp}} = 1$ is calculated using equation 4.1, where the last term in the square root is of minor importance in comparison to the random error in the experimental data and the uncertainty of the LIF model.

$$\sigma_{\frac{\left(S_{\mathrm{LIF}}/S_{\mathrm{R}}\right)_{\mathrm{num}}}{\left(S_{\mathrm{LIF}}/S_{\mathrm{R}}\right)_{\mathrm{exp}}}=1} = \sqrt{\sigma^2_{\left(S_{\mathrm{LIF}}/S_{\mathrm{R}}\right)_{\mathrm{exp}}} + \sigma^2_{\left(S_{\mathrm{LIF}}/S_{\mathrm{R}}\right)_{\mathrm{num}},\mathrm{LIF\ model}} + \sigma^2_{\left(S_{\mathrm{LIF}}/S_{\mathrm{R}}\right)_{\mathrm{num}},\mathrm{BC}+\delta_{\mathrm{PSF}}}} \tag{4.1}$$

As observed in Figure 4.2, the SD mechanism provides the best overall representation of CH formation with $\left(S_{\mathrm{LIF}}/S_{\mathrm{R}}\right)_{\mathrm{num}} / \left(S_{\mathrm{LIF}}/S_{\mathrm{R}}\right)_{\mathrm{exp}}$ agreeing, within uncertainty, with the exact value of 1 for all methane, and rich ethane and propane (except $\phi = 1.1$) cases. However, for lean mixtures of $\mathrm{C_2}$ and $\mathrm{C_3}$ fuels, the SD mechanism increasingly under-predicts the experimental LIF-to-Rayleigh ratio, beyond uncertainty, as the equivalence ratio is reduced. The NUIG mechanism is found to under-predict the experiments by as much as 92%. Its predictive capability improves as the equivalence ratio is increased, agreeing, within uncertainty, with the experimental data for a few rich flames. On the other hand, the USC and GRI mechanisms consistently overestimate CH formation by as much as 268% and 282%, respectively, except for a few lean butane (USC), ethane and propane (GRI) flames where the predicted and measured LIF-to-Rayleigh ratios are in good agreement. Since, for all models, there are cases in Figure 4.2 for which $\left(S_{\mathrm{LIF}}/S_{\mathrm{R}}\right)_{\mathrm{num}} / \left(S_{\mathrm{LIF}}/S_{\mathrm{R}}\right)_{\mathrm{exp}}$ departs from unity significantly beyond the estimated uncertainty, the current CH-LIF measurements are a suitable dataset for the optimization of thermochemical mechanisms.

The LIF diagnostic also permits an assessment of the CH profile thickness, δ_{CH}, which is an important parameter determining NO formation through the prompt (Fenimore) route [69]. Figure 4.3 shows a comparison of measured CH layer thicknesses to the predictions of the thermochemical models. Each experimental value corresponds to the average of the full width at half maximum of two-sided Voigt distributions that are least-squares adjusted to the axial CH-LIF profile of all trials for each value of ϕ. The error bars represent the random uncertainty in the mean value estimated from the Student's t-distribution using a 95% confidence interval. The numerically predicted, PSF-corrected, CH layer thicknesses agree well with the experimental data for $0.8 \leqslant \phi \leqslant 1.3$, a range over which δ_{CH} values predicted by the four mechanisms generally overlap. This confirms the adequacy of the PSF-correction, even though the width of the PSF distribution (δ_{PSF}) was derived from an independent set of CH-LIF measurements. Discrepancies between experiments

and simulations are observed for methane-air and ethane-air flames at $\phi = 0.7$. LIF measurements for these two flames with low [CH] were affected by a non-negligible amount of noise that could have artificially broadened the CH layer thickness. Significant deviations among the models are noticed for $\phi \geqslant 1.3$, and the experimental values generally fall in between the predictions (except for C_4H_{10} which only has predictions from the USC and NUIG mechanisms). Given the width of the error bars, it can be concluded that the CH layer thickness is over-predicted by the SD mechanism for methane ($\phi = 1.3$), and under-predicted by GRI for ethane ($\phi = 1.3$) and propane ($1.3 \leq \phi \leq 1.5$), by USC for butane ($1.3 \leq \phi \leq 1.4$), and by NUIG for methane ($\phi = 1.3$), propane ($\phi = 1.5$) and butane ($1.3 \leq \phi \leq 1.4$).

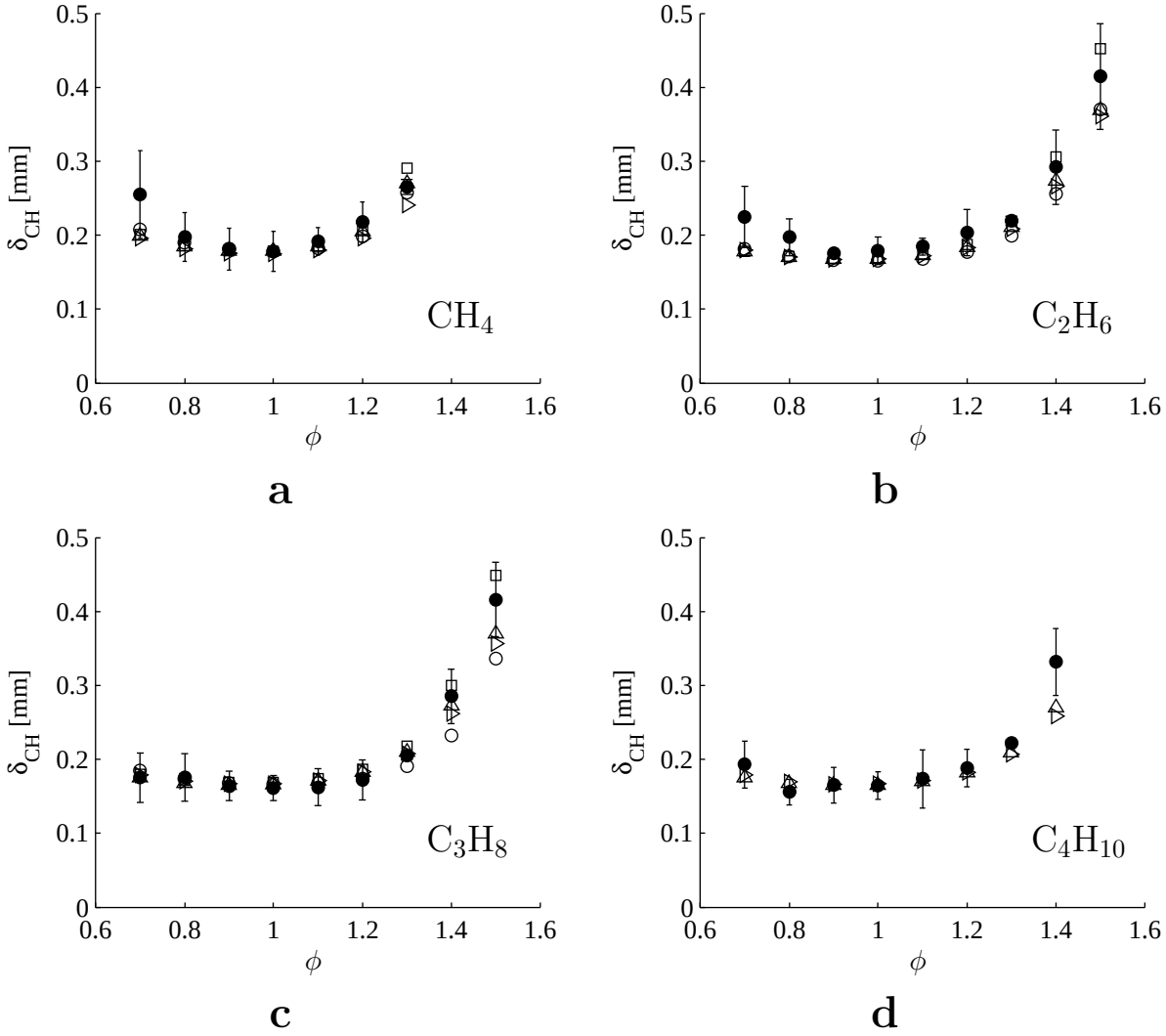

FIGURE 4.3: Measured and simulated CH profile thickness, δ_{CH}, for (a) methane, (b) ethane, (c) propane, and (d) *n*-butane flames. Same legend as Figure 4.1.

4.2 Analysis of variability in predictive performance of the thermochemical mechanisms

As discussed above and presented in Figure 4.1, the ability of currently available chemistry models at predicting CH formation is highly variable. This section seeks to identify the main causes of such differences, namely the order of magnitude variations in $S_{\mathrm{LIF}}/S_{\mathrm{R}}$. Given the complexity of modern thermochemical mechanisms, the potential sources of discrepancies are numerous, and only the most important are presented in this section. Additional information can be found in Appendix D.

Figure 4.4 presents a simplified reaction pathway analysis tracking the flux of carbon through a stoichiometric, unstrained, adiabatic, freely propagating methane-air flame. The network was assembled by identifying the main reaction paths in the RPA diagrams produced using the output of Chemkin-Pro simulations performed with the SD, USC, GRI and NUIG mechanisms. If the contribution of all elementary reactions is included, the RPA diagram becomes so complex that it is almost unreadable. For that reason, only non-CH-related pathways with $R(\mathrm{C}, s_1, s_2) > 0.01$ kmol/s and CH-related pathways with $R(\mathrm{C}, s_1, s_2) > 0.001$ kmol/s are considered in the analysis. The width of the arrows is scaled according to the average of the $R(\mathrm{C}, s_1, s_2)$ values of the four thermochemical mechanisms reported in Figure 4.5(a), and they are coloured according to the average of the logarithmic sensitivities (L.S.) of $[\mathrm{CH}]_{\mathrm{peak}}$ to the specific rate of a given path (see Figure 4.5(b)). The L.S. of a specific pathway is obtained by taking the sum of the L.S. of each individual reaction forming that path. A green (red) arrow indicates a path that upon acceleration causes an increase (decrease) in the maximum concentration of methylidyne, and vice-versa. The order of magnitude variability observed in Figure 4.1 must then be related to significant differences in the specific rate of the reactions making up sensitive channels; mechanisms under-predicting (over-predicting) the peak CH concentration include rates too large for paths with negative (positive) L.S. and/or too small for paths with positive (negative) L.S. It should be noted that a mechanism in reasonable agreement with a given set of experimental data may not have the most accurate chemistry. That is, it could be adjusted such that inaccuracies in the specific rate description of a sensitive path are cancelled out by tuning the rate of another sensitive path.

The RPA diagram presented here qualitatively agrees with the work of Warnatz [196] developed in more detail in [90, 190]. A hydrogen atom is initially abstracted from methane to form methyl, with the initial carbon contained in CH_4 almost completely converted to CH_3, $R(\mathrm{C}, \mathrm{CH_4}, \mathrm{CH_3}) \approx 1$ kmol/s. Most of the produced methyl radicals then react through the main fuel breakdown path,

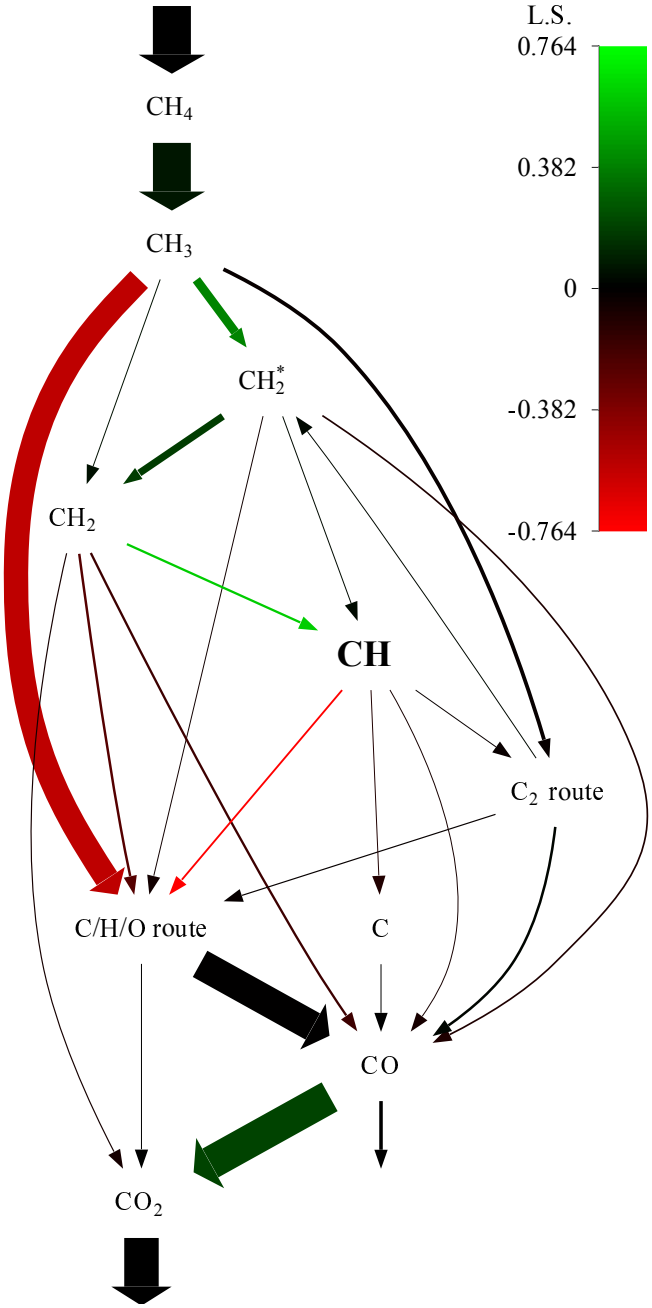

FIGURE 4.4: Simplified RPA diagram for a stoichiometric, unstrained, adiabatic, freely propagating methane-air flame.

simplified here as the C/H/O route:

$$\mathrm{CH_3} \rightarrow \underbrace{\mathrm{CH_2O} \rightarrow \mathrm{HCO}}_{\text{C/H/O route}} \rightarrow \mathrm{CO}, \tag{4.2}$$

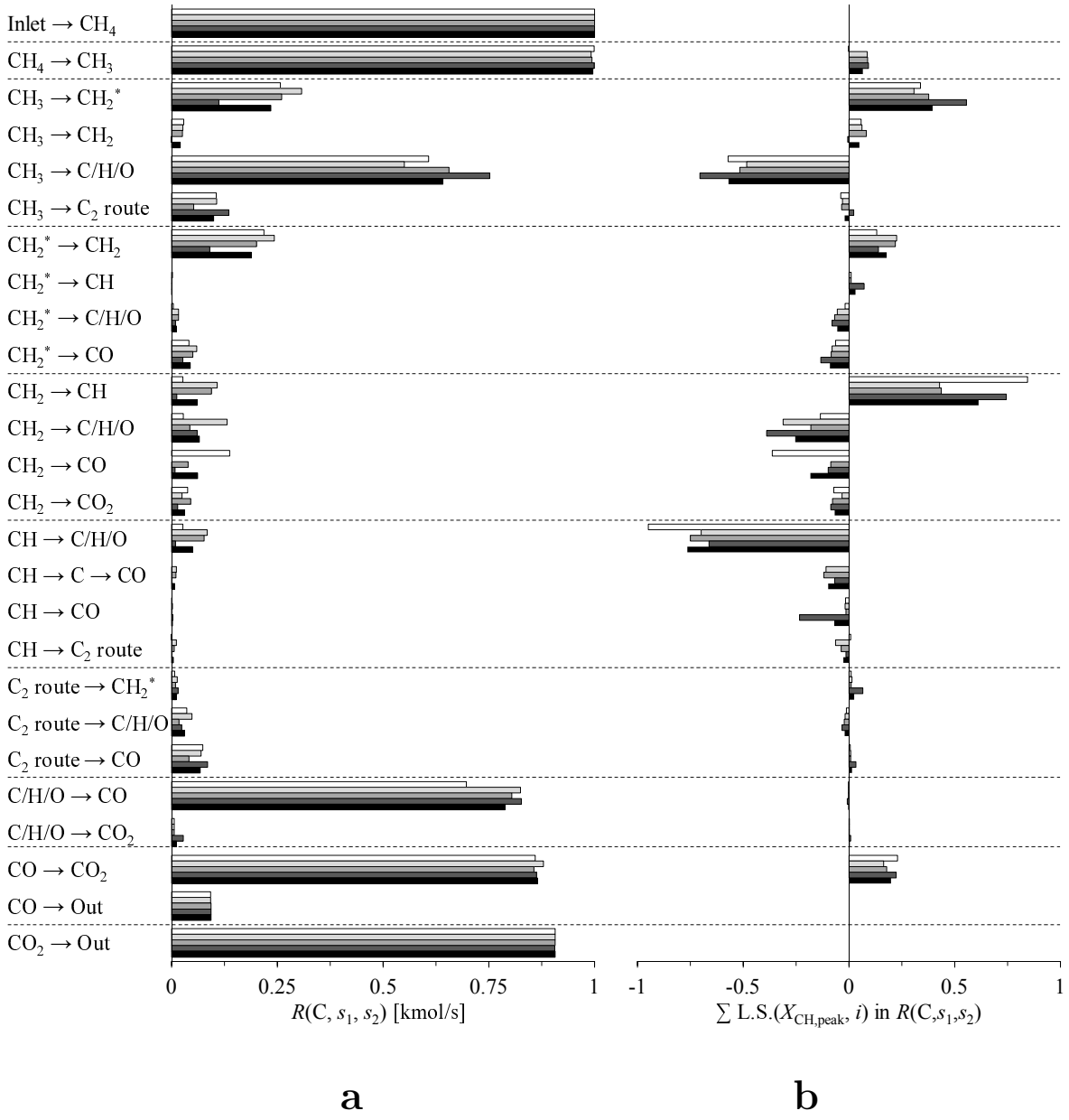

FIGURE 4.5: (a) $R(\mathrm{C}, s_1, s_2)$, and (b) $\sum_{i=1}^{\#\mathrm{reactions}} \mathrm{L.S.}(X_{\mathrm{CH,peak}}, i)$ for the RPA diagram shown in Figure 4.4. Legend: □SD, □USC, ■GRI, ■NUIG, ■Average.

and through other pathways indirectly linking CH_3 to CH_2O via species including CH_3OH, CH_3O, and CH_2OH. The carbon passing through the C/H/O route is then discharged mainly in CO, which either escapes the control volume of the RPA as is, or is transformed into CO_2 and then exhausted. A smaller, yet significant fraction of the carbon (on average about 1/6 of that going to the C/H/O

route) proceeds from CH_3 through a higher-order hydrocarbon route generally described as:

$$CH_3 \rightarrow \underbrace{C_2H_6 \rightarrow C_2H_5 \rightarrow C_2H_4 \rightarrow C_2H_3 \rightarrow C_2H_2 \rightarrow HCCO}_{C_2 \text{ route}} \rightarrow CO, \tag{4.3}$$

which, depending on the thermochemical mechanism, also includes pathways to/from C_2 oxygenated species such as CH_2CHO and CH_2CO. The carbon flowing through the C_2 route is then distributed among the C/H/O route, CO, and singlet-CH_2 (here labelled CH_2^*). The remaining carbon in CH_3 enters the CH formation route presented in equation 4.4 via CH_2^* and CH_2, and methylidyne is consumed mainly to the C/H/O route, and to a lesser extent to C, CO, and C_2 compounds. This main CH formation route is consistent with the reaction networks presented in [105, 130, 190, 197].

$$CH_3 \rightarrow CH_2^* \rightarrow CH_2 \rightarrow CH \tag{4.4}$$

From Figures 4.4 and 4.5, paths flowing carbon in and out of the CH formation route have significant positive and negative L.S., respectively, particularly those directly connected to CH. As discussed in section 3.2.4.1, the overall production rate of CH, q_{CH}, is described by equation 3.23 reproduced below. The production and consumption rate profiles of CH shown in Figure 3.9 are very similar; at the location of maximum [CH], the overall (net) production rate represents only ~1.4% of the rate of production. In this case, the quasi-steady state assumption can be invoked, *i.e.*, $q_{\mathrm{CH}} = 0$, and the concentration profile of CH estimated according to equation 4.5. The presence in the numerator and denominator of the specific rate of the reactions producing and consuming methylidyne, respectively, clearly shows their direct, important impact on its concentration.

$$q_{\mathrm{CH}} = \underbrace{\sum_{i=1}^{R_{\mathrm{in}}} k_i \prod_{j=1}^{N_{r,i}} [\mathrm{M}_j]^{\nu'_j}}_{\text{rate of production}} - \underbrace{\sum_{k=1}^{R_{\mathrm{out}}} k_k [\mathrm{CH}] \prod_{l=1, \mathrm{M}_l \neq \mathrm{CH}}^{N_{r,k}} [\mathrm{M}_l]^{\nu'_l}}_{\text{rate of consumption}} \tag{3.23}$$

$$[\mathrm{CH}] \approx \frac{\sum_{i=1}^{R_{\mathrm{in}}} k_i \prod_{j=1}^{N_{r,i}} [\mathrm{M}_j]^{\nu'_j}}{\sum_{k=1}^{R_{\mathrm{out}}} k_k \prod_{l=1, \mathrm{M}_l \neq \mathrm{CH}}^{N_{r,k}} [\mathrm{M}_l]^{\nu'_l}} \tag{4.5}$$

CH is mainly produced through the path CH_2 to CH, which has the largest positive L.S. of the RPA. The lower plot of Figure 4.6(a) shows the specific rates of the two reactions making that path. The net reaction rates normalized to unity, q_{net}, obtained using the SD mechanism are also shown in the top plot to indicate the temperature range over which the reactions mostly proceed.

Such additional plots will be included for informative purposes in the remainder of this dissertation without additional discussions. While the Arrhenius rate coefficients are exactly identical for the reaction $CH_2 + OH \leftrightarrow CH + H_2O$, there are significant discrepancies for the reaction $CH_2 + H \leftrightarrow CH + H_2$. Namely, the USC and GRI mechanisms predict specific rates approximately one order of magnitude larger than the SD and NUIG models. Comparing the specific rates to the recommendations of Baulch et al., the NUIG and SD mechanisms are in fair and perfect agreement, respectively, with the 1992 report [198]. However, the recommended specific rate was raised in the 2005 review [199], and the USC and GRI mechanisms are in better agreement with this revised rate. The data presented here cannot discriminate exact values for any individual reaction. However, considering the large positive L.S. for that reaction ($\mathrm{L.S.} = 0.34$ on average), the discrepancies in the rates shown in Figure 4.6(a) must have a significant impact on the order of magnitude variability in the predictions shown in Figure 4.1.

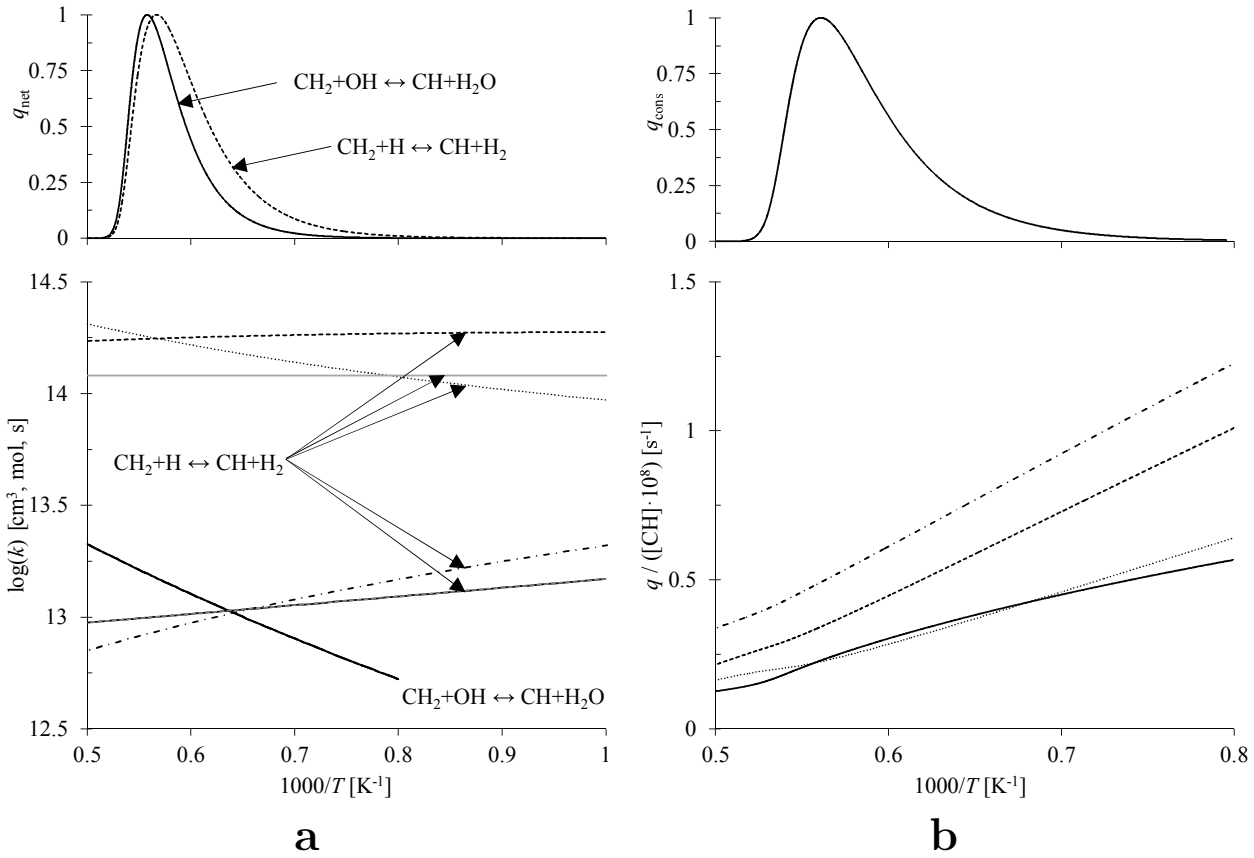

FIGURE 4.6: (a) Normalized net reaction rate (top) and specific rate (bottom) of the main reactions producing CH, and (b) rate of CH consumption normalized to unity (top), and normalized by the CH concentration profile (bottom). Legend: —— SD, ····· USC, - - - - GRI, – · – NUIG, ------ [198], and —— [199].

Many different reactions included in the thermochemical mechanisms consume CH, and the included reactions differ from one mechanism to the other. Their sensitivity is reported in Table 4.1. The SD mechanism includes the fewest number of reactions, although some of the excluded ones have non-negligible L.S. values based on the other models. The USC, GRI, and NUIG mechanisms contain the same reactions, except that the latter includes the additional reaction $\mathrm{CH} + \mathrm{O_2} \leftrightarrow \mathrm{CO} + \mathrm{OH^*}$, which presents the second-largest L.S. value. To compare the models, the rate of consumption of CH normalized by its concentration (denominator of equation 4.5) from each mechanism is shown in the lower plot of Figure 4.6(b) (note the linear scale). This normalized rate practically corresponds to an aggregate rate constant independent of [CH]. The top plot of Figure 4.6(b) presents the rate of consumption normalized to unity, q_{cons}, obtained using the SD mechanism. The SD and USC mechanisms are in fair agreement, while GRI and NUIG predict normalized consumption rates approximately 1.5 and 2 times higher, respectively. Considering the large negative L.S. of that pathway (see last row in Table 4.1), it partially explains the lower predictions of NUIG vs. SD, and GRI vs. USC.

TABLE 4.1: Logarithmic sensitivities, multiplied by 10^3, of the principal reactions consuming CH.

Reaction	SD	USC	GRI	NUIG
$\mathrm{CH + H_2O \leftrightarrow CH_2O + H}$	-201	-288	-199	-455
$\mathrm{CH + CO_2 \leftrightarrow HCO + CO}$	-45	-29	-16	-8
$\mathrm{CH + OH \leftrightarrow HCO + H}$		-28	-18	-18
$\mathrm{CH + O_2 \leftrightarrow HCO + O}$	-702	-354	-516	-181
$\mathrm{CH + O_2 \leftrightarrow CO + OH^*}$				-222
$\mathrm{CH + O \leftrightarrow CO + H}$	-15	-18	-14	-12
$\mathrm{CH + H \leftrightarrow C + H_2}$		-108	-119	-67
$\mathrm{CH + CH_4 \leftrightarrow C_2H_4 + H}$		-38	-27	-14
sum	-963	-863	-909	-977

Additionally, equation 4.5 shows the direct coupling between the concentrations of CH and of the reactants from which it originates. As observed in Figures 4.4 and 4.5(a), methylidyne is principally formed from $\mathrm{CH_2}$. Improper descriptions of the rates of formation and consumption of ground state (triplet) methylene result in inaccurate predictions of its concentration and, as a consequence, impact [CH]. This dependency is highlighted by the non-negligible L.S. of the $\mathrm{CH_2^*}$ to $\mathrm{CH_2}$, $\mathrm{CH_2}$ to $\mathrm{C/H/O}$ route, and $\mathrm{CH_2}$ to CO paths. In addition, the concentration of $\mathrm{CH_2}$ is directly coupled to the concentration of its main precursor, $\mathrm{CH_2^*}$. Hence, inaccuracies in the rates of formation and consumption of singlet methylene cascade down the CH formation route and impact [CH]. Reactions relaxing methylene from its singlet state to its triplet state, and draining carbon atoms out of the CH formation route from $\mathrm{CH_2}$ and $\mathrm{CH_2^*}$ are numerous. Disagreements exist among the mechanisms both in terms of included reactions and their rate coefficients. However,

they do not appear as the main cause of the order of magnitude variability in the predictions shown in Figure 4.1. Further details are provided in Appendix D to keep this dissertation as succinct as possible.

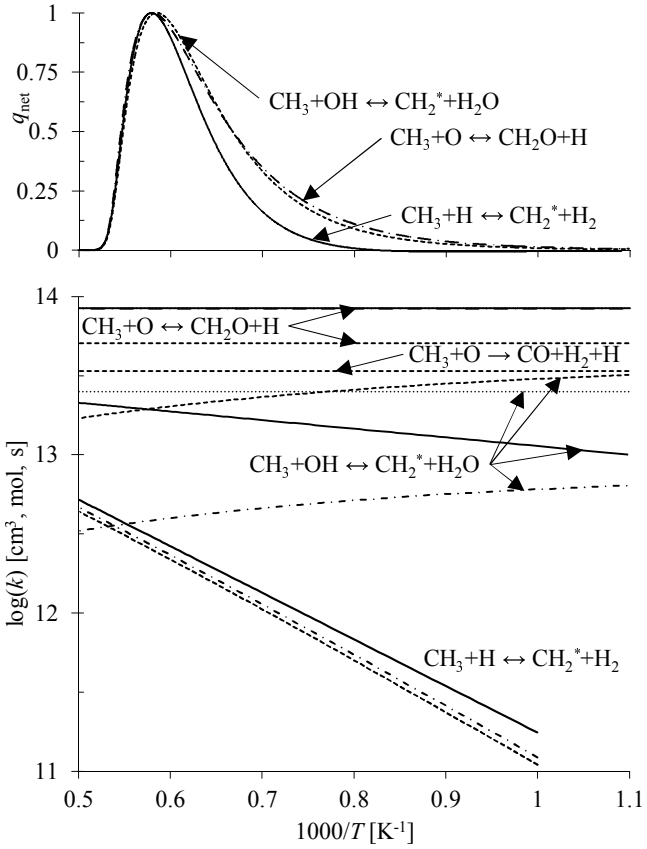

FIGURE 4.7: Normalized net reaction rate (top) and specific rate (bottom) of the principal reactions consuming the methyl radical. Same legend as Figure 4.6.

Carbon flows into the CH formation route principally via the reactions $\mathrm{CH_3 + H \leftrightarrow CH_2^* + H_2}$, and $\mathrm{CH_3 + OH \leftrightarrow CH_2^* + H_2O}$, and bypasses it through the reaction $\mathrm{CH_3 + O \leftrightarrow CH_2O + H}$, which proceeds mostly in the forward direction. Figure 4.7 shows the specific rates included in the thermochemical mechanisms for these reactions. For the first reaction, the GRI, USC, and NUIG models specify the parameters in the backward direction. The ChemRev software, available from the Combustion Chemistry Centre at National University of Ireland Galway [200], was used along with the thermodynamic properties and backward reaction rate coefficients of each mechanism to obtain the forward specific rates. The USC, GRI, and NUIG mechanisms present very similar $k(T)$, while the SD model predicts a specific rate ~25 to ~50% higher. However, the L.S. obtained with the SD mechanism is 0.0366 for that reaction as it contributes only a small fraction to the $\mathrm{CH_3}$ to $\mathrm{CH_2^*}$ path, hence reducing the impact of the higher specific rate predicted by the SD model.

In contrast, the average L.S. for the reaction CH_3+OH $\leftrightarrow$ CH_2^*+H_2O is 0.307, and significant disagreements exist among the models. The reaction mostly proceeds in the high temperature range where the specific rates of the SD, USC and GRI mechanisms are on the same order of magnitude, although they present opposite trends with increasing temperature. On the other hand, the NUIG mechanism predicts a specific rate approximately 5.5 times lower than the other mechanisms at the location of maximum q_{net}. This is certainly an additional cause of the significantly lower $S_{\mathrm{LIF}}/S_{\mathrm{R}}$ predictions by the NUIG model.

The rate descriptions of the SD, USC and NUIG mechanisms for the reaction $\mathrm{CH_3 + O \leftrightarrow CH_2O + H}$ agree very well, while the GRI model has a specific rate 40% lower than the others. However, it includes an additional reaction, $\mathrm{CH_3 + O \rightarrow CO + H_2 + H}$ that is not present in the other mechanisms. Interestingly, the sum of the specific rate in the forward direction of both reactions in the GRI model is equal to the forward specific rate of $\mathrm{CH_3 + O \leftrightarrow CH_2O + H}$ in the SD, USC, and NUIG mechanisms. That is, GRI bypasses carbon from the CH route at the same specific rate as the other mechanisms, but sends it to CO in addition to CH_2O. Hence, the variability in the predicted [CH] is not related to the specific rate of methyl consumption to the C/H/O route.

4.3 Conclusion

This chapter presented the experimental CH concentration data collected following the methodology exposed in Chapter 2. For the four normal-alkane fuels considered in this study (methane, ethane, propane, and *n*-butane), the peak CH-LIF signal is maximized at an equivalence ratio of 1.2, and continuously decreases for leaner and richer mixtures. The similar trend of the experimental LIF-to-Rayleigh ratio with changes in the equivalence ratio observed for all fuels suggests that a limited, common set of elementary reactions determines the formation of CH in premixed alkane-air flames.

Consistent with the methodology of Connelly et al. [153], the predictions of four thermochemical mechanisms (San Diego Mechanism version 2005, USC Mech version II, AramcoMech 1.3, and GRI-Mech version 3.0) were processed into LIF signals using the time-resolved, four-level LIF model presented in Chapter 3. The numerical LIF signal intensities were directly compared to the experimentally determined LIF-to-Rayleigh ratios. Among the four mechanisms, the San Diego model provides the most accurate predictions of CH concentration for the range of fuels and equivalence ratios investigated. The USC Mech and GRI-Mech mechanisms overestimate, and the AramcoMech 1.3 mechanism underestimates, CH formation. A wide variability in the predicted

LIF signals, significantly beyond the limits of uncertainty, was also observed and, as reported in [79, 99], the thermochemical mechanisms generally over-predict the decline in the CH-LIF signal as the mixture is made leaner from $\phi = 1.2$. In general, the models accurately predict the CH layer thickness, except for the richest flames.

Sensitivity and reaction pathway analyses revealed that the significant disagreements among the predictions of the thermochemical mechanisms are caused by differences in the specific rate of reactions directly interacting with the CH formation route, namely $CH_2 + H \leftrightarrow CH + H_2$, and $CH_3 + OH \leftrightarrow CH_2^* + H_2O$. Furthermore, the set of reactions consuming methylidyne is different among the mechanisms, which disagree on the rate at which this important process occurs.

It is anticipated that CH formation may also be sensitive to the thermodynamic and transport properties included in the thermochemical mechanisms. The databases of properties were inspected, and no significant disagreements were observed. The differences in the Arrhenius rate coefficients presented above are the principal reasons for the wide variability in the predictions. Specifically, the reactions $CH_2 + H \leftrightarrow CH + H_2$, $CH_3 + OH \leftrightarrow CH_2^* + H_2O$, and those consuming CH should be addressed in future combustion studies. Other pathways with lower L.S. or better agreement in terms of specific rate were not studied here, but are analyzed in Appendix D. Namely, the H_2/O_2 sub-mechanism and CO to CO_2 path, both having significant L.S., were found to be fairly consistent from one mechanism to the other.

The set of experimental data presented here is made available to chemical modellers for use as validation and optimization targets. Boundary conditions for 1D flame simulations are provided in Appendix F, and numerical values of the experimental data, as well as estimated CH concentrations, in Appendix G.

Chapter 5

Thermochemical model adjustment for accurate stoichiometric trend of $[\mathrm{CH}]_{\mathrm{peak}}$

The experimental data presented in section 4.1 show that the thermochemical mechanisms over-predict the decrease in maximum CH concentration, $[\mathrm{CH}]_{\mathrm{peak}}$, as the stoichiometry is shifted to lean mixtures starting from $\phi = 1.2$. This behaviour was also observed in the studies of Sutton and Driscoll [99], and Bergthorson [79], but its sources and possible remedies have yet to be determined. Remembering the correlation between the production of prompt-NO and the CH concentration profile discussed in section 1.3.2, it follows that this improper stoichiometric dependence of $[\mathrm{CH}]_{\mathrm{peak}}$ impacts the ability of thermochemical mechanisms to accurately predict prompt-NO formation for a wide range of fuel-air mixtures.

The objectives of this chapter are threefold. First, it aims to diagnose the cause of the incorrect dependence of $[\mathrm{CH}]_{\mathrm{peak}}$ predictions on the equivalence ratio, and to highlight the reactions requiring an improved description of their specific rate. Second, it seeks to exemplify how the set of experimental data presented in Chapter 4 can be used to improve the response of thermochemical mechanisms. The third goal is to provide a kinetic model properly describing methylidyne formation in alkane-air flames to enable accurate prompt-NO predictions over a wide range of equivalence ratios. In the following, an optimization procedure is applied to the San Diego mechanism [128], which displayed the best overall predictive performance against the experimental data presented in Chapter 4, while at the same time including the fewest number of species and elementary reactions.

5.1 Methodology

The optimization procedure used here is inspired by [64, 85]. It consists in adjusting the specific rate of a subset of the elementary reactions included in the thermochemical mechanism to reconcile

numerical predictions with a selection of experimental data points. As discussed in Appendix E, the uncertainty in the thermodynamic properties is negligible in comparison to the contribution of the uncertain rate coefficients to the error on $[\mathrm{CH}]_{\mathrm{peak}}$ predictions and, therefore, only the kinetic parameters are considered in the optimization.

For bimolecular reactions, the specific rate is defined as $k(T) = A \cdot T^n \cdot \exp\left(-{}^{E_\mathrm{a}}/_{R_\mathrm{u}T}\right)$, where A is the pre-exponential factor, n the temperature exponent, and E_a the activation energy. Even more parameters are required to describe the specific rate of pressure-dependent, unimolecular reactions [201]. As discussed in Chapter 4, and revealed by the sensitivity analysis presented below (see Figure 5.1), the stoichiometric dependence of $[\mathrm{CH}]_{\mathrm{peak}}$ for all fuels is determined by a limited number of fuel-independent elementary reactions. This implies that the 25 data points for the $\mathrm{C_1}$-$\mathrm{C_3}$ alkane-air flames[1] are not independent, and including all rate coefficients (A, n, and E_a) for all reactions of interest would lead to an ill-resolved optimization problem. As in [64, 85], only the pre-exponential factor of select reactions is adjusted in the current optimization. The procedure seeks to minimize the objective function, F, defined as the sum of squares of the relative difference between the numerical and experimental data, $\left(S_{\mathrm{LIF}}/S_{\mathrm{R}}\right)_{\mathrm{num},j}$ and $\left(S_{\mathrm{LIF}}/S_{\mathrm{R}}\right)_{\mathrm{exp},j}$, respectively:

$$F(\boldsymbol{A}) = \sum_j \left[\frac{\left(S_{\mathrm{LIF}}/S_{\mathrm{R}}\right)_{\mathrm{num},j}(\boldsymbol{A}) - \left(S_{\mathrm{LIF}}/S_{\mathrm{R}}\right)_{\mathrm{exp},j}}{\left(S_{\mathrm{LIF}}/S_{\mathrm{R}}\right)_{\mathrm{exp},j}} \right]^2, \tag{5.1}$$

where the summation is performed for a set of experimental optimization targets j, and the dependence of the objective function and numerical LIF signals to the pre-exponential factors is shown in vector notation as $\boldsymbol{A}$.

The first step of the optimization is to identify the active parameters, which are the pre-exponential factors of the reactions that have the greatest influence on $[\mathrm{CH}]_{\mathrm{peak}}$, while at the same time featuring a relatively large uncertainty in their specific rate. Second, bounds on the active parameters are determined to ensure that the pre-exponential factors remain within a range of physically reasonable values. Then, a selection of experimental data points is made to serve as optimization targets, and a quasi-Newton optimization method is applied to yield the vector $\boldsymbol{A}$ that minimizes the function F.

5.1.1 Identification of the active parameters

Figure 5.1 presents the logarithmic sensitivity of the maximum CH mole fraction ($X_{\mathrm{CH,peak}}$) to the specific rate of individual reactions i, $\mathrm{L.S.}\left(X_{\mathrm{CH,peak}}, i\right)$, obtained from the solution of stagnation

[1] The SD mechanism does not include $\mathrm{C_4}$ chemistry.

flame simulations performed with Chemkin-Pro [112]. The experimental boundary conditions for the 25 $\mathrm{C_1}$-$\mathrm{C_3}$ alkane-air flames are provided in Appendix F. The reactions are sorted according to the sum of squares of $\mathrm{L.S.}\,(X_{\mathrm{CH,peak}}, i)$ for all considered flames, and only the 20 most important reactions are shown for the sake of brevity. For each reaction, the bands of the sensitivity plots are coloured according to the equivalence ratio using a blue ($\phi = 0.7$) to red ($\phi = 1.5$) rainbow colour map.

The over-prediction of the decline in $[\mathrm{CH}]_{\mathrm{peak}}$ as the stoichiometry is shifted to lean mixtures from $\phi = 1.2$ must be related to 1) an overestimation of the specific rate of reactions with increasing values of $\mathrm{L.S.}\,(X_{\mathrm{CH,peak}}, i)$ with ϕ (*e.g.*, $\mathrm{CH}+\mathrm{O_2} \leftrightarrow \mathrm{HCO}+\mathrm{O}$, or $\mathrm{CH_2}+\mathrm{O_2} \leftrightarrow \mathrm{CO}+\mathrm{OH}+\mathrm{H}$); 2) an underestimation of $k(T)$ for reactions with decreasing values of $\mathrm{L.S.}\,(X_{\mathrm{CH,peak}}, i)$ with ϕ (*e.g.*, $\mathrm{CH_3} + \mathrm{OH} \leftrightarrow \mathrm{CH_2^*} + \mathrm{H_2O}$, or $\mathrm{CH} + \mathrm{H_2O} \leftrightarrow \mathrm{CH_2O} + \mathrm{H}$); or 3) a combination of both. Many reactions in Figure 5.1 present the expected relationship between $\mathrm{L.S.}\,(X_{\mathrm{CH,peak}}, i)$ and ϕ, and/or feature significant values of logarithmic sensitivities. However, not all reactions are known to the same level of certainty. As discussed in Chapter 4 and Appendix D, the specific rates of the reactions interacting with the CH formation route are not consistent among the thermochemical mechanisms while, in contrast, there is a relatively well-established consensus regarding $k(T)$ for the principal reactions in the $\mathrm{H_2}/\mathrm{O_2}$ sub-mechanism, CO to $\mathrm{CO_2}$ conversion, and main fuel breakdown route. As suggested in [85], the uncertainty in the specific rate of the individual reactions must also be taken into account in the selection of the active parameters; they must have a significant impact on $[\mathrm{CH}]_{\mathrm{peak}}$, while at the same time allowing a sufficiently wide adjustment to reconcile the numerical and experimental data.

Figure 5.2 presents the product of $\mathrm{L.S.}\,(X_{\mathrm{CH,peak}}, i)$ with the relative error in the specific rate of reaction i, ${}^{\Delta k_i}/_{k_i}$. The uncertainty in k_i is generally provided as $\Delta \log_{10} k_i$, and the lower and upper bounds of the specific rate obtained by division and multiplication, respectively, of k_i by the factor $f_i = 10^{\Delta \log_{10} k_i}$ [198, 199]. It follows that the lower and upper limits of relative error are:

$$\left.\frac{\Delta k_i}{k_i}\right|_{\mathrm{low}} = \frac{{}^{k_i}/_{f_i} - k_i}{k_i} = \frac{1}{f_i} - 1, \tag{5.2}$$

and,

$$\left.\frac{\Delta k_i}{k_i}\right|_{\mathrm{high}} = \frac{k_i \cdot f_i - k_i}{k_i} = f_i - 1, \tag{5.3}$$

respectively. Values of $\left.\frac{\Delta k_i}{k_i}\right|_{\mathrm{high}}$ obtained from [199, 202] are used in Figure 5.2.

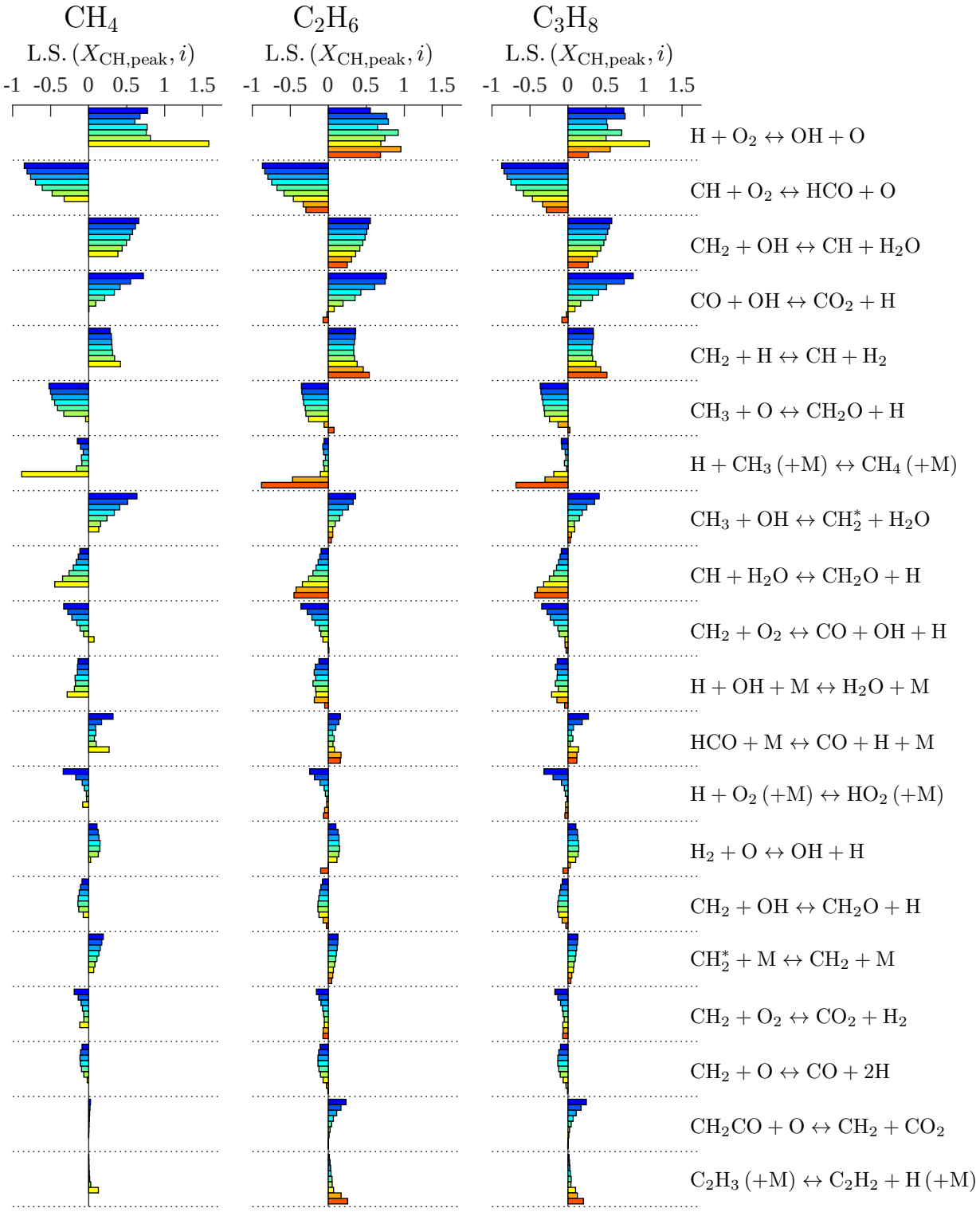

FIGURE 5.1: Logarithmic sensitivity of the maximum CH mole fraction to the specific rate of individual reactions, L.S. $(X_{\mathrm{CH,peak}}, i)$.The reactions are sorted in decreasing order of $\sum_{\mathrm{C}_m\mathrm{H}_n,\phi} \mathrm{L.S.}\,(X_{\mathrm{CH,peak}}, i)^2$. For each reaction, the bands are coloured according to a blue ($\phi = 0.7$) to red ($\phi = 1.5$) rainbow colour map.

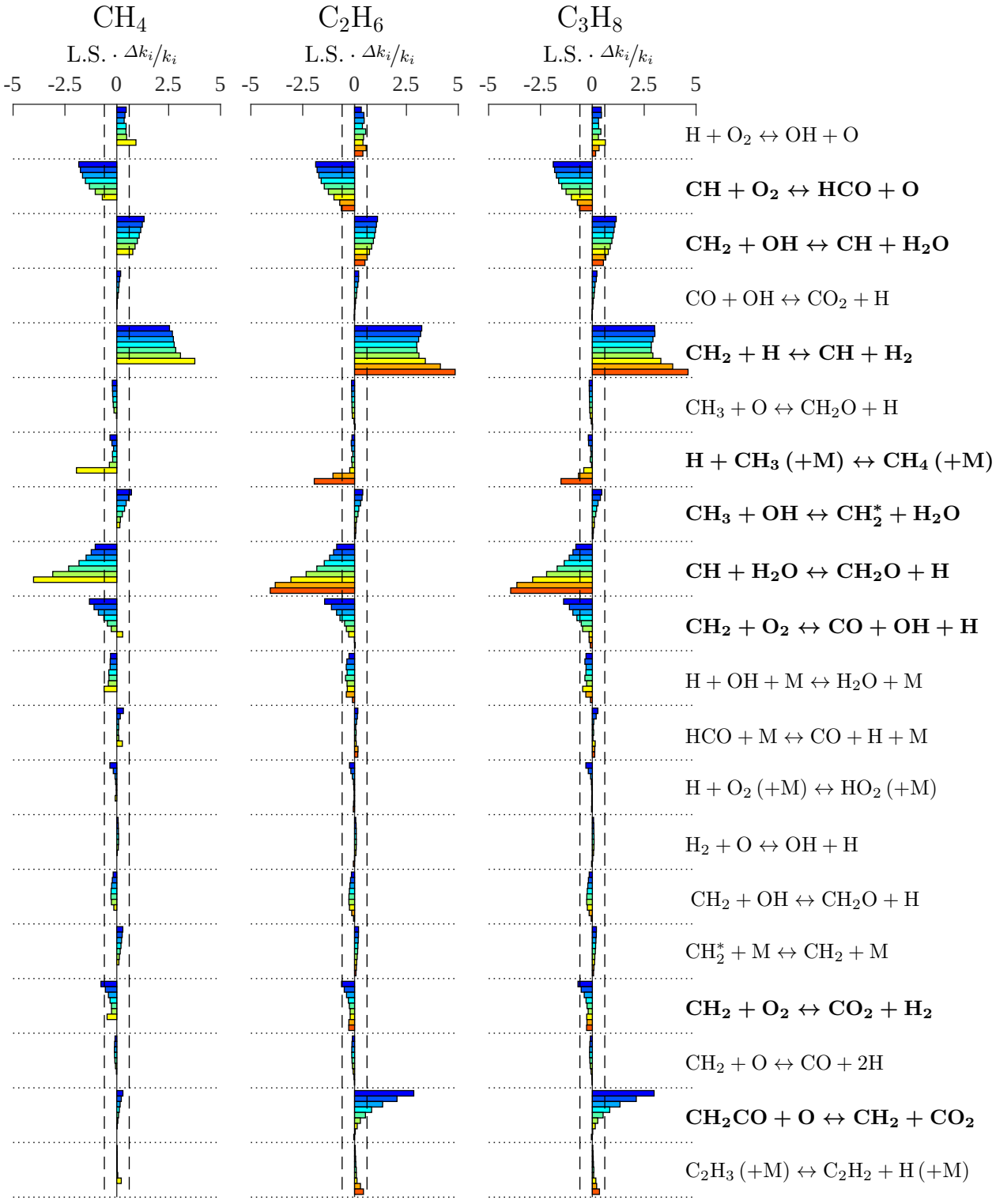

FIGURE 5.2: Product of L.S. $(X_{\mathrm{CH,peak}}, i)$ with $\Delta k_i/k_i$. The relative errors are obtained from the upper uncertainty limits estimated in [199, 202]. The black dashed lines correspond to L.S. $(X_{\mathrm{CH,peak}}, i) \cdot \Delta k_i/k_i = \pm 0.6$.

As observed in Figure 5.2, only a subset of the reactions combines high values of logarithmic sensitivity and $^{\Delta k_i}/_{k_i}$, thus making their pre-exponential factor a suitable candidate as an active parameter. The nine reactions included in the optimization are shown in boldface. They interact with the CH formation route by consuming or producing methylidyne or its precursors, and were observed in the course of the work to have a minimal impact on global combustion properties, such as the strained reference flame speed. Reactions from the $\mathrm{H_2/O_2}$ sub-mechanism, namely $\mathrm{H + O_2 \leftrightarrow OH + O}$, are not considered in the optimization as their specific rates can be, and were, benchmarked against experiments providing a significantly higher level of accuracy than the current experimental data, *e.g.*, flame speed or ignition delay time measurements [65, 134], and the thermochemical mechanisms provide consistent descriptions of $k(T)$ for these reactions (see Appendix D).

5.1.2 Bounds on the value of the active parameters

Bounds for the active parameters must be determined to restrict the specific rates to physically realistic values [85], but they must be sufficiently broad to allow the optimization procedure to converge to an accurate thermochemical mechanism. Lower and upper multiplier values, $f_{i,\mathrm{low}}$ and $f_{i,\mathrm{high}}$, respectively, for the pre-exponential factor of each reaction are determined through comparison of the specific rate included in the SD mechanism to Arrhenius rate coefficients available in the literature. This review does not intend to be comprehensive, but rather to provide a reasonable range of adjustment for the active parameters. During the optimization, the pre-exponential factor of a given reaction i is allowed to take any value between $^{A_i}/_{f_{i,\mathrm{low}}}$ and $A_i \cdot f_{i,\mathrm{high}}$, where A_i is the original pre-exponential factor.

The lower part of Figures 5.3 to 5.10 presents, for each reaction included in the optimization, the specific rate descriptions from various sources. Net reaction rates normalized to unity, q_{net}, extracted from freely propagating, premixed, $\mathrm{CH_4}$-air flame simulations performed with the SD mechanism and solved with Chemkin-Pro [112] at three equivalence ratios ($\phi = 0.7,\ 1.0,\ \mathrm{and}\ 1.3$), are shown in the upper part of these same figures to indicate the range of temperatures over which the reactions proceed.

Reaction $\mathbf{CH + O_2 \leftrightarrow HCO + O}$

Oxidation of CH by $\mathrm{O_2}$ is, along with the reaction $\mathrm{CH + H_2O \leftrightarrow CH_2O + H}$, the principal sink of methylidyne included in the thermochemical mechanisms. Baulch et al. [199] report 5 product

channels for this reaction:

$$\begin{aligned} \mathrm{CH} + \mathrm{O_2} &\leftrightarrow \mathrm{CO_2} + \mathrm{H} && (a) \\ &\leftrightarrow \mathrm{CO} + \mathrm{OH} && (b) \\ &\leftrightarrow \mathrm{CO} + \mathrm{H} + \mathrm{O} && (c) \\ &\leftrightarrow \mathrm{HCO} + \mathrm{O} && (d) \\ &\leftrightarrow \mathrm{CO} + \mathrm{OH^*}, && (e) \end{aligned} \tag{5.4}$$

and the last path is expected to be of negligible importance. The mechanisms generally include a subset of these product channels: the SD, USC and GRI models feature channel (d) only; NUIG and NUIG2 (d) and (e); the model of Konnov [67] (KON) (b) and (d); and Fomin et al. [203] (a)-(d). The overall, forward rate of reaction 5.4 can be written as:

$$\sum_i [\mathrm{CH}]\,[\mathrm{O_2}]\,k_i = [\mathrm{CH}]\,[\mathrm{O_2}] \sum_i k_i = [\mathrm{CH}]\,[\mathrm{O_2}]\,k_{\mathrm{overall}}, \tag{5.5}$$

where i represents each of the product channels. Figure 5.3 reports the overall specific rate ($k_{\mathrm{overall}} = \sum_i k_i$) from various mechanisms, as well as the specific rates recommended by Baulch et al. [199] at low (290-800 K) and high (2200-3500 K) temperatures. $f_{i,\mathrm{high}} = 2.456$ (upper, solid red curve in Figure 5.3) is adjusted to the upper uncertainty limit of the overall specific rate specified in [199] at 2200 K. Essentially, this implies that the SD mechanism is optimized such that all product channels identified in reaction 5.4 are lumped in the reaction $\mathrm{CH} + \mathrm{O_2} \leftrightarrow \mathrm{HCO} + \mathrm{O}$. ${}^{1}/_{f_{i,\mathrm{low}}} = 0.4747$ is set such that the specific rate at $2250\ \mathrm{K}$ coincides with the USC mechanism. Adjusting $f_{i,\mathrm{low}}$ to the lower uncertainty limit at 800 K specified in [199] (lowest of the red-dotted lines in Figure 5.3) would allow the optimization procedure to achieve $k(T)$ values significantly lower than those provided in the mechanisms and the high-temperature recommendation of Baulch et al. [199] over the temperature range where this reaction proceeds (~1355 K for lean flames to ~1975 K for rich flames).

Reaction $\mathbf{CH_2 + OH \leftrightarrow CH + H_2O}$

As shown in Figure 5.4, the specific rate description of the reaction $\mathrm{CH_2} + \mathrm{OH} \leftrightarrow \mathrm{CH} + \mathrm{H_2O}$, one of the two principal pathways forming methylidyne along with the reaction $\mathrm{CH_2} + \mathrm{H} \leftrightarrow \mathrm{CH} + \mathrm{H_2}$, is identical for the SD, USC, GRI, NUIG, and KON mechanisms. This definition of $k(T)$ is used in many other models [135, 204–206]. This consistency must not be interpreted as an absolute exactness in the rate description of the reaction, and translated into narrow bounds of optimization. It is rather the reflection of the common origin of $k(T)$; all these mechanisms use the rate coefficients of the GRI model, which were obtained from [58].

Surprisingly, considering its significant contribution to the formation of CH, the reaction $\mathrm{CH_2} + \mathrm{OH} \leftrightarrow \mathrm{CH} + \mathrm{H_2O}$ is not reported in the kinetic data reviews of Baulch et al. [198, 199, 207]. Because of this lack of independent data, $f_{i,\mathrm{low}}$ and $f_{i,\mathrm{high}}$ are determined by analogy with the reaction $\mathrm{CH_2} + \mathrm{OH} \leftrightarrow \mathrm{CH_2O} + \mathrm{H}$, which has the same reactant species. For this reaction, the specific rates at the uncertainty limits evaluated by Tsang and Hampson [202] are 4.151 times lower and 2.168 times higher than the specific rate included in the SD mechanism. These multiplier values are selected to constrain the optimization of the rate of the reaction $\mathrm{CH_2} + \mathrm{OH} \leftrightarrow \mathrm{CH} + \mathrm{H_2O}$ ($1/f_{i,\mathrm{low}} = 0.2409$, and $f_{i,\mathrm{high}} = 2.168$). As shown in Figure 5.4, these bounds surround the specific rate suggested in [208] for most of the temperature range over which the reaction occurs.

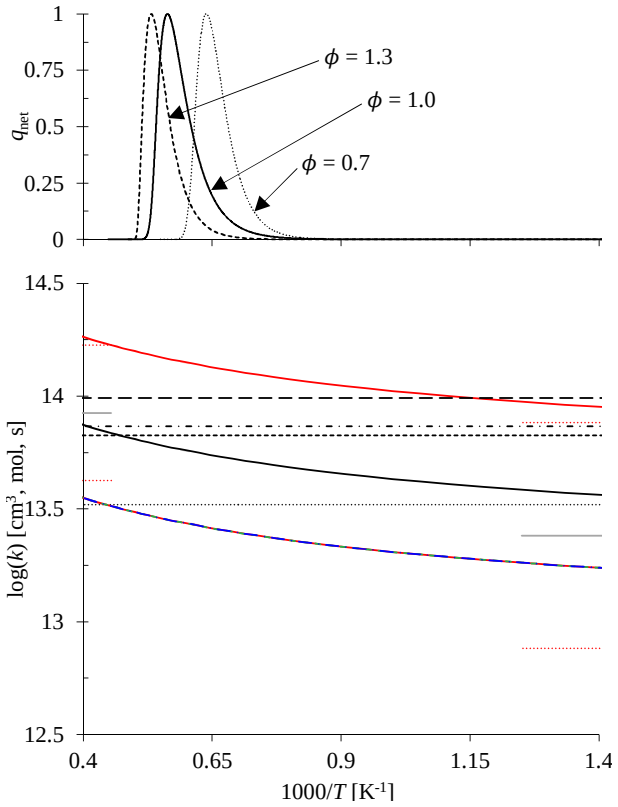

FIGURE 5.3: q_{net} (top) and $k(T)$ (bottom) of the reaction $\mathrm{CH} + \mathrm{O_2} \leftrightarrow$ products. Legend: —— SD, ····· USC, - - - - GRI, - · - NUIG, — — KON, —— Baulch et al. [199] with corresponding uncertainty estimations (k_i/f_i and $k_i \cdot f_i$) ····· , bounds on the active parameter ($f_{i,\mathrm{low}}$, and $f_{i,\mathrm{high}}$) —— , and optimized specific rates corresponding to — — $f_{i,\mathrm{orig}}$ and - · - $f_{i,\mathrm{inv}}$ (see Tables 5.3 and 5.4).

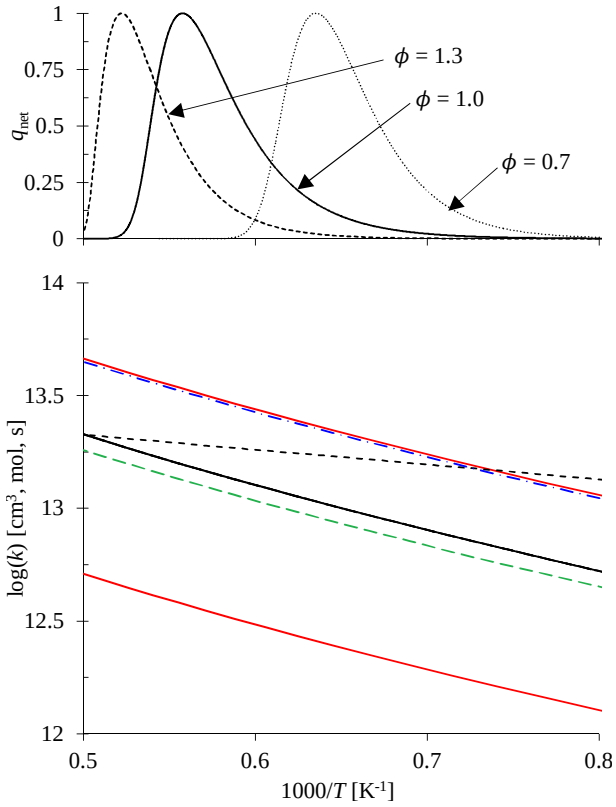

FIGURE 5.4: q_{net} (top) and $k(T)$ (bottom) of the reaction $\mathrm{CH_2} + \mathrm{OH} \leftrightarrow \mathrm{CH} + \mathrm{H_2O}$. Same legend as Figure 5.3, supplemented with - - - - [208].

Reaction $\mathbf{CH_2 + H \leftrightarrow CH + H_2}$

As shown in Figure 5.5 and discussed in section 4.2, the mechanisms significantly disagree with regards to the rate of the reaction $\mathrm{CH_2 + H \leftrightarrow CH + H_2}$. The specific rates included in the USC and GRI mechanisms are in fair agreement with the recommendation made by Baulch et al. in 2005 [199], while the SD and NUIG models best agree with the rate coefficients provided by the same group of authors in 1992 [198]. Including the rate descriptions of the KON and NUIG2 mechanisms does not point towards a preferred set of kinetic data, but rather suggests intermediate values of $k(T)$. The lower bound of optimization, $1/f_{i,\mathrm{low}} = 0.7579$, is adjusted to the specific rate of the NUIG mechanism evaluated at 2000 K, and $f_{i,\mathrm{high}} = 127.6$ corresponds to the upper error limit on $k(T = 2000\ \mathrm{K})$ provided in [199].

Reaction $\mathbf{H + CH_3\ (+M) \leftrightarrow CH_4\ (+M)}$

As shown in Figure 5.6, the rate description of the three-body reaction $\mathrm{H + CH_3\ (+M) \leftrightarrow CH_4\ (+M)}$ is fairly consistent among the SD, USC, GRI, and NUIG mechanisms, and with the recommended specific rate of Baulch et al. [199] specified for temperatures up to 1000 K. The optimization bounds, $1/f_{i,\mathrm{low}} = 0.2577$ and $f_{i,\mathrm{high}} = 3.246$, correspond to the lower and upper error limits found in [199] at 667 K ($1000/T = 1.5\ \mathrm{K^{-1}}$) and 1000 K, respectively.

Reaction $\mathbf{CH_3 + OH \leftrightarrow CH_2^* + H_2O}$

Figure 5.7 shows the significant disagreement among the mechanisms regarding the specific rate of the reaction $\mathrm{CH_3 + OH \leftrightarrow CH_2^* + H_2O}$. The rate coefficients included in the NUIG mechanism (and NUIG2 model, which is not shown in the figure) are consistent with those determined theoretically by Jasper et al. [209]. Increasing values of the specific rate with decreasing temperatures are also noticed for the USC and GRI mechanisms, and the recommendation of Baulch et al. [199]. In contrast, the SD and KON models predict a rise in the specific rate with increasing temperatures. However, in its most recent release [203], the rate description of the KON mechanism was revised and the specific rate presents a temperature dependence similar to the other mechanisms [65, 133–135], theoretical assessment [209], and review [199]. This advocates for an adjustment of the temperature dependence of the specific rate description included in the SD model. For the optimization, the pre-exponential factor ($A = 1.57 \cdot 10^{17}\ \mathrm{cm^3/mol{-}s}$), temperature exponent ($n = -1.225$), and activation energy ($E_\mathrm{a} = 1811\ \mathrm{cal \cdot mol^{-1}}$) are selected such that $k(T)$ agrees with the recommendation of Baulch et al. [199] (note that only the original $k(T)$ of the SD model is shown in Figure 5.7 as the new definition exactly overlaps [199]). The lower and upper bounds of optimization, $1/f_{i,\mathrm{low}} = 0.3653$ and $f_{i,\mathrm{high}} = 2.324$, match the specific rates of the NUIG mechanism at 2000 K and GRI model at 909 K ($1000/T = 1.1\ \mathrm{K^{-1}}$), respectively.

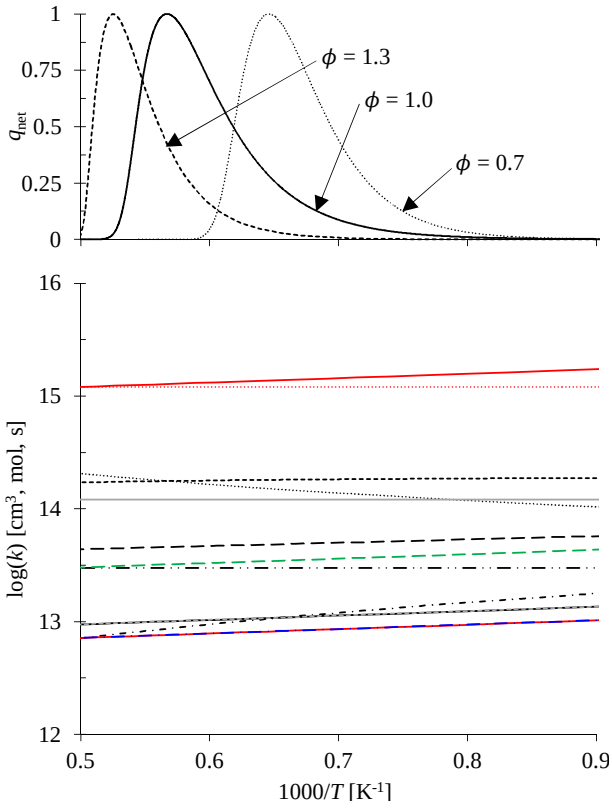

FIGURE 5.5: q_{net} (top) and $k(T)$ (bottom) of the reaction $\mathrm{CH_2}+\mathrm{H} \leftrightarrow \mathrm{CH}+\mathrm{H_2}$. Same legend as Figure 5.3, supplemented with NUIG2 ---···---, and Baulch et al. (1992) [198] ------.

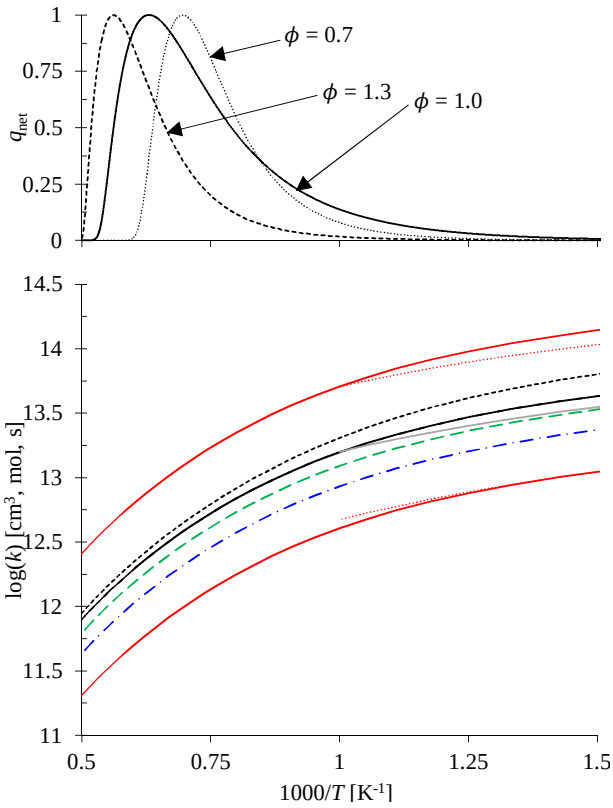

FIGURE 5.6: q_{net} (top) and $k(T)$ (bottom) of the reaction $\mathrm{H} + \mathrm{CH_3}\,(+\mathrm{M}) \leftrightarrow \mathrm{CH_4}\,(+\mathrm{M})$. Same legend as Figure 5.3.

Reaction $\mathbf{CH + H_2O \leftrightarrow CH_2O + H}$

As shown in Figure 5.8, there is a significant level of uncertainty in the rate coefficients of the reaction $\mathrm{CH} + \mathrm{H_2O} \leftrightarrow \mathrm{CH_2O} + \mathrm{H}$. Baulch et al. [199] provide a recommended specific rate for temperatures up to 1000 K, with an uncertainty factor $f = 10$. The rate description of the NUIG mechanism lies close to the upper error limit prescribed in [199], while the rate coefficients included in the SD, GRI, NUIG2 and USC models yield lower values of $k(T)$. The lower bound of optimization, $1/f_{i,\mathrm{low}} = 3.823 \cdot 10^{-2}$, is adjusted to the lower error limit included in [199] evaluated at $T = 1000$ K, while $f_{i,\mathrm{high}} = 5.295$ corresponds to the specific rate at 2000 K of the NUIG mechanism.

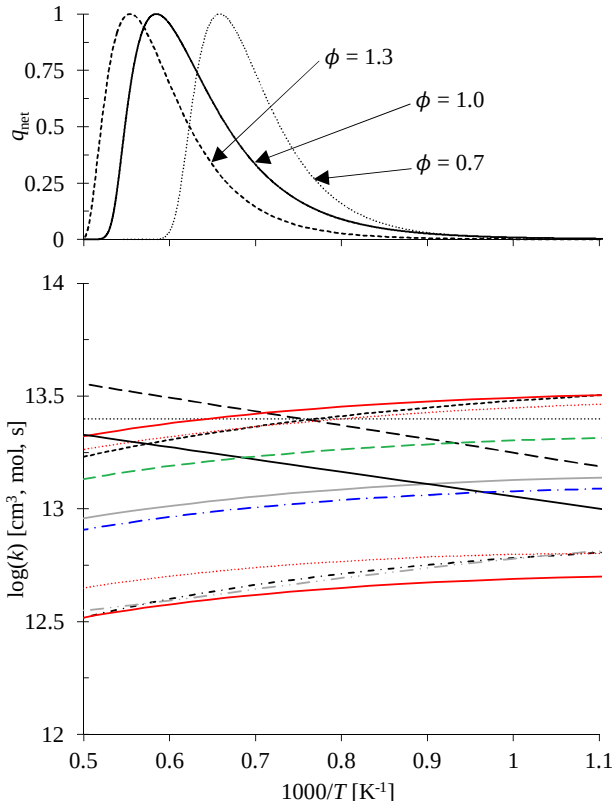

FIGURE 5.7: q_{net} (top) and $k(T)$ (bottom) of the reaction $\mathrm{CH_3 + OH \leftrightarrow CH_2^* + H_2O}$. Same legend as Figure 5.3, supplemented with · · · [209].

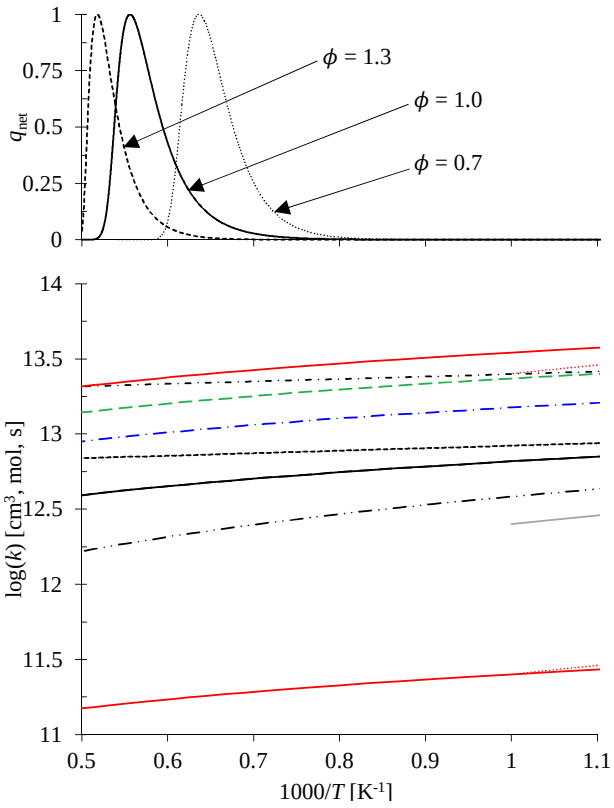

FIGURE 5.8: q_{net} (top) and $k(T)$ (bottom) of the reaction $\mathrm{CH + H_2O \leftrightarrow CH_2O + H}$. Same legend as Figure 5.5.

Reactions $\mathbf{CH_2 + O_2 \leftrightarrow CO + OH + H}$ and $\mathbf{CH_2 + O_2 \leftrightarrow CO_2 + H_2}$

The reaction of triplet methylene with molecular oxygen is expected to possess multiple product channels [199, 203]:

$$\begin{aligned}
\mathrm{CH_2 + O_2} &\leftrightarrow \mathrm{CO_2 + H_2} && (a)\\
&\leftrightarrow \mathrm{CO + OH + H} && (b)\\
&\leftrightarrow \mathrm{CO + H_2O} && (c)\\
&\leftrightarrow \mathrm{HOCO + H} && (d)\\
&\leftrightarrow \mathrm{CO_2 + 2H} && (e)\\
&\leftrightarrow \mathrm{HCO + OH} && (f)\\
&\leftrightarrow \mathrm{CO + H_2 + O} && (g)\\
&\leftrightarrow \mathrm{CH_2O + O.} && (h)
\end{aligned} \tag{5.6}$$

The exact branching among them remains uncertain [199, 210, 211], and the mechanisms generally include all, or a subset, of these reactions. Namely, the SD model considers channels (a) and (b).

Figure 5.9 presents the overall specific rate ($k_{\mathrm{overall}} = \sum_i k_i$) of the reaction $\mathrm{CH_2} + \mathrm{O_2} \rightarrow \mathrm{products}$. Baulch et al., in 1992 [198] and 1994 [207], relying on specific rate measurements at room temperature [212, 213], and using the activation energy suggested by Vinckier and Debruyn [214] based on experiments performed over a temperature range of 295-600 K, recommended $k(T) = 2.5 \cdot 10^{13} \exp\left(-750/T\right)\ \mathrm{cm^3 mol^{-1} s^{-1}}$ (short dashed grey line in Figure 5.9), with an uncertainty factor $f = 10^{0.5} = 3.2$ at 1000 K. Many thermochemical mechanisms adopted the activation energy of ~$1500\ \mathrm{cal \cdot mol^{-1}}$ [65, 128, 133–135, 204], and adjusted the pre-exponential factor yielding specific rate descriptions within the uncertainty limits specified in [198, 207].

However, in 2005, Baulch et al. [199] included in their assessment an additional set of high temperature (1000-1750 K) experimental data [210, 215], which were approximately one order of magnitude below the specific rates predicted using the $k(T)$ description suggested in 1992 and 1994. They provided an updated, temperature-independent specific rate of $1.8 \cdot 10^{12}\ \mathrm{cm^3 mol^{-1} s^{-1}}$ (solid grey line in Figure 5.9), with an uncertainty factor $f = 10^{0.7} = 5.1$ at 1700 K.

Recently, experimental data obtained at temperatures of 1850 to 2050 K [211] contradicted the measurements of Dombrowsky et al. [210, 215], and are instead consistent with the extrapolation of the low-temperature data of Vinckier and Debruyn [214]. Lee et al. [211] proposed $k(T) = 1.65 \cdot 10^{13} \exp\left(-874/T\right)\ \mathrm{cm^3 mol^{-1} s^{-1}}$, which falls within the uncertainty limits estimated by Baulch et al. in 1992 and 1994 [198, 207]. The specific rate included in the KON mechanism was recently updated [203] (long-dashed grey line in Figure 5.9) to be consistent with Lee et al. [211]. For these reasons, the specific rates of the original KON model and Baulch et al. (2005) [199] are excluded from the present analysis, and the uncertainty limits suggested in [198, 207] are used to determine $1/f_{i,\mathrm{low}} = 0.8482$ and $f_{i,\mathrm{high}} = 8.482$.

Through the optimization, the ratio of the specific rates of the reactions $\mathrm{CH_2} + \mathrm{O_2} \leftrightarrow \mathrm{CO} + \mathrm{OH} + \mathrm{H}$ and $\mathrm{CH_2} + \mathrm{O_2} \leftrightarrow \mathrm{CO_2} + \mathrm{H_2}$ remains unchanged. That is, the branching between the product channels is not modified, and this requires the same multiplier to apply to the pre-exponential factor of both reactions. Practically, only eight active parameters are adjusted, while the specific rates of nine reactions are modified.

Reaction $\mathbf{CH_2CO + O \leftrightarrow CH_2 + CO_2}$

The reaction $\mathrm{CH_2CO} + \mathrm{O} \leftrightarrow \mathrm{CH_2} + \mathrm{CO_2}$ has a weak influence on $X_{\mathrm{CH,peak}}$ (see Figure 5.1). However, its rate description is plagued by a significant uncertainty [199], which justifies its inclusion in the optimization. As shown in Figure 5.10, the GRI, USC, NUIG, and NUIG2 mechanisms, and the model from the CRECK modelling group [204], are in fair agreement with

the rate description recommended in [199] for $T \leq 1000$ K. In contrast, at the high temperatures where the reaction mostly proceeds, the specific rate included in the SD mechanism is consistent with the ketone oxidation mechanism prepared by Hidaka et al. [216] to model their shock tube experiments. The lower bound of optimization, $^1/_{f_{i,\mathrm{low}}} = 5.808 \cdot 10^{-03}$, is adjusted to the lower limit of uncertainty of Baulch et al. [199] at 1000 K, while the upper bound, $f_{i,\mathrm{high}} = 1.502$, is set to the specific rate of Hidaka et al. [216] evaluated at 1050 K.

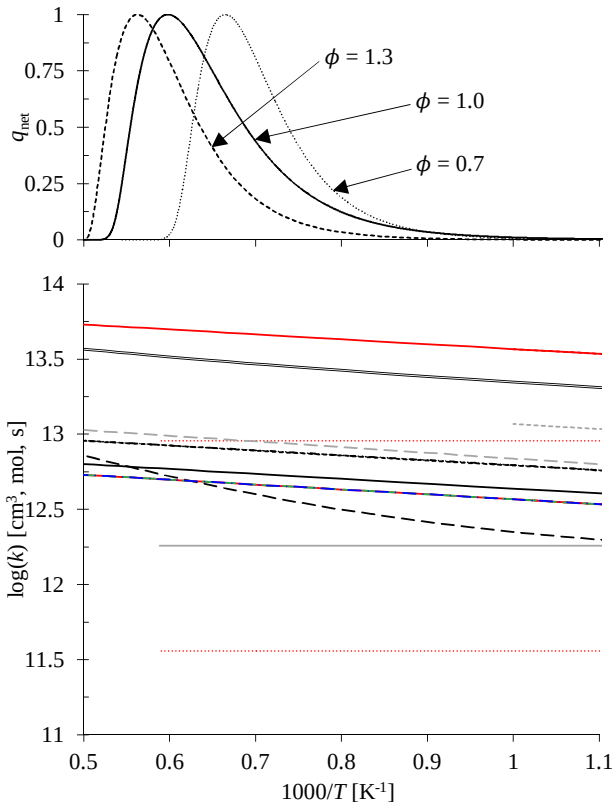

FIGURE 5.9: Normalized net reaction rate of the reaction $CH_2 + O_2 \leftrightarrow CO + OH + H$ (top), and specific rate of the reaction $CH_2 + O_2 \rightarrow$ products. Same legend as Figure 5.5, supplemented with data from the CRECK mechanism (version 1412) [204] ═══, and — — [203].

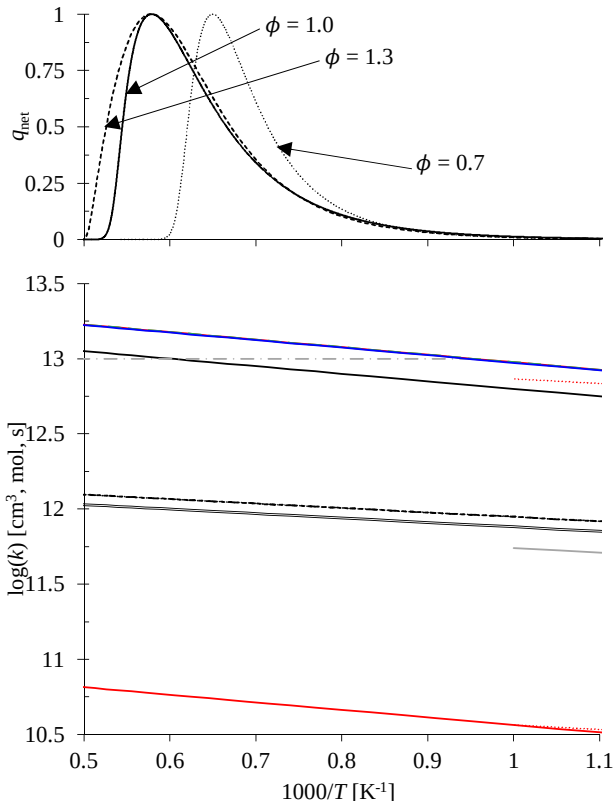

FIGURE 5.10: q_{net} (top) and $k(T)$ (bottom) of the reaction $CH_2CO+O \leftrightarrow CH_2+CO_2$. Same legend as Figure 5.9, supplemented with - · - [216].

5.1.3 Experimental optimization targets

In a classical optimization, the number of degrees of freedom, n_{DOF}, which is the difference between the number of optimization targets, $(S_{\mathrm{LIF}}/S_{\mathrm{R}})_{\mathrm{exp},i}$, and the number of adjustable parameters,

i.e., the pre-exponential factors of the reactions identified above, must be positive [85]. Other constraints, such as the restriction of the optimization space by the bounds $f_{i,\mathrm{low}}$ and $f_{i,\mathrm{high}}$, increase n_{DOF} [85]. On the other hand, as discussed previously, the experimental data points presented in Figure 4.1 are not independent as they are determined by a common set of elementary reactions. Practically, this reduces n_{DOF}, and implies that including all experimental data points would not result in a corresponding increase in n_{DOF}. In the current optimization, 10 experimental targets are selected to adjust 8 pre-exponential factors, yielding $n_{\mathrm{DOF}} = 2$ when excluding the implicit factors discussed above. As reported in [85], the exact determination of n_{DOF} is difficult, and beyond the scope of this dissertation. The experimental data considered in the optimization, presented in Table 5.1, encompass the whole range of fuels and equivalence ratios in an attempt to properly capture the impact of the alkane chain length and stoichiometry on the response of the model.

TABLE 5.1: Experimental optimization targets, $(S_{\mathrm{LIF}}/S_{\mathrm{R}})_{\mathrm{exp},i}$.

ϕ	CH_4	C_2H_6	C_3H_8
0.7		1.8	
0.8			5.5
0.9	5.8		
1.0		13.0	
1.1			24.8
1.2	16.5		
1.3	11.9		23.2
1.4			
1.5		5.5	6.0

5.1.4 Optimization algorithm

As in [64], minimization of the function $F(\boldsymbol{A})$, defined in equation 5.1, is accomplished using the constrained, non-linear, quasi-Newton, multi-variate algorithm (*fmincon*) of Matlab (version R2015b). However, the computation of the numerical values, $(S_{\mathrm{LIF}}/S_{\mathrm{R}})_{\mathrm{num},i}$, differs. In [64, 85], they are obtained from second-order polynomial surfaces adjusted, for each experimental target, to the output of flame simulations performed with various combinations of pre-exponential factors arranged following a central composite factorial design. For an optimization involving eight active parameters and considering a full-factorial design, this results in 273 ($2^8 + 2 \cdot 8 + 1$) combinations of pre-exponential factors, and in a total of 2370 flame simulations (273 simulations per experimental target). This method decouples the simulations from the optimization procedure. The 2370 simulations are first performed then, for each experimental target, the response of the model to changes in the pre-exponential factors is approximated by a polynomial surface and, finally, the optimization problem is solved by comparing the values of $(S_{\mathrm{LIF}}/S_{\mathrm{R}})_{\mathrm{num},i}$ obtained

from the algebraic polynomial surfaces to the experimental targets. The argument is that solving the complete set of differential equations included in the flame simulations, for all experimental targets, at each iteration of the optimization, would be too computationally expensive due to the large size of the optimization space, which is caused by the high level of uncertainty in the specific rate of the elementary reactions [85].

For this study, the flame simulations are solved at each iteration of the optimization and processed into numerical LIF signals, $(S_{\mathrm{LIF}}/S_{\mathrm{R}})_{\mathrm{num},i}$, using the time-resolved, four-level CH-LIF model presented in Chapter 3. Matlab not only solves the optimization problem, it also manages the flame simulations by updating the thermochemical mechanism with the new pre-exponential factors, launching the jet-wall, stagnation flame solver of Cantera 2.2.1 [217] through Python 3.4, and converting the flame solutions to LIF signals. While the current method does require more flame simulations to be performed (2.5 to 3.4 times more), their convergence is significantly easier and faster to achieve. With the exception of a single simulation made with the nominal pre-exponential factors, the factorial design used in [64, 85] requires all simulations to be performed with at least one of the active parameters set to one of its optimization bounds. The changes in $\boldsymbol{A}$ between successive flame simulations are brutal with the pre-exponential factors switching from their lowest to highest allowed values, and vice-versa. For the current method, relatively small changes in $\boldsymbol{A}$ are specified by the algorithm, and the flame solver uses the solutions from the previous optimization iteration as initial guesses to accelerate the computations. Preliminary tests showed that the method used in [64, 85] completes in approximately a week and requires a continuous monitoring, while the current procedure converges with minimal user input in a matter of several hours to a few days. This allows for more flexibility in the analysis; the effects of adding/removing reactions, or changing the optimization bounds, are more rapidly assessed.

5.2 Comparison of the optimized mechanisms to the experimental data

The bounds of optimization for all reactions included in the adjustment are summarized in Table 5.2, while Tables 5.3 and 5.4 present two solutions obtained with the optimization method. The multiplier values $f_{i,\mathrm{orig}}$, yielding an objective function $F(\boldsymbol{A}) = 0.17$, were obtained by using the pre-exponential factors included in the SD mechanism (with revised $k(T)$ for the reaction $\mathrm{CH_3} + \mathrm{OH} \leftrightarrow \mathrm{CH_2^*} + \mathrm{H_2O}$) as the initial conditions. For each reaction i, the optimized pre-exponential factor, $A_{i,\mathrm{opt}}$, is the product of the original value, A_i, with the corresponding multiplier ($A_{i,\mathrm{opt}} = A_i \cdot f_{i,\mathrm{orig}}$). To obtain the $f_{i,\mathrm{inv}}$ multipliers (see Table 5.4), a second adjustment procedure was

TABLE 5.2: Lower and upper optimization bounds, $1/f_{i,\mathrm{low}}$ and $f_{i,\mathrm{high}}$, respectively.

Reactions	Bounds[2]	
	$1/f_{i,\mathrm{low}}$	$f_{i,\mathrm{high}}$
$\mathrm{CH} + \mathrm{O_2} \leftrightarrow \mathrm{HCO} + \mathrm{O}$	0.4747	2.456
$\mathrm{CH_2} + \mathrm{OH} \leftrightarrow \mathrm{CH} + \mathrm{H_2O}$	0.2409	2.168
$\mathrm{CH_2} + \mathrm{H} \leftrightarrow \mathrm{CH} + \mathrm{H_2}$	0.7579	127.6
$\mathrm{H} + \mathrm{CH_3}\,(+\mathrm{M}) \leftrightarrow \mathrm{CH_4}\,(+\mathrm{M})$	0.2577	3.246
$\mathrm{CH_3} + \mathrm{OH} \leftrightarrow \mathrm{CH_2^*} + \mathrm{H_2O}$	0.3653	2.324
$\mathrm{CH} + \mathrm{H_2O} \leftrightarrow \mathrm{CH_2O} + \mathrm{H}$	$3.823 \cdot 10^{-2}$	5.295
$\mathrm{CH_2} + \mathrm{O_2} \leftrightarrow \mathrm{CO} + \mathrm{OH} + \mathrm{H}$ $\leftrightarrow \mathrm{CO_2} + \mathrm{H_2}$	0.8482	8.482
$\mathrm{CH_2CO} + \mathrm{O} \leftrightarrow \mathrm{CH_2} + \mathrm{CO_2}$	$5.808 \cdot 10^{-3}$	1.502

performed taking as initial conditions the pre-exponential factors of the original SD mechanism divided by $f_{i,\mathrm{orig}}$, *i.e.*, $A_i/f_{i,\mathrm{orig}}$, or the lower/upper limit of optimization if the ratio $A_i/f_{i,\mathrm{orig}}$ falls out of bounds. This second adjustment, starting in a remote location of the optimization space, was performed to check for the existence of other local minima of $F(\boldsymbol{A})$.

TABLE 5.3: Rate coefficients corresponding to the $f_{i,\mathrm{orig}}$ set of multipliers, which yield $F(\boldsymbol{A}) = 0.17$.

Reactions	$f_{i,\mathrm{orig}}$	$A_{i,\mathrm{opt}}$ [cm^3, mol, s]	n_i	$E_{\mathrm{a},i}$ [cal/mol]
$\mathrm{CH} + \mathrm{O_2} \leftrightarrow \mathrm{HCO} + \mathrm{O}$	**0.4747**	$8.403 \cdot 10^{10}$	0.760	-478.01
$\mathrm{CH_2} + \mathrm{OH} \leftrightarrow \mathrm{CH} + \mathrm{H_2O}$	0.8519	$9.626 \cdot 10^{6}$	2.000	2999.52
$\mathrm{CH_2} + \mathrm{H} \leftrightarrow \mathrm{CH} + \mathrm{H_2}$	3.198	$1.925 \cdot 10^{13}$	0.000	-1787.76
$\mathrm{H} + \mathrm{CH_3}\,(+\mathrm{M}) \leftrightarrow \mathrm{CH_4}\,(+\mathrm{M})$				
High-pressure limit	0.7847	$9.965 \cdot 10^{15}$	-0.630	383.00
Low-pressure limit		$1.938 \cdot 10^{33}$	-4.760	2440.00
$\mathrm{CH_3} + \mathrm{OH} \leftrightarrow \mathrm{CH_2^*} + \mathrm{H_2O}$	1.502	$2.357 \cdot 10^{17}$	-1.225	1811.00
$\mathrm{CH} + \mathrm{H_2O} \leftrightarrow \mathrm{CH_2O} + \mathrm{H}$	**3.549**	$4.152 \cdot 10^{15}$	-0.750	0.00
$\mathrm{CH_2} + \mathrm{O_2} \leftrightarrow \mathrm{CO} + \mathrm{OH} + \mathrm{H}$	**0.8482**	$5.581 \cdot 10^{12}$	0.000	1491.40
$\leftrightarrow \mathrm{CO_2} + \mathrm{H_2}$		$2.231 \cdot 10^{12}$	0.000	1491.40
$\mathrm{CH_2CO} + \mathrm{O} \leftrightarrow \mathrm{CH_2} + \mathrm{CO_2}$	**1.502**	$3.003 \cdot 10^{13}$	0.000	2294.46

Figure 5.11 compares numerical values of $S_{\mathrm{LIF}}/S_{\mathrm{R}}$ and δ_{CH}, obtained with the non-modified SD mechanism and the two optimized models corresponding to $f_{i,\mathrm{orig}}$ and $f_{i,\mathrm{inv}}$, against the experimental data reported in Chapter 4. As in Figure 4.3, δ_{CH} represents the full width at half maximum of the one-dimensional CH-LIF profiles, which corresponds to the width of the 1D CH concentration profiles magnified by the imaging-system blur (see section 3.3). The error bars applied on the experimental data represent the 95% interval of confidence for the variability in the measurements

[2]For the reaction $\mathrm{CH_3} + \mathrm{OH} \leftrightarrow \mathrm{CH_2^*} + \mathrm{H_2O}$, the multiplier values apply to the updated specific rate description $k(T) = 1.57 \cdot 10^{17} \cdot T^{-1.225} \cdot \exp\left(-1811/R_{\mathrm{u}} \cdot T\right)$ $\mathrm{cm^3/mol-s}$, not to the nominal specific rate included in the SD mechanism.

TABLE 5.4: Rate coefficients corresponding to the $f_{i,\mathrm{inv}}$ set of multipliers, which yield $F(\boldsymbol{A}) = 0.25$.

Reactions	$f_{i,\mathrm{inv}}$	$A_{i,\mathrm{opt}}$ [cm^3, mol, s]	n_i	$E_{\mathrm{a},i}$ [cal/mol]
$\mathrm{CH} + \mathrm{O_2} \leftrightarrow \mathrm{HCO} + \mathrm{O}$	$\mathbf{0.4747}$	$8.403 \cdot 10^{10}$	0.760	-478.01
$\mathrm{CH_2} + \mathrm{OH} \leftrightarrow \mathrm{CH} + \mathrm{H_2O}$	$\mathbf{2.102}$	$2.375 \cdot 10^{7}$	2.000	2999.52
$\mathrm{CH_2} + \mathrm{H} \leftrightarrow \mathrm{CH} + \mathrm{H_2}$	0.7596	$4.573 \cdot 10^{12}$	0.000	-1787.76
$\mathrm{H} + \mathrm{CH_3}\,(+\mathrm{M}) \leftrightarrow \mathrm{CH_4}\,(+\mathrm{M})$				
High-pressure limit	0.5453	$6.926 \cdot 10^{15}$	-0.630	383.00
Low-pressure limit		$1.347 \cdot 10^{33}$	-4.760	2440.00
$\mathrm{CH_3} + \mathrm{OH} \leftrightarrow \mathrm{CH_2^*} + \mathrm{H_2O}$	0.8936	$1.403 \cdot 10^{17}$	-1.225	1811.00
$\mathrm{CH} + \mathrm{H_2O} \leftrightarrow \mathrm{CH_2O} + \mathrm{H}$	$\mathbf{2.281}$	$2.669 \cdot 10^{15}$	-0.750	0.00
$\mathrm{CH_2} + \mathrm{O_2} \leftrightarrow \mathrm{CO} + \mathrm{OH} + \mathrm{H}$	$\mathbf{0.8482}$	$5.581 \cdot 10^{12}$	0.000	1491.40
$\leftrightarrow \mathrm{CO_2} + \mathrm{H_2}$		$2.231 \cdot 10^{12}$	0.000	1491.40
$\mathrm{CH_2CO} + \mathrm{O} \leftrightarrow \mathrm{CH_2} + \mathrm{CO_2}$	$\mathbf{1.490}$	$2.981 \cdot 10^{13}$	0.000	2294.46

(precision). As shown in Figure 5.12, where the error bands of Figure 4.2 are reproduced, all values of $S_{\mathrm{LIF}}/S_{\mathrm{R}}$ predicted by the optimized models are within the limits of uncertainty considering the accuracy and the precision of the measurements. Hence, even if the set of $f_{i,\mathrm{inv}}$ multipliers presents a slightly higher value of $F(\boldsymbol{A})$, both mechanisms are equally valid based on the comparison with experimental $S_{\mathrm{LIF}}/S_{\mathrm{R}}$ values.

For all fuels, the optimization significantly improves the agreement of the numerical LIF signals with the experiments, namely by correcting the over-predicted decline in $S_{\mathrm{LIF}}/S_{\mathrm{R}}$ as the stoichiometry is shifted to leaner mixtures starting from $\phi = 1.2$. The reactions improving the stoichiometric dependence of CH formation have their multiplier shown in boldface in Tables 5.3 and 5.4. They are reactions with a decreasing (increasing) trend of $\mathrm{L.S.}\,(X_{\mathrm{CH,peak}}, i)$ with ϕ (see Figure 5.1), and for which the specific rate is raised (reduced) during the adjustment, *i.e.*, that have a multiplier value $> 1\,(< 1)$. The larger are the $\mathrm{L.S.}\,(X_{\mathrm{CH,peak}}, i)$ and the relative change in the specific rate ($\Delta k_i/k_i$), the larger is the impact on the model response. The main contributors are the reactions $\mathrm{CH} + \mathrm{O_2} \leftrightarrow \mathrm{HCO} + \mathrm{O}$ and $\mathrm{CH} + \mathrm{H_2O} \leftrightarrow \mathrm{CH_2O} + \mathrm{H}$, as well as $\mathrm{CH_2} + \mathrm{OH} \leftrightarrow \mathrm{CH} + \mathrm{H_2O}$ for the model with the $f_{i,\mathrm{inv}}$ multipliers. These reactions are directly involved in the formation and consumption of methylidyne. It must be remembered that the specific rate of the reaction $\mathrm{CH_3} + \mathrm{OH} \leftrightarrow \mathrm{CH_2^*} + \mathrm{H_2O}$ was updated prior to the optimization process (see Figure 5.7 and related discussion). In this context, changing $k(T)$ from the nominal definition in the SD mechanism to the optimized rate is expected not to significantly improve ($f_{i,\mathrm{orig}}$), or to worsen ($f_{i,\mathrm{inv}}$), the trend of $[\mathrm{CH}]_{\mathrm{peak}}$ vs. ϕ. The other, non-boldface, reactions in Tables 5.3 and 5.4 mostly impact CH predictions for rich flames, *e.g.*, $\mathrm{H} + \mathrm{CH_3}\,(+\mathrm{M}) \leftrightarrow \mathrm{CH_4}\,(+\mathrm{M})$, or compensate for the change in the specific rate of the other reactions to achieve the proper amplitude (absolute value) of $[\mathrm{CH}]_{\mathrm{peak}}$.

Interestingly, the agreement in terms of δ_{CH} for rich, $\phi \geq 1.3$, flames is also enhanced, even

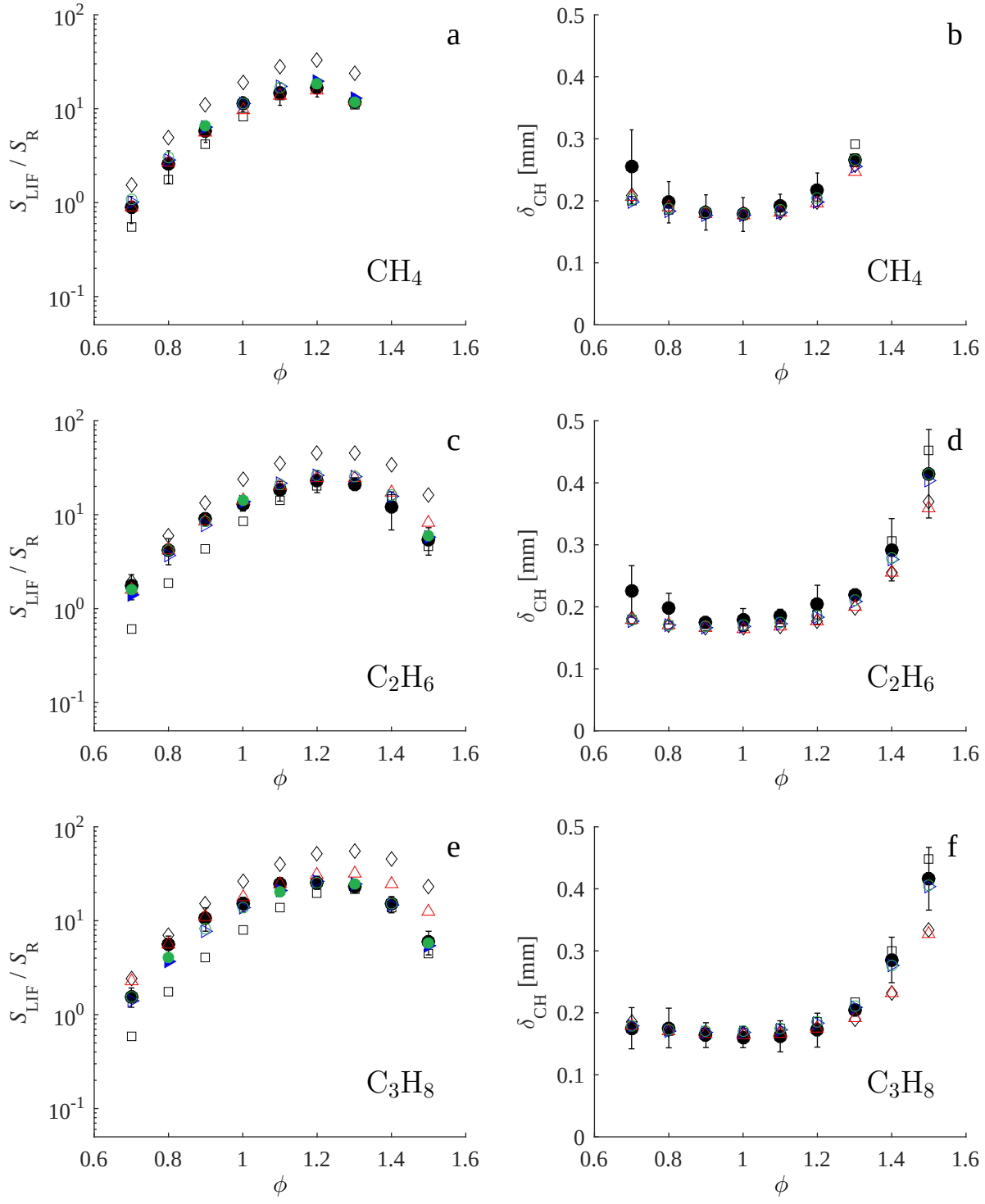

FIGURE 5.11: Measured and simulated values of $S_{\mathrm{LIF}}/S_{\mathrm{R}}$ and δ_{CH} for methane, ethane, and propane premixed flames. Legend: • experiments, □ SD (non-modified), ○ $f_{i,\mathrm{orig}}$ (Table 5.3), ▷ $f_{i,\mathrm{inv}}$ (Table 5.4), ◇ GRI (non-modified), and △ GRI with the rate coefficients of Table 5.3. The solid blue and green symbols correspond to data points included in the optimization and adjusted against the experimental targets presented in Table 5.1. Note the logarithmic scale on plots a, c, and e.

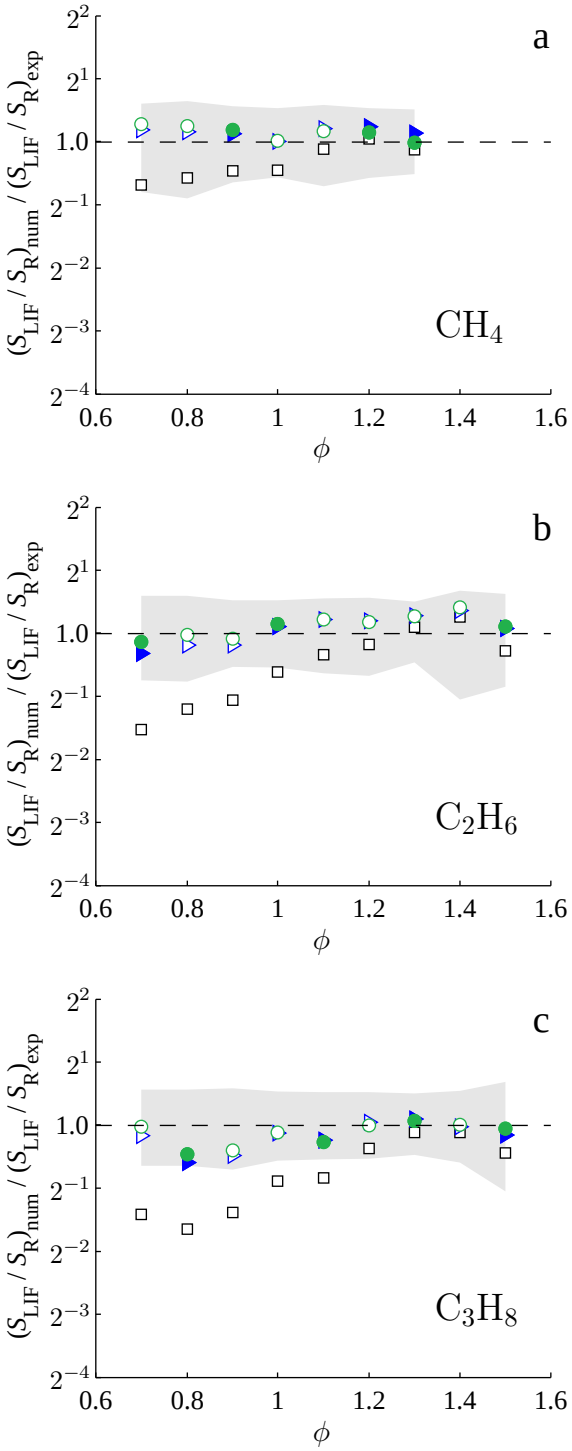

FIGURE 5.12: Numerical $S_{\mathrm{LIF}}/S_{\mathrm{R}}$ normalized by the experimental value for (a) methane, (b) ethane, and (c) propane flames. $(S_{\mathrm{LIF}}/S_{\mathrm{R}})_{\mathrm{num}} / (S_{\mathrm{LIF}}/S_{\mathrm{R}})_{\mathrm{exp}} = 1$ shown by dashed lines indicates exact agreement of the predictions with the experimental data. As in Figure 4.2, the shaded grey bands present the uncertainty resulting from the LIF model, δ_{PSF}, the flame boundary conditions, and the scatter in the measurements (see section 4.1). Same legend as Figure 5.11.

if the thickness of the CH layer was not considered as an optimization target. From flame theory, the reaction zone thickness is proportional to α/s_{L}, where α is the thermal diffusivity, and S_{L} is the laminar flame speed [190]. Among the reactions included in the optimization, the laminar flame speed is principally sensitive to the rate of the reaction $\mathrm{H} + \mathrm{CH_3}\,(+\mathrm{M}) \leftrightarrow \mathrm{CH_4}\,(+\mathrm{M})$, particularly for rich mixtures [65, 134]. Decreasing the specific rate of this reaction as prescribed by the two optimized mechanisms leads to an increase in the burning rate of rich flames which, based on flame theory, should make the flame, and consequently the CH layer, thinner thus improving the accuracy of the predicted δ_{CH} values. For lean methane and ethane flames, the discrepancies between the numerical and experimental values of δ_{CH} were attributed in Chapter 4 to weak signal-to-noise ratios at these conditions artificially broadening the experimental CH layer thickness. For all other fuels and equivalence ratios, the values of δ_{CH} predicted by the optimized mechanisms are consistent with the already accurate estimations of the SD model.

To determine if the specific rates derived in the current work apply to other thermochemical mechanisms, additional simulations were performed with the GRI model. As shown in Figure 5.11, the original GRI mechanism generally over-predicts the experiments beyond uncertainty and, for ethane and propane flames, the disagreement grows with the equivalence ratio. Inserting the optimized rate coefficients of Table 5.3 in the GRI mechanism results in CH-LIF signals and δ_{CH} values agreeing, within uncertainty, with the experimental data for methane, ethane, and propane ($\phi \leq 1.2$) flames. Consequently, the sets of optimized specific rates presented in this study are not restricted to the SD model. They can be used in other kinetic mechanisms, which should be benchmarked against the experimental data presented in this dissertation.

The two sets of optimized specific rates are superimposed as green long-dashed ($f_{i,\mathrm{orig}}$), and blue dash-dotted ($f_{i,\mathrm{inv}}$) curves in Figures 5.3 to 5.10. It is difficult, as all mechanisms have their own set of elementary reactions, to identify a single cause for the generalized problem of over-predicted decline in $[\mathrm{CH}]_{\mathrm{peak}}$ as ϕ decreases, and to suggest a single solution to make all kinetic models accurate. Nevertheless, a few observations can be made based on the current optimization:

- both optimized mechanisms have a multiplier of 0.4747 for the reaction $\mathrm{CH} + \mathrm{O_2} \leftrightarrow \mathrm{HCO} + \mathrm{O}$, which yields a $k(T)$ description lower than all considered models, and in line with the low temperature recommendation of Baulch et al. [199] (see Figure 5.3). The specific rate of this reaction is likely overestimated in most thermochemical mechanisms and, since $\mathrm{L.S.}\,(X_{\mathrm{CH,peak}}, i)$ increases with ϕ for this reaction, reducing its $k(T)$ would improve the stoichiometric dependence of $[\mathrm{CH}]_{\mathrm{peak}}$ predictions.

- the improper stoichiometric dependence of $[\mathrm{CH}]_{\mathrm{peak}}$ is solved by adjusting the specific rate of a few key reactions identified in Figure 5.2. Additional reactions do not need to be included

in the mechanism; the simple structure of the SD model is sufficient to accurately predict CH formation over a wide range of equivalence ratios.

- the existence of two sets of optimized multipliers, which yield CH-LIF signal predictions agreeing, within uncertainty, with the experimental data, demonstrates the need for 1) further experimental and/or numerical fundamental studies to reduce the uncertainty in the specific rate of the reactions, and/or 2) additional, independent experimental targets to constrain the optimization and decide on a single set of rate coefficients.

- as shown in Figure 5.4, $k(T)$ for the $f_{i,\mathrm{orig}}$ set of multipliers is in fair agreement with the widely used rate description for the reaction $\mathrm{CH_2 + OH \leftrightarrow CH + H_2O}$, while the specific rate of the mechanism with the $f_{i,\mathrm{inv}}$ multipliers lies close to the upper optimization bound. Furthermore, the former is fairly consistent with the rates included in the NUIG2 and KON mechanisms for the reaction $\mathrm{CH_2 + H \leftrightarrow CH + H_2}$, while the latter sits on the lower bound of optimization, below the specific rate descriptions of all mechanisms (see Figure 5.5). Based on these arguments, one could favour the $f_{i,\mathrm{orig}}$ set of multipliers.

- both optimizations suggest a decrease in the specific rate of the reaction $\mathrm{H + CH_3\,(+M) \leftrightarrow CH_4\,(+M)}$ (see Figure 5.6) which, as discussed above, is the likely cause of the improved predictions of δ_{CH} for rich flames. Such a reduction in $k(T)$ is consistent with the results of the optimization of the SD mechanism based on the strained reference flame speeds and thermal-NO formation rates of stoichiometric, $\mathrm{C_1}$-$\mathrm{C_3}$ alkanes and $\mathrm{C_1}$-$\mathrm{C_2}$ alcohols, premixed flames presented in [64].

- both optimizations maintain a specific rate description approximately one order of magnitude higher than the mechanisms [65, 133–135] and the recommendation of Baulch et al. [199] for the reaction $\mathrm{CH_2CO + O \leftrightarrow CH_2 + CO_2}$. Based on Figure 5.1, increasing the specific rate of this reaction contributes to solve the problem with the stoichiometric dependence of $[\mathrm{CH}]_{\mathrm{peak}}$, which aggravates for alkane chain lengths longer than $\mathrm{C_1}$.

5.3 Conclusion

This chapter presented an optimization of the San Diego mechanism [128] against the experimentally determined CH-LIF signal and layer thickness data presented in Chapter 4. Nine elementary

reactions were selected, which featured a large uncertainty in their specific rate and a significant impact on the formation of methylidyne. These reactions, interacting with the CH formation route, require further consideration from the combustion community to converge towards a unique, accurate description of their specific rate. The optimization was constrained by meticulously selected bounds on the value of the pre-exponential factors, and performed using a non-linear, quasi-Newton, multi-variate algorithm minimizing an objective function defined as the sum of squares of the relative difference between numerical CH-LIF signals and a selection of experimental data points.

The adjustment procedure provided two mechanisms that agree, within uncertainty, with the experimentally determined CH-LIF layer thicknesses and signal intensities presented in Chapter 4. Namely, the over-predicted decrease in CH formation as the stoichiometry is shifted to lean mixtures, also observed in [79, 99], is resolved, primarily by adjusting the specific rate of the reactions $\mathrm{CH} + \mathrm{O_2} \leftrightarrow \mathrm{HCO} + \mathrm{O}$, $\mathrm{CH_2} + \mathrm{OH} \leftrightarrow \mathrm{CH} + \mathrm{H_2O}$, and $\mathrm{CH} + \mathrm{H_2O} \leftrightarrow \mathrm{CH_2O} + \mathrm{H}$, and does not require the addition of supplementary reactions to the simple structure of the San Diego mechanism. The specific rate of the other reactions was adjusted to improve the predictions for rich flames, or to achieve the proper absolute values of LIF signal intensities. A single, common cause explaining the improper trend of CH formation with the equivalence ratio could not be identified due to the lack of consistency among the mechanisms in terms of elementary reactions and specific rates. However, the results suggest that the rate of the reaction $\mathrm{CH} + \mathrm{O_2} \leftrightarrow \mathrm{HCO} + \mathrm{O}$ should be reduced, and that of the reaction $\mathrm{CH_2CO} + \mathrm{O} \leftrightarrow \mathrm{CH_2} + \mathrm{CO_2}$ increased, in most thermochemical mechanisms.

Finally, the optimized specific rates provided in this study are not exclusive to the San Diego mechanism. They were successfully implemented in the GRI Mech 3.0 model to improve its predictive performance in terms of CH concentrations.

Chapter 6

Conclusion

6.1 Synopsis

Increasingly stringent regulations on NO_x emissions are enforced by governments because of their contribution to the formation of ozone, smog, fine aerosols, acid precipitations, and nutrient pollution of surface water, which affect human health and the environment. The design of high-efficiency engines achieving these ever-decreasing emission standards requires thermochemical mechanisms of sufficiently high accuracy for use as design tools. The experimental study of Watson, Versailles, and Bergthorson [64], reporting velocity, temperature, CH, and NO concentration profiles in atmospheric, jet-wall, stagnation, premixed flames of C_1-C_4 alkane and alcohol fuels, demonstrated a strong correlation between the maximum concentration of the methylidyne radical scaled by the flow residence time within the CH layer and the formation of NO through the prompt (Fenimore) route. This confirms the dominant role of CH as a precursor to NO, and requires that thermochemical models accurately describe methylidyne formation for a wide range of fuels and equivalence ratios.

In this study, CH formation in premixed flames of C_1 to n-C_4 alkanes is quantitatively measured by laser induced fluorescence in a jet-wall burner. This configuration, described in Chapter 2, provides stable, small-scale, quasi-one-dimensional lifted flames well suited for laser diagnostics. The ability to measure all necessary boundary conditions allows for direct and accurate comparisons between experiments and flame simulations based on detailed thermochemical mechanisms. A complete description of the particle tracking velocimetry method, as well as an uncertainty analysis of the velocity boundary conditions for the quasi-one-dimensional flame simulations, is provided in Chapter 2. The CH concentration is probed by quantitative, planar laser-induced fluorescence calibrated by the Rayleigh scattering signal of nitrogen. Consistent with the methodology proposed by Connelly et al. [153], experimentally determined ratios of CH-LIF to Rayleigh scattering signals are directly compared to simulations.

The predictions of four thermochemical mechanisms (San Diego Mechanism version 2005, USC Mech version II, AramcoMech 1.3, and GRI-Mech version 3.0) are converted into units compatible with the LIF measurements using a time-resolved, four-level LIF model developed in the course of the work, and thoroughly discussed in Chapter 3. The validity of the assumptions commonly made in the analysis of CH-LIF in the A-X electronic system is assessed. It is shown that steady-state populations in the ground and electronically excited states, a condition usually hypothesized in the development of an algebraic equation relating the LIF signal to the number density of CH, are not achieved for short, nanosecond laser pulses and, therefore, the adequacy of steady-state LIF models is fortuitous. Furthermore, the concerns raised in [98, 118] with regards to the comparable time scales of the LIF system and flame chemistry potentially affecting the CH-LIF diagnostic are addressed. It is demonstrated that the overall (net) chemical production rate of methylidyne in the ground and electronically excited states is too small to significantly interact with the nanosecond LIF system. The uncertainty in the signals predicted by the LIF model, based on the flame simulations, is also quantified.

The experimental data, presented in Chapter 4, show that the peak CH-LIF signal is observed for flames with an equivalence ratio of 1.2, and decreases monotonically for leaner and richer mixtures. The consistency of this behaviour for all considered alkanes suggests that the formation of methylidyne is determined by a common, limited set of fuel-independent elementary reactions. Among the four thermochemical mechanisms studied in this dissertation, the San Diego model yields the best overall performance over the range of fuels and equivalence ratios investigated, while the GRI-Mech mechanism provides the most accurate predictions for lean ethane and propane flames. The USC Mech and GRI-Mech mechanisms consistently over-predict, and the AramcoMech 1.3 mechanism under-predicts, the experimental data. Variability in the predictions over more than an order of magnitude is observed, significantly beyond the estimated errors in the measurements and the time-resolved, four-level LIF model. It is also noted, as in [79, 99], that the thermochemical mechanisms generally over-predict the decrease in the maximum CH concentration as the stoichiometry is shifted to leaner mixtures from its maximum value observed at an equivalence ratio of 1.2. The thickness of the CH layer is well reproduced when the point-spread function of the imaging system is accounted for, except for the richest flames for which discrepancies among the models, and against the experimental data, are noticed.

The source of the variability in the predictive performance of the mechanisms is investigated using reaction pathway and sensitivity analyses. Significant differences in the specific rates are observed for reactions interacting with the CH formation route, namely $\mathrm{CH_2 + H \leftrightarrow CH + H_2}$, and $\mathrm{CH_3 + OH \leftrightarrow CH_2^* + H_2O}$. Furthermore, the mechanisms disagree regarding which reactions

consume methylidyne, and also regarding their rate coefficients. To correct the deficiencies identified in the numerical LIF signals, an optimization of the specific rate of nine elementary reactions included in the San Diego mechanism, interacting with the CH formation route, is performed (see Chapter 5). A quasi-Newton algorithm is used to minimize an objective function defined as the sum of squares of the relative difference between the numerical and experimental CH-LIF data, while constraining the specific rates to physically reasonable values. Two mechanisms properly describing, within uncertainty, CH formation for lean to rich $\mathrm{C_1}$-$\mathrm{C_3}$ alkane-air flames are obtained. The optimized mechanisms also provide improved values of CH layer thickness for the richest flames, even if it was not included as an optimization target. These optimized mechanisms will enable accurate predictions of prompt-NO formation over a wide range of equivalence ratios and alkane fuels. Suggestions regarding which reactions require further investigations, either through experimental or theoretical assessments of the individual specific rates, are also provided.

6.2 Contributions

Given its primary role as a precursor to prompt-NO, the global objective of this work was to evaluate the ability of thermochemical mechanisms to predict CH formation in flames. For this assessment, 33 premixed, $\mathrm{C_1}$-$\mathrm{C_4}$ normal alkane-air flames were experimentally investigated. A series of contributions resulted from that effort:

- the assembly of a time-resolved, four-level LIF model, and an evaluation of the commonly made hypotheses in modelling CH-LIF in the A-X electronic system. Upon proper readjustment of its constituting parameters, this model could be used for other molecules, or energy levels, not affected by predissociation, photoionization, and electronic and vibrational energy transfers.

- a first set of quantitative, experimental CH concentration data at atmospheric pressure for a variety of alkane fuels and equivalence ratios. This dataset provides validation and optimization targets for future combustion model revisions.

- a thorough discussion on the sources of the order of magnitude variability in CH predictions among currently available thermochemical mechanisms, and on the causes of the improper variation in CH concentration with the equivalence ratio predicted by most models.

– the identification, via a novel optimization method, of the reactions requiring further attention from the combustion community for future thermochemical models to accurately capture the sensitivity of the CH concentration to changes in the stoichiometry of the reactant mixture.

– optimized thermochemical mechanisms properly describing CH formation for premixed ($0.7 \leq \phi \leq 1.5$), C_1-C_3 alkane-air flames, and enabling accurate predictions of prompt-NO formation.

Through these contributions, it was demonstrated that:

– the formation of methylidyne in premixed alkane-air flames is controlled by a limited, common set of fuel-independent elementary reactions.

– current thermochemical mechanisms are unable to accurately describe CH formation for lean to rich combustible mixtures of normal alkanes with air and, as such, cannot provide accurate predictions of prompt-NO concentration, which is the second most important NO formation route in the majority of premixed flames [61]. These deficiencies have important implications for the conception of low-emission engines, which often relies on thermochemical mechanisms as design tools.

– the error induced by the uncertain Arrhenius rate coefficients is so important that all thermochemical mechanisms feature CH-LIF signal predictions lying outside of the experimental uncertainty limits (see Figure 4.2). Therefore, the current experimentally determined LIF-to-Rayleigh ratios can be used as optimization and validation targets to improve the accuracy of thermochemical mechanisms.

– the adjustment of the specific rate of a few key reactions allows to reconcile the CH-LIF signal predictions with the experimental data. Furthermore, the optimization procedure did not require to modify the structure, *i.e.*, adding or removing chemical reactions, of the San Diego model, which includes the fewest number of species and elementary reactions among the mechanisms considered in this study. Therefore, the inclusion of all possible product channels for a given reaction, *e.g.*, for the reactions $CH + O_2 \rightarrow \text{products}$ and $CH_2 + O_2 \rightarrow \text{products}$ (see equations 5.4 and 5.6), as performed in large, comprehensive thermochemical mechanisms, is unnecessary for the models to serve as efficient and accurate engineering design tools.

6.3 Future research directions

6.3.1 Experimental study of NO formation at high-pressure conditions

The experimental data produced by the Alternative Fuels Laboratory over the last five years provide important insight on the formation of nitric oxide in flames of fossil and bio-derived fuels [60, 61, 64, 69, 92, 122, 218]. These studies demonstrate the inability of modern thermochemical mechanisms to accurately describe the formation of nitric oxide due to improper predictions of 1) the rate of the reaction initiating the thermal-NO formation route (see equation 1.11), 2) the flame burning rate, and 3) the concentration profile of CH. The comprehensive set of experimental data presented in these publications allows the development of accurate thermochemical models for atmospheric-pressure flames.

With a few exceptions, namely the $\phi \approx 0.7$ flames reported in [60, 61, 218], the thermal and prompt NO formation routes are the most important in the atmospheric-pressure flames studied by the Alternative Fuels Laboratory. However, internal combustion engines operate at pressures several times higher than atmospheric conditions [14], and uncertainty remains regarding the contribution of the individual NO formation routes at engine relevant pressures [219, 220]. Namely, the N_2O pathway, which consists of reactions 6.1 to 6.3, is initiated by a termolecular recombination reaction expected to become increasingly important at higher pressures [57, 59], therefore favouring NO formation through this route as predicted by flame simulations [57, 219, 221]. Even more, Gokulakrishnan and Klassen [57] claim that the N_2O pathway is a major route of NO formation in gas turbine combustors operating in the lean-premixed mode.

$$N_2 + O + M \leftrightarrow N_2O + M \tag{6.1}$$

$$N_2O + O \leftrightarrow NO + NO \tag{6.2}$$

$$N_2O + H \leftrightarrow NO + NH \tag{6.3}$$

In contrast, simulations of lean, premixed, methane-air flames [57, 219] suggest that the formation of NO through the NNH route of equations 6.4 and 6.5 [57, 59, 222] will decrease and become negligible at sufficiently high pressures. However, exploratory simulations performed with the GRI-Mech 3.0 mechanism, not presented here for the sake of brevity, revealed that the NNH route is dominant at all pressures, from atmospheric to gas turbine conditions, for premixed

hydrogen-air flames. The NNH route is also expected to be an important NO formation pathway in high-pressure, premixed flames of coal gas (syngas mixed with methane) [223]. Therefore, the study of the NNH route has important implications for the development of advanced internal combustion engines operating on biofuels, such as hydrogen and syngas.

$$\mathrm{N_2 + H \leftrightarrow NNH} \tag{6.4}$$

$$\mathrm{NNH + O \leftrightarrow NO + NH} \tag{6.5}$$

It must be noted that these effects of the pressure on the formation of nitric oxide are expected based on simulations performed with thermochemical mechanisms whose NO chemistry was not, or minimally, validated at high pressures. Given the wide variability observed in the NO predictions at atmospheric conditions [60, 61, 64, 69], these conclusions should be considered with caution.

NO concentration data in high-pressure, premixed flames are relatively sparse. Laurendeau and co-workers reported NO-LIF measurements in premixed flames of methane [220], ethane [224], ethylene [225], and synthesized coal gas ($\mathrm{CH_4/H_2/CO}$) [223] stabilized above the surface of a sintered-bronze McKenna burner at pressures up to 14.6 atm. This type of burner is characterized by the flame front sitting very close to the water-cooled surface, and increasing the pressure exacerbates that effect [220]. Because of intense light scattering off the burner surface, it is nearly impossible to perform laser-based diagnostics through the flame front, and only point measurements [224, 225] or partial NO profiles [220, 223] can be obtained in the post-flame region. Furthermore, these flames are stabilized through heat loss to the burner, which impacts their thermodynamics and chemistry [226]. Recently, Pillier et al. [219] presented NO-LIF measurements obtained in lean, counterflow, stagnation, premixed methane-air flames at pressures up to 0.7 MPa. Even though lifted stagnation flames are free from influences from the burner boundaries and allow for spatially resolved laser diagnostics throughout the flame, the data of Pillier et al. [219] are limited to a single equivalence ratio, $\phi = 0.7$. Furthermore, they did not report flame speed nor temperature measurements, even if NO formation is highly sensitive to these factors, as shown in our previous publications [64, 69]. Therefore, there is a need for a comprehensive set of experimental data including NO, CH, temperature, and velocity profiles in high-pressure flames for a variety of fuels and a wide range of equivalence ratios to 1) test the ability of current thermochemical mechanisms at predicting the formation of NO, and 2) thoroughly investigate the NO formation routes.

A high-pressure combustion apparatus was designed and built in parallel to the work presented

in this dissertation. It consists of a jet-wall, stagnation burner installed in a vessel capable of continuous operation at the full-load pressure of modern aero-derivative gas turbine combustors. The three-dimensional computer-aided design model of the apparatus is presented in Figure 6.1(a). The vessel, made of duplex and super-duplex grades of stainless steel, is equipped with two pairs of sapphire glass windows for laser-based diagnostics. The jet-wall, stagnation burner, optimized for high-pressure operation, is shown in Figure 6.1(b). The interior contour of the inner nozzle was designed using a CFD-validated, Thwaites method [123], while the passage between the inner and outer nozzles (inert, co-flowing stream), the exterior surface of the outer nozzle, and the shape of the water-cooled stagnation plate were iteratively optimized through a sequence of CFD computations performed with ANSYS Fluent. The mass flow rates of fuel, air, and inert delivered to the burner are metered by Bronkhorst thermal mass controllers, and fed into the vessel through the lower flange. To prevent water vapour condensation on the interior surfaces of the enclosure, namely the windows, it is continuously purged by a stream of nitrogen. The pressure in the vessel is controlled by a Bronkhorst controller, based on a diaphragm piezo-resistive sensor, driving a pneumatic valve. The apparatus, surrounded by all the necessary equipment for its operation and laser-based diagnostics, is shown in Figure 6.2.

Thus far, premixed methane-air flames were successfully stabilized for pressures ranging between 1 and 16 atm, and equivalence ratios from 0.7 to 1.3. The maximum pressure is currently limited by the gas cylinder regulators, not by the apparatus. A few sample flame images are shown in Figure 6.3. As expected from the careful design, the flames are flat and devoid of oscillations, therefore allowing PTV and LIF diagnostics, which require several thousand images of the same flame to be recorded over a few minutes. For this future test campaign, the PTV and NO-LIF methods were extended to provide two-dimensional velocity, NO, and temperature fields to confirm that the assumptions underlying the quasi-one-dimensional model of Kee et al. [114] apply. Through the next years, important data will be provided by this state-of-the-art apparatus, which can readily be adapted to study partially and non-premixed flames by integrating a second, counter-flowing nozzle assembly in place of the stagnation plate.

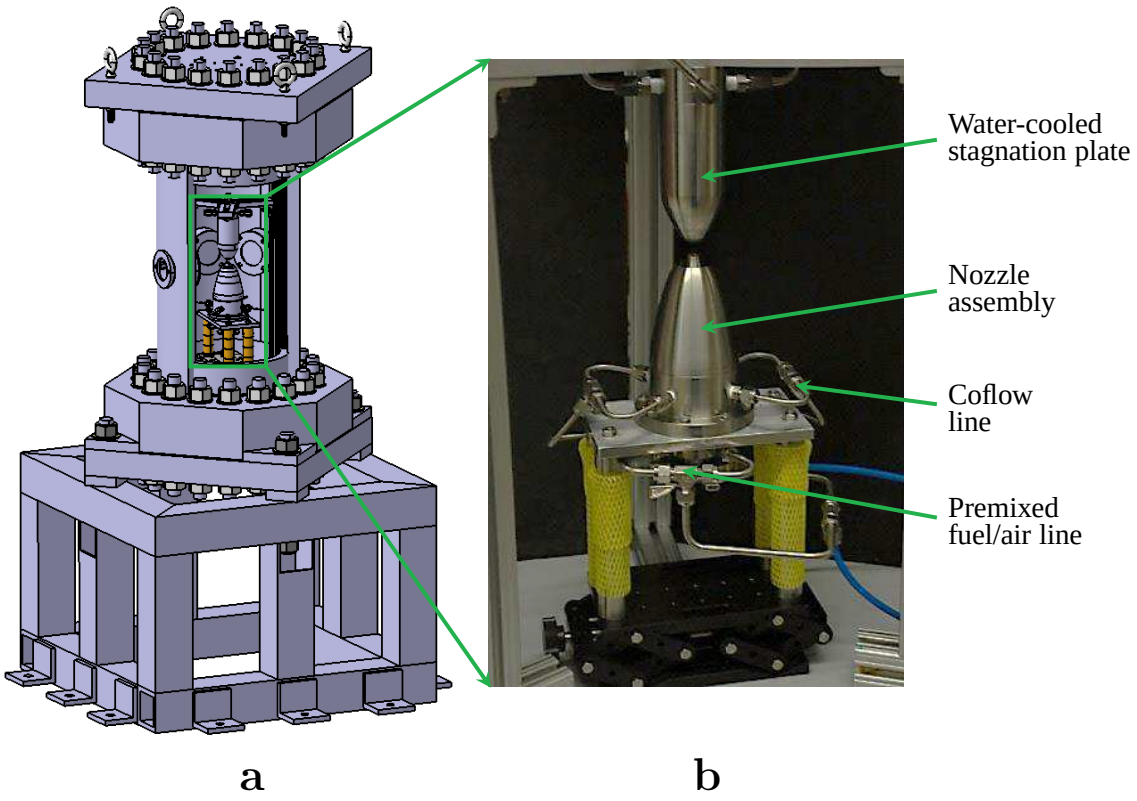

FIGURE 6.1: (a) Computer-aided design model of the apparatus, and (b) jet-wall, stagnation flame burner optimized for high-pressure operation.

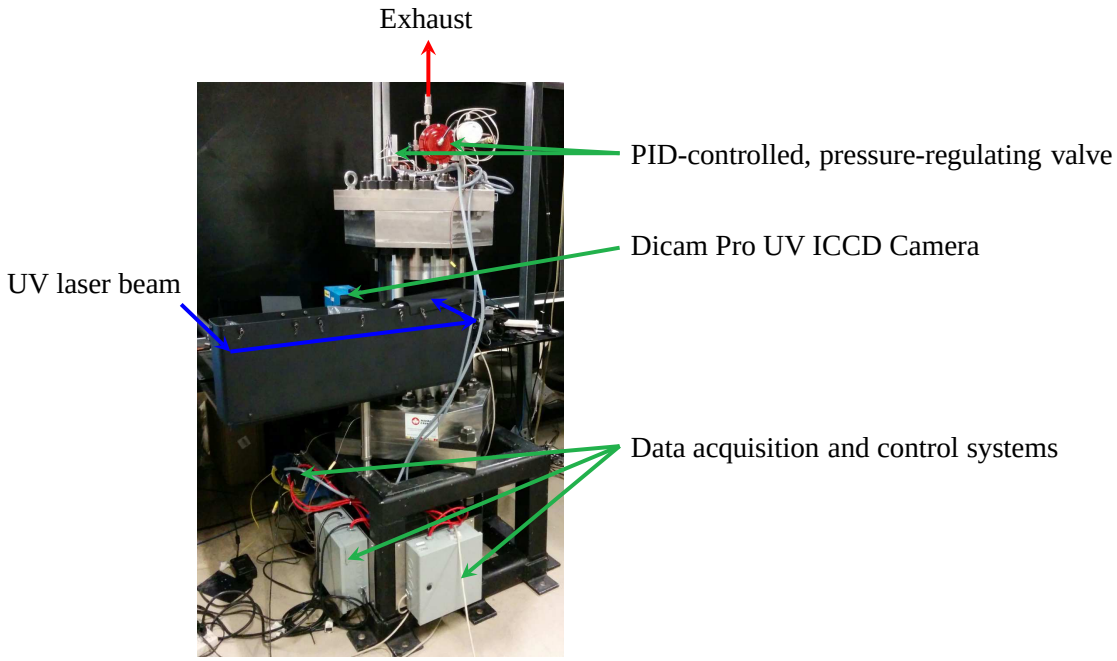

FIGURE 6.2: High-pressure combustion apparatus surrounded by all the necessary equipment for its operation and laser-based diagnostics. The UV (~226 nm) laser beam, shown by the blue arrows, is covered by a flat black enclosure for the sake of safety. The PTV camera and laser beam are hidden behind the vessel.

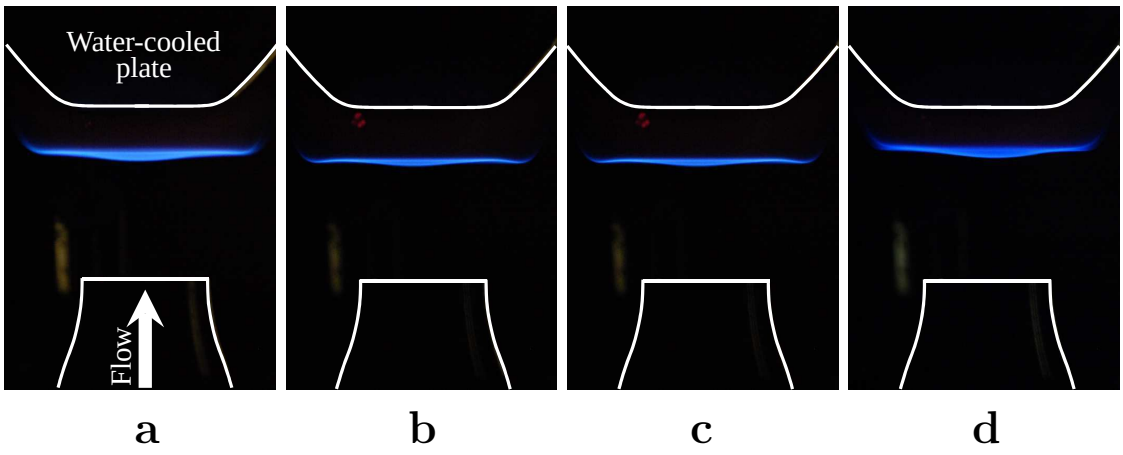

FIGURE 6.3: Sample images of methane-air premixed flames at (a) $P = 4$ atm, and $\phi \approx 0.80$, (b) $P = 5$ atm, and $\phi \approx 0.76$, (c) $P = 6$ atm, and $\phi \approx 0.73$, and (d) $P = 7$ atm, and $\phi \approx 0.73$.

Appendix A

Reaction pathway analysis

Modern thermochemical mechanisms are becoming increasingly complex, including hundreds to thousands of species and reactions [128, 135, 203, 204]. This level of complexity hinders straightforward conclusions regarding the combustion process of interest; it is impossible through inspection of the databases of reactions to find the dominant ones, or to determine the principal pathways through which reactants are made into products. Reaction pathway analysis (RPA) is a useful tool to visualize and understand the complex chemistry included in modern thermochemical mechanisms. It produces a directed graph (a network), where the nodes are chemical species, which are linked together by arrows representing the chemical reactions (see Figure 4.4). In the literature, a convention for the scaling of the width of the arrows has yet to be adopted [136]. Some RPA methods rely on non-conserved, molar-based quantities, *e.g.*, the rate of progress of individual reactions [219, 227, 228]. This yields directed graphs in which the sums of the width of the arrows directed towards and away from a given species are not equal. Others present directed graphs with arrows of equal width, omitting any quantitative information [229], or conveying it through superimposed numerical values [130, 131, 219, 230]. In this case, the dominant chemical pathways are not intuitively identified.

The current RPA method is inspired by the work of Grcar et al. [136] in which the flux of a given atom (*e.g.*, C, N, O, H, etc.), a conserved scalar, is tracked as the reactants are made into products, and the width of the arrows in the directed graph scaled accordingly. In this appendix, the RPA method is described in detail, along with its integration into a computer-based script. The principal modifications in comparison to the formulation of Grcar et al. [136] are also discussed.

A.1 Mathematical formulation

In the current formulation, the width of the arrows connecting the species in the RPA diagram is linearly scaled with the rate of transfer of element e from species s_1 to s_2 integrated over the control

volume V, $R(e, s_1, s_2)$ [kmol/s]. It is defined in equation A.1, where $n_l(e, s_1, s_2)$ is the number of atoms of element e transferred from species s_1 to s_2 through reaction l, $q_l(x, y, z)$ [kmol/m^3-s] is the rate of progress variable of reaction l (see equation A.2), and V [m^3] is the volume over which the reaction pathway analysis is performed . As atoms are neither produced nor consumed in chemical reactions, $R(e, s_1, s_2)$ is a conserved scalar. It follows that $\sum_i R(e, s_i, s_2) = \sum_j R(e, s_2, s_j)$ or, in other words, that the sum of the width of the arrows directed towards a species is equal to the sum of the width of the arrows directed away from that same molecule.

$$R(e, s_1, s_2) = \sum_l \int_V n_l(e, s_1, s_2) \cdot q_l(x, y, z) \cdot \mathrm{d}V \tag{A.1}$$

$$q_l = k_{f,l} \prod_{i=1}^{N} [\mathrm{M}_i]^{\nu'_{i,l}} - k_{b,l} \prod_{j=1}^{N} [\mathrm{M}_j]^{\nu''_{j,l}} \tag{A.2}$$

Here, the volumetric formulation of Grcar et al. [136] is modified to process simulations of one-dimensional (1D), freely propagating flames (Figure A.1(a)), and quasi-1D, axisymmetric, stagnation flames (Figure A.1(b)). In both cases, the fields of temperature and species concentrations solely depend on the axial position, z. Consequently, the rate of progress variable simplifies to $q_l(z)$. Also, the integral is performed over a cylindrical control volume (CV) of fixed radius, r_{CV}, adjusted to achieve an influx of element e of 1 kmol/s. As such, $R(e, s_1, s_2)$ can be thought of as an absolute flux of element e, or as a fraction of the flux of e-atoms entering the control volume. Including these simplifications in equation A.1 yields:

$$R(e, s_1, s_2) = \sum_l \int_{z_{\mathrm{in}}}^{z_{\mathrm{out}}} n_l(e, s_1, s_2) \cdot q_l(z) \cdot \pi r_{\mathrm{CV}}^2 \cdot \mathrm{d}z. \tag{A.3}$$

For freely propagating, 1D flames (Figure A.1(a)), the inlet and outlet of the control volume are placed sufficiently far upstream and downstream of the flame front, respectively, to ensure negligible molecular transport at the boundaries. For stagnation flames (Figure A.1(b)), z_{in} is placed at a sufficient distance upstream of the flame front to make the diffusion of species negligible, while z_{out} coincides with the stagnation surface. As discussed in section 2.1.2.1, the boundary conditions of the quasi-1D model imply no-flux of species at the stagnation surface. Furthermore, as the temperature and species concentration fields are unidimensional for both types of flame simulation, molecular transport through the side surface of the control volume does not occur. Therefore, e-atoms traverse the boundaries of the control volume solely through convection. For freely propagating flames, the control volume is a stream tube, and the e-atoms enter through the surface at

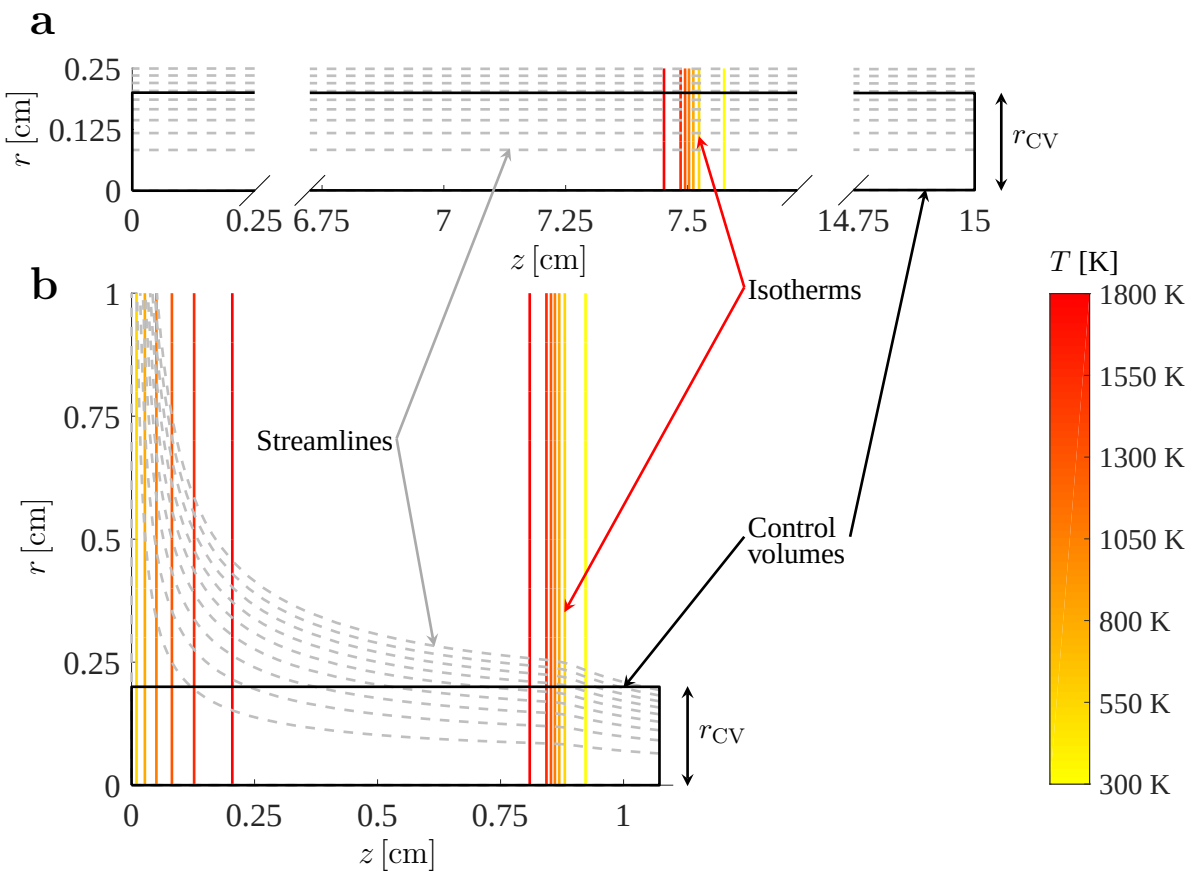

FIGURE A.1: Control volumes for the reaction pathway analysis of (a) freely propagating, premixed flames, and (b) premixed stagnation flames. Flow is right to left. The isotherms and streamlines are obtained from solutions of lean ($\phi = 0.8$), premixed methane-air flames simulated with the SD mechanism.

$z = z_{\text{in}}$, and exit at $z = z_{\text{out}}$. In contrast, for stagnation flames, e-atoms are entering the CV at the upstream boundary ($z = z_{\text{in}}$), and leaving through the side surface ($r = r_{\text{CV}}$).

The rate at which e-atoms enter the control volume via convection of species s_i, $R(e, \text{inlet}, s_i)$, is calculated as the product of the molar flow rate of species s_i, $\dot{n}_i$, with the number of e-atoms per molecule of species s_i, $\nu_{e,i}$ [kmol$_e$/kmol$_i$]:

$$\begin{aligned} R(e, \text{inlet}, s_i) &= \dot{n}_i(z_{\text{in}}) \cdot \nu_{e,i} \\ &= \frac{\dot{m}_i(z_{\text{in}})}{W_i} \cdot \nu_{e,i} \\ &= \rho(z_{\text{in}}) \cdot Y_i(z_{\text{in}}) \cdot u(z_{\text{in}}) \cdot \pi r_{\text{CV}}^2 \cdot \frac{1}{W_i} \cdot \nu_{e,i}, \end{aligned} \tag{A.4}$$

where $\dot{m}_i$ is the mass flow rate of species s_i [kg/s], ρ [kg/m^3] is the density, Y_i is the mass fraction

of species s_i, $u(z)$ [m/s] is the axial velocity, and W_i [kg/kmol] is the molar mass of species s_i. It is noted that for both types of flame simulation, the axial velocity does not vary radially and, therefore, $u(z,r) = u(z)$. For freely propagating flames, the e-atoms leave the control volume by convection of species s_i at a rate $R(e, s_i, \text{outlet})$ defined as:

$$\begin{aligned} R(e, s_i, \text{outlet}) &= \dot{m}_i(z_{\text{out}}) \cdot \nu_{e,i} \\ &= \frac{\dot{m}_i(z_{\text{out}})}{W_i} \cdot \nu_{e,i} \\ &= \rho(z_{\text{out}}) \cdot Y_i(z_{\text{out}}) \cdot u(z_{\text{out}}) \cdot \pi r_{\text{CV}}^2 \cdot \frac{1}{W_i} \cdot \nu_{e,i}. \end{aligned} \tag{A.5}$$

On the other hand, for stagnation flames, e-atoms leave the control volume through the side surface. In this case, the radially outward rate of e-atoms due to convection of species s_i is calculated as:

$$R(e, s_i, \text{outlet}) = \frac{\nu_{e,i}}{W_i} \cdot \int_{z_{\text{in}}}^{z_{\text{out}}} \rho(z) \cdot Y_i(z) \cdot v(z, r_{\text{CV}}) \cdot 2\pi r_{\text{CV}} \cdot \mathrm{d}z, \tag{A.6}$$

where $v(z, r_{\text{CV}})$ [m/s] is the radial velocity at $r = r_{\text{CV}}$. Commonly, the radial velocity is not output by the flame solver as it depends on the radial coordinate. Instead, the parameter $G(z)$ is provided, which through the stream function is linked to the radial velocity [114]:

$$G(z) = \frac{-\rho(z) \cdot v(z,r)}{r}. \tag{A.7}$$

Equation A.6 then becomes:

$$R(e, s_i, \text{outlet}) = -\frac{\nu_{e,i}}{W_i} \cdot \int_{z_{\text{in}}}^{z_{\text{out}}} Y_i(z) \cdot G(z) \cdot 2\pi r_{\text{CV}}^2 \cdot \mathrm{d}z. \tag{A.8}$$

A.2 Implementation of the RPA method in a computer program

The rate of transfer of element e from species s_1 to s_2, $R(e, s_1, s_2)$, was defined in equation A.3. The rate of progress variable of each reaction l, q_l, is extracted from discrete flame solutions. Therefore, the integral in equation A.3 cannot be computed analytically, and must rather be approximated through numerical integration which, as shown in equation A.10, consists of integrating an interpolation polynomial, $p_n(z)$. However, this approximation of the integral is plagued by

an error, $\int_{z_0}^{z_n} E_n(z)\mathrm{d}z$. Inspection of equation A.3 reveals that for each (s_1, s_2) couple, the computation of $R(e, s_1, s_2)$ can require the numerical integral to be performed as many times as there are reactions in the thermochemical mechanism studied. Hence, the numerical integration errors can accumulate into a significant level of inaccuracy in $R(e, s_1, s_2)$. Taking advantage of the sum rule in integration, equation A.3 is rearranged as:

$$R(e, s_1, s_2) = \int_{z_{\mathrm{in}}}^{z_{\mathrm{out}}} \sum_{l} n_l(e, s_1, s_2) \cdot q_l(z) \cdot \pi r_{\mathrm{CV}}^2 \cdot \mathrm{d}z. \tag{A.9}$$

For each value of $R(e, s_1, s_2)$, the contributions of all reactions l are first summed at each node of the computational mesh. Then, the numerical integral is performed once, therefore reducing the overall error in $R(e, s_1, s_2)$.

$$\int_{z_0}^{z_n} f(z)\mathrm{d}z = \int_{z_0}^{z_n} p_n(z)\mathrm{d}z + \int_{z_0}^{z_n} E_n(z)\mathrm{d}z \tag{A.10}$$

To further reduce the integration error, a composite Simpson's $1/3$ rule is used here instead of the simpler composite Trapezoidal method. The former is a fourth-order-accurate method and yields exact values of integral for third-order and lower-order polynomials, while the latter is a second-order-accurate method, and is only exact for first and zeroth-order polynomials [145]. The Simpson's $1/3$ rule assumes fixed separation ($\Delta z = z_i - z_{i-1}$) of the discrete grid points [145]:

$$\int_{z_0}^{z_2} f(z)\mathrm{d}z \simeq \frac{\Delta z}{3}\left[f(z_0) + 4f(z_1) + f(z_2)\right]. \tag{A.11}$$

However, accurate flame simulations require significant mesh refinement in zones of steep gradient and/or high curvature of the solution. The Simpson's $1/3$ method is redeveloped here to apply to meshes with unequally distributed grid points. As shown in equation A.12, the function $f(z)$ is approximated by a second-order polynomial, $p_2(z)$, in which the divided differences $f[z_i, z_{i+1}]$ and $f[z_i, z_{i+1}, z_{i+2}]$ are defined in equations A.13 and A.14, respectively. The method is made composite by successively evaluating equation A.12 over [z_{2i}, z_{2i+2}] intervals. For meshes with an even number of grid points, the integral over the last interval [z_{N-1}, z_N] is performed with the Trapezoidal integration rule. For stagnation flame simulations, the composite Simpson's $1/3$ rule

is also used to compute $R(e, s_i, \text{outlet})$ defined in equation A.8.

$$\begin{aligned}
\int_{z_0}^{z_2} f(z)\mathrm{d}z &\simeq \int_{z_0}^{z_2} p_2(z)\mathrm{d}z \\
&= \int_{z_0}^{z_2} \left\{ f(z_0) + f\left[z_0, z_1\right](z - z_0) + f\left[z_0, z_1, z_2\right](z - z_0)(z - z_1) \right\} \mathrm{d}z \\
&= (z_2 - z_0) \cdot \{ f(z_0) - f[z_0, z_1] z_0 + f[z_0, z_1, z_2] \cdot z_0 \cdot z_1 \} \\
&\quad + \frac{(z_2^2 - z_0^2)}{2} \cdot \{ f[z_0, z_1] - f[z_0, z_1, z_2] \cdot (z_0 + z_1) \} \\
&\quad + \frac{(z_2^3 - z_0^3)}{3} \cdot f[z_0, z_1, z_2]
\end{aligned} \tag{A.12}$$

$$f[z_i, z_{i+1}] = \frac{f(z_{i+1}) - f(z_i)}{z_{i+1} - z_i} \tag{A.13}$$

$$f[z_i, z_{i+1}, z_{i+2}] = \frac{f[z_{i+1}, z_{i+2}] - f[z_i, z_{i+1}]}{z_{i+2} - z_i} \tag{A.14}$$

A.2.1 Automated determination of $n_l(e, s_1, s_2)$

At this point, only the number of atoms of element e transferred from species s_1 to s_2 through reaction l, $n_l(e, s_1, s_2)$, remains to be determined to compute $R(e, s_1, s_2)$ via equation A.9. $n_l(e, s_1, s_2)$ is conveniently represented in matrix form, as shown in Table A.1 for the arbitrary chemical reaction $r_1 + r_2 \leftrightarrow p_1 + p_2 + p_3$, and it must be noted that $n_l(e, s_1, s_2) = n_l(e, s_2, s_1)$. As modern thermochemical mechanisms include thousands of chemical reactions, the manual determination of all values of $n_l(e, s_1, s_2)$ is impractical, and an automated method must be implemented.

TABLE A.1: Representation of $n_l(e, s_1, s_2)$ in matrix form for the arbitrary reaction $r_1 + r_2 \leftrightarrow p_1 + p_2 + p_3$.

prod. / reac.	p_1	p_2	p_3
r_1	$n_l(e, r_1, p_1)$	$n_l(e, r_1, p_2)$	$n_l(e, r_1, p_3)$
r_2	$n_l(e, r_2, p_1)$	$n_l(e, r_2, p_2)$	$n_l(e, r_2, p_3)$

The method developed in this work initially determines all possible combinations of $n_l(e, r_i, p_j)$ for a given reaction. Then, improper configurations are eliminated through a series of decisions until a single set of $n_l(e, r_i, p_j)$ values remains. To populate all possible configurations, it is first

recognized that the maximum value of $n_l(e, r_i, p_j)$ corresponds to the smallest number of e-atoms in species r_i and p_j. For example, the maximum value of $n_l(\mathrm{H}, \mathrm{CH_3}, \mathrm{CH_4})$ is 3, *i.e.*, the number of hydrogen atoms in the methyl radical. However, $n_l(\mathrm{H}, \mathrm{CH_3}, \mathrm{CH_4})$ could be 0, 1, or 2. Once all maximum values of $n_l(e, r_i, p_j)$ are determined for a given reaction, a full-factorial design is applied to yield a set of matrices similar to Table A.1. An example is given in Table A.2 for the reaction H + O_2 $\leftrightarrow$ OH + O. In this case, the maximum values of $n_l(\mathrm{O}, \mathrm{H}, \mathrm{OH})$, $n_l(\mathrm{O}, \mathrm{H}, \mathrm{O})$, $n_l(\mathrm{O}, \mathrm{O_2}, \mathrm{OH})$, and $n_l(\mathrm{O}, \mathrm{O_2}, \mathrm{O})$ are 0, 0, 1 and 1, respectively, which results in the four possible configurations shown in Table A.2.

The first decision applied on this set of configurations involves the conservation of e-atoms. Namely, the total number of e-atoms given away by a reactant must equal the total number of e-atoms it contains and, similarly, the number of e-atoms a product receives must be equal to the number of e-atoms it comprises. These two conditions are mathematically shown in equations A.15 and A.16, where N_r and N_p are the numbers of reactants and products in reaction l, respectively, and $\nu_{r_i,e}$ and $\nu_{p_j,e}$ are the numbers of e-atoms in the reactant i and the product j, respectively. Applying these conditions to the reaction H + O_2 $\leftrightarrow$ OH + O leads to a single possible configuration as shown in Table A.2, where the violated conditions are appended underneath the incorrect combinations of $n_l(\mathrm{O}, r_i, p_j)$ values. Generally, applying equations A.15 and A.16 identifies the proper distribution of e-atoms for 66% (AramcoMech 1.3) to 95% (GRI-Mech version 3.0) of the reactions, depending on the complexity of the thermochemical mechanism; the simpler the mechanism, the larger the fraction of reactions properly characterized through conservation of atoms.

$$\sum_{j=1}^{N_p} n_l(e, r_i, p_j) = \nu_{e,r_i} \tag{A.15}$$

$$\sum_{i=1}^{N_r} n_l(e, r_i, p_j) = \nu_{e,p_j} \tag{A.16}$$

A.2.1.1 Ambiguous reactions

The reactions that remain unresolved by invoking atomic balance, termed "ambiguous reactions" by Grcar et al. [136], can amount to hundreds for comprehensive thermochemical mechanisms. While it is generally straightforward to identify the proper distribution of e-atoms by inspecting the structure of the molecules, additional criteria must be developed and integrated into the computer

TABLE A.2: $n_l(\mathrm{O}, r_i, p_j)$ for the reaction H + O_2 ↔ OH + O. The correct configuration is on the right.

	OH	O
H	0	0
O_2	0	0

$\sum_j^2 n_l(\mathrm{O}, \mathrm{O_2}, p_j) \neq 2$

$\sum_i^2 n_l(\mathrm{O}, r_i, \mathrm{OH}) \neq 1$

$\sum_i^2 n_l(\mathrm{O}, r_i, \mathrm{O}) \neq 1$

	OH	O
H	0	0
O_2	1	0

$\sum_j^2 n_l(\mathrm{O}, \mathrm{O_2}, p_j) \neq 2$

$\sum_i^2 n_l(\mathrm{O}, r_i, \mathrm{O}) \neq 1$

	OH	O
H	0	0
O_2	0	1

$\sum_j^2 n_l(\mathrm{O}, \mathrm{O_2}, p_j) \neq 2$

$\sum_i^2 n_l(\mathrm{O}, r_i, \mathrm{OH}) \neq 1$

	OH	O
H	0	0
O_2	1	1

code to identify a single set of $n_l(e, r_i, p_j)$ values for each reaction. Grcar and co-workers proposed three heuristic rules [136]:

> Rule 1. Prefer single exchanges over double exchanges.
> Rule 2. Among single exchanges, prefer those that shuffle the fewest atoms, and among these with the same quantity of atoms, prefer those that shuffle the least atomic weight.
> Rule 3. If possible preserve carbon-oxygen bonds by avoiding exchanges that separate carbon and oxygen atoms or that transfer a single carbon atom.

While these rules are easily understandable, their implementation is not described in [136]. In the current section, four criteria developed in the present study, and inspired by the three heuristic rules presented above, are presented along with examples. They are applied in the same sequence in the program as presented in the following. When two or more configurations remain after this series of decisions, the user is prompted to select the proper one. The "ambiguous reactions" are reported in a text file, which allows the user to confirm the selection of the $n_l(e, r_i, p_j)$ values made by the program. For a given atom e, this verification only needs to be performed once for each mechanism. To date, the present method was demonstrated successful for the San Diego (versions 2005 and 2011) [66, 128], GRI-Mech (version 3.0) [65], USC Mech (version II) [133], and AramcoMech 1.3 [134] thermochemical mechanisms.

A.2.1.1.1 Criterion 1: minimize the shuffle of atoms (Rule 2)

Table A.3 presents two configurations, both ensuring conservation of carbon atoms, through which the reaction HCO + CH_3 ↔ CO + CH_4 can proceed. From inspection of the structure of the

molecules shown in Figure A.2, it is unlikely that the carbon atoms are transferred from HCO to CH_4 and from CH_3 to CO. This would require one C=O and three C−H bonds to be broken and reformed. Instead, the reaction more probably proceeds through hydrogen abstraction from HCO and subsequent recombination with the methyl radical to form methane.

TABLE A.3: $n_l(\mathrm{C}, r_i, p_j)$ for the reaction HCO + CH_3 ↔ CO + CH_4. The correct configuration is on the right.

	CO	CH_4
HCO	0	1
CH_3	1	0

$$\sum_{i,j} [\Delta N(r_i, p_j) \cdot n_l(\mathrm{C}, r_i, p_j)] = 8$$

	CO	CH_4
HCO	1	0
CH_3	0	1

$$\sum_{i,j} [\Delta N(r_i, p_j) \cdot n_l(\mathrm{C}, r_i, p_j)] = 2$$

TABLE A.4: $\Delta N(r_i, p_j)$ for the reaction HCO + CH_3 ↔ CO + CH_4.

$\Delta N(r_i, p_j)$	CO	CH_4
HCO	1	4
CH_3	4	1

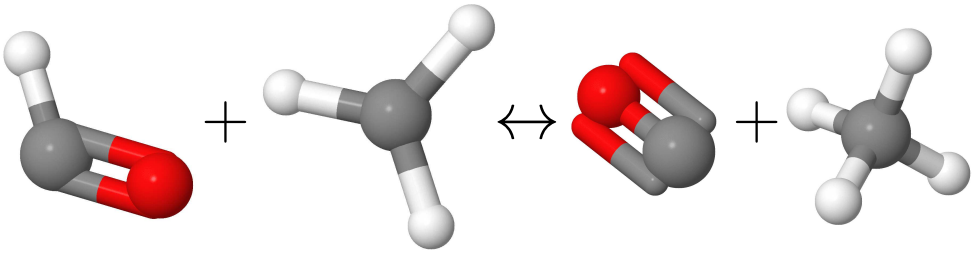

FIGURE A.2: Graphical representation of the reaction HCO + CH_3 ↔ CO + CH_4. The three-dimensional molecular structures are from [231, 232].

For the computer program to make the decision, the variable $\Delta N(r_i, p_j)$, defined in equation A.17, is introduced. It quantifies the change in atomic composition between the reactant r_i and the product p_j. Table A.4 shows the values of $\Delta N(r_i, p_j)$ for the species involved in the reaction HCO + CH_3 ↔ CO + CH_4. The least amount of bonds is broken and reformed or, in other words, the shuffle of atoms is minimized, for the configuration achieving the lowest value of $\sum_{i,j} [\Delta N(r_i, p_j) \cdot n_l(e, r_i, p_j)]$. This criterion is calculated for each configuration in Table A.3.

As expected, the method selects hydrogen abstraction from HCO and recombination with CH_3 to form CH_4 as the reaction path.

$$\Delta N(r_i, p_j) = \sum_e \left| \nu_{e,r_i} - \nu_{e,p_j} \right| \quad \text{for } e = \text{O, N, C, H, etc.} \tag{A.17}$$

A.2.1.1.2 Criterion 2: preserve carbon-oxygen bonds (Rule 3)

The reaction CH_3 + $CH_3OH \leftrightarrow CH_2OH$ + CH_4 is presented schematically in Figure A.3. Two possible configurations, which remain after invoking the conservation of C atoms and applying Criterion 1,[1] are shown in Table A.5. This reaction is expected to proceed via abstraction of a hydrogen atom from methanol that recombines with the methyl radical to form methane. The C−O bond is then conserved, which implies that $n_l(\text{O}, \text{CH}_3\text{OH}, \text{CH}_2\text{OH}) = 1$ and $n_l(\text{C}, \text{CH}_3\text{OH}, \text{CH}_2\text{OH}) = 1$. As most $C_\alpha H_\beta O_\gamma$ molecules involved in combustion processes include as many, or more, carbon than oxygen atoms (an exception is CO_2), this condition can be generalized as:

$$n_l(\text{C}, r_i, p_j) \geq n_l(\text{O}, r_i, p_j) \quad \forall (r_i, p_j). \tag{A.18}$$

As shown in Tables A.5 and A.6, this criterion selects hydrogen abstraction and recombination as the reaction pathway.

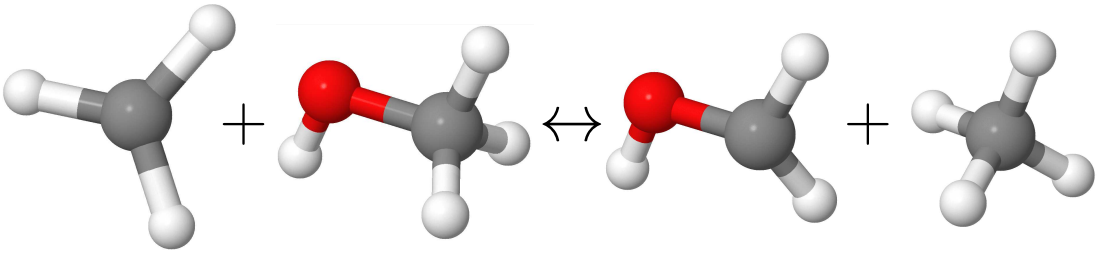

FIGURE A.3: Graphical representation of the reaction CH_3 + $CH_3OH \leftrightarrow CH_2OH$ + CH_4. The three-dimensional molecular structures are from [231].

A.2.1.1.3 Criterion 3: minimize exchange of atomic weight (Rule 2)

The variable $\Delta N(r_i, p_j)$ is filled with ones for the reaction CH_3 + $C_2H_4 \leftrightarrow C_2H_3$ + CH_4 presented in Figure A.4. It follows that the configurations presented in Table A.8 are both valid as per Criterion 1. In such a case, where two configurations shuffle the same number of atoms, Grcar and co-workers [136] suggest to select the one transferring the least atomic weight. Implicitly, this

[1] $\Delta N(r_i, p_j)$ is a 2 x 2 matrix filled with ones, thus $\sum_{i,j} [\Delta N(r_i, p_j) \cdot n_l(\text{C}, r_i, p_j)] = 2$ for both configurations.

TABLE A.5: $n_l(\mathrm{C}, r_i, p_j)$ for the reaction CH_3 + $CH_3OH \leftrightarrow CH_2OH$ + CH_4. The correct configuration is on the right.

$n_l(\mathrm{C}, r_i, p_j)$	CH_2OH	CH_4
CH_3	1	0
CH_3OH	0	1

$n_l(\mathrm{C}, \mathrm{CH_3OH}, \mathrm{CH_2OH}) < n_l(\mathrm{O}, \mathrm{CH_3OH}, \mathrm{CH_2OH})$

$n_l(\mathrm{C}, r_i, p_j)$	CH_2OH	CH_4
CH_3	0	1
CH_3OH	1	0

$n_l(\mathrm{C}, r_i, p_j) \geq n_l(\mathrm{O}, r_i, p_j)\ \forall (r_i, p_j)$

TABLE A.6: $n_l(\mathrm{O}, r_i, p_j)$ for the reaction CH_3 + $CH_3OH \leftrightarrow CH_2OH$ + CH_4.

$n_l(\mathrm{O}, r_i, p_j)$	CH_2OH	CH_4
CH_3	0	0
CH_3OH	1	0

favours reactions occurring through hydrogen abstraction and recombination. Criterion 3 is similar to Criterion 1, with $\Delta N(r_i, p_j)$ replaced by $\Delta W(r_i, p_j)$ defined as:

$$\Delta W(r_i, p_j) = |W_{r_i} - W_{p_j}|. \tag{A.19}$$

$\Delta W(r_i, p_j)$ for the reaction CH_3 + $C_2H_4 \leftrightarrow C_2H_3$ + CH_4 is shown in Table A.7. The configuration achieving the lowest value of $\sum_{i,j} [\Delta W(r_i, p_j) \cdot n_l(e, r_i, p_j)]$ transfers the smallest atomic weight. For the current reaction, hydrogen abstraction from ethylene and recombination with the methyl radical is the preferred reaction pathway as shown in Table A.8.

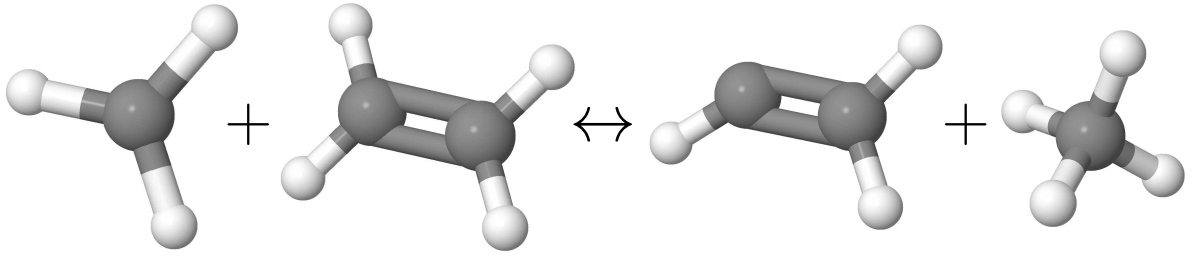

FIGURE A.4: Graphical representation of the reaction CH_3 + $C_2H_4 \leftrightarrow C_2H_3$ + CH_4. The three-dimensional molecular structures are from [231].

TABLE A.7: $\Delta W(r_i, p_j)$ for the reaction CH_3 + $C_2H_4 \leftrightarrow C_2H_3$ + CH_4.

$\Delta W(r_i, p_j)$ [kg/kmol]	C_2H_3	CH_4
CH_3	12.0110	1.0079
C_2H_4	1.0079	12.0110

TABLE A.8: $n_l(\mathrm{C}, r_i, p_j)$ for the reaction CH_3 + C_2H_4 $\leftrightarrow$ C_2H_3 + CH_4. The correct configuration is on the right.

	C_2H_3	CH_4
CH_3	1	0
C_2H_4	1	1

$$\sum_{i,j} [\Delta W(r_i, p_j) \cdot n_l(\mathrm{C}, r_i, p_j)] = 25.03$$

	C_2H_3	CH_4
CH_3	0	1
C_2H_4	2	0

$$\sum_{i,j} [\Delta W(r_i, p_j) \cdot n_l(\mathrm{C}, r_i, p_j)] = 3.02$$

A.2.1.1.4 Criterion 4: prefer single exchanges over double exchanges (Rule 1)

The last criterion implemented in the current RPA method corresponds to Rule 1 of Grcar et al. [136]. It is applied here to the reaction C_2H_4 + C_2H_4 $\leftrightarrow$ C_2H_3 + C_2H_5 shown in Figure A.5. The three possible configurations through which the reaction can proceed are shown in Table A.9. It must be noted that the two configurations on the right are equivalent, and a condition is included in the program to account for such duplicates.

The first reaction path in Table A.9 involves the rupture of the C=C bond in both ethylene molecules, and the recombination of the carbon atoms originally in the first ethylene molecule with the C atoms of the second C_2H_4 molecule (double exchange). In addition, this configuration involves the abstraction of a hydrogen atom and subsequent recombination. The most likely path for this reaction is to solely undergo hydrogen abstraction from the first ethylene molecule, therefore producing C_2H_3, and recombination with the second C_2H_4 to form C_2H_5, in which the original double covalent bond is reduced to a single bond. This criterion is mathematically translated into the variable S defined as:

$$S = \sum_{i,j} \left(n_l(e, r_i, p_j) \neq 0\right), \tag{A.20}$$

which corresponds to the number of non-null cells in the matrix $n_l(e, r_i, p_j)$. Single exchanges are characterized by smaller values of S than double exchanges.

Although the correct configurations are those with $S = 2$ (which are equivalent) in Table A.9, using the reaction path with $S = 4$ would not affect the computed values of $R(\mathrm{C}, \mathrm{C_2H_4}, \mathrm{C_2H_3})$ and $R(\mathrm{C}, \mathrm{C_2H_4}, \mathrm{C_2H_5})$ for the current reaction since, together, the two ethylene molecules give two carbon atoms to C_2H_3 and two to C_2H_5. Whether these carbon atoms come from the same, or different, ethylene molecules does not change the net transfer of carbon atoms. This behaviour is better understood when the rows of the $n_l(e, r_i, p_j)$ matrices in Table A.9 are summed to yield the matrix in Table A.10. For the thermochemical mechanisms studied so far with the RPA method,

Criterion 4 only applied to reactions involving two identical reactants or products, making the choice of the reaction path unimportant. The criterion is kept in the decision loop as a single configuration needs to be selected, and in case it would be required in the future for reactions with different reactants and products.

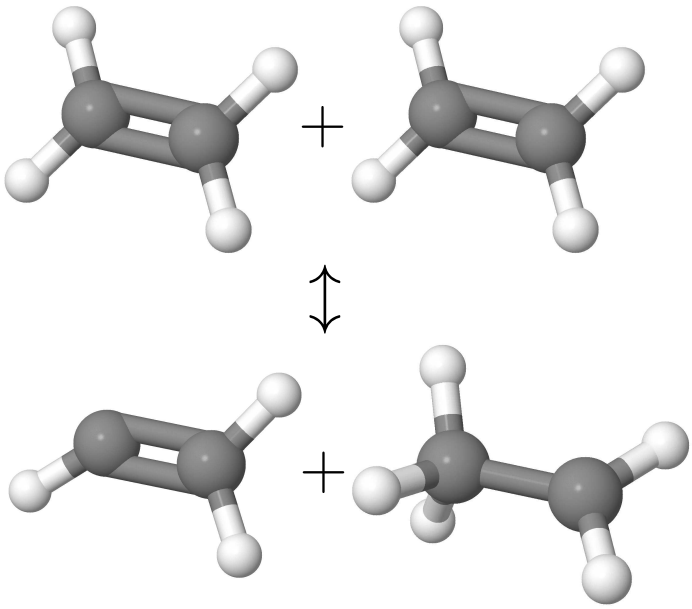

FIGURE A.5: Graphical representation of the reaction C_2H_4 + C_2H_4 $\leftrightarrow$ C_2H_3 + C_2H_5. The three-dimensional molecular structures are from [231].

TABLE A.9: $n_l(\mathrm{C}, r_i, p_j)$ for the reaction C_2H_4 + C_2H_4 $\leftrightarrow$ C_2H_3 + C_2H_5.

	C_2H_3	C_2H_5
C_2H_4	1	1
C_2H_4	1	1

$S = 4$

	C_2H_3	C_2H_5
C_2H_4	2	0
C_2H_4	0	2

$S = 2$

	C_2H_3	C_2H_5
C_2H_4	0	2
C_2H_4	2	0

$S = 2$

TABLE A.10: Simplified $n_l(\mathrm{C}, r_i, p_j)$ matrix for the reaction C_2H_4 + C_2H_4 $\leftrightarrow$ C_2H_3 + C_2H_5.

	C_2H_3	C_2H_5
C_2H_4	2	2

A.3 Example of a reaction pathway analysis

The RPA method described in this appendix was implemented in Matlab and interfaced with GraphViz 2.38 [233], which builds the directed graphs. Figure A.6 presents a RPA diagram produced based on the solution of a freely propagating, adiabatic, premixed CH_4-air flame simulated with the San Diego mechanism [128]. This RPA diagram tracks carbon atoms, which enter the system via methane and leave as CO and CO_2. Only the pathways carrying more than 1% of the carbon atoms entering the system are shown, *i.e.*, $R(e, s_1, s_2) > 0.010$ kmol/s, as including all pathways would make the RPA diagram very complex and difficult to understand.

An additional feature of the current RPA method is the colouring of the arrows based on the sensitivity of a scalar value of interest to the rate of the individual pathways. The logarithmic sensitivity of a pathway is taken as the sum of the logarithmic sensitivities of the scalar value to the specific rate of the reactions making that path. In Figure A.6, the scalar value is the maximum concentration of methylidyne through the flame front, but it could be other variables, such as the laminar flame speed, the concentration of another species, or the temperature at a given position. The arrows are coloured based on the linear colour scale at the left of Figure A.6. The details of the conversion of methane into products, the formation of methylidyne, as well as the influence of the rate of the different pathways, are thoroughly covered in section 4.2.

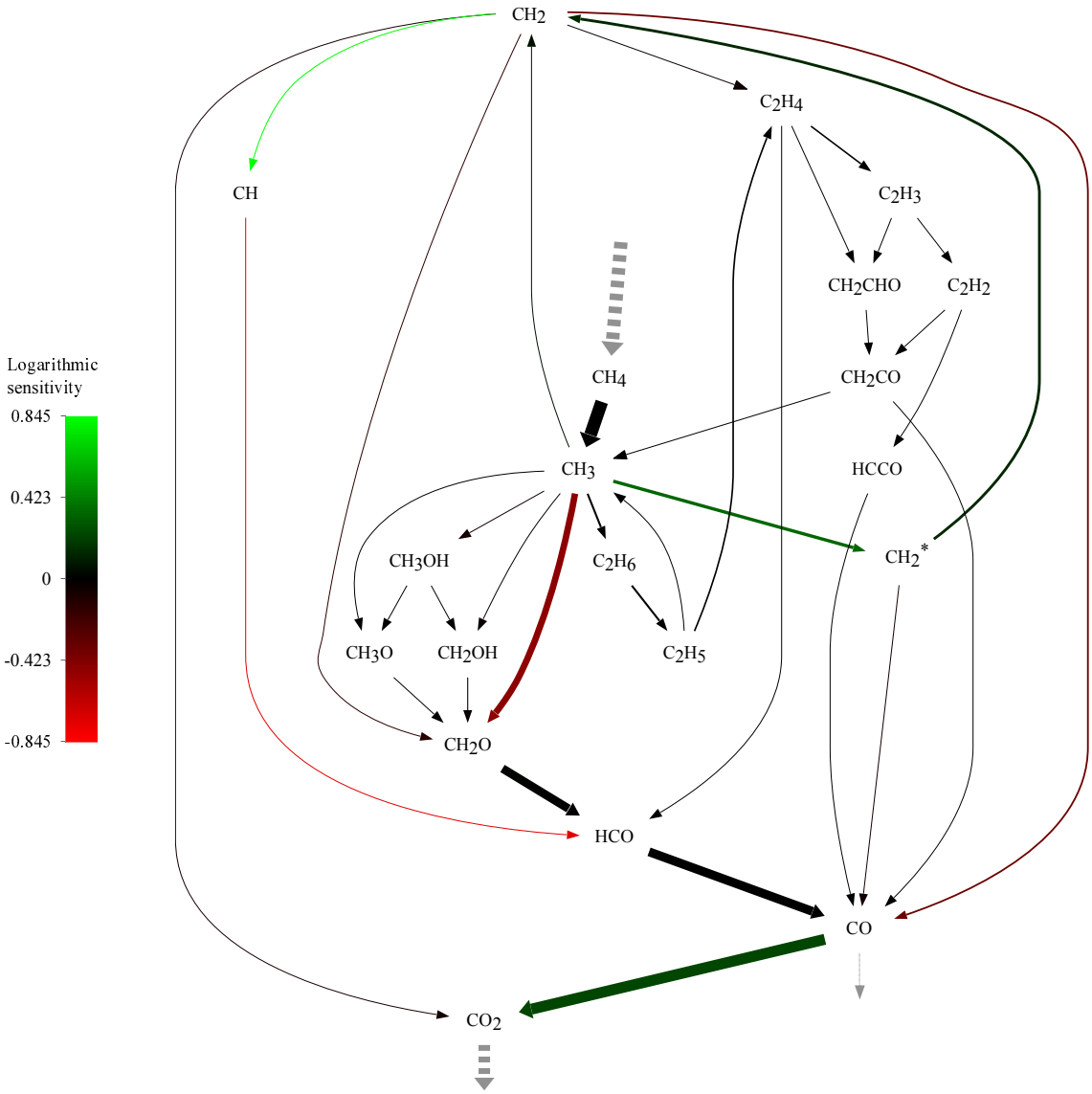

FIGURE A.6: Reaction pathway diagram tracking the flux of carbon atoms through a freely propagating, adiabatic, premixed CH_4-air flame simulated with the San Diego mechanism (version 2005). The arrows are coloured according to the logarithmic sensitivity of the maximum CH concentration through the flame to the rate of the individual pathways.

Appendix B

Analytical solution of the time-resolved, four-level LIF model

The system of linear, homogeneous, ordinary differential equations presented in equations 3.1-3.4 represents an eigenvalue problem that can be solved analytically [176]. In addition to the benefit of being exact, the solution can be compiled into a stand-alone executable program not requiring libraries other than the commonly used ones, or third-party software tools. This appendix describes the development of the analytical solution of the time-resolved, four-level LIF model of section 3.1.1. Given the complexity of the problem, the solution is obtained using the Symbolic Math Toolbox of Matlab, and automatically written in a C script compiled into an executable program using Microsoft Visual Studio 2015. Being approximately 31 MB in size when written in a text file, the complete solution is not transcribed here.

B.1 Analytical solution during laser irradiation

The system of linear, homogeneous, ordinary differential equations (ODE) 3.1-3.4 can be written in compact matrix notation as:

$$\dot{\mathbf{N}} = \mathbf{E}\mathbf{N}, \tag{B.1}$$

where $\dot{\mathbf{N}}$, $\mathbf{N}$, and $\mathbf{E}$ are described by equations B.16 and B.17. Analogously to single, linear, homogeneous, ordinary differential equations, the solution is hypothesized to be of the form [176]:

$$\mathbf{N} = \boldsymbol{\xi}_i e^{\lambda_i t}, \tag{B.2}$$

where $\boldsymbol{\xi}_i$ is a vector of constants. Inserting equation B.2 in equation B.1 yields [176]:

$$\lambda_i \boldsymbol{\xi}_i e^{\lambda_i t} = \mathbf{E}\boldsymbol{\xi}_i e^{\lambda_i t}. \tag{B.3}$$

Simplifying and rearranging allows to obtain the following set of linear equations [176]:

$$(\mathbf{E} - \lambda_i \mathbf{I})\, \boldsymbol{\xi}_i = \mathbf{0}, \tag{B.4}$$

where $\mathbf{I}$ is the identity matrix. Solving the system of linear equations B.4 by finding the eigenvalues, λ_i, and vectors, $\boldsymbol{\xi}_i$, provides the solution to the set of ODEs B.1.

To find the eigenvalues, it is first noticed that the system of equations B.4 admits a non-trivial solution if, and only if, the determinant of the matrix $(\mathbf{E} - \lambda_i \mathbf{I})$ equals zero. For a system including four ODEs, this condition results in a quartic equation having four roots:

$$|\mathbf{E} - \lambda_i \mathbf{I}| = c_4 \cdot \lambda_i^4 + c_3 \lambda_i^3 + c_2 \lambda_i^2 + c_1 \lambda_i + c_0 = 0. \tag{B.5}$$

For the current ODE system, the constant c_0 was found to equal zero. Therefore, equation B.5 can be rewritten as:

$$|\mathbf{E} - \lambda_i \mathbf{I}| = \left(c_4 \cdot \lambda_i^3 + c_3 \lambda_i^2 + c_2 \lambda_i + c_1\right) \lambda_i = 0. \tag{B.6}$$

It follows that one of the eigenvalues equals zero, and the remaining λ_i are found by solving the cubic equation within parentheses using the methodology of Neumark [234].

First, the cubic equation is rewritten in the following form:

$$(3c_4 \cdot \lambda_i + c_3)^3 - 3(c_3^2 - 3c_4 c_2)(3c_4 \cdot \lambda_i + c_3) + (27c_4^2 c_1 + 2c_3^3 - 9c_4 c_3 c_2) = 0. \tag{B.7}$$

Acknowledging that for the current ODE system $c_3^2 - 3c_4 c_2 > 0$, the substitution:

$$\lambda_i = \frac{-c_3 - 2\Lambda_i \sqrt{c_3^2 - 3c_4 c_2}}{3c_4}, \tag{B.8}$$

is performed in equation B.7, which reduces to:

$$4\Lambda_i^3 - 3\Lambda_i = \Delta, \tag{B.9}$$

where,

$$\Delta = \frac{27c_4^2 c_1 + 2c_3^3 - 9c_4 c_3 c_2}{2\left(c_3^2 - 3c_4 c_2\right)^{\frac{3}{2}}}. \tag{B.10}$$

For the current ODE system, Δ is found to be consistently lower than 1, and the cubic equation B.9 is solved through trigonometric functions. To obtain the first root, Λ_i is substituted by $\cos(\beta)$ in equation B.9 yielding:

$$4\cos(\beta)^3 - 3\cos(\beta) = \cos(3\beta) = \Delta. \tag{B.11}$$

The first root of equation B.9 is then:

$$\Lambda_1 = \cos\beta = \cos\left(\frac{\cos^{-1}\Delta}{3}\right). \tag{B.12}$$

To find the two remaining roots, $(\Lambda - \Lambda_1)$ is factored out of equation B.9 to yield[1]:

$$4\Lambda^3 - 3\Lambda - \Delta = 0 = (\Lambda - \Lambda_1)\left[4\Lambda^2 + 4\Lambda_1\Lambda + (4\Lambda_1^2 - 3)\right]. \tag{B.13}$$

Λ_2 and Λ_3 are obtained by applying the quadratic formula to the right-hand side term of equation B.13:

$$\Lambda_{2,3} = \frac{-\Lambda_1}{2} \pm \frac{\sqrt{3}\cdot\sqrt{1 - 1\Lambda_1^2}}{2}. \tag{B.14}$$

Finally, the eigenvalues of equation B.6, complementing $\lambda_1 = 0$, are obtained by replacing the results of equations B.12 and B.14 in equation B.8. Then, the four eigenvalues, λ_i, are sequentially inserted in equation B.4 and each eigenvector, $\boldsymbol{\xi}_i$, found by reducing the system of equations in reduced row echelon form through Gauss-Jordan elimination. The four (λ_i, $\boldsymbol{\xi}_i$) couples represent a fundamental set of solutions, which can be assembled into a general solution through [176]:

$$\mathbf{N} = \sum_{i=1}^{4} d_i \boldsymbol{\xi}_i e^{\lambda_i t}, \tag{B.15}$$

where d_i are arbitrary constants. Their value is determined by applying the initial conditions $(N_{1a,0},\ N_{1b,0},\ N_{2a,0},\ N_{2b,0}) = (N_{0,\mathrm{CH}}\cdot f_{\mathrm{B},N_{1a}},\ N_{0,\mathrm{CH}}\cdot(1 - f_{\mathrm{B},N_{1a}}),\ 0,\ 0)$, where $N_{0,\mathrm{CH}}$ is the number density of methylidyne in the ground electronic state predicted by flame simulations.

B.2 Analytical solution following laser irradiation

The system of ODEs following laser irradiation, *i.e.*, with $b_{12} = 0$ and $b_{21} = 0$, is described by equation B.1, where $\dot{\mathbf{N}}$, $\mathbf{N}$, and $\mathbf{E}$ are described by equations B.16 and B.18. The solution for the system of ODEs is obtained following the procedure presented in the previous section. The determinant of the matrix $(\mathbf{E} - \lambda_i\mathbf{I})$ is given in equation B.19, which can be rearranged to yield equation B.20. Inspection of the terms in the first set of brackets of equation B.20 reveals that two eigenvalues are $\lambda_1 = 0$ and $\lambda_2 = -(R_{1a1b} + R_{1b1a})$. The two remaining eigenvalues are found by applying the quadratic formula to the expression in the second set of brackets. As previously, the eigenvectors, $\boldsymbol{\xi}_i$, are found by solving equation B.4 for each eigenvalue, λ_i, and the fundamental

[1]Note that, as per equation B.9, $4\Lambda_1^3 - 3\Lambda_1 = \Delta$.

set of solutions is assembled into the general solution, equation B.15. The initial conditions used to determine the arbitrary constants, d_i, correspond to the populations (N_{1a}, N_{1b}, N_{2a}, N_{2b}) at the end of the laser pulse ($t = \tau_{\mathrm{Laser}}$).

$$\mathbf{N} = \begin{bmatrix} N_{1a} \\ N_{1b} \\ N_{2a} \\ N_{2b} \end{bmatrix} \qquad \dot{\mathbf{N}} = \begin{bmatrix} \dot{N}_{1a} \\ \dot{N}_{1b} \\ \dot{N}_{2a} \\ \dot{N}_{2b} \end{bmatrix} \tag{B.16}$$

$$\mathbf{E} = \begin{bmatrix} -(b_{12} + R_{1a1b}) & R_{1b1a} & b_{21} + A_{2a1a} & 0 \\ R_{1a1b} & -R_{1b1a} & A_{2a1b} + Q_{2a1} & A_{2b1} + Q_{2b1} \\ b_{12} & 0 & -(b_{21} + A_{2a1a} + A_{2a1b} + Q_{2a1} + R_{2a2b}) & R_{2b2a} \\ 0 & 0 & R_{2a2b} & -(A_{2b1} + Q_{2b1} + R_{2b2a}) \end{bmatrix} \tag{B.17}$$

$$\mathbf{E} = \begin{bmatrix} -R_{1a1b} & R_{1b1a} & A_{2a1a} & 0 \\ R_{1a1b} & -R_{1b1a} & A_{2a1b} + Q_{2a1} & A_{2b1} + Q_{2b1} \\ 0 & 0 & -(A_{2a1a} + A_{2a1b} + Q_{2a1} + R_{2a2b}) & R_{2b2a} \\ 0 & 0 & R_{2a2b} & -(A_{2b1} + Q_{2b1} + R_{2b2a}) \end{bmatrix} \tag{B.18}$$

$$\begin{aligned} |\mathbf{E} - \lambda_i \mathbf{I}| = -(R_{1a1b} + \lambda_i) & \begin{vmatrix} -(R_{1b1a} + \lambda_i) & A_{2a1b} + Q_{2a1} & A_{2b1} + Q_{2b1} \\ 0 & -(A_{2a1a} + A_{2a1b} + Q_{2a1} + R_{2a2b} + \lambda_i) & R_{2b2a} \\ 0 & R_{2a2b} & -(A_{2b1} + Q_{2b1} + R_{2b2a} + \lambda_i) \end{vmatrix} \\ -R_{1a1b} & \begin{vmatrix} R_{1b1a} & A_{2a1a} & 0 \\ 0 & -(A_{2a1a} + A_{2a1b} + Q_{2a1} + R_{2a2b} + \lambda_i) & R_{2b2a} \\ 0 & R_{2a2b} & -(A_{2b1} + Q_{2b1} + R_{2b2a} + \lambda_i) \end{vmatrix} \end{aligned} \tag{B.19}$$

$$
\begin{aligned}
|\mathbf{E} - \lambda_i \mathbf{I}| = & \left[(R_{1a1b} + \lambda_i) \cdot (R_{1b1a} + \lambda_i) - R_{1a1b} R_{1b1a} \right] \\
& \cdot \left[(A_{2a1a} + A_{2a1b} + Q_{2a1} + R_{2a2b} + \lambda_i) \cdot (A_{2b1} + Q_{2b1} + R_{2b2a} + \lambda_i) - R_{2a2b} R_{2b2a} \right] \\
= & \, 0
\end{aligned}
\tag{B.20}
$$

Appendix C

Adequacy of two-level, steady-state LIF models in the linear regime

As demonstrated in Chapter 3, the CH $A^2\Delta$-$X^2\Pi$ LIF system does not reach steady-state conditions for nanosecond duration laser pulses. However, two-level, steady-state models are commonly used to process CH-LIF measurements in the linear regime [100, 101]. In this appendix, it is shown that, under particular conditions, the models invoking the steady-state assumption fortuitously provide accurate results. The demonstration is made using the time-resolved, two-level LIF model with ${}^{R_{kakb}}/_{Q} = 0$, but it also applies to the other models presented in Chapter 3.

The analytical solutions of the two-level LIF model with ${}^{R_{kakb}}/_{Q_{21}} = 0$ during ($N_{2,\mathrm{on}}$) and following ($N_{2,\mathrm{off}}$) a laser pulse were provided in equations 3.14 and 3.15, respectively, which are reproduced here:

$$N_{2,\mathrm{on}}(t) = \frac{b_{12} \cdot N_{0,\mathrm{CH}} \cdot f_{\mathrm{B},N_{1a}}}{b_{21} + b_{12} + A_{21} + Q_{21}} \cdot \left(1 - e^{-(b_{21}+b_{12}+A_{21}+Q_{21})\cdot t}\right) \qquad 0 \leq t \leq \tau_{\mathrm{Laser}}, \tag{3.14}$$

and,

$$N_{2,\mathrm{off}}(t) = N_{2,\mathrm{on}}(\tau_{\mathrm{Laser}}) \cdot e^{-(A_{21}+Q_{21})\cdot(t-\tau_{\mathrm{Laser}})} \qquad \tau_{\mathrm{Laser}} < t \leq \tau_{\mathrm{cam}}. \tag{3.15}$$

Inspection of equation 3.14 reveals that the number density of electronically excited molecules in steady-state conditions is:

$$N_{2,\mathrm{on,SS}} = \lim_{t\to\infty} N_{2,\mathrm{on}} = \frac{b_{12} \cdot N_{0,\mathrm{CH}} \cdot f_{\mathrm{B},N_{1a}}}{b_{21} + b_{12} + A_{21} + Q_{21}}. \tag{C.1}$$

The total number of photons emitted per unit volume is calculated as:

$$\begin{aligned} N_\mathrm{p} &= \int_0^{\tau_\mathrm{Laser}} A_{21} \cdot N_{2,\mathrm{on}}(t)\mathrm{d}t + \int_{\tau_\mathrm{Laser}}^{\infty} A_{21} \cdot N_{2,\mathrm{off}}(t)\mathrm{d}t \\ &= A_{21} \cdot \left[\int_0^{\tau_\mathrm{Laser}} N_{2,\mathrm{on}}(t)\mathrm{d}t + \int_{\tau_\mathrm{Laser}}^{\infty} N_{2,\mathrm{off}}(t)\mathrm{d}t \right]. \end{aligned} \tag{C.2}$$

It must be noted that the second integral is performed over a semi-infinite period of time, implicitly assuming that the camera exposure time is sufficiently long to collect most of the LIF signal. To obtain N_p, the first integral corresponding to the laser irradiated part of the LIF process is performed, and the equation is simplified:

$$\begin{aligned} \int_0^{\tau_\mathrm{Laser}} N_{2,\mathrm{on}}(t)\mathrm{d}t &= \int_0^{\tau_\mathrm{Laser}} \left[\frac{b_{12} \cdot N_{0,\mathrm{CH}} \cdot f_{\mathrm{B},N_{1a}}}{b_{21}+b_{12}+A_{21}+Q_{21}} \cdot \left(1 - e^{-(b_{21}+b_{12}+A_{21}+Q_{21})\cdot t}\right) \right] \mathrm{d}t \\ &= \frac{b_{12} \cdot N_{0,\mathrm{CH}} \cdot f_{\mathrm{B},N_{1a}}}{b_{21}+b_{12}+A_{21}+Q_{21}} \cdot \left[t + \frac{e^{-(b_{21}+b_{12}+A_{21}+Q_{21})\cdot t}}{(b_{21}+b_{12}+A_{21}+Q_{21})} \right] \Bigg|_0^{\tau_\mathrm{Laser}} \\ &= \frac{b_{12} \cdot N_{0,\mathrm{CH}} \cdot f_{\mathrm{B},N_{1a}}}{b_{21}+b_{12}+A_{21}+Q_{21}} \cdot \tau_\mathrm{Laser} - \frac{N_{2,\mathrm{on}}(\tau_\mathrm{Laser})}{b_{21}+b_{12}+A_{21}+Q_{21}}. \end{aligned} \tag{C.3}$$

Similarly, the integral of the electronically excited state population following the laser pulse is calculated as:

$$\begin{aligned} \int_{\tau_\mathrm{Laser}}^{\infty} N_{2,\mathrm{off}}(t)\mathrm{d}t &= \int_{\tau_\mathrm{Laser}}^{\infty} N_{2,\mathrm{on}}(\tau_\mathrm{Laser}) \cdot e^{-(A_{21}+Q_{21})\cdot(t-\tau_\mathrm{Laser})}\mathrm{d}t \\ &= N_{2,\mathrm{on}}(\tau_\mathrm{Laser}) \cdot \left[\frac{-e^{-(A_{21}+Q_{21})\cdot(t-\tau_\mathrm{Laser})}}{A_{21}+Q_{21}} \right] \Bigg|_{\tau_\mathrm{Laser}}^{\infty} \\ &= \frac{N_{2,\mathrm{on}}(\tau_\mathrm{Laser})}{A_{21}+Q_{21}}. \end{aligned} \tag{C.4}$$

Inserting the results of equations C.3 and C.4 in equation C.2 yields:

$$\begin{aligned} N_\mathrm{p} &= A_{21} \cdot \left[\int_0^{\tau_\mathrm{Laser}} N_{2,\mathrm{on}}(t)\mathrm{d}t + \int_{\tau_\mathrm{Laser}}^{\infty} N_{2,\mathrm{off}}(t)\mathrm{d}t \right] \\ &= A_{21} \cdot \left[\frac{b_{12} \cdot N_{0,\mathrm{CH}} \cdot f_{\mathrm{B},N_{1a}}}{b_{21}+b_{12}+A_{21}+Q_{21}} \cdot \tau_\mathrm{Laser} - \frac{N_{2,\mathrm{on}}(\tau_\mathrm{Laser})}{b_{21}+b_{12}+A_{21}+Q_{21}} + \frac{N_{2,\mathrm{on}}(\tau_\mathrm{Laser})}{A_{21}+Q_{21}} \right]. \end{aligned} \tag{C.5}$$

For weak laser irradiation (linear LIF regime), the rate constants of stimulated absorption and emission are much smaller than the rate constant of collisional quenching, *i.e.*, $b_{21} \ll Q_{21}$ and

$b_{12} \ll Q_{21}$, such that equation C.5 can be rearranged as:

$$\begin{aligned} N_{\mathrm{p}} &\approx A_{21} \cdot \left[\frac{b_{12} \cdot N_{0,\mathrm{CH}} \cdot f_{\mathrm{B},N_{1a}}}{A_{21}+Q_{21}} \cdot \tau_{\mathrm{Laser}} - \frac{N_{2,\mathrm{on}}(\tau_{\mathrm{Laser}})}{A_{21}+Q_{21}} + \frac{N_{2,\mathrm{on}}(\tau_{\mathrm{Laser}})}{A_{21}+Q_{21}} \right] \\ &= A_{21} \cdot \frac{b_{12} \cdot N_{0,\mathrm{CH}} \cdot f_{\mathrm{B},N_{1a}}}{A_{21}+Q_{21}} \cdot \tau_{\mathrm{Laser}} \\ &= A_{21} \cdot N_{2,\mathrm{on,SS}} \cdot \tau_{\mathrm{Laser}}. \end{aligned} \tag{C.6}$$

That is, the number of photons emitted per unit volume calculated using the steady-state population and the laser pulse duration (equation C.6) is accurate in the linear LIF regime, if the camera exposure time is sufficiently long to collect most of the LIF signal. This is because the deficit in terms of emitted photons of the time-resolved solution in comparison to the steady-state case for $t \leq \tau_{\mathrm{Laser}}$ (blue area (A_{on}) in Figure C.1) is compensated by the photons emitted after the laser pulse ($t > \tau_{\mathrm{Laser}}$, red area labelled as A_{off} in Figure C.1). In other words, the zones A_{on} and A_{off} in Figure C.1 have the same surface area. This result does not imply that the steady-state assumption is valid; it is rather a coincidental behaviour caused by the similar characteristic time scales of the exponential rise and decay of the electronically excited state population, which are both determined by the rate constant of collisional quenching, Q_{21}, under weak laser irradiation[1].

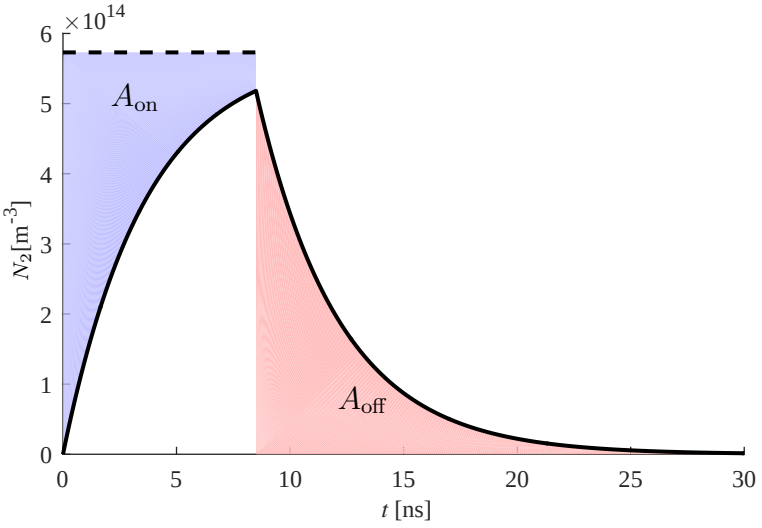

FIGURE C.1: Excited-state population, N_2, for an absorption rate, b_{12}, of $1 \cdot 10^6$ s^{-1} (linear LIF regime), computed with the two-level, LIF model with $R_{kakb}/Q_{21} = 0$. The laser pulse duration, τ_{Laser}, is 8.5 ns. Legend: solid curve is the time-resolved solution, dashed line is the steady-state solution.

[1]The rate constant of spontaneous emission, A_{21}, is of negligible importance in comparison to Q_{21}.

Appendix D

Analysis of $[\mathrm{CH}]_{\mathrm{peak}}$ predictions variability (continued)

The main causes of the significant variability in the predictive capability of modern thermochemical mechanisms were covered in section 4.2. Other discrepancies were observed during the detailed analysis and, although they do not cause the order of magnitude variation in the predictions, they should be of interest for fine adjustments of the thermochemical mechanisms. Furthermore, there are paths for which the reactions included, as well as their rate parameters, are fairly consistent among the mechanisms. These pathways are also presented in this appendix. First, the discussion undertaken in section 4.2 with regards to discrepancies in the paths draining carbon out of the CH formation route from $\mathrm{CH_2^*}$ and $\mathrm{CH_2}$, and in the pathway relaxing methylene from its singlet to its ground triplet state, is completed. Then, paths impacting the pool of colliders involved in the reactions interacting with the CH formation route are reviewed.

D.1 Reactions involving $\mathrm{CH_2^*}$ and $\mathrm{CH_2}$

As explained in section 4.2 based on equation 4.5, [CH] is strongly coupled to the concentration of its main precursor, triplet methylene ($\mathrm{CH_2}$), which is in turn dependent on $\mathrm{CH_2^*}$. Hence, inaccurate descriptions of the rates of production and consumption of singlet and triplet methylene impact the concentration of CH.

As observed in Figures 4.4 and 4.5(a), $\mathrm{CH_2}$ is principally formed from $\mathrm{CH_2^*}$, which proceeds through the relaxation reaction $\mathrm{CH_2^* + M \leftrightarrow CH_2 + M}$. The SD mechanism uses the third-body formulation with efficiencies attributed to the various colliders, while the USC, GRI, and NUIG mechanisms include individual reactions for $\mathrm{CH_2^*}$ colliding with N_2, Ar, H_2O, CO, and CO_2. The specific rates for M=N_2 and M=H_2O are shown in Figure D.1(a, bottom). The USC and NUIG mechanisms use the rate coefficients originally included in the GRI model, which explains their

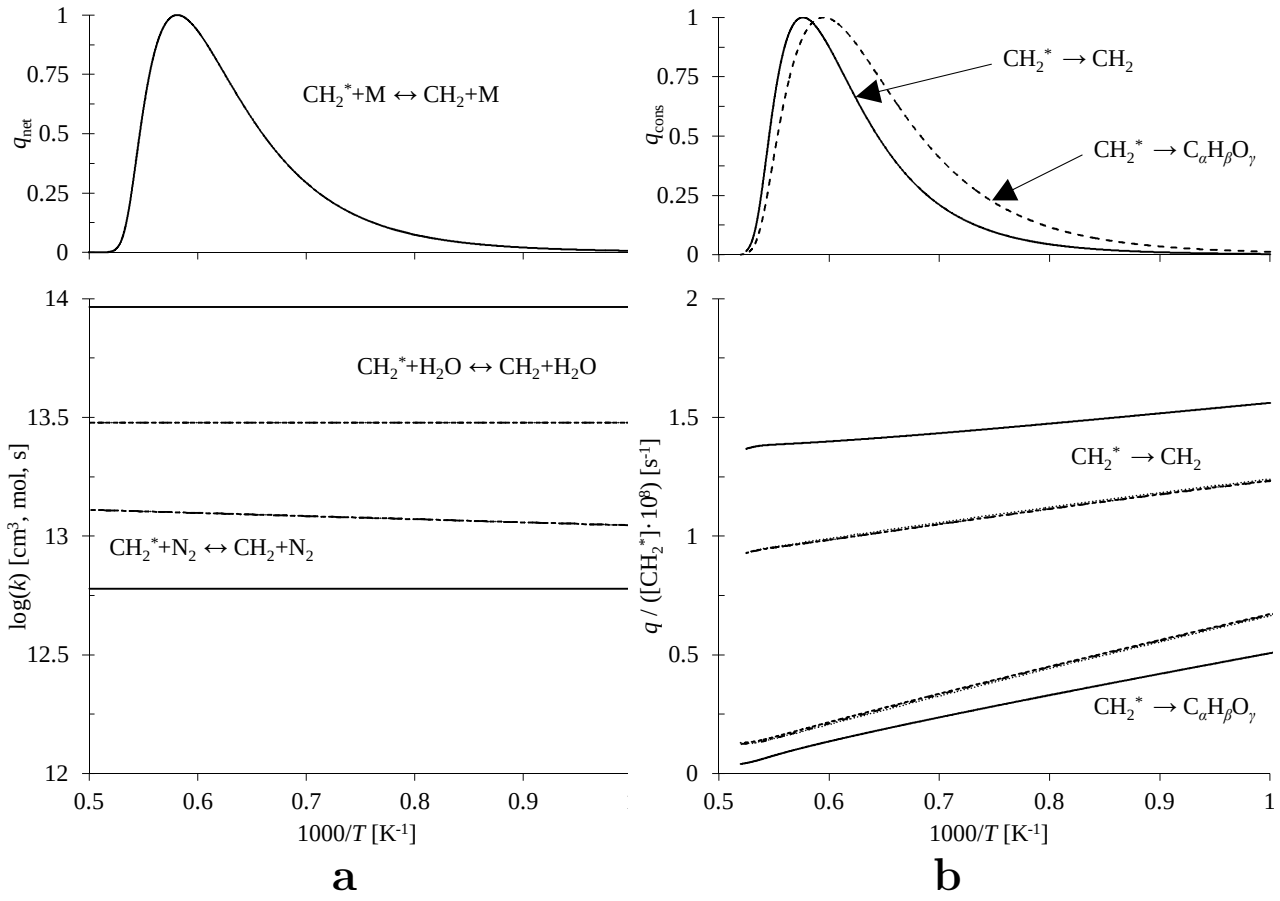

FIGURE D.1: (a) Normalized net reaction rate (top) and specific rate (bottom) of the main reactions producing $\mathrm{CH_2}$, and (b) rate of $\mathrm{CH_2^*}$ consumption normalized to unity (top), and normalized by the $\mathrm{CH_2^*}$ concentration profile (bottom). Same legend as Figure 4.6.

exact agreement. On the other hand, the SD model has $k(T)$ approximately 2 times lower and 5 times higher for M=N_2 and M=H_2O, respectively. This prevents any conclusion on the agreement with the other mechanisms in terms of the overall rate of methylene relaxation as it depends on the specific rates and on the concentration of the third-body colliders. For that reason, Figure D.1(b, bottom) shows the forward rate of consumption of singlet to triplet methylene normalized by the concentration profile of $\mathrm{CH_2^*}$. Similarly to the specific rate, the USC, GRI, and NUIG models are in very good agreement while the SD mechanism predicts a normalized rate of reaction from $\mathrm{CH_2^*}$ to $\mathrm{CH_2}$ approximately 40% higher. However, this difference is clearly not the source of the order of magnitude variability in Figure 4.1 as the NUIG, GRI, and USC mechanisms feature consistent rates of methylene relaxation.

The reactions draining carbon atoms out of the CH formation route from singlet methylene are

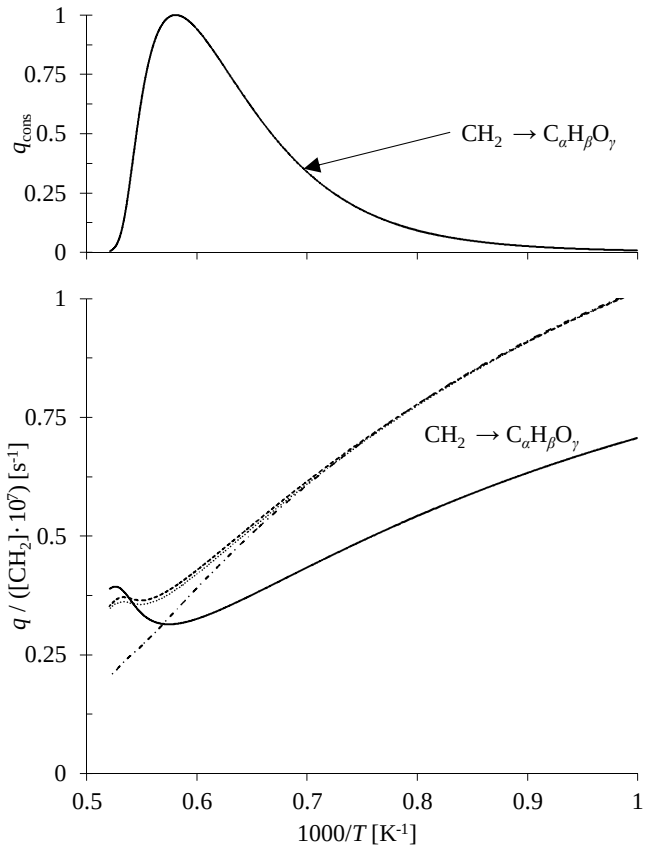

FIGURE D.2: Rate of $\mathrm{CH_2}$ consumption normalized to unity (top), and normalized by the $\mathrm{CH_2}$ concentration profile (bottom). Same legend as Figure 4.6.

presented in Table D.1. While the reactions $\mathrm{CH_2^* + O \leftrightarrow CO + H_2}$, $\mathrm{CH_2^* + OH \leftrightarrow H + CH_2O}$ and $\mathrm{CH_2^* + H_2O \leftrightarrow H_2 + CH_2O}$ appear of negligible importance owing to their low L.S., no reaction stands out as the dominant drain of carbon atoms and differences exist among the models in terms of included reactions. Figure D.1(b, bottom) presents the rate of singlet methylene consumption to $\mathrm{C_\alpha H_\beta O_\gamma}$ compounds normalized by $[\mathrm{CH_2^*}]$. The USC, GRI, and NUIG mechanisms are in close agreement, while the SD model yields a rate ~24% to ~48% lower. As concluded for the rate of methylene relaxation, this discrepancy does not explain the significant variability in $[\mathrm{CH}]_{\mathrm{peak}}$ predictions as the normalized rates of singlet methylene consumption computed with the NUIG, GRI, and USC mechanisms are in good agreement.

The reactions consuming $\mathrm{CH_2}$ and draining carbon out of the CH formation route are reported along with their respective L.S. in Table D.2. None of the reactions included in Table D.2 are present in all models, even if some of them feature fairly large negative logarithmic sensitivities. Figure D.2 (bottom) shows the normalized rate of $\mathrm{CH_2 \rightarrow C_\alpha H_\beta O_\gamma}$ consumption. While agreeing

very well at low temperatures, the NUIG model departs from the normalized rate predicted by the USC and GRI mechanisms at higher temperatures. On the other hand, the SD mechanism predicts slower consumption of methylene over most of the temperature range, and presents a sharp increase in the normalized rate at high temperatures. If this path was determining the ordering and variability of the predicted $[\mathrm{CH}]_{\mathrm{peak}}$ values, one would expect the rate of $\mathrm{CH_2}$ consumption to be the highest for NUIG, followed by SD, GRI, and USC. This is not the case as shown in Figure D.2.

TABLE D.1: Logarithmic sensitivities, multiplied by 10^3, of the principal reactions consuming $\mathrm{CH_2^*}$.

Reaction	SD	USC	GRI	NUIG
$\mathrm{CH_2^* + O \leftrightarrow CO + H_2}$		-1	-1	-2
$\mathrm{CH_2^* + O_2 \leftrightarrow CO + OH + H}$	-63	-46	-49	-88
$\mathrm{CH_2^* + O_2 \leftrightarrow CO + H_2O}$		-32	-33	-43
$\mathrm{CH_2^* + OH \leftrightarrow H + CH_2O}$	-8	-7	-6	-11
$\mathrm{CH_2^* + H_2O \leftrightarrow H_2 + CH_2O}$			-6	
$\mathrm{CH_2^* + CO_2 \leftrightarrow CO + CH_2O}$	-11	-39	-39	-54

TABLE D.2: Logarithmic sensitivities, multiplied by 10^3, of the principal reactions consuming $\mathrm{CH_2}$.

Reaction	SD	USC	GRI	NUIG
$\mathrm{CH_2 + O \leftrightarrow CO + 2H}$	-112			-99
$\mathrm{CH_2 + O \leftrightarrow CO + H_2}$	-70			
$\mathrm{CH_2 + O \leftrightarrow HCO + H}$		-63	-70	
$\mathrm{CH_2 + O_2 \leftrightarrow CO + OH + H}$	-180		-85	
$\mathrm{CH_2 + O_2 \leftrightarrow CO_2 + H_2}$	-72			
$\mathrm{CH_2 + O_2 \leftrightarrow HCO + OH}$		-191		-389
$\mathrm{CH_2 + O_2 \leftrightarrow CO_2 + 2H}$		-32	-77	-86
$\mathrm{CH_2 + O_2 \leftrightarrow O + CH_2O}$			-57	
$\mathrm{CH_2 + OH \leftrightarrow CH_2O + H}$	-135	-58	-52	
$\mathrm{CH_2 + HO_2 \leftrightarrow CH_2O + OH}$		-0.5	-0.8	

D.2 Reactions in the CO to $\mathrm{CO_2}$ path

Interestingly, Figures 4.4 and 4.5 show that the CO to CO_2 path has a significant influence on the maximum concentration of methylidyne although it is not directly connected to the CH formation route. This large positive L.S. value comes from the reaction $\mathrm{CO + OH \leftrightarrow CO_2 + H}$, while reactions $\mathrm{CH_2^* + CO_2 \leftrightarrow CO + CH_2O}$ and $\mathrm{CH + CO_2 \leftrightarrow HCO + CO}$ contribute negatively to $\sum \mathrm{L.S.}(X_{\mathrm{CH,peak}}, i)$ in the CO to CO_2 path (see Tables 4.1 and D.1). A simulation performed with the SD mechanism with the pre-exponential factor of the former reaction multiplied by two showed that, as a first order effect, the mole fraction of H is increased throughout the reaction zone

enhancing reactions having atomic hydrogen as a collider. This then raises the maximum [CH] owing to the increased rate of formation of CH (see equation 4.5 and Figure 4.6(a)). Figure D.3 (bottom) shows that the rate coefficients included in the mechanisms for the reaction $\mathrm{CO} + \mathrm{OH} \leftrightarrow \mathrm{CO_2} + \mathrm{H}$ are in relatively good agreement. The specific rates remain within approximately -10% and 16.5% of the average specific rate over the temperature range shown in the figure. Along with an average L.S of 0.250, the effect on the variability of the $[\mathrm{CH}]_{\mathrm{peak}}$ predictions should then be relatively weak in comparison to the factors discussed in section 4.2.

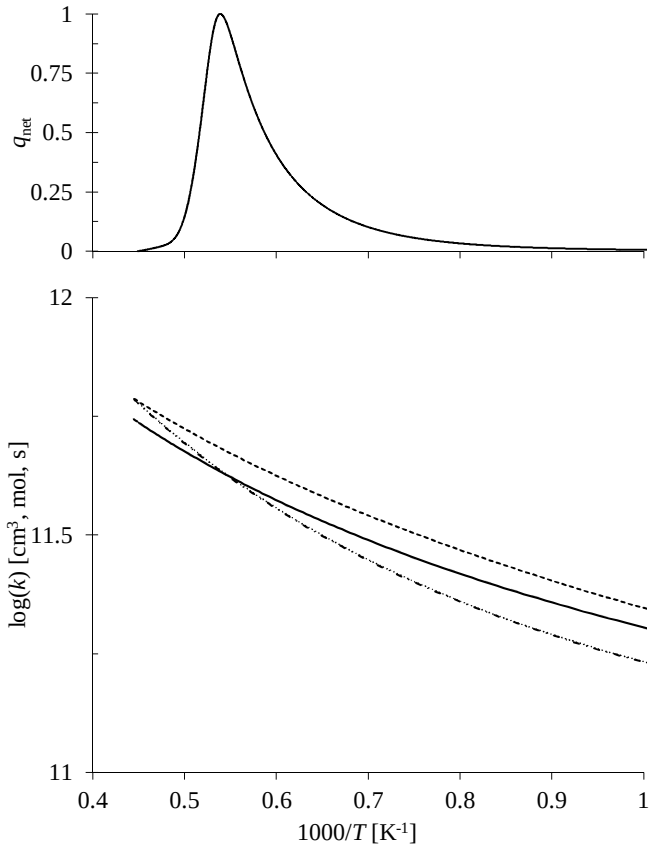

FIGURE D.3: Normalized net reaction rate (top) and specific rate (bottom) of the reaction $\mathrm{CO} + \mathrm{OH} \leftrightarrow \mathrm{CO_2} + \mathrm{H}$. Same legend as Figure 4.6.

D.3 Reactions in the $\mathrm{H_2}/\mathrm{O_2}$ sub-mechanism

H/O compounds act as colliders in many reactions forming or consuming species involved in the CH formation route. Hence, reactions of the $\mathrm{H_2}/\mathrm{O_2}$ sub-mechanism, not shown in the RPA diagram since they do not involve carbon containing species, impact the concentration of CH. Figure

D.4 shows the logarithmic sensitivity of the maximum CH concentration to the specific rate of the most important reactions of the $\mathrm{H_2}/\mathrm{O_2}$ sub-mechanism. The reactions, reversible by nature, are written in the direction of positive overall (net) production rate. Generally, chain-branching reactions have positive L.S., chain-terminating reactions feature negative logarithmic sensitivities, and chain-propagation reactions have the least impact on $[\mathrm{CH}]_{\mathrm{peak}}$.

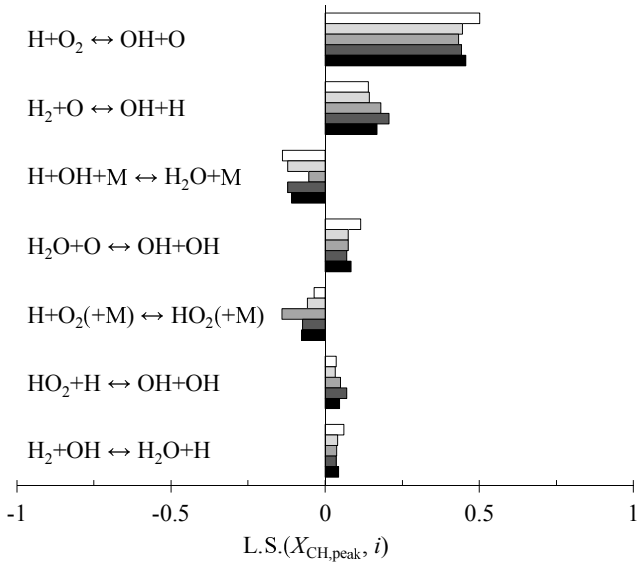

FIGURE D.4: Logarithmic sensitivity of the maximum CH concentration to the specific rate of $\mathrm{H_2}/\mathrm{O_2}$ reactions. Same legend as Figure 4.5.

The specific rate relationships for the reactions included in Figure D.4 are shown for each thermochemical mechanism in Figure D.5. While the agreement is good for the reaction $\mathrm{H}+\mathrm{O_2} \leftrightarrow \mathrm{OH}+\mathrm{O}$, likely because of its significant impact on important combustion properties as the ignition delay time and flame speed [65, 134], there are some disagreements for the reactions with lower values of L.S.

To assess the impact of these discrepancies on the maximum [CH], Figure D.6 presents the difference, relative to the average of the four thermochemical mechanisms, in the specific rate of each reaction taken at the temperature of maximum overall reaction rate against its logarithmic sensitivity. As explained in section 4.2, over-predictions (under-predictions) of the maximum [CH] are due to overestimation (underestimation) of the specific rate of reactions having positive L.S. and/or underestimation (overestimation) for reactions with a negative value of L.S. Then, an overestimation of the concentration of methylidyne would be indicated by data points in the first and third quadrants of Figure D.6, and in the second and fourth quadrants for an under-prediction. In Figure D.6, the dashed and dashed-dotted curves correspond to the iso-contours of $^{\Delta k}/_{k} \cdot \mathrm{L.S.} = 0.03$ and

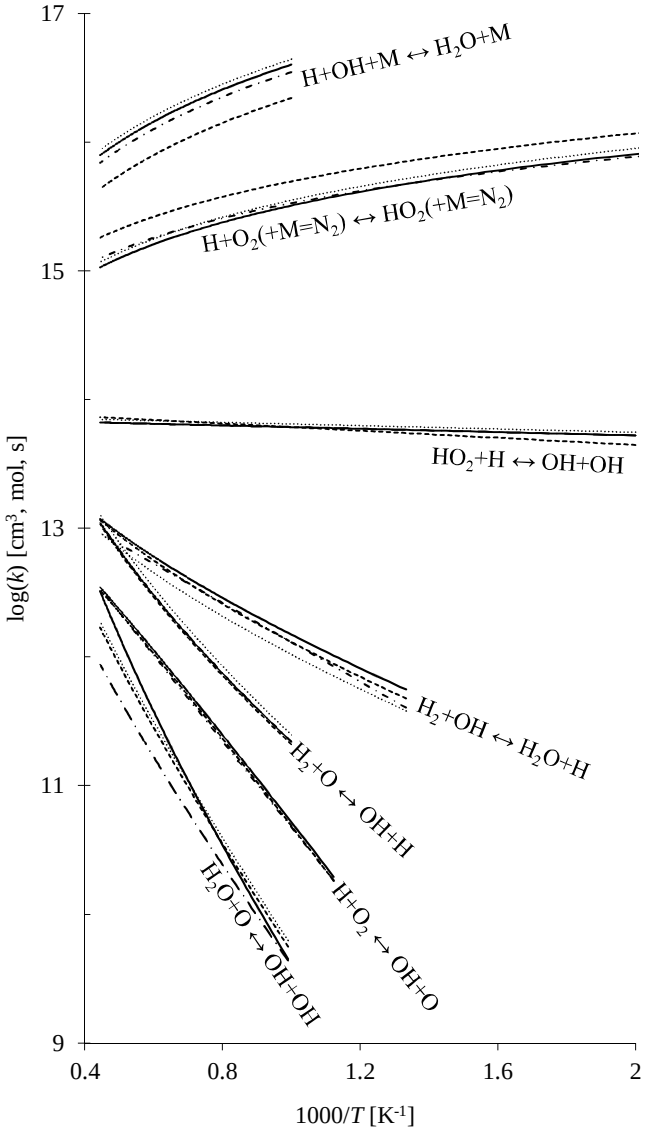

FIGURE D.5: Specific rate of individual $\mathrm{H_2/O_2}$ reactions. Same legend as Figure 4.6.

0.06, respectively. For a first-order linear response, which is obviously not the case in the presence of complex transport, thermodynamic, and chemistry processes, the iso-contours would represent relative differences in maximum [CH] of 3% and 6%, respectively. In Figure D.6, all the data points lie within the $^{\Delta k}/_{k} \cdot \mathrm{L.S.} = 0.06$ iso-contour, and most of them within the $^{\Delta k}/_{k} \cdot \mathrm{L.S.} = 0.03$ iso-contour. Hence, the order of magnitude variability in CH formation observed in Figure 4.1 is not explained by inconsistencies in the $\mathrm{H_2/O_2}$ chemistry among the thermochemical mechanisms.

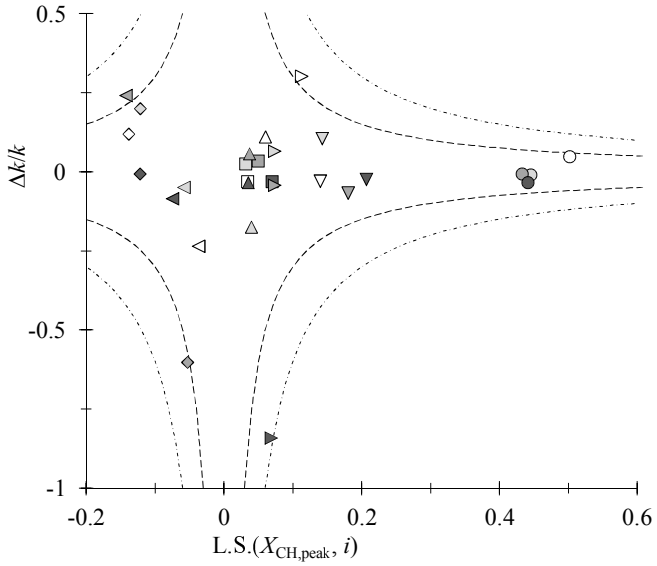

FIGURE D.6: Difference in the specific rate relative to the average value vs. $\mathrm{L.S.}(X_{\mathrm{CH,peak}}, i)$. Colours according to Figure 4.5. Symbols: $\circ$ $\mathrm{H}+\mathrm{O_2} \leftrightarrow \mathrm{OH}+\mathrm{O}$, $\square$ $\mathrm{HO_2}+\mathrm{H} \leftrightarrow \mathrm{OH}+\mathrm{OH}$, $\diamond$ $\mathrm{H}+\mathrm{OH}+\mathrm{M} \leftrightarrow \mathrm{H_2O}+\mathrm{M}$, $\triangle$ $\mathrm{H_2}+\mathrm{OH} \leftrightarrow \mathrm{H_2O}+\mathrm{H}$, $\triangleright$ $\mathrm{H_2O}+\mathrm{O} \leftrightarrow \mathrm{OH}+\mathrm{OH}$, $\triangledown$ $\mathrm{H_2}+\mathrm{O} \leftrightarrow \mathrm{OH}+\mathrm{H}$, $\triangleleft$ $\mathrm{H}+\mathrm{O_2}(+\mathrm{M}=\mathrm{N_2}) \leftrightarrow \mathrm{HO_2}(+\mathrm{M}=\mathrm{N_2})$. Dashed and dashed-dotted curves correspond to iso-contours of $\Delta k/k \cdot \mathrm{L.S.}(X_{\mathrm{CH,peak}}, i) = 0.03$ and 0.06, respectively.

Appendix E

Effect of the uncertain thermodynamic properties on the $[\mathrm{CH}]_{\mathrm{peak}}$ predictions

The optimization procedure presented in Chapter 5 solely considers the uncertainties in the rate coefficients of the elementary reactions. However, inaccuracies in the thermodynamic properties can induce errors in the local temperature and, consequently, impact the computed specific rates. Furthermore, in most thermochemical mechanisms, the specific rate of the reactions is only specified in the forward direction. The backward specific rate is obtained from the equilibrium constant computed from the entropy and heat of formation $\left(\bar{h}_k^\circ\right)$ data, the latter generally bearing the largest uncertainty of all thermodynamic properties [235]. Therefore, in addition to the rate coefficients, the uncertainties in the thermodynamic parameters have the potential to induce errors in the [CH] predictions.

To assess if thermodynamic properties should be included in the optimization, an analysis similar to that presented in Figures 5.1 and 5.2 is performed. Figure E.1 presents the logarithmic sensitivity of the maximum CH concentration to changes in the heat of formation of the individual species, $\mathrm{L.S.}\left(X_{\mathrm{CH,peak}}, k\right)$, extracted from jet-wall stagnation flame simulations. It is observed that $\mathrm{L.S.}\left(X_{\mathrm{CH,peak}}, k\right)$ can be as much as one order of magnitude larger than the logarithmic sensitivity of $[\mathrm{CH}]_{\mathrm{peak}}$ to variations in the specific rates (see Figure 5.2). However, the values of $\bar{h}_k^\circ$ are known to a greater level of accuracy than the rate coefficients. Figure E.2 presents the product of $\mathrm{L.S.}\left(X_{\mathrm{CH,peak}}, k\right)$ with the relative uncertainty in the heat of formation of each species obtained from [236]. These values are as much as three orders of magnitude lower than the products of the logarithmic sensitivity with the relative uncertainty in the specific rates presented in Figure 5.2. Therefore, the error induced in $[\mathrm{CH}]_{\mathrm{peak}}$ by the uncertain thermodynamic parameters is negligible in comparison to the contribution of the rate coefficients. Consequently, only the pre-exponential factors of key reactions involved in the CH formation route are optimized in this study.

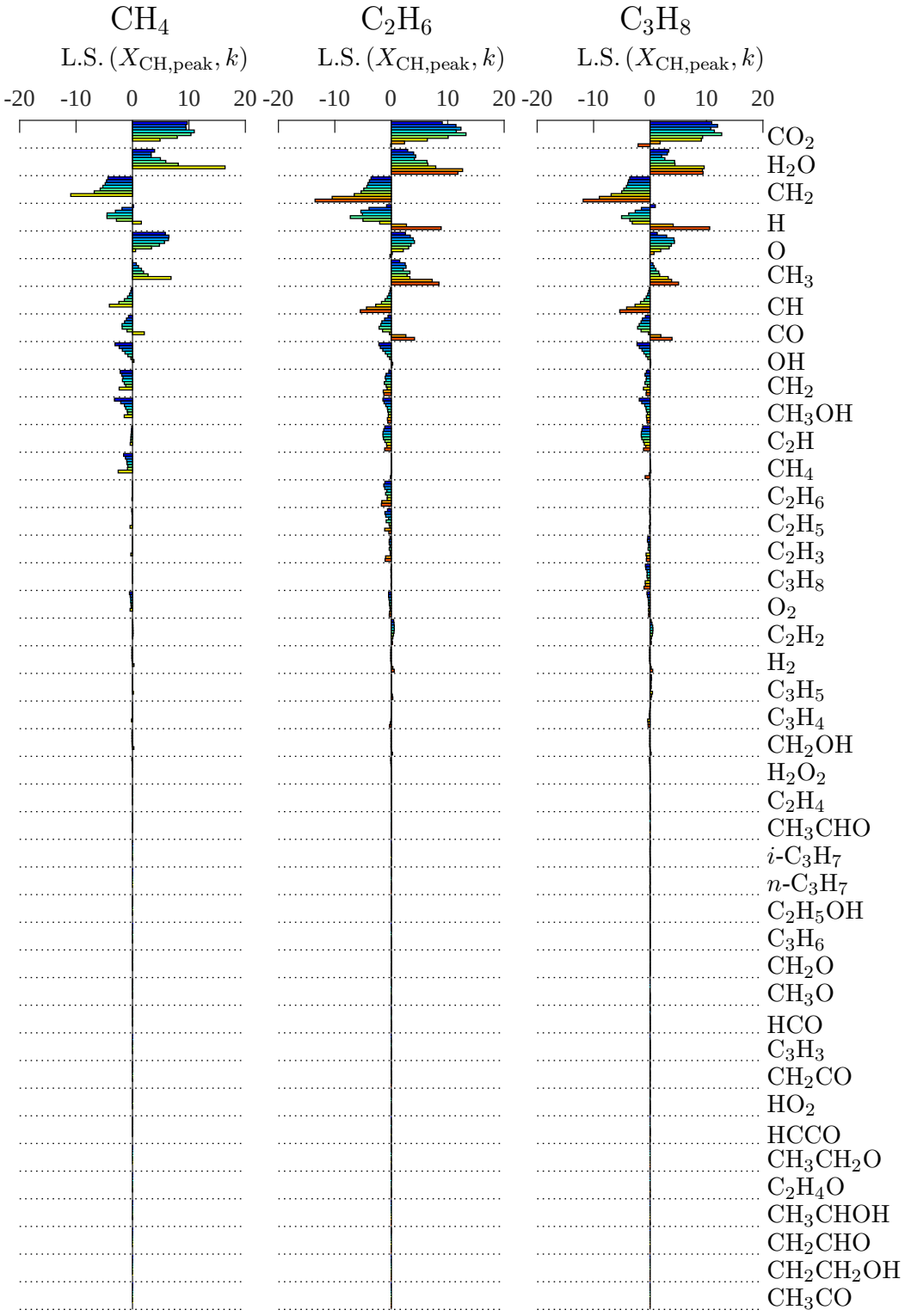

FIGURE E.1: Logarithmic sensitivity of the maximum CH mole fraction to the heat of formation of individual species, L.S. $(X_{\mathrm{CH,peak}}, k)$. The species are sorted in decreasing order of $\sum_{\mathrm{C}_m\mathrm{H}_n,\phi} \mathrm{L.S.}\,(X_{\mathrm{CH,peak}}, k)^2$.

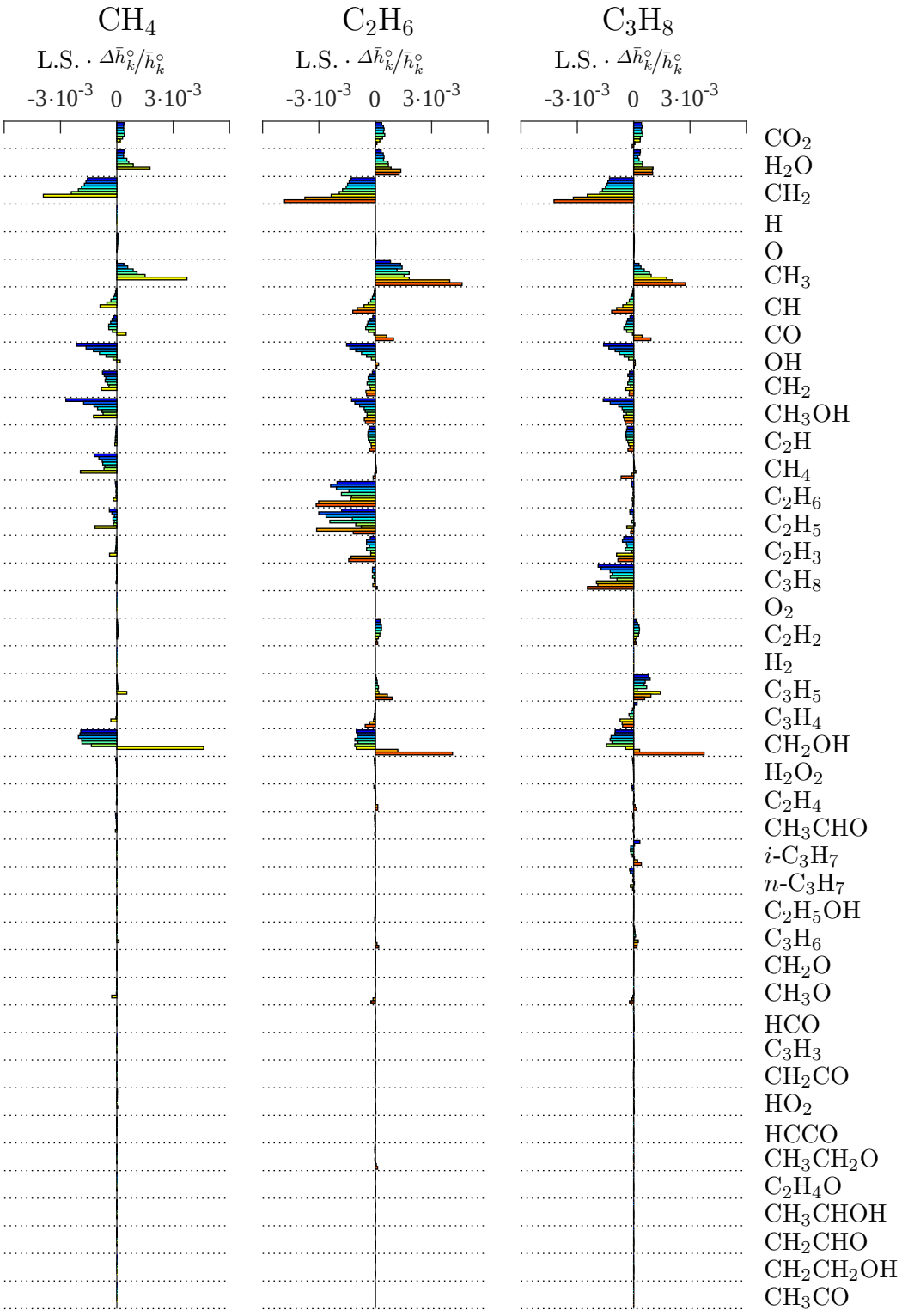

FIGURE E.2: Product of L.S. $(X_{\mathrm{CH,peak}}, k)$ with $^{\Delta \bar{h}^\circ_k}/_{\bar{h}^\circ_k}$. The relative errors are obtained from [236].

Appendix F

Experimental boundary conditions

The boundary conditions required to perform the quasi-1D stagnation flame simulations are presented in Table F.1, and their acquisition is described in Chapter 2. The origin of the computational domain coincides with the stagnation surface, *i.e.*, $z_{\mathrm{plate}} = 0$. The uncertainties are given in parentheses.

TABLE F.1: Experimentally determined boundary conditions for stagnation flame simulations.

Fuel	ϕ	z_{inlet} [mm]	u_{inlet} [m/s]	$\mathrm{d}u/\mathrm{d}z\|_{\mathrm{inlet}}$ [1/s]	T_{inlet} [K]	T_{plate} [K]
CH_4	0.7 (0.004)	11.04 (0.05)	0.258 (0.002)	50.4 (4.8)	296 (3)	316 (9)
	0.8 (0.005)	10.73 (0.05)	0.420 (0.004)	84.1 (7.0)	296 (3)	331 (10)
	0.9 (0.006)	10.87 (0.05)	0.549 (0.005)	119.2 (6.6)	296 (3)	344 (10)
	1.0 (0.006)	10.80 (0.05)	0.634 (0.006)	139.0 (4.0)	296 (3)	353 (11)
	1.1 (0.007)	11.00 (0.05)	0.613 (0.007)	145.3 (18.9)	296 (3)	353 (11)
	1.2 (0.008)	12.00 (0.06)	0.567 (0.005)	115.1 (5.8)	296 (3)	345 (10)
	1.3 (0.008)	12.80 (0.06)	0.425 (0.004)	82.9 (4.5)	296 (3)	334 (10)
C_2H_6	0.7 (0.004)	10.97 (0.05)	0.369 (0.004)	72.9 (5.7)	296 (3)	323 (10)
	0.8 (0.005)	10.99 (0.05)	0.512 (0.005)	109.8 (7.0)	296 (3)	338 (10)
	0.9 (0.006)	10.56 (0.05)	0.641 (0.006)	140.9 (7.5)	296 (3)	344 (10)
	1.0 (0.006)	10.65 (0.05)	0.730 (0.007)	167.0 (12.2)	296 (3)	363 (11)
	1.1 (0.007)	10.99 (0.05)	0.761 (0.008)	170.5 (11.8)	296 (3)	360 (11)
	1.2 (0.008)	10.76 (0.05)	0.726 (0.008)	167.8 (13.2)	296 (3)	359 (11)
	1.3 (0.008)	11.29 (0.05)	0.618 (0.006)	132.6 (6.3)	296 (3)	350 (10)
	1.4 (0.009)	12.58 (0.06)	0.454 (0.004)	91.8 (12.3)	296 (3)	336 (10)
	1.5 (0.010)	10.63 (0.05)	0.349 (0.003)	76.5 (4.0)	296 (3)	331 (10)
C_3H_8	0.7 (0.004)	10.66 (0.05)	0.367 (0.003)	74.9 (4.9)	296 (3)	324 (10)
	0.8 (0.005)	10.79 (0.05)	0.507 (0.004)	108.1 (4.3)	296 (3)	338 (10)
	0.9 (0.006)	10.76 (0.05)	0.627 (0.006)	139.4 (5.0)	296 (3)	351 (11)
	1.0 (0.006)	10.60 (0.05)	0.704 (0.006)	161.2 (7.0)	296 (3)	363 (11)
	1.1 (0.007)	10.82 (0.05)	0.727 (0.007)	169.5 (7.9)	296 (3)	361 (11)
	1.2 (0.008)	10.98 (0.05)	0.679 (0.006)	152.6 (6.9)	296 (3)	356 (11)
	1.3 (0.008)	11.43 (0.05)	0.568 (0.005)	125.5 (6.6)	296 (3)	347 (10)
	1.4 (0.009)	12.01 (0.06)	0.411 (0.004)	86.8 (5.5)	296 (3)	334 (10)
	1.5 (0.010)	12.15 (0.06)	0.289 (0.003)	55.0 (7.5)	296 (3)	323 (10)
n-C_4H_{10}	0.7 (0.004)	12.88 (0.06)	0.382 (0.003)	69.1 (3.9)	296 (3)	327 (10)
	0.8 (0.005)	12.07 (0.06)	0.512 (0.005)	104.8 (4.4)	296 (3)	341 (10)
	0.9 (0.006)	11.80 (0.06)	0.620 (0.006)	129.2 (5.0)	296 (3)	354 (11)
	1.0 (0.006)	11.01 (0.05)	0.673 (0.006)	152.5 (7.8)	296 (3)	362 (11)
	1.1 (0.007)	11.00 (0.05)	0.675 (0.006)	160.7 (6.9)	296 (3)	361 (11)
	1.2 (0.008)	10.84 (0.05)	0.625 (0.006)	141.4 (6.4)	296 (3)	357 (11)
	1.3 (0.008)	10.80 (0.05)	0.485 (0.004)	110.6 (8.3)	296 (3)	345 (10)
	1.4 (0.009)	10.10 (0.05)	0.348 (0.003)	83.5 (13.1)	296 (3)	335 (10)

Appendix G

CH concentration target data

This study provides quantitative measurements of CH production in premixed flames of methane, ethane, propane and *n*-butane mixed with air. As discussed in section 2.3, the measured CH-LIF signal intensity is made quantitative through normalization by the Rayleigh scattering signal of nitrogen. The solutions of flame simulations performed with various thermochemical models are provided to a LIF model generating numerical profiles of LIF-to-Rayleigh ratio. The maximum value of $S_{\mathrm{LIF}}/S_{\mathrm{R}}$, a scalar value selected as a surrogate measure of CH formation, is extracted from the experimental and numerical profiles and compared to assess the accuracy of thermochemical mechanisms. The benefit of this direct comparative approach is that it separates measured and simulated values in order to achieve the highest accuracy of the experimental data for the validation of thermochemical models. Table G.1 presents, in numerical form, the experimental data previously presented in Figure 4.1.

TABLE G.1: Measured, maximum values of $S_{\mathrm{LIF}}/S_{\mathrm{R}}$. The 95% interval of confidence accounting for the scatter in the experimental data is shown in parentheses.

ϕ	CH_4	C_2H_6	C_3H_8	n-C_4H_{10}
0.7	0.9 (0.3)	1.8 (0.5)	1.6 (0.4)	2.6 (0.7)
0.8	2.6 (1.0)	4.3 (1.3)	5.5 (1.3)	7.2 (1.4)
0.9	5.8 (1.4)	9.0 (1.3)	10.7 (3.0)	11.3 (3.5)
1.0	11.4 (2.1)	13.0 (2.1)	15.0 (2.7)	17.9 (4.1)
1.1	14.9 (4.0)	18.3 (4.3)	24.8 (4.0)	23.5 (2.9)
1.2	16.5 (3.2)	23.3 (6.1)	25.6 (4.1)	24.2 (4.3)
1.3	11.9 (1.0)	21.0 (1.6)	23.2 (1.9)	22.6 (1.4)
1.4	—	12.2 (5.3)	15.1 (3.0)	11.5 (2.6)
1.5	—	5.5 (1.8)	6.0 (1.7)	—

To employ the direct comparative methodology, fairly accurate numerical predictions of the temperature and major species concentrations are required to generate the LIF-to-Rayleigh intensity profiles. These predictions might not be available, or sufficiently accurate, in the early stages of thermochemical model development. It is then more convenient to use concentration data as initial targets. Maximum values of methylidyne mole fraction [ppm] and concentration $[\mathrm{mol/m^3}]$

are presented in Tables G.2 and G.3, respectively. For modellers, it is also more time consuming to generate numerical profiles of $S_{\mathrm{LIF}}/S_{\mathrm{R}}$ than to compare the raw output of flame simulations to experimental data reduced to mole fractions. The data presented in Tables G.2 and G.3 can be used to rapidly verify the progress made in the development of thermochemical mechanisms. However, as discussed in section 2.3, the highest degree of accuracy will be obtained through direct comparison of experimentally and numerically determined LIF intensities, the latter modelled using species and temperature profiles provided by the thermochemical mechanism under study.

TABLE G.2: Estimated maximum mole fraction of methylidyne in premixed flames of $\mathrm{C_1}$-$\mathrm{C_4}$ alkanes in parts per million.

ϕ	$\mathrm{CH_4}$	$\mathrm{C_2H_6}$	$\mathrm{C_3H_8}$	n-$\mathrm{C_4H_{10}}$
0.7	0.1	0.2	0.2	0.3
0.8	0.4	0.7	0.8	1.1
0.9	1.1	1.7	1.9	2.1
1.0	2.4	2.8	3.0	3.7
1.1	3.4	4.3	5.5	5.2
1.2	3.8	5.6	5.9	5.5
1.3	2.6	4.8	5.3	4.9
1.4	—	2.6	3.2	2.3
1.5	—	1.1	1.2	—

TABLE G.3: Estimated maximum number density of methylidyne in premixed flames of $\mathrm{C_1}$-$\mathrm{C_4}$ alkanes in mol/m^3.

ϕ	$\mathrm{CH_4}$	$\mathrm{C_2H_6}$	$\mathrm{C_3H_8}$	n-$\mathrm{C_4H_{10}}$
0.7	$8.8 \cdot 10^{-7}$	$1.9 \cdot 10^{-6}$	$1.5 \cdot 10^{-6}$	$2.7 \cdot 10^{-6}$
0.8	$3.0 \cdot 10^{-6}$	$5.2 \cdot 10^{-6}$	$6.4 \cdot 10^{-6}$	$8.7 \cdot 10^{-6}$
0.9	$7.5 \cdot 10^{-6}$	$1.2 \cdot 10^{-5}$	$1.4 \cdot 10^{-5}$	$1.5 \cdot 10^{-5}$
1.0	$1.6 \cdot 10^{-5}$	$1.9 \cdot 10^{-5}$	$2.1 \cdot 10^{-5}$	$2.6 \cdot 10^{-5}$
1.1	$2.2 \cdot 10^{-5}$	$2.9 \cdot 10^{-5}$	$3.7 \cdot 10^{-5}$	$3.5 \cdot 10^{-5}$
1.2	$2.5 \cdot 10^{-5}$	$3.6 \cdot 10^{-5}$	$3.9 \cdot 10^{-5}$	$3.6 \cdot 10^{-5}$
1.3	$1.7 \cdot 10^{-5}$	$3.1 \cdot 10^{-5}$	$3.5 \cdot 10^{-5}$	$3.2 \cdot 10^{-5}$
1.4	—	$1.7 \cdot 10^{-5}$	$2.1 \cdot 10^{-5}$	$1.5 \cdot 10^{-5}$
1.5	—	$7.1 \cdot 10^{-6}$	$7.8 \cdot 10^{-6}$	—

The data presented in Tables G.2 and G.3 were obtained by adjusting, for each fuel and equivalence ratio, the [CH] profile output by a flame simulation and provided to the LIF model such that the maximum numerical LIF-to-Rayleigh ratio agrees with the experimental value. This post-processing methodology did not require new simulations. Instead, the profile of CH number density predicted by the GRI mechanism (USC for *n*-butane) was multiplied by a factor adjusted using a root-finding secant method to minimize (absolute tolerance of $1 \cdot 10^{-6}$) the error between the modelled and measured maximum values of $S_{\mathrm{LIF}}/S_{\mathrm{R}}$.

Bibliography

[1] US Energy Information Administration. *International Energy Outlook 2016 With Projections to 2040*. Tech. rep. Report DOE/EIA-0484(2016). Washington D.C., 2016, p. 276.

[2] IPCC 2014. *Climate Change 2014: Synthesis Report. Contribution of Working Groups I, II and III to the Fifth Assessment Report of the Intergovernmental Panel on Climate Change*. Ed. by R.K. Pachauri and L.A. Meyer. Geneva, Switzerland, 2014, p. 151.

[3] M.Z. Jacobson. "Review of solutions to global warming, air pollution, and energy security". In: *Energy Environ. Sci.* 2.2 (2008), pp. 148–173.

[4] M.Z. Jacobson and M.A. Delucchi. "Providing all global energy with wind, water, and solar power, Part I: Technologies, energy resources, quantities and areas of infrastructure, and materials". In: *Energy Policy* 39.3 (2011), pp. 1154–1169.

[5] M. Schiemann, J.M. Bergthorson, P. Fischer, V. Scherer, D. Taroata, and G. Schmid. "A review on lithium combustion". In: *Appl. Energy* 162 (2016), pp. 948–965.

[6] H. Ibrahim, A. Ilinca, and J. Perron. "Energy storage systems-characteristics and comparisons". In: *Renew. Sustainable Energy Rev.* 12.5 (2008), pp. 1221–1250.

[7] Y. Hou, R. Vidu, and P. Stroeve. "Solar Energy Storage Methods". In: *Ind. Eng. Chem. Res.* 50.15 (2011), pp. 8954–8964.

[8] J.M. Bergthorson et al. "Direct combustion of recyclable metal fuels for zero-carbon heat and power". In: *Appl. Energy* 160 (2015), pp. 368–382.

[9] T.M. Mata, A.A. Martins, and N.S. Caetano. "Microalgae for biodiesel production and other applications: a review". In: *Renew. Sustainable Energy Rev.* 14.1 (2010), pp. 217–232.

[10] L. Brennan and P. Owende. "Biofuels from microalgae - A review of technologies for production, processing, and extractions of biofuels and co-products". In: *Renew. Sust. Energy Rev.* 14.2 (2010), pp. 557–577.

[11] M. Romero and A. Steinfeld. "Concentrating solar thermal power and thermochemical fuels". In: *Energy Environ. Sci.* 5.11 (2012), pp. 9234–9245.

[12] G.P. Smestad and A. Steinfeld. “Review: Photochemical and thermochemical production of solar fuels from H_2O and CO_2 using metal oxide catalysts”. In: *Ind. Eng. Chem. Res.* 51.37 (2012), pp. 11828–11840.

[13] US Environmental Protection Agency. *2011 National Emissions Inventory (NEI) Data*. Available: https://www.epa.gov/air-emissions-inventories/2011-national-emissions-inventory-nei-data, Accessed: 2016-09-15.

[14] A.H. Lefebvre and D.R. Ballal. *Gas Turbine Combustion: Alternative Fuels and Emissions*. CRC Press, 2010.

[15] D. Vallero. “Effects on health and human welfare”. In: *Fundamentals of Air Pollution*. Fourth Edit. Academic Press, 2008. Chap. 11, pp. 359–396.

[16] D.J. Jacob. *Introduction to Atmospheric Chemistry*. Princeton University Press, 2000, p. 280.

[17] D.J. Jacob. “Heterogeneous chemistry and tropospheric ozone”. In: *Atmos. Environ.* 34 (2000), pp. 2131–2159.

[18] N.F.M. Porta and R.H. Steinhorn. “Pulmonary vasodilator therapy in the NICU: inhaled nitric oxide, Sildenafil, and other pulmonary vasodilating agents”. In: *Clin. Perinatology* 39.1 (2012), pp. 149–164.

[19] D. Vallero. “Air pollutant hazards”. In: *Fundamentals of Air Pollution*. Fifth Edit. Academic Press, 2014. Chap. 7, pp. 197–214.

[20] World Health Organization. *Ambient (outdoor) air quality and health*. Available: http://www.who.int/mediacentre/factsheets/fs313/en/, Accessed: 2016-09-21.

[21] R.C. Flagan and J.H. Seinfeld. *Fundamentals of Air Pollution Engineering*. Prentice Hall, 1988, p. 542.

[22] US Environmental Protection Agency. *Nitrogen oxides* (NO_x), *why and how they are controlled*. Technical report EPA-456/F-99-006R. 1999.

[23] US Environmental Protection Agency. *Health Effects of Ozone Pollution*. Available: https://www.epa.gov/ozone-pollution/health-effects-ozone-pollution, Accessed: 2016-09-22.

[24] US Environmental Protection Agency. “National ambient air quality standards for ozone”. In: *Federal Register* 80.206 (2015), pp. 65291–65468.

[25] US Environmental Protection Agency. *2015 Ozone Standards*. Available: https://ozoneairqualitystandards.epa.gov/OAR_OAQPS/OzoneSliderApp/index.html, Accessed: 2016-09-22.

[26] D. Vallero. “Air pollution’s impact on ecosystems”. In: *Fundamentals of Air Pollution*. Fifth Edit. Academic Press, 2014. Chap. 14, pp. 341–368.

[27] E. Malek, T. Davis, R.S. Martin, and P.J. Silva. “Meteorological and environmental aspects of one of the worst national air pollution episodes (January, 2004) in Logan, Cache Valley, Utah, USA”. In: *Atmos. Res.* 79.2 (2006), pp. 108–122.

[28] R.M. Harrison and R.E. van Grieken, eds. *Atmospheric particles*. John Wiley & Sons, Ltd., 1998, p. 610.

[29] D.W. Sparling, T.P. Lowe, and P.G.C. Campbell. “Ecotoxicology of aluminum to fish and wildlife”. In: *Research Issues in Aluminum Toxicity*. Ed. by R.A. Yokel and M.S. Golub. Taylor & Francis, 1997, pp. 47–68.

[30] US Environmental Protection Agency. *Effects of Acid Rain*. Available: https://www.epa.gov/acidrain/effects-acid-rain, Accessed: 2016-09-14.

[31] C.T. Driscoll et al. “Acidic deposition in the Northeastern United States: sources and inputs, ecosystem effects, and management strategies”. In: *Biosci.* 51.3 (2001), pp. 180–198.

[32] C.T. Driscoll, K.M. Driscoll, M.J. Mitchell, and D.J. Raynal. “Effects of acidic deposition on forest and aquatic ecosystems in New York State”. In: *Environ. Pollut.* 123.3 (2003), pp. 327–336.

[33] H. Bravo A. et al. “Effect of acid rain on building material of the El Tajín archaeological zone in Veracruz, Mexico”. In: *Environ. Pollut.* 144.2 (2006), pp. 655–660.

[34] D. Vallero. “Air pollution’s impact on materials and structures”. In: *Fundamentals of Air Pollution*. Fifth Edit. Academic Press, 2014. Chap. 15, pp. 369–378.

[35] US Environmental Protection Agency. *Nutrient Pollution*. Available: https://www.epa.gov/nutrientpollution, Accessed: 2016-11-16.

[36] H.W. Paerl, R.L. Dennis, and D.R. Whitall. “Atmospheric deposition of nitrogen: Implications for nutrient over-enrichment of coastal waters”. In: *Estuaries* 25.1 (2002), pp. 677–693.

[37] F. Paulot, D.J. Jacob, R.W. Pinder, J.O. Bash, K. Travis, and D.K. Henze. "Ammonia emissions in the United States, European Union, and China derived by high-resolution inversion of ammonium wet deposition data: Interpretation with a new agricultural emissions inventory (MASAGE_NH_3)". In: *J. Geophysical Res. Atmos.* 119.7 (2014), pp. 4343–4364.

[38] R. Martin, R. Coulombe, and R. Brain. "Utah air quality: PM 2.5". In: *All Current Publications*. 784. Utah State University Extension, 2016, pp. 1–4.

[39] P.H. McMurry, M.F. Shepherd, and J.S. Vickery, eds. *Particulate Matter Science for Policy Makers: A NARSTO Assessment*. Cambridge University Press, 2004, p. 510.

[40] M.L. Bell, F. Dominici, K. Ebisu, S.L. Zeger, and J.M. Samet. "Spatial and temporal variation in $PM_{2.5}$ chemical composition in the United States for health effects studies". In: *Environ. Health Perspect.* 115.7 (2007), pp. 989–995.

[41] US Environmental Protection Agency. *Air Quality Index - A Guide to Air Quality and Your Health*. Brochure EPA-456/F-14-00. 2014.

[42] A.K. Benton et al. "Night-time chemistry above London: measurements of NO_3 and N_2O_5 from the BT Tower". In: *Atmos. Chem. Phys.* 10.20 (2010), pp. 9781–9795.

[43] B.R. Ayres et al. "Organic nitrate aerosol formation via NO_3^+ biogenic volatile organic compounds in the southeastern United States". In: *Atmos. Chem. Phys.* 15.23 (2015), pp. 13377–13392.

[44] US Environmental Protection Agency. *Health and Environmental Effects of Particulate Matter (*PM*)*. Available: https://www.epa.gov/pm-pollution/health-and-environmental-effects-particulate-matter-pm, Accessed: 2016-09-14.

[45] US Environmental Protection Agency. "National ambient air quality standards for particulate matter". In: *Federal Register* 78.10 (2013), pp. 3085–3287.

[46] T. Godish and J.S. Fu. *Air Quality*. Third edition. CRC Press, 1997, p. 464.

[47] E.V. Fischer et al. "Atmospheric peroxyacetyl nitrate (PAN): a global budget and source attribution". In: *Atmos. Chem. Phys.* 14.5 (2014), pp. 2679–2698.

[48] G. Lee, Y. Jang, H. Lee, J.-S. Han, K.-R. Kim, and M. Lee. "Characteristic behavior of peroxyacetyl nitrate (PAN) in Seoul megacity, Korea". In: *Chemosphere* 73.4 (2008), pp. 619–628.

[49] I.B. Pollack, T.B. Ryerson, M. Trainer, J.A. Neuman, J.M. Roberts, and D.D. Parrish. "Trends in ozone, its precursors, and related secondary oxidation products in Los Angeles, California: A synthesis of measurements from 1960 to 2010". In: *J. Geophysical Res. Atmos.* 118.11 (2013), pp. 5893–5911.

[50] E.L. Williams II, E. Grosjean, and D. Grosjean. "Ambient levels of the peroxyacyl nitrates PAN, PPN and MPAN in Atlanta, Georgia". In: *Air & Waste* 43.6 (1993), pp. 873–879.

[51] T.C. Lieuwen and V. Yang. *Gas Turbine Emissions*. Cambridge Edition, 2013, p. 382.

[52] US Environmental Protection Agency. *Emission Standards Reference Guide for On-road and Nonroad Vehicles and Engines*. Available: https://www.epa.gov/emission-standards-reference-guide, Accessed: 2016-09-27.

[53] Environment and Climate Change Canada. *Vehicle and Engine Regulations*. Available: https://www.ec.gc.ca/air/default.asp?lang=En&n=AE4ECEC1-1, Accessed: 2016-09-28.

[54] T.C. Lieuwen, M. Chang, and A. Amato. "Stationary gas turbine combustion: Technology needs and policy considerations". In: *Combust. Flame* 160.8 (2013), pp. 1311–1314.

[55] J.M. Bergthorson and M.J. Thomson. "A review of the combustion and emissions properties of advanced transportation biofuels and their impact on existing and future engines". In: *Renew. Sust. Energy Rev.* 42 (2015), pp. 1393–1417.

[56] A.C.A. Lipardi, J.M. Bergthorson, and G. Bourque. "NO_x emissions modeling and uncertainty from exhaust-gas-diluted flames". In: *J. Eng. Gas Turbines Power* 138.5 (2016), pp. 051506-1–051506-10.

[57] P. Gokulakrishnan and M.S. Klassen. "NO_x and CO formation and control". In: *Gas Turbine Emissions*. Ed. by T.C. Lieuwen and V. Yang. Cambridge Edition, 2013. Chap. 7, pp. 125–341.

[58] J.A. Miller and C.T. Bowman. "Mechanism and modeling of nitrogen chemistry in combustion". In: *Prog. Energy Combust. Sci.* 15 (1989), pp. 287–338.

[59] A.M. Dean and J.W. Bozzelli. "Combustion chemistry of nitrogen". In: *Gas-phase combustion chemistry*. Ed. by W.C. Gardiner Jr. Springer-Verlag, 2000. Chap. 2, pp. 125–341.

[60] G.M.G. Watson, J.D. Munzar, and J.M. Bergthorson. "Diagnostics and modeling of stagnation flames for the validation of thermochemical combustion models for NO_x predictions". In: *Energy Fuels* 27 (2013), pp. 7031–7043.

[61] G.M.G. Watson, J.D. Munzar, and J.M. Bergthorson. “NO formation in model syngas and biogas blends”. In: *Fuel* 124 (2014), pp. 113–124.

[62] Y.B. Zeldovich. “The oxidation of nitrogen in combustion and explosions”. In: *Acta Physicochim.* 21 (1946), p. 577.

[63] G.A. Lavoie, J.B. Heywood, and J.C. Keck. “Experimental and theoretical study of nitric oxide formation in internal combustion engines”. In: *Combust. Sci. Technol.* 1.4 (1970), pp. 313–326.

[64] G.M.G. Watson, P. Versailles, and J.M. Bergthorson. “NO Formation in premixed flames of C_1-C_3 alkanes and alcohols”. In: *Combust. Flame* 169 (2016), pp. 242–260.

[65] G.P. Smith et al. *GRI-Mech 3.0*. http://www.me.berkeley.edu/gri_mech/. 1999.

[66] University of California at San Diego. *“Chemical-Kinetic Mechanisms for Combustion Applications”, San Diego Mechanism web page, Mechanical and Aerospace Engineering (Combustion Research), University of California at San Diego*. http://combustion.ucsd.edu. 2011.

[67] A.A. Konnov. “Implementation of the NCN pathway of prompt-NO formation in the detailed reaction mechanism”. In: *Combust. Flame* 156.11 (2009), pp. 2093–2105.

[68] E. Ranzi et al. “Hierarchical and comparative kinetic modeling of laminar flame speeds of hydrocarbon and oxygenated fuels”. In: *Prog. Energy Combust. Sci.* 38.4 (2012), pp. 468–501.

[69] G.M.G. Watson, P. Versailles, and J.M. Bergthorson. “NO formation in rich premixed flames of C_1-C_4 alkanes and alcohols”. In: *Proc. Combust. Inst.* 36.31 (2017), pp. 627–635.

[70] C.P. Fenimore. “Formation of nitric oxide in premixed hydrocarbon flames”. In: *Proc. Combust. Inst.* 13.1 (1971), pp. 373–380.

[71] M. Riad Manaa and D.R. Yarkony. “On the mechanism of the reaction CH($\mathrm{X}^2\Pi$) + $\mathrm{N}_2(\mathrm{X}^1\Sigma_g^+) \rightarrow$ HCN($\mathrm{X}^1\Sigma^+$) +N(^{4}S). I. A theoretical treatment of the electronic structure aspects of the intersystem crossing”. In: *J. Chem. Phys.* 95.3 (1991), pp. 1808–1816.

[72] M. Riad Manaa and D.R. Yarkony. “The mechanism of the reaction CH ($\mathrm{X}^2\Pi$) + N_2 ($\mathrm{X}^1\Sigma_g^+$) $\rightarrow$ ($\mathrm{X}^1\Sigma^+$) +N(^{4}S).: II. The intermediate complex region”. In: *Chem. Phys. Lett.* 188.3-4 (1992), pp. 352–358.

[73] L.V. Moskaleva and M.C. Lin. "The spin-conserved reaction CH+N_2 $\rightarrow$ H+NCN: A major pathway to prompt NO studied by quantum/statistical theory calculations and kinetic modeling of rate constant". In: *Proc. Combust. Inst.* 28.2 (2000), pp. 2393–2401.

[74] L.V. Moskaleva, W.S. Xia, and M.C. Lin. "The CH+N_2 reaction over the ground electronic doublet potential energy surface: a detailed transition state search". In: *Chem. Phys. Lett.* 331.2-4 (2000), pp. 269–277.

[75] J.A. Sutton and J.W. Fleming. "Towards accurate kinetic modeling of prompt NO formation in hydrocarbon flames via the NCN pathway". In: *Combust. Flame* 154.3 (2008), pp. 630–636.

[76] J.A. Sutton, B.A. Williams, and J.W. Fleming. "Laser-Induced Fluorescence measurements of NCN in low-pressure $CH_4/O_2/N_2$ flames and its role in prompt NO formation". In: *Combust. Flame* 153.3 (2008), pp. 465–478.

[77] P.A. Berg, D.A. Hill, A.R. Noble, G.P. Smith, J.B. Jeffries, and D.R. Crosley. "Absolute CH concentration measurements in low-pressure methane flames: comparisons with model results". In: *Combust. Flame* 121.1-2 (2000), pp. 223–235.

[78] J.A. Sutton, B.A. Williams, and J.W. Fleming. "Investigation of NCN and prompt-NO formation in low-pressure C_1-C_4 alkane flames". In: *Combust. Flame* 159.2 (2012), pp. 562–576.

[79] J.M. Bergthorson. "Experiments and modeling of impinging jets and premixed hydrocarbon flames". PhD thesis. California Institute of Technology, 2005.

[80] J.M. Bergthorson, D.G. Goodwin, and P.E. Dimotakis. "Particle streak velocimetry and CH laser-induced fluorescence diagnostics in strained, premixed, methane-air flames". In: *Proc. Combust. Inst.* 30 (2005), pp. 1637–1644.

[81] J.M. Bergthorson and P.E. Dimotakis. "Premixed laminar C_1–C_2 stagnation flames: Experiments and simulations with detailed thermochemistry models". In: *Proc. Combust. Inst.* 31.1 (2007), pp. 1139–1147.

[82] J.M. Bergthorson, S.D. Salusbury, and P.E. Dimotakis. "Experiments and modelling of premixed laminar stagnation flame hydrodynamics". In: *J. Fluid Mech.* 681 (2011), pp. 1–30.

[83] B.A. Williams and J.W. Fleming. "Experimental and modeling study of NO formation in 10 torr methane and propane flames: Evidence for additional prompt-NO precursors". In: *Proc. Combust. Inst.* 31 (2007), pp. 1109–1117.

[84] L. Pillier, A. El Bakali, X. Mercier, A. Rida, J.F. Pauwels, and P. Desgroux. “Influence of C_2 and C_3 compounds of natural gas on NO formation: An experimental study based on LIF/CRDS coupling”. In: *Proc. Combust. Inst.* 30.1 (2005), pp. 1183–1191.

[85] M. Frenklach, H. Wang, and M.J. Rabinowitz. “Optimization and analysis of large chemical kinetic mechanisms using the solution mapping method - combustion of methane”. In: *Prog. Energy Combust. Sci.* 18 (1992), pp. 47–73.

[86] M. Frenklach. “Transforming data into knowledge - Process Informatics for combustion chemistry”. In: *Proc. Combust. Inst.* 31.1 (2007), pp. 125–140.

[87] R. Bunsen. “LXV. On the temperature of the flames of carbonic oxide and hydrogen”. In: *Philos. Mag. Series 4* 34.233 (1867), pp. 489–502.

[88] F.E. Mallard and H. Le Chatelier. “Recherches expérimentales et théoriques sur la combustion des mélanges gazeux et explosifs. Deuxième mémoire sur la vitesse de propagation de la flamme dans les mélanges gazeux”. In: *Ann. des Mines* 8.4 (1883), pp. 296–378.

[89] G.E. Andrews and D. Bradley. “Determination of burning velocities: A critical review”. In: *Combust. Flame* 18 (1972), pp. 133–153.

[90] C.K. Law. “Fuel options for next-generation chemical propulsion”. In: *AIAA J.* 50.1 (2012), pp. 19–36.

[91] F.N. Egolfopoulos, N. Hansen, Y. Ju, K. Kohse-Höinghaus, C.K. Law, and F. Qi. “Advances and challenges in laminar flame experiments and implications for combustion chemistry”. In: *Prog. Energy Combust. Sci.* 43 (2014), pp. 36–67.

[92] P. Versailles, G.M.G. Watson, A.C.A. Lipardi, and J.M. Bergthorson. “Quantitative CH measurements in atmospheric-pressure, premixed flames of C_1-C_4 alkanes”. In: *Combust. Flame* 165 (2016), pp. 109–124.

[93] J. Luque, P.A. Berg, J.B. Jeffries, G.P. Smith, D.R. Crosley, and J.J. Scherer. “Cavity ring-down absorption and laser-induced fluorescence for quantitative measurements of CH radicals in low-pressure flames”. In: *Appl. Phys. B* 78.1 (2004), pp. 93–102.

[94] J. Luque, G.P. Smith, and D.R. Crosley. “Quantitative CH determinations in low-pressure flames”. In: *Proc. Combust. Inst.* 26.1 (1996), pp. 959–966.

[95] P.A. Berg, D.A. Hill, A.R. Noble, G.P. Smith, J.B. Jeffries, and D.R. Crosley. “Absolute CH concentration measurements in low pressure hydrocarbon flames: comparison with model predictions”. In: *35th Aerospace Sciences Meeting*. Paper 97-0905. Reno, Nevada, 1997.

[96] J. Luque and D.R. Crosley. “Absolute CH concentrations in low-pressure flames measured with laser-induced fluorescence”. In: *Appl. Phys. B* 63.1 (1996), pp. 91–98.

[97] R.G. Joklik, J.W. Daily, and W.J. Pitz. “Measurements of CH radical concentrations in an acetylene/oxygen flame and comparisons to modeling calculations”. In: *Proc. Combust. Inst.* 21.1 (1986), pp. 895–904.

[98] J. Luque, R.J.H. Klein-Douwel, J.B. Jeffries, G.P. Smith, and D.R. Crosley. “Quantitative laser-induced fluorescence of CH in atmospheric pressure flames”. In: *Appl. Phys. B* 75 (2002), pp. 779–790.

[99] J.A. Sutton and J.F. Driscoll. “Optimization of CH fluorescence diagnostics in flames: range of applicability and improvements with hydrogen addition”. In: *Appl. Opt.* 42.15 (2003), pp. 2819–2828.

[100] K.T. Walsh, M.B. Long, M.A. Tanoff, and M.D. Smooke. “Experimental and computational study of CH, CH^*, and OH^* in an axisymmetric laminar diffusion flame”. In: *Proc. Combust. Inst.* (1998), pp. 615–623.

[101] C. Gibaud, J.A. Snyder, V. Sick, and R.P. Lindstedt. “Laser-Induced Fluorescence measurements and modeling of absolute CH concentrations in strained laminar methane/air diffusion flames”. In: *Proc. Comb. Inst.* 30.1 (2005), pp. 455–463.

[102] S.V. Naik and N.M. Laurendeau. “Measurements of absolute CH concentrations by cavity ring-down spectroscopy and linear laser-induced fluorescence in laminar, counterflow partially premixed and nonpremixed flames at atmospheric pressure”. In: *Appl. Opt.* 43.26 (2004), pp. 5116–5125.

[103] M.W. Renfro, A. Chaturvedy, and N.M. Laurendeau. “Semi-quantitative measurements of CH concentration in atmospheric-pressure counterflow diffusion flames using picosecond laser-induced fluorescence”. In: *Combust. Sci. Tech.* 169.1 (2001), pp. 25–43.

[104] R. Evertsen, R.L. Stolk, and J.J. Ter Meulen. “Investigations of cavity ring down spectroscopy applied to the detection of CH in atmospheric flames”. In: *Combust. Sci. Tech.* 149.1-6 (1999), pp. 19–34.

[105] K. Schofield and M. Steinberg. “CH and C_2 measurements imply a radical pool within a pool in acetylene flames”. In: *J. Phys. Chem. A* 111 (2007), pp. 2098–2114.

[106] P.A. Bonczyk and J.A. Shirley. “Measurement of CH and CN concentration in flames by laser-induced saturated fluorescence”. In: *Combust. Flame* 34 (1979), pp. 253–264.

[107] P.A. Bonczyk and J.F. Verdieck. “Laser-induced saturated fluorescence investigations of CH, CN and NO in flames”. In: *Combust. Flame* 34 (1981), pp. 253–264.

[108] J.F. Verdieck and P.A. Bonczyk. “Laser-induced saturated fluorescence investigations of CH, CN and NO in flames”. In: *Proc. Combust. Inst.* 18.1 (1981), pp. 1559–1566.

[109] X. Mercier, P. Jamette, J.F. Pauwels, and P. Desgroux. “Absolute CH concentration measurements by cavity ring-down spectroscopy in an atmospheric diffusion flame”. In: *Chem. Phys. Lett.* 305.5-6 (1999), pp. 334–342.

[110] K.A. Peterson and D.B. Oh. “High-sensitivity detection of CH radicals in flames by use of a diode-laser-based near-ultraviolet light source”. In: *Opt. Lett.* 24.10 (1999), pp. 667–669.

[111] S.V. Naik and N.M. Laurendeau. “LIF measurements and chemical kinetic analysis of methylidyne formation in high-pressure counter-flow partially premixed and non-premixed flames”. In: *Appl. Phys. B* 79.7 (2004), pp. 891–905.

[112] Reaction Design. *Chemkin-Pro Release 15131*. San Diego, 2013.

[113] D.D. Thomsen and N.M. Laurendeau. “LIF measurements and modeling of nitric oxide concentration in atmospheric counterflow premixed flames”. In: *Combust. Flame* 124 (2001), pp. 350–369.

[114] R.J. Kee, J.A. Miller, G.H. Evans, and G. Dixon-Lewis. “A computational model of the structure and extiction of strained, opposed flow, premixed methane-air flames”. In: *Proc. Combust. Inst.* 22.2 (1989), pp. 1479–1494.

[115] U. Niemann, K. Seshadri, and F.A. Williams. “Accuracies of laminar counterflow flame experiments”. In: *Combust. Flame* 162 (2015), pp. 1540–1549.

[116] R.F. Johnson, A.C. Vandine, G.L. Esposito, and H.K. Chelliah. “On the axisymmetric counterflow flame simulations : is there an optimal nozzle diameter and separation distance to apply quasi one-dimensional theory ?” In: *Combust. Sci. Technol.* 187.1–2 (2015), pp. 37–59.

[117] A.C. Eckbreth. *Laser Diagnostics for Combustion Temperature and Species*. Taylor & Francis, 1996.

[118] J.W. Daily. “Laser induced fluorescence spectroscopy in flames”. In: *Prog. Energy Combust. Sci.* 23.2 (1997), pp. 133–199.

[119] K. Kohse-Höinghaus. “Laser techniques for the quantitative detection of reactive intermediates in combustion systems”. In: *Prog. Energy Combust. Sci.* 20.3 (1994), pp. 203–279.

[120] J.R. Reisel, C.D. Carter, and N.M. Laurendeau. “Measurements and modeling of OH and NO in premixed $\mathrm{C_2H_6/O_2/N_2}$ flames at atmospheric pressure”. In: *Energy Fuels* 11.5 (1997), pp. 1092–1100.

[121] J.D. Munzar, A. Zia, P. Versailles, R. Jiménez, B. Akih-Kumgeh, and J.M. Bergthorson. “Comparison of laminar flame speeds, extinction strain rates and vapour pressures of Jet A-1/HRJ biojet fuel blends”. In: *Proc. ASME Turbo Expo 2014*. Paper GT2014-25951. Düsseldorf, Germany, 2014.

[122] G.A. Chung, B. Akih-Kumgeh, G.M.G. Watson, and J.M. Bergthorson. “NO_x formation and flame velocity profiles of iso- and n- isomers of butane and butanol”. In: *Proc. Combust. Inst.* 34.1 (2012), pp. 831–838.

[123] P. Versailles and J.M. Bergthorson. “Optimized laminar axisymmetrical nozzle design using a numerically-validated Thwaites method”. In: *J. Fluids Eng.* 134.10 (2012).

[124] F.N. Egolfopoulos, H. Zhang, and Z. Zhang. “Wall effects on the propagation and extinction of steady, strained, laminar premixed flames”. In: *Combust. Flame* 109.1-2 (1997), pp. 237–252.

[125] J.M. Bergthorson and P.E. Dimotakis. “Particle velocimetry in high-gradient / high-curvature flows”. In: *Exp. Fluids* 41.2 (2006), pp. 255–263.

[126] L. Benezech, J.M. Bergthorson, and P. Dimotakis. “Premixed laminar $\mathrm{C_3H_8}$- and $\mathrm{C_3H_6}$-air stagnation flames: Experiments and simulations with detailed kinetic models”. In: *Proc. Combust. Inst.* 32.1 (2009), pp. 1301–1309.

[127] D. Woiki, M. Votsmeier, D.F. Davidson, R.K. Hanson, and C.T. Bowman. “CH-radical concentration measurements in fuel-rich $\mathrm{CH_4/O_2}$/Ar and $\mathrm{CH_4/O_2}$/NO/Ar mixtures behind shock waves”. In: *Combust. Flame* 113.4 (1998), pp. 624–626.

[128] University of California at San Diego. *“Chemical-Kinetic Mechanisms for Combustion Applications”, San Diego Mechanism web page, Mechanical and Aerospace Engineering (Combustion Research)*. http://combustion.ucsd.edu. 2005.

[129] M.V. Petrova and F.A. Williams. “A small detailed chemical-kinetic mechanism for hydrocarbon combustion”. In: *Combust. Flame* 144 (2006), pp. 526–544.

[130] S.C. Li and F.A. Williams. “Formation of NO_x, CH_4, and C_2 species in laminar methanol flames”. In: *Proc. Combust. Inst.* 27.1 (1998), pp. 485–493.

[131] S.C. Li and F.A. Williams. “NO_x formation in two-stage methane-air flames”. In: *Combust. Flame* 118.3 (1999), pp. 399–414.

[132] P. Saxena and F.A. Williams. “Numerical and experimental studies of ethanol flames”. In: *Proc. Combust. Inst.* 31.1 (2007), pp. 1149–1156.

[133] H. Wang et al. *USC Mech Version II. High-Temperature Combustion Reaction Model of H_2/CO/C_1–C_4 Compounds*. http://ignis.usc.edu/USC_Mech_II.htm. 2007.

[134] W.K. Metcalfe, S.M. Burke, S.S. Ahmed, and H.J. Curran. “A hierarchical and comparative kinetic modeling study of C_1-C_2 hydrocarbon and oxygenated fuels”. In: *Int. J. Chem. Kin.* 45.10 (2013), pp. 638–675.

[135] C.W. Zhou et al. “A comprehensive experimental and modeling study of isobutene oxidation”. In: *Combust. Flame* 167 (2016), pp. 353–379.

[136] J.F. Grcar, M.S. Day, and J.B. Bell. “A taxonomy of integral reaction path analysis”. In: *Combust. Theory Model.* 10.4 (2006), pp. 559–579.

[137] B. Vukasinovic, M.K. Smith, and A. Glezer. “Spray characterization during vibration-induced drop atomization”. In: *Phys. Fluids* 16.2004 (2004), pp. 306–316.

[138] P. O’Brien and C. McKenna Neuman. “A wind tunnel study of particle kinematics during crust rupture and erosion”. In: *Geomorphology* 173-174 (2012), pp. 149–160.

[139] B. Lüthi, A. Tsinober, and W. Kinzelbach. “Lagrangian measurement of vorticity dynamics in turbulent flow”. In: *J. Fluid Mech.* 528 (2005), pp. 87–118.

[140] M.G. Echekki T and. Mungal. “Flame speed measurments at the tip of a slot burner: Effects of flame curvature and hydrodynamic stretch”. In: *Proc. Combust. Inst.* 23 (1991), pp. 455–461.

[141] L. Benezech. “Premixed hydrocarbon stagnation flames: Experiments and simulations to validate combustion chemical-kinetic models”. Engineer’s Thesis. California Institute of Technology, 2008.

[142] Y. Ju and C.K. Law. “Dynamics and extinction of non-adiabatic particle-laden premixed flames”. In: *Proc. Combust. Inst.* 28.2 (2000), pp. 2913–2920.

[143] R. Theunissen, F. Scarano, and M.L. Riethmuller. “An adaptive sampling and windowing interrogation method in PIV”. In: *Meas. Sci. Technol.* 18 (2006), pp. 275–287.

[144] M. Glass and I.M. Kennedy. “An improved seeding method for high temperature laser doppler velocimetry”. In: *Combust. Flame* 29 (1977), pp. 333–335.

[145] A. Fortin. *Analyse Numérique pour Ingénieurs - Deuxième édition*. Presses Internationales Polytechnique, 2001.

[146] C.J. Sung, C.K. Law, and R.L. Axelbaum. “Thermophoretic effects on seeding particles in LDV measurements of flames”. In: *Combust. Sci. Technol.* 99 (1994), pp. 119–132.

[147] C.J. Sung, J.S. Kistler, M. Nishioka, and C.K. Law. “Further studies on effects of thermophoresis on seeding particles in LDV measurements of strained flames”. In: *Combust. Flame* 105 (1996), pp. 189–201.

[148] W.W. Hines, D.C. Montgomery, D.M. Goldsman, C.M. Borror, L.-D. Adjengue, and J.-P. Carmichael. *Probabilités et statistique pour ingénieurs*. 1st edition. Translated by L. Collet and J.L. Massé. Chenelière Éducation, 2005, p. 597.

[149] K. Bell (Litron Lasers - North America). Personal communication. Oct. 22, 2012.

[150] J. Luque and D.R. Crosley. *LIFBASE Database and Spectral Simulation Program (Version 1.6)*. Tech. rep. MP 99-009. SRI International, 1999.

[151] E.C. Rea, A.Y. Chang, and R.K. Hanson. “Shock-tube study of pressure broadening of the $A^2\Sigma^+$- $X^2\Pi$ (0,0) band of OH by Ar and N_2”. In: *J. Quant. Spectrosc. Radiat. Transfer* 37.2 (1987), pp. 117–127.

[152] V. Vasudevan, R.K. Hanson, C.T. Bowman, D.M. Golden, and D.F. Davidson. “Shock tube study of the reaction of CH with N_2: overall rate and branching ratio.” In: *J. Phys. Chem. A* 111.46 (2007), pp. 11818–11830.

[153] B.C. Connelly, B.A.V. Bennett, M.D. Smooke, and M.B. Long. “A paradigm shift in the interaction of experiments and computations in combustion research”. In: *Proc. Combust. Inst.* 32.1 (2009), pp. 879–886.

[154] N.L. Garland and D.R. Crosley. “Energy transfer processes in CH $A^2\Delta$ and $B^2\Sigma^-$ in an atmospheric pressure flame”. In: *Appl. Opt.* 24.23 (1985), pp. 4229–4237.

[155] R.J. Cattolica, D. Stepowski, D. Puechberty, and M. Cottereau. “Laser-induced fluorescence of the CH molecule in a low-pressure flame”. In: *J. Quant. Spectrosc. Radiat. Transfer* 32.4 (1984), pp. 363–370.

[156] R.G. Joklik and J.W. Daily. “LIF study of CH $A^2\Delta$ collision dynamics in a low pressure oxy-acetylene flame”. In: *Combust. Flame* 69.2 (1987), pp. 211–219.

[157] S.V. Naik and N.M. Laurendeau. “Spectroscopic, calibration and RET issues for linear laser-induced fluorescence measurements of nitric oxide in high-pressure diffusion flames”. In: *Appl. Phys. B* 79.5 (2004), pp. 641–651.

[158] W.G. Bessler, V. Sick, and J.W. Daily. “A versatile modeling tool for nitric oxide LIF spectra”. In: *Proc. 3rd Joint Meeting, U.S. Sections of the Combust. Inst.* 105 (2003), pp. 1–6.

[159] N.M. Laurendeau. *Statistical Thermodynamics: Fundamentals and Applications*. Cambridge University Press, 2005, p. 466.

[160] K.P. Huber and G. Herzberg. “Constants of Diatomic Molecules”. In: *NIST Chemistry WebBook, NIST Standard Reference Database Number 69*. Ed. by P.J. Linstrom and W.G. Mallard. Gaithersburg, MD: National Institute of Standards and Technology.

[161] V.N. Ochkin. “Appendix D: Information on some diatomic molecules for the identification and processing of low-temperature plasma spectra”. In: *Spectroscopy of Low Temperature Plasma*. Wiley-VCH Verlag GmbH & Co. KGaA, 2009, pp. 505–567.

[162] R.P. Lucht, D.W. Sweeney, and N.M. Laurendeau. “Balanced cross-rate model for saturated molecular fluorescence in flames using a nanosecond pulse length laser”. In: *Applied optics* 19.19 (1980), pp. 3295–3300.

[163] P.H. Paul. “A model for temperature-dependent collisional quenching of OH $A^2\Sigma^+$”. In: *J. Quant. Spectrosc. Radiat. Transfer* 51.3 (1994), pp. 511–524.

[164] D.R. Crosley, R.A. Copeland, and J.B. Jeffries. *State-specific energy transfer in diatomic radicals*. Tech. rep. Menlo Park, CA, USA: SRI International, 1988, p. 28.

[165] N.L. Garland and D.R. Crosley. “On the collisional quenching of electronically excited OH, NH and CH in flames”. In: *Proc. Comb. Inst.* 21.1 (1988), pp. 1693–1702.

[166] K. Kohse-Höinghaus, J.B. Jeffries, R.A. Copeland, G.P. Smith, and D.R. Crosley. “The quantitative LIF determination of OH concentrations in low-pressure flames”. In: *Proc. Comb. Inst.* 22.1 (1989), pp. 1857–1866.

[167] W.P. Partridge and N.M. Laurendeau. “Formulation of a dimensionless overlap function to account for spectrally distributed interactions in fluorescence studies”. In: *Appl. optics* 34.15 (1995), pp. 2645–2647.

[168] A. Bülter, U. Rahmann, A. Brockhinke, and K. Kohse-Höinghaus. “Study of energy transfer processes in CH as prerequisite for quantitative minor species concentration measurements”. In: *Appl. Phys. B* 79.1 (2004), pp. 113–120.

[169] M. Tamura et al. “Collisional quenching of CH(A), OH(A), and NO(A) in low pressure hydrocarbon flames”. In: *Combust. Flame* 114.3-4 (1998), pp. 502–514.

[170] M.W. Renfro, K.K. Venkatesan, and N.M. Laurendeau. “Cross sections for quenching of CH $\mathrm{A}^2\Delta$, $\nu' = 0$, by $\mathrm{N_2}$ and $\mathrm{H_2O}$ from 1740 to 2160 K”. In: *Proc. Combust. Inst.* 29 (2002), pp. 2695–2702.

[171] B. Nizamov, P.J. Dagdigian, Y.R. Tzeng, and M.H. Alexander. “Experimental and theoretical study of Λ-doublet resolved rotationally inelastic collisions of highly rotationally excited CH($\mathrm{A}^2\Delta$, $v = 0$) with Ar”. In: *J. Chem. Phys.* 115.2 (2001), pp. 800–809.

[172] H.J. Crichton, C. Murray, and K.G. McKendrick. “Rotational energy transfer in collisions of CH $\mathrm{A}^2\Delta$, $v = 0$ with Ar, $\mathrm{N_2}$ and $\mathrm{CO_2}$”. In: *Phys. Chem. Chem. Phys.* 4.23 (2002), pp. 5768–5777.

[173] J. Joshua Driscoll, V. Sick, P.E. Schrader, and R.L. Farrow. “Measurements of NO distributions and fluorescence lifetimes in a non-premixed counterflow $\mathrm{CH_4}$/air flame using picosecond time-resolved laser-induced fluorescence”. In: *Proc. Combust. Inst.* 29.2 (2002), pp. 2719–2726.

[174] J.A. Sutton and J.F. Driscoll. “Rayleigh scattering cross sections of combustion species at 266, 355, and 532 nm for thermometry applications.” In: *Opt. Lett.* 29.22 (2004), pp. 2620–2622.

[175] T.A. Cool and P.J.H. Tjossem. “Direct observations of chemi-ionization in hydrocarbon flames enhanced by laser excited $\mathrm{CH}^*(\mathrm{A}^2\Delta)$ and $\mathrm{CH}^*(\mathrm{B}^2\Sigma^-)$”. In: *Chem. Phys. Lett.* 111.1-2 (1984), pp. 82–88.

[176] W.E. Boyce and R.C. DiPrima. *Elementary Differential Equations and Boundary Value Problems*. John Wiley & Sons, Inc., 2001.

[177] J.D. Corless, J.A. West, J. Bromage, and C.R. Stroud. “Pulsed single-mode dye laser for coherent control experiments”. In: *Rev. Sci. Instrum.* 68 (1997), pp. 2259–2264.

[178] G.P. Smith, J. Luque, C. Park, J.B. Jeffries, and D.R. Crosley. “Low pressure flame determinations of rate constants for OH(A) and CH(A) chemiluminescence”. In: *Combust. Flame* 131.02 (2002), pp. 59–69.

[179] G.P. Smith, C. Park, and J. Luque. “A note on chemiluminescence in low-pressure hydrogen and methane-nitrous oxide flames”. In: *Combust. Flame* 140.4 (2005), pp. 385–389.

[180] A.L. Sánchez and F.A. Williams. “Recent advances in understanding of flammability characteristics of hydrogen”. In: *Prog. Energy Combust. Sci.* 41.1 (2014), pp. 1–55.

[181] J. Hall, J. de Vries, A. Amadio, and E.L. Petersen. “Towards a kinetics model of CH chemiluminescence”. In: *43rd AIAA Aerosp. Sci. Meet. Exhib.* Aerospace Sciences Meetings. AIAA, 2005.

[182] V.N. Nori and J.M. Seitzman. “CH^* chemiluminescence modeling for combustion diagnostics”. In: *Proc. Combust. Inst.* 32 (2009), pp. 895–903.

[183] J. de Vries, J.M. Hall, S.L. Simmons, M.J.A. Rickard, D.M. Kalitan, and E.L. Petersen. “Ethane ignition and oxidation behind reflected shock waves”. In: *Combust. Flame* 150.1-2 (2007), pp. 137–150.

[184] E.L. Petersen, M. Kopp, N. Donato, and F. Güthe. “Assessment of current chemiluminescence kinetics models at engine conditions”. In: *J. Eng. Gas Turbines Power* 134.5 (2012), pp. 51501-1–51501-7.

[185] M. Bozkurt, M. Fikri, and C. Schulz. “Investigation of the kinetics of OH^* and CH^* chemiluminescence in hydrocarbon oxidation behind reflected shock waves”. In: *Appl. Phys. B* 107.3 (2012), pp. 515–527.

[186] T. Kathrotia, U. Riedel, A. Seipel, K. Moshammer, and A. Brockhinke. “Experimental and numerical study of chemiluminescent species in low-pressure flames”. In: *Appl. Phys. B* 107.3 (2012), pp. 571–584.

[187] R.M.I. Elsamra, S. Vranckx, and S.A. Carl. “$CH(A^2\Delta)$ formation in hydrocarbon combustion: the temperature dependence of the rate constant of the reaction $C_2H + O_2 \rightarrow CH(A^2\Delta)+CO_2$”. In: *J. Phys. Chem.* 109 (2005), pp. 10287–10293.

[188] K. Devriendt, H. Van Look, B. Ceursters, and J. Peeters. “Kinetics of formation of chemiluminescent $CH(A^2\Delta)$ by the elementary reactions of $C_2H(X^2\Sigma^+)$ with $O(^3P)$ and $O_2(X^3\Sigma_g^-)$: A pulse laser photolysis study”. In: *Chem. Phys. Lett.* 261.4-5 (1996), pp. 450–456.

[189] E. Goos, A. Burcat, and B. Ruscic. *Extended Third Millenium Ideal Gas Thermochemical Database with updates from Active Thermochemical Tables*. http://burcat.technion.ac.il/dir. 2016.

[190] C.K. Law. *Combustion Physics*. Cambridge University Press, 2006, p. 722.

[191] K.K. Kuo. *Principles of Combustion*. 2nd. John Wiley & Sons, Inc., 2005, p. 732.

[192] E. Hecht. *Optics - 3rd edition*. Addison-Wesley, 1998, p. 694.

[193] R.J. Adrian and C.S. Yao. "Pulsed laser technique application to liquid and gaseous flows and the scattering power of seed materials." In: *App. Optics* 24.1 (1985), pp. 44–52.

[194] W.C. Gardiner, Y. Hidaka, and T. Tanzawa. "Refractivity of combustion gases". In: *Combust. Flame* 40 (1981), pp. 213–219.

[195] A. Wloka (Sirah Lasertechnik). Personal communication. July 29, 2016.

[196] J. Warnatz. "The structure of laminar alkane-, alkene-, and acetylene flames". In: *Proc. Combust. Inst.* 18.1 (1981), pp. 369–384.

[197] K. Schofield. "Large scale chemical kinetic models of fossil fuel combustion: adequate as engineering models-No More, no Less". In: *Energy Fuels* 26.9 (2012), pp. 5468–5480.

[198] D.L. Baulch et al. "Evaluated kinetic data for combustion modelling". In: *J. Phys. Chem. Ref. Data* 21.3 (1992), pp. 411–734.

[199] D.L. Baulch et al. "Evaluated kinetic data for combustion modeling: Supplement II". In: *J Phys. Chem Ref. Data* 34.3 (2005), pp. 757–1397.

[200] S. Rolland and J.M. Simmie. "The comparison of detailed chemical kinetic mechanisms; forward versus reverse rates with CHEMRev". In: *Int. J. Chem. Kinet.* 37.1 (2005), pp. 119–125.

[201] R.G. Gilbert, K. Luther, and J. Troe. "Theory of thermal unimolecular reactions in the fall-off range. II Weak collision rate constants". In: *Ber. Bunsenges. Phys. Chem.* 87 (1983), pp. 169–177.

[202] W. Tsang and R.F. Hampson. "Chemical kinetic data base for combustion chemistry. Part I. Methane and related compounds". In: *J. Phys. Chem. Ref. Data* 15.3 (1986), pp. 1087–1279.

[203] A. Fomin, T. Zavlev, V.A. Alekseev, I. Rahinov, S. Cheskis, and A.A. Konnov. "Experimental and modelling study of $^1CH_2$ in premixed very rich methane flames". In: *Combust. Flame* 171 (2016), pp. 198–210.

[204] CRECK Modeling Group. *CRECK Kinetics Model (Version 1412)*. http://creckmodeling.chem.polimi.it/index.php/menu-kinetics/menu-kinetics-detailed-mechanisms. 2014.

[205] P. Gokulakrishnan et al. "Experiments and modeling of propane combustion with vitiation". In: *Combust. Flame* 161.8 (2014), pp. 2038–2053.

[206] K.M. Leung and R.P. Lindstedt. "Detailed kinetic modeling of C_1-C_3 alkane diffusion flames". In: *Combust. Flame* 102.94 (1995), pp. 129–160.

[207] D.L. Baulch et al. "Evaluated kinetic data for combustion modeling. Supplement I". In: *J. Phys. Chem. Ref. Data* 23.6 (1994), pp. 847–848.

[208] P. Glarborg, J.A. Miller, and R.J. Kee. "Kinetic modeling and sensitivity analysis of nitrogen oxide formation in well-stirred reactors". In: *Combust. Flame* 65 (1986), pp. 177–202.

[209] A.W. Jasper, S.J. Klippenstein, L.B. Harding, and B. Ruscic. "Kinetics of the reaction of methyl radical with hydroxyl radical and methanol decomposition". In: *J. Phys. Chem. A* 111.10 (2007), pp. 3932–3950.

[210] C. Dombrowsky and H.G. Wagner. "Investigation of the $^3CH_2$ + O_2 reaction in shock waves". In: *Ber. Bunsenges. Phys. Chem.* 96.8 (1992), pp. 1048–1055.

[211] P.-F. Lee, H. Matsui, W.-Y. Chen, and N.-S. Wang. "Production of H and $O\,(^3P)$ atoms in the reaction of CH_2 with O_2". In: *J. Phys. Chem. A* 116.37 (2012), pp. 9245–9254.

[212] T. Böhland, F. Temps, and H.G. Wagner. "Direct determination of the rate constant for the reaction $CH_2 + O_2$ with a LMR-spectrometer". In: *Ber. Bunsenges. Phys. Chem.* 88.5 (1984), pp. 455–458.

[213] D.C. Darwin, A.T. Young, H.S. Johnston, and C.B. Moore. "Rate constants for $CH_2\left(\tilde{X}^3 B_1\right)$ removal by O_2, NO and C_2H_2 from infrared diode laser flash kinetic spectroscopy". In: *J. Phys. Chem.* 93.3 (1989), pp. 1074–1078.

[214] C. Vinckier and W. Debruyn. "Temperature dependence of the reactions of methylene with oxygen atoms, oxygen, and nitric oxide". In: *J. Phys. Chem.* 83.16 (1979), pp. 2057–2062.

[215] C. Dombrowsky, S.M. Hwang, M. Röhrig, and H.G. Wagner. "The formation of O and H Atoms in the reaction of CH_2 with O_2 at high temperatures". In: *Ber. Bunsenges. Phys. Chem.* 96.2 (1992), pp. 194–198.

[216] Y. Hidaka, K. Kimura, K. Hattori, and T. Okuno. "Shock tube and modeling study of ketene oxidation". In: *Combust. Flame* 106.1-2 (1996), pp. 155–167.

[217] D.G. Goodwin, H.K. Moffat, and R.L. Speth. *Cantera: An Object-oriented Software Toolkit for Chemical Kinetics, Thermodynamics, and Transport Processes*. http://www.cantera.org. Version 2.2.1. 2016.

[218] A.C.A Lipardi, P. Versailles, G.M.G. Watson, G. Bourque, and J.M. Bergthorson. “Experimental and numerical study on NO_x formation in CH_4-air mixtures diluted with exhaust gas components”. In: *Combust. Flame* 179 (2017), pp. 325–337.

[219] L. Pillier, M. Idir, J. Molet, A. Matynia, and S. De Persis. “Experimental study and modelling of NO_x formation in high pressure counter-flow premixed CH_4/air flames”. In: *Fuel* 150 (2015), pp. 394–407.

[220] D.D. Thomsen, F.F. Kuligowski, and N.M. Laurendeau. “Modeling of NO formation in premixed, high-pressure methane flames”. In: *Combust. Flame* 119.3 (1999), pp. 307–318.

[221] M.C. Drake and R.J. Blint. “Calculations of NO_x formation pathways in propagating laminar, high pressure premixed CH_4/air flames”. In: *Combust. Sci. Technol.* 75.4-6 (1991), pp. 261–285.

[222] J.W. Bozzelli and A.M. Dean. “O+NNH: A possible new route for NO_x formation in flames”. In: *Int. J. Chem. Kinet.* 27 (1995), pp. 1097–1109.

[223] Charlston–Goch, D., B.L. Chadwick, R.J.S. Morrison, A. Campisi, D.D. Thomsen, and N.M. Laurendeau. “Laser-Induced fluorescence measurements and modeling of nitric oxide in premixed flames of CO+H_2+CH_4 and air at high pressures: I.Nitrogen fixation”. In: *Combust. Flame* 125.1-2 (2001), pp. 729–743.

[224] J.R. Reisel and N.M. Laurendeau. “Laser-Induced Fluorescence measurements and modeling of nitric oxide formation in high-pressure flames”. In: *Combust. Sci. Tech.* 98.1-3 (1994), pp. 137–160.

[225] J.R. Reisel and N.M. Laurendeau. “Quantitative LIF measurements and modeling of nitric oxide in high-pressure $C_2H_4/O_2/N_2$ flames”. In: *Combust. Flame* 101 (1995), pp. 141–152.

[226] V.M. Van Essen, A.V. Sepman, A.V. Mokhov, and H.B. Levinsky. “The effects of burner stabilization on Fenimore NO formation in low-pressure, fuel-rich premixed $CH_4/O_2/N_2$ flames”. In: *Proc. Combust. Inst.* 31.1 (2007), pp. 329–337.

[227] J. Lim, J. Gore, and R. Viskanta. “A study of the effects of air preheat on the structure of methane/air counterflow diffusion flames”. In: *Combust. Flame* 121.1-2 (2000), pp. 262–274.

[228] A.B. Sahu and R.V. Ravikrishna. “Quantitative LIF measurements and kinetics assessment of NO formation in H_2/CO syngas–air counterflow diffusion flames”. In: *Combust. Flame* 173 (2016), pp. 208–228.

[229] A. Hossain and Y. Nakamura. “A numerical study on the ability to predict the heat release rate using CH^* chemiluminescence in non-sooting counterflow diffusion flames”. In: *Combust. Flame* 161.1 (2014), pp. 162–172.

[230] S.M. Sarathy et al. “A comprehensive chemical kinetic combustion model for the four butanol isomers”. In: *Combust. Flame* 159.6 (2012), pp. 2028–2055.

[231] P.J. Linstrom and W.G. Mallard, eds. *NIST Chemistry WebBook, NIST Standard Reference Database Number 69*. Gaithersburg MD: National Institute of Standards and Technology.

[232] National Center for Biotechnology Information. *PubChem Compound Database; CID = 281*. https://pubchem.ncbi.nlm.nih.gov/compound/281, Accessed: 2016-06-22.

[233] E.R. Gansner and S.C. North. “An open graph visualization system and its applications to software engineering”. In: *Softw. Pract. Exp.* 30.11 (2000), pp. 1203–1233.

[234] S. Neumark. *Solution of Cubic and Quartic Equations*. Pergamon, 1965.

[235] T. Turányi, L. Zalotai, S. Dóbé, and T. Bérces. “Effect of the uncertainty of kinetic and thermodynamic data on methane flame simulation results”. In: *Phys. Chem. Chem. Phys.* 4.12 (2002), pp. 2568–2578.

[236] Argonne National Laboratory. *“Active Thermochemical Tables, version 1.118”*. Available: http://atct.anl.gov/, Accessed: 2017-02-08.